

# **Comparison of single bubble and bubble swarm behavior in narrow gaps inside flat sheet membrane modules**

vorgelegt von  
Dipl.-Ing.  
Lutz Peter Böhm  
geb. in Berlin

von der Fakultät III – Prozesswissenschaften  
der Technischen Universität Berlin  
zur Erlangung des akademischen Grades

Doktor der Ingenieurwissenschaften  
- Dr.-Ing. -

genehmigte Dissertation

Promotionsausschuss:

Vorsitzender: Prof. Dr.-Ing. Felix Ziegler

Gutachter: Prof. Dr. Pierre Bérubé

Gutachter: Prof. Dr.-Ing. Matthias Kraume

Gutachter: Prof. Dr.-Ing. Michael Schlüter

Tag der wissenschaftlichen Aussprache: 16.04.2015

Berlin 2015



“Your project is so easy!” (unnamed colleague)

Me to a student who was looking for a Bachelor thesis project:

“Do you want me to show you my project as well?”

The student’s reply: “No, I know your project, it’s boring!”

“They say, the definition of madness is doing the same thing  
and expecting a different result.” (The Hives - Try It Again)

# Acknowledgements

This first paragraph is in German: Vielen Dank an meine Familie, im Speziellen an meine Eltern. Ihr habt mich immer in meinem Leben unterstützt und vor allem meine Ausbildung vorangetrieben. Ihr seid in unterschiedlichen Aspekten meines Lebens wichtig, aber in Bezug auf die Promotion hat mein Vater sicherlich den größten Einfluss. Du hast mich in diversen Gesprächen vor der Promotion, dazu bringen wollen, diese überhaupt erst zu machen, und während dessen hast du mich auf deine Art und Weise antreiben wollen. Das war nicht immer leicht für mich, aber ich hoffe, du bist mit dem Endprodukt (das es bis hierhin erstmal ist; ich denke, du wirst vermutlich nicht aufhören, mich antreiben zu wollen) zufrieden. Vielen Dank aber auch an meine Mutter dafür, eine Art ausgleichenden Gegenpart dazu darzustellen.

And now in English: Thank you to Prof. Kraume. From the beginning on, I felt the trust you had in me although I quickly had to learn that trust is followed by working load. You (often) surprised me with soon to come colleagues from somewhere in the world that should work on my project. Mostly, it worked out somehow and, although often strenuous, mostly to the best. I also want to thank you for the opportunity to present my work at such numerous and diverse conferences around the world. Thank you for your guidance throughout the whole project.

Anja, first of all, thank you for leaving the Chair because that is how I got my job. But actually, I have to start earlier: Thanks for trusting me without knowing me too well and getting me in contact with the guys at UNSW in Sydney. This was a great experience and, I think, it had a huge impact on me, personally and professionally, nonetheless as it was kind of a foundation of our friendship. We had a great time there and it gave me the chance to meet most of the ‘big guys’ in MBR research before even knowing who they are. As they still don’t know me, I still keep on telling them, whenever I meet them on a conference, that I once served them beer in Australia. Since then you have always been an almost always accessible membrane specialist to discuss professional matters with and, maybe even more important, a long-term member of the group available to discuss Chair internal matters, helping sometimes to put things in the right perspective. Last but not least, thank you for your help to improve this thesis.

I want to thank all colleagues I had, while working at the Chair. I decided to work here because of the atmosphere and I was right with my decision. I am lucky to say that a lot of you are not only colleagues but friends. Only some can be listed here (sorted alphabetically): Ansor, for the opportunity to do my internship in Switzerland, Christoph, for introducing the love-office, Friedemann, for being such a strong personality in the group, Helmut, for being Helmut, I never met someone like you, Jochen, for being the surprising personality you are, Johannes, I am happy that I once wrote in an Excel file ‘quite okay’ under your name (special thanks for the proof reading), Jörn, my tell-me-more bro, Manuel, for the constant enlargement of your working space, Mirco, for being such a professional role-model, Niklas, for being a social life monster and brainiac at the same time (special thanks for the proof reading), Sebastian, for being my first boss at the Chair, So-Jin, for being who you are, Stefan, for constantly losing the manger game, Subhamoy and Evgenij, for being this unique Indo-Russian combination of office mates, Tina, for your styling tips, Ute, for your enduring laugh, no matter what, Vera, for giving me the first experience in Powerpoint Karaoke and, finally, Verena, for being a fellow student, colleague and friend for such a long time.

I want to thank Professor Pierre Bérubé for teaching me the EDM (although I cursed the technique sometimes) and for giving me the opportunity to work in his group at UBC. Living and working in Vancouver for a few months is not the worst thing that happened to me. Additionally, thank you to Jarda (Jaroslav) Tihon and Professor Ondrej Wein for your help on enhancing my knowledge of the EDM and your hospitality during my visit in Prague.

During the numerous trips I did, I met important persons who influenced my work and life. Thank you to: Steffen Buetehorn, for the great time in Australia and the friendship that followed, Nicolas Ratkovich, for being such a nice guy, professionally and personally, and Sepideh Jankhah, for our philosophical discussions as we are doing a Doctor of Philosophy (which I am actually not but that didn’t convince you).



Thank you to all the helping hands who are usually more in the background. Nothing would work without you. Thanks you to: Andrea, for your sheer interest in my project and your support in making progress, to Rainer, Werner and the Azubis, for your enduring dedication to make things work, to Ulla, for keeping bureaucracy away from us although you are often exasperated about it, and to Bernd and Gabi, for trying to keep up with all the inquiries we have. Finally, although sadly not possible in person anymore, I want to thank Christine, one of the good souls at the Chair when I started working here, always dedicated to safety and justice, never afraid to stand up for her opinion, now resting in peace in nature as it was her wish.

I want to thank all students working on my project and I do so chronologically in the following: Alex, for our simultaneous EDM learning experience, Tim, for his weekend trips to Berlin to do the LabVIEW programming which still works so perfectly smooth that it's hard to believe, Jan-Paul, for his unbelievable skills in improving the hardware and writing a Matlab code making it possible in the first place to handle this huge amount of collected data, Nikolay, for his interest he put in the serial tests using EDM and PIV, Eva, for our great simultaneous PIV learning experience resulting in such a good thesis that it will be a standard work for almost everybody working with PIV at our Chair in the future, Sven, for his effort on the Xanthan solution experiments, Kenny, for the enthusiasm he had for the HSC measurements, Paul, for his natural self-dependence in developing the HSC analysis up to such a high standard, Tokihiro, for the effort he put into learning to operate the rig in such a short time resulting in having his fair share on generating substantial data, Sascha, for having the patience on getting the bubble swarm experiments to work and having the endurance to analyze all the data with all the 'great' ideas to incorporate I had like every second day, Juliane, for her enthusiasm on the project and her open-minded nature and finally Patrick, for his EDM hardware building skills and the really unique bubble swarm-in-non-Newtonian liquid experiments.

I also want to use this opportunity to thank my friends for their patience with me. The last years, this job was very time-demanding which is why friendships suffered from it. Balancing life and work was not an easy task to do. A guilty conscience was my constant companion. Although I am not sure I can keep up to this promise, I want to do better in the future.

Finally, I want to thank the love of my life and mother of our son. Without your patience and understanding, especially during the writing period of this thesis, this would not have been possible. Additionally, thank you to my son who is still smiling at me, even if I come home late, sometimes even so late that I can only see him smiling while he dreams.

For TnT.

# Table of Content

1	Introduction .....	1
2	State of the art .....	4
3	Scope and outline of this thesis .....	21
4	Materials and methods .....	26
4.1	The experimental set-up .....	26
4.2	The continuous phases.....	30
4.3	High Speed Camera Imaging (HSC) .....	35
4.4	Particle Image Velocimetry (PIV) .....	38
4.5	The electrodiffusion method (EDM) .....	42
5	Results and discussion.....	46
5.1	Single bubbles rising in the flow channel.....	46
5.1.1	Rising behavior of a single bubble.....	46
5.1.2	Flow field in the liquid surrounding single bubble.....	56
5.1.3	Wall shear stress generated by a single bubble .....	66
5.1.4	Conclusions from the single bubble experiments.....	71
5.2	Bubble swarms rising in the flow channel.....	73
5.2.1	Flow behavior of the bubble swarm .....	73
5.2.2	Wall shear stress generated by the bubble swarm .....	80
5.2.3	Conclusions from the bubble swarm experiments.....	84
5.3	Engineering recommendations .....	85
6	Summary .....	90
6.1	Conclusions .....	90
6.2	Outlook.....	92
7	References .....	94
8	Appendix .....	105
8.1	Own publications and presentations .....	105
8.1.1	Articles in Journals.....	105
8.1.2	Presentations and Posters with publication in Proceedings.....	106
8.1.3	Presentations and Posters without publication .....	107
8.1.4	Supervised student projects.....	109
8.2	Own publications used for the cumulative thesis (full text) .....	111

# Table of Figures

Figure 1.1: Sorting of particulate two-phase systems into processes and facilities by the respective continuous phase (grey boxes are the branches of interest for this thesis, only cases with two different phases are shown).....	1
Figure 1.2: (a) Scheme of an aerated flat sheet membrane module, (b) illustration of the rectangular spacing between the membrane plates and (c) profile of a single bubble and (d) bubble swarm rising in this confining geometry .....	2
Figure 2.1: Forces acting on a deposited particle normal to the membrane surface [1] .....	5
Figure 3.1: Structure of the thesis .....	24
Figure 4.1: (a) Scheme of the flow channel used in the single bubble EDM measurements (b) and of the flow channel used in the single bubble (SB) HSC/PIV and bubble swarm (BS) HSC/EDM measurements (in parts from [3, 6]) .....	27
Figure 4.2: Results of the calibration test of the propeller flow meter used with Xanthan solution .....	28
Figure 4.3: (a) Flow sheet for the single bubble (SB) HSC/PIV/EDM and (b) the changed part for the bubble swarm (BS) HSC/EDM investigation (in parts from [3, 6]) .....	29
Figure 4.4: Apparent viscosity of the waters and different Xanthan solutions against the shear rate and of activated MBR sludge based on the correlation by Rosenberger et al. [131] .....	31
Figure 4.5: Interfacial tension of water doped with sodium sulphate, SDS and the EDM salts .....	32
Figure 4.6: (a) Field of view in the HSC experiments, either for the movement parallel to the plates (x-y-plane) or between the plates (y-z-plane) and (b) example for a rising path of a single bubble ( $d_c = 5$ mm, $d_B = 5$ mm, $v_L = 0$ m/s) (based on [4]) .....	36
Figure 4.7: Development and the standard deviation of the mean absolute terminal rise velocity and the relative change of the mean and standard deviation in comparison to the prior measurement point against the number of measurements .....	37
Figure 4.8: Field of view in the PIV measurements (retrieved from [7], based on [141]) .....	40
Figure 4.9: (a) Qualitative, instantaneous velocity fields (brighter color of the vectors indicating higher values of the velocity magnitude $w_{abs}$ ) near the bubble in water, (b) position of the bubble for 30 bubble ascents with phase locked recording (here, e.g., in water) and (c) CDF of the velocity magnitude $w_{abs}$ accumulated from 30 images plotted in a probability grid (based on [7]) .....	41
Figure 4.10: (a) Theoretical dimensionless liquid velocity profile in a rectangular cross section flow channel for water calculated based on Papanastasiou et al. [143] in the contour plot for one quarter of the cross section, (b) the velocity profile in z-direction at central x-position and (c) the velocity profile in x-direction at central z-position; (b) and (c) include velocity profiles for non-Newtonian liquids as well .....	43
Figure 4.11: (a) Shear stress data over time of three sensors for one bubble ( $d_c = 7$ mm, $d_B = 9$ mm, $v_L = 0.2$ m/s) with the maximum shear stress marked with a black o, (b) the CDF plots based on 1500 bubble rises of the maximum shear stress, and (c) of the global shear stress level (median marked with a white x) (based on [3]) .....	44
Figure 4.12: Shear stress data over time of three sensors for a bubble swarm ( $d_c = 5$ mm, $Q_g = 400$ L/h, $v_L = 0.2$ m/s) with the mean value and the standard deviation marked in the plot.....	45

Figure 5.1: (a) Terminal bubble rise velocity in pure and contaminated water for freely rising bubbles and the respective value ranges of this investigation (illustrated as dash/dot-lines) and (b) the chart showing the shape regimes depending on the Re-, Eo- and Mo-number (dash/dot-lines for this investigation, dashed line for freely rising bubbles; based on [10]) .....	47
Figure 5.2: Rising paths in the front view of the channel (x-y-plane, a-d) and in the side view normal to the (y-z-plane, e-h) (based in parts on [6]) .....	48
Figure 5.3: Relative terminal rise velocities of the single bubbles (a) in water and (c) in Xanthan solution (in comparison to Margaritis et al. [146]) and the specific rise velocities related to the respective maximum relative terminal rise velocity (b) in water and (d) Xanthan solution (symbols explained in Table 5.2; based on [6]) .....	50
Figure 5.4: Friction factor against Reynolds number (a) calculated with the horizontal dimension of the bubble for Xanthan solution (in comparison to [146]) and (b) calculated with the equivalent bubble diameter for water (in parts retrieved from [6] with $K = 0.238 \text{ Pas}^n$ , $n = 0.42$ for the Xanthan solution) .....	52
Figure 5.5: Horizontal dimension $d_{B,h}$ of the bubble (a) in Xanthan solution and (b) in water (based on [6]) .....	53
Figure 5.6: Relationship between the bubble Reynolds number and the Weber and Morton number (in parts retrieved from [6] with $K = 0.238 \text{ Pas}^n$ , $n = 0.42$ for the Xanthan solution, in comparison to [149]) .....	54
Figure 5.7: (a) Relationship between the amplitude and the frequency and (b) the specific amplitude and the Strouhal number (with $K = 0.238 \text{ Pas}^n$ , $n = 0.42$ for the Xanthan solution; based on [6]) .....	55
Figure 5.8: Two consecutively recorded flow fields determined with PIV for a large bubble ( $d_c = 7 \text{ mm}$ , $d_B = 9 \text{ mm}$ , $v_L = 0 \text{ m/s}$ ) with a minor rising path oscillation (based on [7]) .....	57
Figure 5.9: Flow pattern in the wake of a bubble rising in water (a) from CFD simulations ( $d_c = 5 \text{ mm}$ , $d_B = 5 \text{ mm}$ , [17]) and (b) from PIV measurements ( $d_c = 5 \text{ mm}$ , $d_B = 7 \text{ mm}$ ) (based on [2]) .....	58
Figure 5.10: (a) Flow field around a freely rising bubble in a shear-thinning liquid as found by Funfschilling and Li [101], (b) flow field determined with PIV near a 5 mm bubble in the confining system ( $d_c = 5 \text{ mm}$ ) and (c) qualitative flow field around the smaller bubbles as found in this investigation (based on [7]) ..	59
Figure 5.11: Velocity magnitude in the liquid surrounding the bubble (a) in water and (b) Xanthan solution together with the respective absolute and relative terminal rise velocities (based on data from [6, 7]) ..	60
Figure 5.12: Relative velocity magnitude interval size in the liquid surrounding the bubble against the relative bubble size along with relative horizontal dimension of the bubble (based on data from [6, 7]) .....	61
Figure 5.13: (a) Shear rate in the liquid surrounding the bubble in water and Xanthan solution and (b) the respective shear stress (based on data from [7]) .....	62
Figure 5.14: Factor between the 99 %-value of the shear rate and shear stress in water (W) and Xanthan solution (X) (based on data from [7]) .....	63
Figure 5.15: (a) Flow field in the y-z-plane for $d_c = 7 \text{ mm}$ and $d_B = 7 \text{ mm}$ , (b) field of view for the test with exchanged camera and laser position to record the area between the walls in the y-z-plane, (c, d) potential out of plane positions of the bubble during the recording (based in parts on [141]) .....	64
Figure 5.16: (a) Snapshots of one bubble oscillating between the walls in the y-z-plane, (b) raw PIV image of the bubble at a height of approx. 133 mm in the field of view, (c) according instantaneous flow field and (d) vorticity distribution for a 3 mm bubble in a 7 mm channel (retrieved from [154], based on [141]) .....	65
Figure 5.17: Cumulative distribution functions of the occurring maximum wall shear stress for different parameter combinations (steady state analysis) .....	67

Figure 5.18: (a) Comparison of the probability ranges of the occurring global wall shear stress level to previously discussed PIV results [7] and (b) maximum wall shear stresses (transient corrected analysis) (based on [3]) compared to CFD [17] .....	69
Figure 5.19: Bubble patterns for the different continuous phases (a-d) and bubble paths for varied liquid velocities (e-h) recorded in the x-y-plane (based on [8]) .....	74
Figure 5.20: Gas hold-ups of the two different channel depths $d_c$ and the four different continuous phases (based on [8]) .....	77
Figure 5.21: Parity plot for the gas hold-up with the modelled values based on eq.(5.26) against the experimental data (continuous phases W: water, WI: water+ions, X: Xanthan solution, XI: Xanthan solution with ions) (based on [8]) .....	79
Figure 5.22: Median of the shear rates and shear stresses found in water+EDM salts for the two different channel depths $d_c$ in comparison to global shear stress values $\tau_{glob,99\%}$ found for single bubbles (dashed lines, data based on [3, 8]) and a wall shear stress estimate further described in Section 5.3 (triangles).....	81
Figure 5.23: Median of the shear rates and shear stresses found in Xanthan solution+EDM salts for the two different channel depths $d_c$ (based on [8]) and a wall shear rate and stress estimate further described in Section 5.3 (triangles) .....	82
Figure 5.24: (a) Standard deviation (fluctuations) against the median of the wall shear stress and (b) effective maximum wall shear stress against effective velocity in comparison to maximum wall shear stress values found for single bubbles (WI: water+EDM salts, XI: Xanthan solution+EDM salts) (data based on [3, 8]) .....	83
Figure 5.25: Relative change of the wall shear stress against the relative change of the gas velocity (data based on [8]) .....	86
Figure 5.26: Average wall shear stress (in an activated sludge with an MLSS concentration of 6.4 g/L equivalent to the system Xanthan solution+ions) for different commercially available flat sheet membrane modules calculated with the shear stress correlation found in this study (eq.(5.29)) .....	87
Figure 5.27: Sensitivity of the average shear stress on the bubble size, the sum of gas and liquid velocity, the flow consistency index and the hydraulic diameter (based of eq.(5.27) to (5.29)) .....	88
Figure 5.28: Forces acting on a particle (calculated with the effective maximum wall shear stress) against the particle diameter (data based on [8] and [33]) .....	89

## Table of Tables

Table 2.1: Publications dealing experimentally with fluid dynamics in membrane research sorted by the different measurement techniques (based on [1]) .....	8
Table 2.2: Publications dealing with the rise of single bubbles with high speed camera imaging sorted by the different working groups (based on [6]) .....	13
Table 2.3: Publications of single bubbles investigated with particle image velocimetry sorted by the different working groups (based on [7]) .....	17
Table 2.4: Recent publications dealing with experimental investigations of bubble swarms in bubble columns with rectangular cross section (based on [8]) .....	19
Table 3.1: Overview of the different varied parameters for the investigations (SB: single bubble tests; BS: bubble swarm tests) .....	22
Table 3.2: Capabilities of CFD simulations in comparison to the applied measurement techniques in this work (CFD results in parts presented in [17]) .....	23
Table 4.1: Material properties of the different continuous phases (in parts based on [8]) .....	33
Table 5.1: Overview of dimensionless numbers determined in this work (based on [6]) .....	47
Table 5.2: Investigated parameter combinations and respective symbols (S: CFD simulation in water, W: water, X: Xanthan solution, –: not tested) (based on [6]) .....	49
Table 5.3: Qualitative dependencies found in the single bubble behavior experiments (W: water; X: Xanthan solution, ↑: increasing value, ↓: decreasing value, const.: constant value/no clear trend) .....	72
Table 5.4: Qualitative dependencies found in the single bubble surrounding liquid experiments (W: water; X: Xanthan solution, ↑: increasing value/range, ↓: decreasing value/range, const.: constant value/range; 1-99 %: probability range from the 1st to 99th percentile) (retrieved from [7], grey background is used for quantities not discussed in this thesis) .....	72
Table 5.5: Qualitative dependencies found in the single bubble wall shear stress experiments (W: water+EDM salts, ↑: increasing value, ↓: decreasing value) .....	72
Table 5.6: Qualitative dependencies found in the bubble swarm behavior and wall shear stress experiments (W: water w/ and w/o EDM salts; X: Xanthan solution w/ and w/o EDM salts, ↑: increasing value, ↓: decreasing value, const.: constant value/no clear trend) .....	85

# Nomenclature

## Latin symbols

$A$	cross sectional area	$[m^2]$
$C_D$	friction factor	$[-]$
$C_{D,h}$	friction factor calculated with the horizontal dimension of the bubble	$[-]$
$C_{D,N}$	friction factor for Newtonian liquids	$[-]$
$C_{D,nN}$	friction factor for non-Newtonian liquids	$[-]$
$C_{D,nN,adj}$	adjusted friction factor for non-Newtonian liquids	$[-]$
$c_{MLSS}$	MLSS concentration	$g/L$
$c_{surf}$	surfactant concentration	$mol/L$
$c_{Xanthan}$	Xanthan gum concentration	$g/L$
$c_{Xanthan,w/ions}$	Xanthan gum concentration in ionic solution	$g/L$
$d_c$	channel depth	$m$
$d_B$	equivalent bubble diameter	$m$
$d_{B,h}$	horizontal dimension of the deformed bubble	$m$
$d_{B,min}$	minimum tested bubble diameter	$m$
$d_{B,v}$	vertical dimension of the deformed bubble	$m$
$d_h$	hydraulic diameter	$m$
$d_w$	width of the channel	$m$
$Eo$	Eötvös number	$[-]$
$F_{drag}$	drag force	$N$
$F_{lift}$	lift force	$N$
$f_B$	frequency of the oscillating bubble	$Hz$
$g$	gravitational constant	$m/s^2$
$H$	height	$m$
$I$	current	$A$
$J$	flux	$L/(m^2h)$
$J_{crit}$	critical flux	$L/(m^2h)$
$K$	flow consistency index	$Pas^n$
$k_{Cot}$	Cottrell coefficient	$As^{1/2}$
$k_{Lev}$	Leveque coefficient	$A/s^{1/3}$
$M$	mass	$kg$
$m$	exponent	$[-]$
$Mo$	Morton number	$[-]$
$Mo_w$	Morton number in water	$[-]$
$Mo_x$	Morton number in Xanthan solution	$[-]$
$n$	flow behavior index	$[-]$
$P$	power input	$[W]$

$p$	pressure	Pa
$Q_{f,real}$	real liquid flow rate	L/h
$Q_{f,set}$	set liquid flow rate	L/h
$Q_g$	gas flow rate	L/h
$R$	universal gas constant	J/(molK)
$Re_B$	bubble Reynolds number	[-]
$Re_{B,h}$	bubble Reynolds number calculated with the horizontal dimension of the bubble	[-]
$Re_{B,N,adj}$	bubble Reynolds number (adjusted correlation for Newtonian liquids)	[-]
$Re_{B,nN,adj}$	bubble Reynolds number (adjusted correlation for non-Newtonian liquids)	[-]
$Re_{B,W}$	bubble Reynolds number in water	[-]
$Re_{B,X}$	bubble Reynolds number in Xanthan solution	[-]
$SAD_m$	specific aeration demand per membrane area	$m^3/(m^2h)$
$SAD_p$	specific aeration demand per permeate flow	$m^3/(m^3)$
$Sr$	Strouhal number	[-]
$St$	Stokes number	[-]
$T$	temperature	K
$t$	time	s
$V_B$	bubble volume	$m^3$
$v_g$	superficial gas velocity	m/s
$w_{abs}$	velocity magnitude of the bubble surrounding liquid	m/s
$w$	liquid velocity	m/s
$w_{abs,1\%}$	velocity magnitude value of the bubble surrounding liquid at the 1 <sup>st</sup> quantile	m/s
$w_{abs,99\%}$	velocity magnitude value of the bubble surrounding liquid at the 99 <sup>th</sup> quantile	m/s
$w_{B,abs}$	absolute terminal bubble rise velocity	m/s
$w_{B,rel}$	relative terminal bubble rise velocity	m/s
$w_{B,rel,W,max}$	maximum measured relative terminal bubble rise velocity in water	m/s
$w_{B,rel,X,max}$	maximum measured relative terminal bubble rise velocity in Xanthan solution	m/s
$w_{f,c}$	liquid circulation velocity	m/s
$We$	Weber number	[-]
$x$	x-coordinate	m
$\hat{x}$	amplitude of the oscillating bubble	m
$\hat{x}^*$	specific amplitude of the oscillating bubble	[-]
$Y$	correction factor for the friction factor in case of a non-Newtonian liquid phase	[-]
$y$	y-coordinate	m
$z$	z-coordinate	m

### Greek symbols

$\alpha_k$	function used in <b>eq. (4.18)</b>	[-]
$\epsilon_g$	gas hold-up	[-]
$\lambda$	liquid film thickness between the bubble and the wall	m



$\mu$	dynamic liquid viscosity	Pa s
$\gamma$	shear rate	s <sup>-1</sup>
$\gamma_c$	wall shear rate (transient corrected analysis)	s <sup>-1</sup>
$\gamma_{glob}$	global wall shear rate level (SB)	s <sup>-1</sup>
$\gamma_{liq}$	shear rate in the bubble surrounding liquid (SB)	s <sup>-1</sup>
$\gamma_{max}$	maximum wall shear rate (SB)	s <sup>-1</sup>
$\gamma_{median}$	median of the wall shear rate (BS)	s <sup>-1</sup>
$\gamma_s$	wall shear rate (steady analysis)	s <sup>-1</sup>
$\gamma_{std}$	standard deviation of the wall shear rate (BS)	s <sup>-1</sup>
$\rho_f$	density of the liquid	kg/m <sup>3</sup>
$\rho_g$	density of the gas	kg/m <sup>3</sup>
$\rho_p$	density of solid particles	kg/m <sup>3</sup>
$\sigma$	interfacial tension	N/m
$\sigma_{ave}$	average standard deviation	[-]
$\tau_B$	characteristic time for the rising bubble	s
$\tau_{glob}$	global wall shear stress level (SB)	Pa
$\tau_{glob,1\%}$	global wall shear stress level value at the 1 <sup>st</sup> quantile (SB)	Pa
$\tau_{liq}$	shear stress in the bubble surrounding liquid (SB)	Pa
$\tau_{max}$	maximum wall shear stress (SB)	Pa
$\tau_{max,99\%}$	maximum wall shear stress value at the 99 <sup>th</sup> quantile (SB)	Pa
$\tau_{max,CFD}$	maximum wall shear stress (SB) from Prieske et al. (CFD results)	Pa
$\tau_{max,eff}$	effective maximum wall shear stress (BS)	Pa
$\tau_{median}$	median of the wall shear stress (BS)	Pa
$\tau_{min}$	minimum wall shear stress (SB)	Pa
$\tau_p$	relaxation time of the particle	s
$\tau_{single-phase}$	(wall) shear stress generated by single-phase liquid flow	Pa
$\tau_{std}$	standard deviation of the wall shear stress (BS)	Pa
$\vec{\omega}$	vorticity in the bubble surrounding liquid	s <sup>-1</sup>

## Abbreviations

ADV	acoustic doppler velocimetry
AOM	acoustic optical modular
BS	bubble swarm
BOP	bi-optical probe
CDF	cumulative distribution function
CFD	computational fluid dynamics
CW	continuous wave (laser)
DFM	double frame mode
DO	direct observation
EDM	electrodiffusion method

EVM	electromagnetic velocity meter
FFT	fast Fourier transformation
HSC	high speed camera
HWA	hot wire anemometer
IA	impeller anemometer
IAC	Intelligent Aeration Control
MBR	membrane bioreactor
MLSS	mixed liquor suspended solids
NMR	nuclear magnetic resonance imaging
OP	orifice plate
PEEK	polyether ether ketone
PIV	particle image velocimetry
PMMA	poly methyl methacrylate
PTFE	polytetrafluoroethylene
PVC	polyvinyl chloride
RPG	rotating polygonial
SB	single bubble
SDS	sodium dodecyl sulphate
SFM	single frame mode
SSS	shear stress scale

## Abstract

In this thesis, a study of a gas/liquid system in a confining geometry is presented. The project was motivated by flat sheet membrane modules used in membrane bioreactors (MBRs). Such systems are often operated as air-lift loop reactors. These are aerated to induce two-phase crossflows along the membrane surfaces. These crossflows reduce the growth of deposition layers on the membrane surface which develop during the filtration process. It would be possible to generate such crossflows as single-phase liquid flows, as well, but bubbles rising together with the liquid proved to enhance the cleaning effect. The cleaning effect is based on wall shear stresses due to velocity gradients at the wall in the narrow gaps between the membranes. Although aeration is one of the main cost factors during the operation of MBRs, a deeper understanding how constructional and operation parameters influence the process is not known. For such confining geometries as they are found between two flat sheet membranes, neither for single bubbles nor for bubble swarms sufficient literature can be found. Besides the specific geometry apparent in flat sheet membrane modules, in MBRs complex compositions of the liquid are found, leading to a shear-thinning non-Newtonian rheology. The idea of this thesis is closing the gap of knowledge about fluid dynamics in a system taking all the mentioned parameters into account. Single bubble experiments were chosen as a fundamental approach to understand the influence of such a system in comparison to commonly investigated bubbles rising in unconfined geometries. The parameters channel depth (equal to the distance between the membranes), bubble size, superimposed liquid velocity and rheology of the liquid were varied in a model system allowing the optical access to the inside of the gap. High speed camera imaging, particle image velocimetry and the electrodiffusion method were applied as measurement techniques. This allowed the determination of quantities regarding the bubble dynamics, the flow surrounding the bubble and the wall shear stress generated by the bubble ascent. While the bubble size, superimposed liquid velocity and rheology influenced almost all measured quantities, the channel depths influenced mainly the rise velocity (in comparison to freely rising bubbles) and the generated wall shear stress. Especially the identification of the influence of the rheology of the liquid phase is important in the field of membrane research. In MBR literature, a statement can be found that fluid dynamic findings in water are transferable to real systems. Up to here only for single bubbles, this statement cannot be confirmed. For the bubble swarm experiments, the varied parameters were again the channel depth and superimposed liquid velocity. Additionally, in contrast to the single bubble experiments, the superficial gas velocity was varied and the liquid phase variation was expanded by also testing water and the non-Newtonian liquid doped with ions. The ions were added for coalescence hindrance which can happen in real systems, as well, as these are complex compositions of diverse materials. High speed camera imaging and the electrodiffusion method were applied to measure the gas hold-up and the generated wall shear stress. While the channel depth did not significantly influence the gas hold-up, the same is valid for the superimposed liquid velocity regarding the wall shear stress. The properties of the liquid phase influenced both measured quantities. For the gas hold-up and wall shear stress, correlations were developed taking all varied parameters into account. Concluding, it was found that the type of continuous phase used in the fluid dynamic measurement does have a significant influence on the measured quantities. With respect to the membrane cleaning potential, it can be stated that an increase of the aeration rate does not have a strong enough impact on the wall shear stress to justify the additional operating cost resulting from it.

**Keywords:** bubbles, aeration, gas/liquid-flow, non-Newtonian liquid, image analysis, particle image velocimetry, electrodiffusion method, rise velocity, bubble oscillation, shear stress, gas hold-up

## Zusammenfassung

Diese Arbeit diskutiert die Untersuchung eines Gas/Flüssig-Systems motiviert durch Anwendung von Flachmembranmodulen in Membranbioreaktoren (MBR). Solche Systeme werden häufig als Air-Lift-Schlaufenreaktoren betrieben, deren Belüftung zu einem Cross-Flow entlang der Membranoberflächen führen soll. Cross-Flows reduzieren die Ausbildung von Deckschichten auf den Membranen, die sich während der Filtration ausbilden. Obwohl es auch möglich wäre, im einphasigen System einen Cross-Flow-Betrieb zu realisieren, wird dennoch häufig belüftet, da sich dies als vorteilhaft für den Reinigungsprozess erwiesen hat. Dieser Reinigungseffekt kann auf die Wandschubspannungen zurückgeführt werden, die durch die Geschwindigkeitsgradienten an den Wänden in den engen Kanäle zwischen den Membranen auftreten. Obwohl die Belüftung einen der größten Anteile an den Betriebskosten von MBRs ausmacht, gibt es kein tieferes Verständnis, wie Konstruktions- und Betriebsparameter den Reinigungsprozess beeinflussen. Für enge Kanäle, wie sie in Flachmembranmodulen auftreten, gibt es weder für den Einzelblasenaufstieg noch für Blasenschwärme ausreichend Literatur. Neben der speziellen Geometrie, wie sie in Flachmembranmodulen zu finden ist, ist in MBRs auch eine komplex zusammengesetzte Flüssigphase zu finden. Diese Flüssigphase weist üblicherweise eine scherverdünnende, nicht-Newtonsche Rheologie auf. Die Grundidee dieser Arbeit ist es, die Wissenslücke über die Fluidodynamik in einem solchen System zu schließen und dabei alle benannten Parameter in Betracht zu ziehen. Einzelblasenuntersuchungen wurden als grundlegender Ansatz gewählt, um den Einfluss der für diesen Fall speziellen Größen im Vergleich zum üblicherweise untersuchten Blasenanstieg ohne Wandeinfluss zu untersuchen. Die Parameter Kanaltiefe (die dem Abstand zwischen den Membranen entspricht), Blasengröße, überlagerte Flüssigkeitsgeschwindigkeit und Rheologie der Flüssigphase wurden in einem Modellsystem, das den optischen Zugang zum Spalt erlaubt, variiert. Hochgeschwindigkeitskameraaufnahmen, Particle Image Velocimetry und die Elektrodiffrusionsmethode wurden als Messtechniken angewendet. Dies ermöglicht die Ermittlungen der Blasendynamik, der Dynamik der die Blase umgebenden Flüssigkeit und der durch die Blase induzierten Wandschubspannung. Während die Blasengröße, die überlagerte Flüssigkeitsgeschwindigkeit und die Rheologie der Flüssigphase alle gemessenen Größen beeinflusst, zeigte sich der hauptsächliche Einfluss der Kanaltiefe bei den Aufstiegsgeschwindigkeiten (im Vergleich zu frei aufsteigenden Blasen) und den Wandschubspannungen. Speziell die Identifikation des Einflusses der Rheologie der Flüssigphase ist von Interesse für die Membranforschung. In der MBR Literatur lässt sich die Aussage finden, dass fluiddynamische Untersuchungen mit Wasser auf reale Systeme übertragbar sind. Für den Einzelblasenaufstieg kann dies nicht bestätigt werden.

Bei den Blasenschwarmuntersuchungen wurden wiederum die Kanaltiefe und die überlagerte Flüssigkeitsgeschwindigkeit variiert. Im Gegensatz zu den Einzelblasenuntersuchungen wurde hier nicht direkt die Blasengröße sondern die Gasleerrohrgeschwindigkeit variiert und weitere kontinuierliche Phasen getestet. Durch die Zugabe von Ionen sollte ein koaleszenzgehindertes System erzeugt werden, da, wie bereits erwähnt, die Flüssigphase im realen System ebenfalls eine komplexe Zusammensetzung diverser Stoffe darstellt. Hochgeschwindigkeitskameraaufnahmen und die Elektrodiffrusionsmethode wurden angewendet, um den Gasgehalt und die Wandschubspannung zu messen. Während im Fall des Gasgehalts die Kanaltiefe keinen starken Einfluss hatte, war das gleiche der Fall für den Einfluss der überlagerten Flüssigkeitsgeschwindigkeit auf die Wandschubspannung. Die Eigenschaften der Flüssigphase beeinflussten beide gemessenen Größen. Für den Gasgehalt und Wandschubspannung wurden jeweils beschreibende Korrelationen entwickelt, die alle variierten

Parameter mit einbeziehen. Zusammenfassend kann gesagt werden, dass die Art der Flüssigphase in diesen fluiddynamischen Untersuchungen einen Einfluss auf die gemessenen Größen hat. In Bezug auf das Potential, die Membranoberfläche zu reinigen, kann festgestellt werden, dass eine erhöhte Begasungsrate keinen starken Einfluss auf die auftretende Wandschubspannung hat und somit nicht die zusätzlichen Betriebskosten rechtfertigt.

## List of publications used for this thesis

This cumulative thesis is based on the following publications. The ordering of respective numbers is in chronological order of publication of the articles. In the following, whenever cited, the citation will be based on the numbering of the publication. The complete list of publications can be found in the Appendix.

- [1] L. Böhm, A. Drews, H. Prieske, P. Bérubé and M. Kraume, The importance of fluid dynamics for MBR fouling mitigation, *Bioresour. Technol.* 122, (2012) 50-61
- [2] L. Böhm and M. Kraume, Hydrodynamic investigation of single bubbles (presented at the 19th International Conference of Process Engineering and Chemical Plant Design, Krakow, Poland), *Czasopismo Techniczne Mechanika* 109, 5 (2012) 21-29
- [3] L. Böhm, A. Drews and M. Kraume, Bubble induced shear stress in flat sheet membrane systems - Serial examination of single bubble experiments with the electrodiffusion method, *J. Membr. Sci.* 437, (2013) 131-140
- [4] L. Böhm, H. Prieske and M. Kraume, Fluid dynamic optimization of flat sheet membrane modules - movement of bubbles in vertical channels (presented at the 11th International Conference on Chemical and Process Engineering, Milan, Italy), *Chem. Eng. Trans.* 32, (2013) 1501-1506
- [5] L. Böhm, S. Jankhah, J. Tihon, P. Bérubé and M. Kraume, Application of the electrodiffusion method to measure wall shear stress: Integrating theory and practice, *Chem. Eng. Technol.* 37, 6 (2014) 938-950
- [6] L. Böhm, T. Kurita, K. Kimura and M. Kraume, Rising behaviour of single bubbles in narrow rectangular channels in Newtonian and non-Newtonian liquids, *Int. J. Multiphase Flow* 65, (2014) 11-23
- [7] L. Böhm and M. Kraume, Quantitative comparison of the single bubble ascent in a Newtonian and a non-Newtonian continuous phase: A phenomenological PIV study, *Exp. Fluids*. submitted, (2014)
- [8] L. Böhm and M. Kraume, Fluid dynamics of bubble swarms rising in Newtonian and non-Newtonian liquids in flat sheet membrane systems, *J. Membr. Sci.* 475, (2015) 533-544







# 1 Introduction

Leonardo da Vinci discussed the spiraling motion of bubbles in water approximately 500 years ago in his Codex Leicester [9] which shows that particulate gas bubbles rising in a liquid phase have been a common topic in engineering and science for hundreds of years. Looking at published works, such systems are applied in chemical, civil, energy, mechanical, nuclear, process and safety engineering, life science, cryogenics, biology, chemistry and physics with the goal of all three types of transfer - energy, mass and momentum.

Globally viewed, a multiphase system is investigated here. In **Figure 1.1**, a rough overview is given over different types of multiphase (here in particular: two-phase) systems, with examples of the related processes and facilities. Clift et al. [10] and Chhabra [11] gave a broad overview over the behavior bubbles, drops and particles in various systems. Bubbly flows related to energy transfer are often found in pool or convective boiling investigations (see, e.g., [12, 13]). Common topics in this field are the bubble nucleation, growth, coalescence, heat transfer coefficients and mixing properties. Mass transfer related investigations (see, e.g., [14, 15]) often deal with bubble sizes, concentration profiles surrounding the bubble, dispersion and mass transfer coefficients. Both heat and mass transfer cannot be uncoupled from momentum transfer. Due to the density difference between the two phases, in all (gravitational) cases a momentum transfer between the two phases occurs as the bubbles rise in the liquid.

In the application of interest for this thesis, the filtration of mixed liquor from waste water treatment in a submerged flat sheet membrane bioreactor (MBR), actually a three-phase system is found with solid particles in

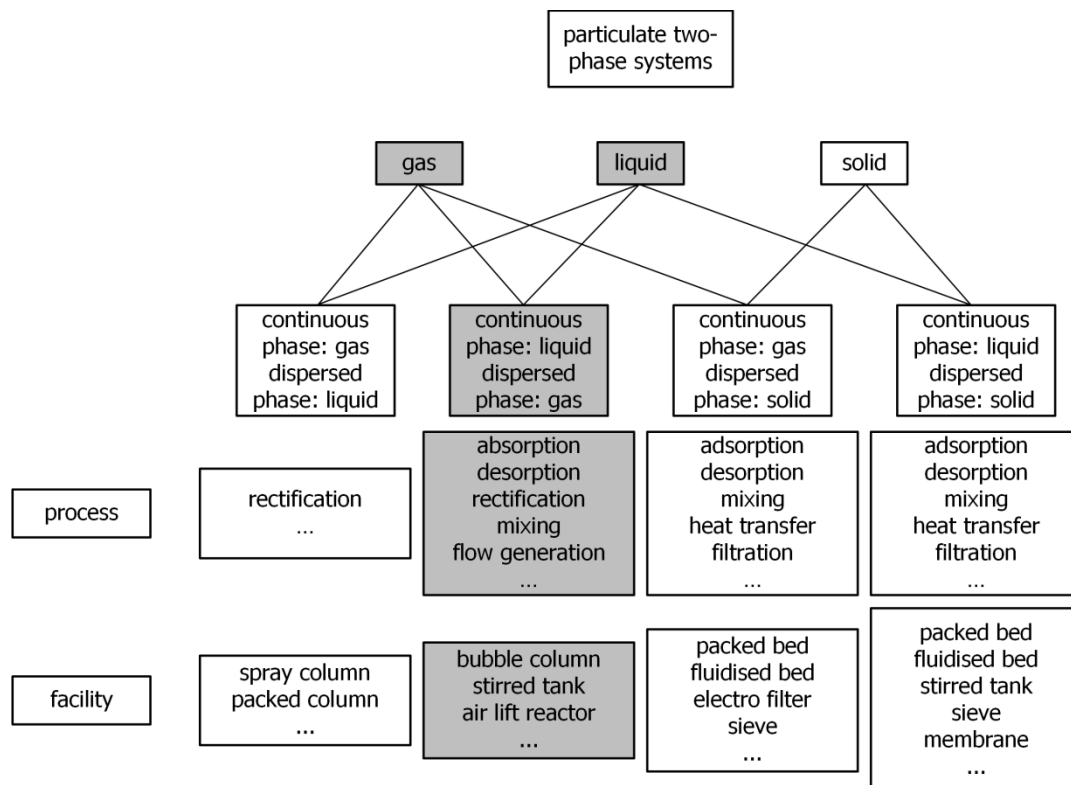


**Figure 1.1: Sorting of particulate two-phase systems into processes and facilities by the respective continuous phase (grey boxes are the branches of interest for this thesis, only cases with two different phases are shown)**

an, often aerated, liquid solution mainly consisting of water. Strictly speaking, in this biological system, not only solid particles but also soft matter (e.g., colloids, gel-like macromolecules) appears. For simplicity, in the following both are called solid phase. While the solid and liquid phases are the feed supposed to be filtered by the system, the third phase - the gas bubbles - is added for other purposes. Depending on the application, the intention of aerating the system, is

- on the one hand side, the delivery of oxygen (= mass transfer) from the bubbles to the liquid and then from the liquid to the microorganisms, responsible for the digestion of certain compounds in the solution (for aerobic processes) and/or
- on the other hand, the generation of a liquid (cross) flow, e.g., for the promotion of turbulent eddies (= momentum transfer), responsible for membrane fouling mitigation [16].

This cleaning process which can be applied without stopping the actual operation can reduce external fouling such as deposition of solid particles and biopolymer structures on the membrane surface. Its working principle is based on the shear forces that move material away from the membrane into the bulk flow due to the velocity gradient (= shear rate) and the respective difference in the dynamic pressure normal to the membrane surface. Such systems can be built as an air lift loop reactor (**Figure 1.2a**), with a stack of flat sheet membranes aerated from below and an non-aerated outer part of the module which allows a recirculation of the liquid. Therefore, due to the aeration, a cross flow operation is established.

Although the aeration is one of largest cost factors in the operation of MBR systems [16], commercially available (flat sheet) membrane modules are still not optimized, both in terms of construction and operation parameters [17]. One of the reasons for this situation is the fact that a deeper understanding of what actually

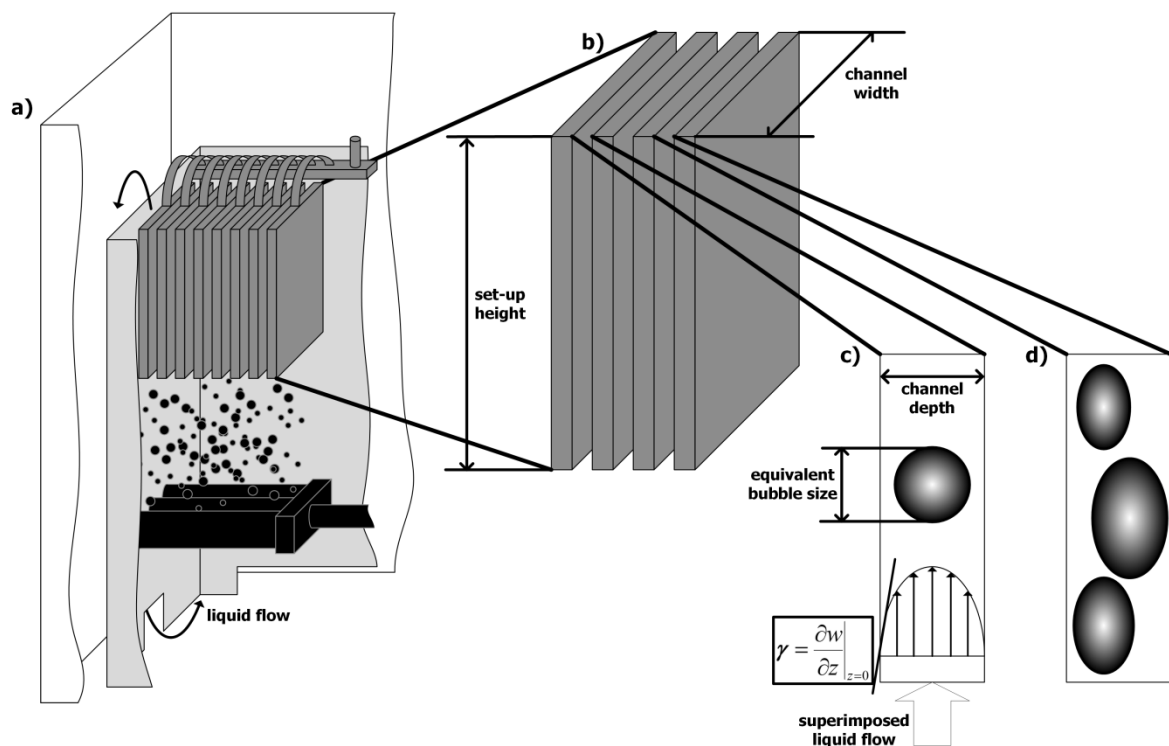


**Figure 1.2: (a) Scheme of an aerated flat sheet membrane module, (b) illustration of the rectangular spacing between the membrane plates and (c) profile of a single bubble and (d) bubble swarm rising in this confining geometry**

happens inside of the aerated membrane module during the aeration (and, therefore, cleaning) process is not known in detail. This is simply due to the fact that

- bubbly flows are generally a complex system to investigate experimentally and theoretically
- the given geometry is difficult to access experimentally and
- the actual quantity responsible for the cleaning, the wall shear stress acting on the membrane surface, cannot easily be determined experimentally (especially the local resolution of the wall shear stress).

This thesis' aim is to overcome these challenges by

- using model system approaches,
- starting the investigation from a fundamental point of view and
- increasing the complexity of the investigated system step by step in the attempt to get a deeper understanding of the process of interest.

## 2 State of the art

Even after decades of MBR research, fouling is still a current topic. A literature search reveals 30 years of published research articles with the keyword ‘membrane bioreactor’ (5680 articles) of which 2145 (38 %) deal with (membrane or bio-)fouling. Furthermore, 231 of these articles (10 %) discuss fouling control. Several broad reviews discussing the topic of fouling in MBRs can be found in the last decade by Cui et al., Drews, Judd, Le-Clech et al. and, most recently published, Wang et al. and Wibisono et al. [16, 18-22]. Generally, differentiations can be made between reversible and irreversible and internal and external fouling [23]. Different fouling processes include

- the formation of a deposition layer (or filter cake, consisting of particles and/or biomaterial building up in a biofilm),
- the blockage of pores and
- adsorption of material within the pores.

Most of these types of fouling can be reduced by chemical and physical cleaning but some of these procedures are only possible when the actual filtration process is stopped or even when the whole module is taken out of the system.

Counter-measures discussed in the field of fouling mitigation can roughly be sorted by its type (an extensive literature review can be found in Drews [19], example references are given here):

- construction: (fluid dynamic) improvements of the geometry of system parts (e.g., baffles between the membranes [24, 25]), membrane surface conditioning [26]
- operation: start-up [27], pre-settling [28], feedback control [29], backflush, relaxation, crossflow, two-phase flow [18]
- additives: flux enhancers for flocculation [30], granules [31], quorum quenching [32], chemical cleaning

Sometimes, the cleaning methods are also limited by the membrane geometry. Regarding flat sheet membrane modules, backflushing is actually impossible in most cases, as the separate membrane cushions (stacked in the module, **Figure 1.2b**) inflate during this process which can affect their integrity.

As mentioned previously, crossflow is the simplest cleaning method that can be established during operation. This fluid dynamic approach is based on the forces acting on the deposition layer on the membrane surface due to flow [33]. **Figure 2.1** illustrates the forces acting on a particle near the membrane. Due to the actual filtration, a drag force  $F_{drag}$

$$F_{drag} = 3\pi\mu_L d_P J \quad (2.1)$$

(with  $\mu_L$  as the liquid viscosity in Pas,  $d_P$  as the particle diameter and  $J$  as the flux in L/(hm<sup>2</sup>)) is moving the particle into the direction of the membrane surface. This force can be controlled by the set flux (volumetric flow rate through the membrane per membrane area) during the filtration. The force potentially moving the particle away from the membrane is the lift force  $F_{lift}$

$$F_{lift} = 0.761 \frac{\tau^{1.5} d_P^3 \rho^{0.5}}{\mu} \quad (2.2)$$

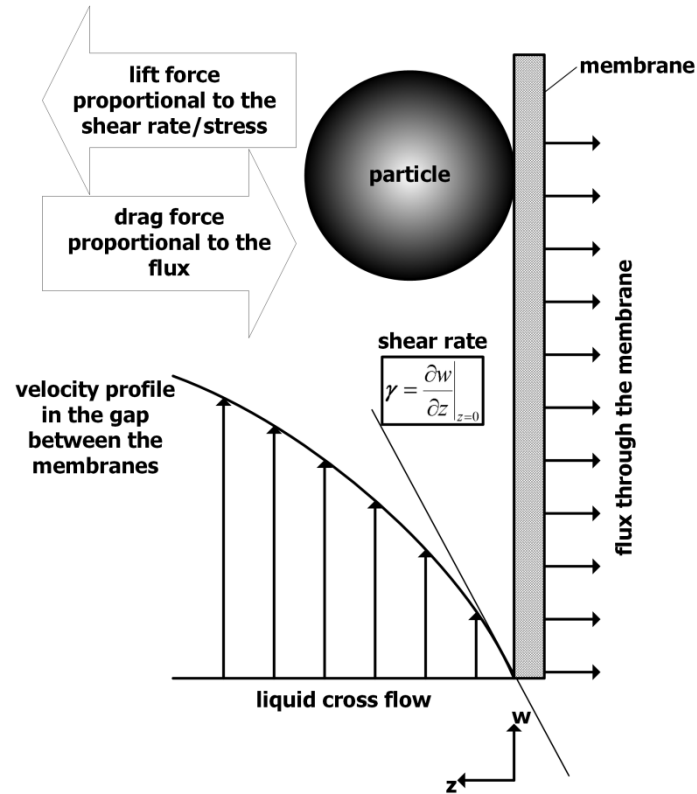


**Figure 2.1: Forces acting on a deposited particle normal to the membrane surface [1]**

with  $\tau$  as the shear stress in Pa and  $\rho$  as the density of the liquid in  $\text{kg/m}^3$ . This force can be controlled by the velocity gradient at the wall which is equal to the shear rate and proportional to the shear stress. Whenever the lift force is larger than the drag force, the particle with the according diameter will be removed from the membrane surface.

Only 151 (7 %) of the aforementioned articles about fouling discuss hydrodynamics (see also **Table 2.1** for an overview). Topics are, inter alia, critical particle diameters for deposition (diameter  $> 1 \text{ mm}$  being removed by hydrodynamics, below  $< 0.1 \mu\text{m}$  by molecular diffusion [34]), positive effects of fluctuating flows on the detachment of biofilms [35] and negative effects of the shear stress (high shear forces leading to a predominant deposition of small particles which in turn leads to denser deposition layers [20]). Regarding the biofilm, several authors investigated the influence of shear stress on biofilms and found, e.g., an influence of the shear stress on the biofilm composition [36], on the release of fouling-promoting substances [19] and an influence of the shear stress fluctuations on the detachment of biofilms [35].

Basically, a crossflow can also be generated without gas, e.g., by a pump in a side stream MBR [37]. If the crossflow is generated by aeration in an air-lift loop reactor, bubbles rise together with the liquid/solid suspension between the membrane plates which proved to have a significant enhancing effect on the cleaning process. This can be confirmed by transmembrane pressure (TMP) measurements in constant flux experiments [18, 24]. Besides the actual crossflow, the enhancing effect is based on a stronger liquid flow fluctuation or induced eddies, respectively. Additionally, higher shear forces occur due to thin liquid films between the bubble surface and the membrane or deposition layer, respectively. Still, a deeper understanding of this cleaning process with a three-phase cross flow operation is not existent. This is noteworthy as the aeration of submerged MBRs is responsible for 40 to 70 % of their energy demand [16, 38] and has been shown to be optimally used only 10 %

of the time [19]. Still, recent approaches have been made to improve the efficiency of this cleaning procedure. One operational approach is to apply a pulsating aeration [39-42] which also has already been applied in commercial products as, e.g., the GE LEAPmbr hollow fiber membrane system is operated with an Intelligent Aeration Control (IAC) [43, 44].

Looking at construction and operation parameters of commercially available flat sheet membrane modules for waste water treatment [17], it can be concluded that no optimum has been found yet. The membrane spacing ranges from 6 mm to 10 mm and the aeration is suggested to be done with fine or coarse bubbles at superficial gas velocities from  $1.25 \cdot 10^{-2}$  m/s to  $7.6 \cdot 10^{-2}$  m/s.

Evaluating publications not related to membrane systems, neither fundamental single bubble (**Figure 1.2c**) nor bubble swarm investigations (**Figure 1.2d**) can be found in geometries comparable to MBRs with a variation of parameters of specific interest for membrane research. In spite of this fact, the investigations most comparable to this study are summarized in **Table 2.2** and **Table 2.3** for single bubbles and in **Table 2.4** for bubble swarms.

Taking a look at the fluid dynamic research done in this field [1], usually no general recommendations were given as most groups only varied one parameter or the other and only analyzed one quantity or the other.

Common shortcomings are:

- Too small flow channel dimensions:

Setup heights (see **Figure 1.2b**) below approximately 500 mm can be regarded as too small. Real setups are usually larger than this and the flow cannot fully develop; channel depths below 3 mm and above 11 mm are not of industrial interest as channels with a too small depth tend to block and at too large channel depths the membrane area per volume (= packing density) would be fairly small.

- The use of water as the continuous phase:

Actually, most fluid dynamic investigations in this field used water (in parts doped with ions) as the continuous phase [1]. In their review on activated sludge rheology, Ratkovich et al. [45] discussed that usually in MBR systems, a non-Newtonian rheology is found. Still, Ozaki and Yamamoto [46] stated that results found in water are transferrable to waste water systems despite the Newtonian characteristic of water. This is surprising, as the viscosity of activated sludge does not only have a shear-thinning character but is generally higher than that of water. Their statement was based on a difference of the viscosity of water and activated sludge of only 10 %. Besides the rheology, activated sludge is actually a complex composition of liquors and ions which affect the interfacial tension between gas and liquid and the coalescence behavior of the bubbles. This has to be especially considered for the bubble swarm behavior.

- The application of only one measurement technique:

Most groups showed only results gained with one measurement technique either measuring, e.g., the occurring shear stress or the quantities of the liquid surrounding the bubble (like, e.g., the flow field around the bubble) and so on. To get a fundamental understanding, the application of other measurement techniques is beneficial and it also helps to show the comparability of systems of different groups.

- The variation of only a few parameters:

To be able to give advice on the improvement of MBR systems, as many parameters as possible should be covered as most of these interact.

Three groups are worth mentioning in the field of flat sheet systems as they covered most of the shortcomings. Gaucher et al. [47-51] did a broad investigation with the electrodiffusion method (EDM) and particle image velocimetry (PIV), even including the actual filtration, but their channel height was very low with 122 mm and they only used water (in parts doped with ions) as the continuous phase. They tested the influence of distributor types on the spatial distribution of the wall shear stress over the membrane area. They found an influence of

1. the ratio of the inlet to mean gas velocity on the wall shear stress and determined average wall shear stresses up to 10 Pa (local maximum values up to 50 Pa) and
2. the suction towards the membrane surface when the filtration was switched on which increased the wall shear stress by a factor of up to 2.5 and evened out the spatial distribution of the wall shear stress while dampening the fluctuations.

Cabassud's group [52-54] applied EDM, high speed camera imaging (HSC) and computational fluid dynamics (CFD), in parts for single bubbles as well, but also used a very low channel height of 147 mm, varied only a few parameters and only used water (in parts doped with ions) as the continuous phase. They did not give actual wall shear stress values but rather ratios:

1. They defined the ratio, average wall shear stress generated by a two phase flow over wall shear stress generated by a single phase flow. For this ratio they found values up to 4 which increased the flux (for constant transmembrane pressure experiments) in comparison to the case without air sparging by a factor of up to 1.7.
2. In addition, they defined the ratio, difference between maximum and minimum wall shear stress generated by two phase flow over the wall shear stress generated by a single phase flow. This ratio takes the fluctuations of the wall shear stress into account and values up to 40 were found. The enhancing effect on the flux performance was the same as discussed for the first ratio.

Regarding the bubble swarm experiments, Yamanoi and Kageyama [55] are the closest to this investigation, applying a shear stress measurement method (shear stress scale, SSS) and HSC but, again, they only used water as the continuous phase and they did not control an important influencing parameter: the co-current liquid velocity. Among their findings was:

1. The average wall shear stress increases with the superficial gas velocity with values up to 1.5 Pa.
2. The average wall shear stress is strongly affected by the appearing bubble size, with bubbles larger by a factor of 3 to 4 leading to higher average wall shear stresses by a factor of approximately 2.
3. For the wall shear stress generated by a two phase flow, the average value and the respective standard deviation (where the later one represents the bubble swarm induced fluctuations) are equal.

With all the assembled knowledge, e.g., Wang et al. still came to the conclusion, that cleaning protocols still have to be optimized and to some extent they have to be specifically adjusted to the respective application [21].

**Table 2.1: Publications dealing experimentally with fluid dynamics in membrane research sorted by the different measurement techniques (based on [1])**

reference	measurement technique	membrane geometry / single, several	setup height [mm]	system	filtration	varied parameters	measured quantity	results in brief
Böhm et al. [3, 8]	EDM	flat sheet / single	1500	air/ electrolytic solution / +Xanthan	no	bubble size/aeration rate, channel depth, superimposed liquid velocity, viscosity	wall shear stress	shear stress correlation, relation between shear stress fluctuations and average, influence of non-Newtonian viscosity
Gaucher et al. [47-51]	EDM	flat sheet / single	122	air/ electrolytic solution (with particles)	yes	channel width, liquid distributor shapes, viscosity	wall shear stress, flux	fluctuating shear stress has positive effect on the cleaning
Ducom et al. [53, 54]	EDM	flat sheet / single	147	air/ electrolytic solution	yes	aeration rate	wall shear stress, flux	shear stress not evenly distributed on the membrane
Bérubé et al. [56]	EDM	hollow fiber / single	~500	air/ electrolytic solution	no	single/two-phase, fiber swaying and tightness	wall shear stress	two-phase flow produces higher shear stress than single phase
Chan et al. [57]	EDM	hollow fiber / several	~150	air/ electrolytic solution	no	packing density	wall shear stress	Fiber packing density and looseness, as well as bubble size affect shear stress
Fulton et al. [58, 59]	EDM	hollow fiber / real module	2160	air/ electrolytic solution	no	aeration rate	wall shear stress	3-D maps of the shear stress distribution
Ratkovich et al. [60-62]	EDM	tubular/ single	2000	air/ electrolytic solution	no	liquid flow rate, gas flow rate	wall shear stress	conditions for fluctuating shear stress
Jankhah and Bérubé [63, 64]	EDM	hollow fibre / several	2000	air/ electrolytic solution	yes	air flow rate, air sparging frequencies, sparger type	wall shear stress	influence of pulsed sparging, fouling rate depending on average shear stress
Ye et al. [42]	EDM	hollow fibre / several	2600	air / electrolytic solution/ +bentonite particle	yes	air flow rate, air sparging frequencies, sparger type	wall shear stress	fouling rate depending on average shear stress



**Table 2.1: Publications dealing experimentally with fluid dynamics in membrane research sorted by the different measurement techniques (based on [1], continued)**

reference	measurement technique	membrane geometry / single, several	setup height [mm]	system	filtration	varied parameters	measured quantity	results in brief
Zhang et al. [65]	EDM	flat sheet / single	1000	air/ electrolytic solution	no	air flow rate, bubble size and frequency	wall shear stress	strong influence of bubble size and frequency on shear stress
Böhm et al. [6, 8]	DO	flat sheet / single	1500	air/ electrolytic solution / +Xanthan	no	bubble size/aeration rate, channel depth, superimposed liquid velocity, viscosity	rise velocity, bubble shape, rising paths, gas hold-up	gas hold-up correlation, influence of non-Newtonian viscosity
Ndinisa et al. [24, 25]	DO	flat sheet / single	490	air/ water or synthetic wastewater	yes	aerator configuration, baffles	bubble size + distribution	influence of design and operating conditions on the filtration
Essemiani et al. [52]	DO	flat sheet / single	147	air/ water	no	-	bubble velocity	results for bubble behavior
Wang et al. [21]	DO	tubular + flat sheet / single	200	air/water	no	spacer type, liquid/gas flow rates	bubble size, bubble shapes	bubble behavior depends on type of spacer
Davis et al. [66]	DO	flat sheet / single	380	air/ glycerol-water with particles	yes	TMP, liquid flow rate, solid volume fraction	cake thickness	model describing the cake thickness
Jankhah and Bérubé [64]	DO	hollow fibre / several	2000	air/ electrolytic solution	yes	air sparging frequencies, sparger type	bubble size, rise velocity, rising path	fibre swaying depending on bubble properties
Khalili-Garakani et al. [67, 68]	DO	flat sheet / module	700	air/ act. sludge	yes	riser and downcomer area, air flow rate	bubble size, shear stress, resistance	influence of the flux on the shear stress
Li et al. [69]	DO	flat sheet / single	96	protein solution	yes	liquid flow rate	cake thickness	composition of the cake depends on the liquid flow rate

**Table 2.1: Publications dealing experimentally with fluid dynamics in membrane research sorted by the different measurement techniques (based on [1], continued)**

reference	measurement technique	membrane geometry / single, several	setup height [mm]	system	filtration	varied parameters	measured quantity	results in brief
Phattaranawik et al. [70]	DO	flat sheet / module	~125	air/ synthetic wastewater	yes	air flow rate, flux, bubble size	bubble size	larger bubble size better for bubble distribution and fouling control
Prieske et al. [71]	DO	flat sheet / module	1700	air/ water	no	air flow rate, bubble size	gas holdup, bubble distribution	model for the liquid circulation velocity in air lift loop configurations
Ratkovich et al. [72]	DO	tubular / single	2000	air/ electrolytic solution (with carboxy methyl cellulose)	no	liquid flow rate, air flow rate	gas slug rising velocity	gas slug behavior in Non-Newtonian liquids
Drews et al. [73]	DO	flat sheet / single	1700	air/ water, air/ act. sludge	(yes)	channel width, bubble size, air flow rate, liquid flow rate	bubble velocity, liquid velocity	air and liquid flow affect the composition of the cake
Ye et al. [74]	DO	hollow fiber / single	50	bentonite and sodium alginate solutions	yes	backwash periods	cake thickness	composition of the cake depends on the hydrodynamics
Yamanoi et al. [55]	SSS	flat sheet / single	600	air/ water	no	air flow rate, channel width, aerator type	shear stress, resistance	mean and standard deviation of the shear stress can be regarded as one parameter
Nagaoka et al. [75]	SSS	flat sheet / single	1000	air/ water (with methyl cellulose)	no	air flow rate, Newtonian viscosity of the liquid	shear stress	influence of different Newtonian viscosities on the shear stress
Le-Clech et al. [76]	HWA	flat sheet / single	105	air/ whey-based solution	no	feed concentration, sensor position, gas flow rate	liquid velocity	potentials and limitations of HWA in membrane applications
Wicaksana et al. [77]	HWA	hollow fiber / several	~250	water with particles	yes	various operating conditions	permeate flow distribution	potentials and limitations of HWA in membrane applications

**Table 2.1: Publications dealing experimentally with fluid dynamics in membrane research sorted by the different measurement techniques (based on [1], continued)**

reference	measurement technique	membrane geometry / single, several	setup height [mm]	system	filtration	varied parameters	measured quantity	results in brief
Böhm and Kraume [7]	PIV	flat sheet / single	1500	air/ electrolytic solution / +Xanthan	no	bubble size, channel depth, superimposed liquid velocity, viscosity	liquid velocity, vorticity, shear stress	influence of a single bubble on the surrounding liquid, influence of non-Newtonian viscosity
Gaucher et al. [48]	PIV	flat sheet / single	122	air/ water (with particles)	yes	channel width, liquid distributor shapes, viscosity	shear stress, flux	fluctuating shear stress has positive effect on the cleaning
Martinelli et al. [78]	PIV	hollow fiber / several	~820	air/ water (with particles)	yes	air flow rate, bubble size	liquid velocity, shear stress	air flow rate is more important for the high shear stress than bubble size
Wereley et al. [79]	PIV	rotating disc / single	~450	glycerol-water with salt and particles	no	type of fluid and particles	velocity profiles	distribution of the particles
Jankhah and Bérubé [64]	PIV	hollow fibre / several	2000	air/ electrolytic solution	yes	air flow rate, air sparging frequencies, sparger type	vorticity	in combination with DO and PIV results: power transferred efficiency over air flow rate
Chung et al. [80]	NMR	curved flat sheet / single	~350	water doped with copper(II) sulphate	no	liquid flow rate	Dean vortices	turbulence promoters suggested
Heath et al. [81]	NMR	hollow fiber / single/ several	~310	water doped with copper(II) chloride	no	liquid flow rate	liquid flow distribution	improvements of the design and operation
Pangrle et al. [82, 83]	NMR	hollow fiber / module	50	water	no	liquid flow rate	liquid flow distribution	comparison of measurement methods
Poh et al. [84]	NMR	hollow fiber / module	~220	water doped with copper(II) sulphate	no	liquid flow rate, baffles	liquid flow distribution	baffles did not improve the liquid flow distribution

**Table 2.1: Publications dealing experimentally with fluid dynamics in membrane research sorted by the different measurement techniques (based on [1], continued)**

reference	measurement technique	membrane geometry / single, several	setup height [mm]	system	filtration	varied parameters	measured quantity	results in brief
Prieske et al. [17]	IA	flat sheet / module	1200	air/water	no	channel width, air flow rate	rise velocity, shear stress, liquid velocity	aerator modification for better bubble distribution, model describing the liquid circulation velocity
Ozaki and Yamamoto [46]	OP	flat sheet / single	570	water / act. sludge	yes	channel width, air flow rate	liquid velocity	hydrodynamic results obtained with water can be used for sludge as well
Yamanoi and Kageyama [55]	EVM	flat sheet / single	600	air / water	no	air flow rate, channel width, aerator type	liquid velocity	mean and standard deviation of the shear stress can be regarded as one parameter
Nguyen Cong Duc et al. [85]	BOP	hollow fiber / module	3150	air/ water	no	air flow rate	bubble size + distribution, gas hold-up	gas distribution in a membrane tank
Sofia et al. [86]	EVM	flat sheet / single	400	air / act. sludge	yes	air flow rate	liquid velocity	smaller bubbles preferable for higher circulation liquid vel.
Tacke et al. [87]	ADV	flat sheet / module	3080	air / water (with glycerol)	no	aeration rate	liquid velocity, flow distribution	bubbles unevenly distributed in the module

**Table 2.2: Publications dealing with the rise of single bubbles with high speed camera imaging sorted by the different working groups (based on [6])**

reference	high speed camera setup	setup geometry (cyl.: i.d. x h, rect.: d <sub>w</sub> x d <sub>c</sub> x h)	bubble size d <sub>B</sub>	varied parameters	measured quantity	remark / results in brief
Drews et al. [33, 73]	752x582 pixel <sup>2</sup> / 350 Hz	rectangular 3-11x160x700 mm <sup>3</sup>	3-24 mm	bubble size, viscosity	bubble velocity	- / -
Acharya et al. [88]	- / -	rectangular 165x165x245 mm <sup>3</sup>	-	injector type	bubble velocity, shape, deformation	- / -
Clanet et al. [89]	- / 25 Hz	several	Taylor bubbles	geometry, viscosity	bubble velocity	Taylor bubbles / -
Dekée et al. [90]	- / 6 Hz	rectangular 230x230x772 mm <sup>3</sup>	2.6-26.7 mm	bubble size, viscosity	bubble velocity	investigation of coalescence / -
Ellingsen and Risso [91]	- / 1 kHz	rectangular 150x150x650 mm <sup>3</sup>	2.48 mm	-	rising path, shape	- / -
Figuroa-Espinoza et al. [92]	- / -	rectangular 3.6-4.7x200x400 mm <sup>3</sup>	<1.4 mm	Re	rising path	- / drag coefficients
Brücker [93]	512x512 pixel <sup>2</sup> / shadowgraphy	rectangular 100x100x1200 mm <sup>3</sup>	5-7 mm	bubble size	rising path, oscillation frequency, shape, bubble velocity	counter current flow cell / physical description of the bubble behavior during its ascent
Liu et al. [94]	1200x1600 pixel <sup>2</sup> / shadowgraphy	rectangular 68x88x450mm <sup>3</sup>	~6 mm	viscosity, gas flow rate	rising path, shape	bubble train / influence of the viscosity on the rising path
Maneri and Zuber [95]	- / -	rectangular 9.5-1.3x63-86x914mm <sup>3</sup>	<55 mm	inclination, viscosity	bubble velocity	/ viscosity influences bubble velocity for inclined channels
Miyahara et al. [96]	- / -	cylindrical 10x1000mm <sup>2</sup>	2-30 mm	viscosity	shape, bubble velocity, oscillation	- / -

**Table 2.2: Publications dealing with the rise of single bubbles with high speed camera imaging sorted by the different working groups (based on [6])**

reference	high speed camera setup	setup geometry (cyl.: i.d. x h, rect.: $d_w \times d_c \times h$ )	bubble size $d_B$	varied parameters	measured quantity	remark / results in brief
Tokuhiro et al. [97]	768x493 pixel <sup>2</sup> / shadowgraphy	rectangular 100x100x1000 mm <sup>3</sup>	9.12 mm	investigation of a bubble and a solid particle	shape, rising path	counter current flow cell / -
Fujiwara et al. [98]			8 mm	viscosity		one side of the channel is a movable belt / influence of the shear flow field on the rising path
Fujiwara et al. [99, 100]			2-6 mm	bubble size		+ 3D bubble shape
Funfschilling et al. [101]	- / -	rectangular 60x60x500 mm <sup>3</sup>	<12 mm	viscosity	shape, bubble velocity, coalescence behavior	- / bubble interaction
Frank and Funfschilling et al. [102, 103]		cylindrical 300x500 mm <sup>2</sup>	3-14 mm			
Li et al. [104]		cylindrical 300x1500 mm <sup>2</sup>	6.5- 7.2 mm			
Roudet et al. [105]	1280x1024 pixel <sup>2</sup> / 500 Hz	Rectangular 1x400x800mm <sup>3</sup>	2.6- 8.3 mm	bubble size, channel inclination	shape, bubble velocity, oscillation	- / -
Sanada et al. [106]	2 times 512x512 pixel <sup>2</sup> / 1 kHz	rectangular 150x150x400mm <sup>3</sup>	0.66- 0.93 mm	bubble size, viscosity	shape, rising path	- / -
Takagi and Matsumoto [107]	-	-	-	-	-	review / influence of surfactants

**Table 2.2: Publications dealing with the rise of single bubbles with high speed camera imaging sorted by the different working groups (based on [6])**

reference	high speed camera setup	setup geometry (cyl.: i.d. x h, rect.: $d_w \times d_c \times h$ )	bubble size $d_B$	varied parameters	measured quantity	remark / results in brief
Hassan and Ortiz-Villafuerte et al. [108, 109]	640x480 pixel <sup>2</sup> / shadowgraphy, 2D hybrid particle tracking and 3D reconstruction	cylindrical 12.7x1300 mm <sup>2</sup>	3 mm	-	rising path, bubble velocity	stagnant water / physical description of the bubble behavior during its ascent
Dewsbury and Hassan et al. [110, 111]	- / -	rectangular 300x300x240mm <sup>3</sup>	1.5-33 mm	Re number	bubble velocity	- / -
Sakakibara et al. [112]	960x960 pixel <sup>2</sup> / shadowgraphy	rectangular 150x150x270/500m <sup>3</sup>	~2.9 mm	-	rising path, shape	- / -
Saito et al. [113]				surfactant concentration		- / influence of surfactants on bubble motion
Yoshimoti and Saito [114]	1024x1024 pixel <sup>2</sup> / shadowgraphy	octagon, 160x160x230mm <sup>3</sup>		-		- / relation between bubble shape, velocity and path
de Vries et al. [115]	-	rectangular 15x15x500mm <sup>3</sup>	0.8-1.8 mm	bubble size	rising path	- / wall interaction
van Wachem and Schouten [116]	- / 955 Hz	rectangular 15x300x2000mm	15-80 mm	bubble size	shape, bubble velocity	comparison with CFD / -
Zaruba et al. [117]	2times 1280x1024 pixel <sup>2</sup> / 500 Hz	rectangular 50x50x1300mm <sup>3</sup>	1-4 mm	bubble size	rising path	with superimposed liquid velocity / -

**Table 2.2: Publications dealing with the rise of single bubbles with high speed camera imaging sorted by the different working groups (based on [6])**

reference	high speed camera setup	setup geometry (cyl.: i.d. x h, rect.: $d_w \times d_c \times h$ )	bubble size $d_B$	varied parameters	measured quantity	remark / results in brief
Zhang et al. [118]	752x582 pixel <sup>2</sup> / -	rectangular 210x210x600mm <sup>3</sup>	2.7- 5.2 mm	bubble size, viscosity	bubble velocity, bubble size	- / -
Sathe et al. [119]	2048x2048 pixel <sup>2</sup> / shadowgraphy	rectangular 200x15x500 mm <sup>3</sup>	0.1-15 mm	bubble size, liquid velocity	shape	bubbly flow / comparison between single bubble behavior and bubble swarms
Sathe et al. [120]		+ cylindrical 150x650mm <sup>2</sup>	-	geometry		bubbly flow / -
Sathe et al. [121]		rectangular 200x15x1000 mm <sup>3</sup>	2-35 mm	bubble size	bubble diameter	bubbly flow / -

d: diameter; h: height; i.d.: inner diameter



**Table 2.3: Publications of single bubbles investigated with particle image velocimetry sorted by the different working groups (based on [7])**

reference	PIV setup	particles	setup geometry	bubble size $d_B$	varied parameters	measured quantity	remark / results in brief
Brücker [93]	CW Laser, RPG mirror, SFM, 512x512 pix <sup>2</sup> , shadowgraphy	polyamid particles 30 $\mu$ m	rectangular 100x100x1200 mm <sup>3</sup>	4-7 mm	bubble size	rising path position, path oscillation frequency, bubble shape oscillation, velocity, vorticity	counter current flow cell / physical description of the bubble behavior during its ascent
Liu et al. [94]	Double pulsed laser, DFM, 15Hz, 1200x1600 pix <sup>2</sup> , shadowgraphy	fluorescent particles 7 $\mu$ m	rectangular 68x88x450 mm <sup>3</sup>	~6 mm	Viscosity, gas flow rate	velocity, vorticity, turbulence intensity, Reynolds stress	averaging of flow fields, bubble train / influence of the viscosity on the rising path
Tokuhiro et al. [97]	CW Laser, AOM cell, SFM, 768x493 pix <sup>2</sup> , shadowgraphy + 2 <sup>nd</sup> shadowgraphy camera for 3D bubble shape reconstruction	fluorescent particles (RhB) 1-10 $\mu$ m	rectangular 100x100x1000 mm <sup>3</sup>	9.12 mm	investigation of a bubble and a solid particle	velocity, RMS velocity, Reynolds stress, turbulent kinetic energy	counter current flow cell / -
Fujiwara et al. [98]				8 mm	viscosity	rising path position, velocity, vorticity	one side of the channel is a movable belt / influence of the shear flow field on the rising path
Fujiwara et al. [99, 100]				2-6 mm	bubble size		+ 3D bubble shape
Funfschilling, Frank and Li et al. [101, 102, 104]	Double pulsed laser, DFM, 2D planar	fluorescent particles 75 $\mu$ m	rectangular 60x60x500 mm <sup>3</sup>	<12 mm	viscosity	Velocity, residual stress	non-Newtonian liquid / bubble behavior during its ascent in nN fluid
Ortiz-Villafuerte and Hassan et al. [108, 109]	CW Laser, volume illumination AOM cell, SFM, 3 cameras, 640x480 pix <sup>2</sup> , shadowgraphy, 2D hybrid particle tracking and 3D reconstruction	polysterene particles 40 $\mu$ m	cylindrical 12.7x1300 mm <sup>2</sup>	3 mm	-	rising path position, velocity, vorticity, turbulence intensity, Reynolds stress, turbulent kinetic energy	stagnant water, averaging of flow fields, Kolmogorov scales / influence of the wall to the wake structure, physical description of the bubble behavior during its ascent, turbulence induced by the bubble reaches 20 $d_B$

**Table 2.3: Publications of single bubbles investigated with particle image velocimetry sorted by the different working groups (based on [7])**

reference	PIV setup	particles	setup geometry	bubble size $d_B$	varied parameters	measured quantity	remark / results in brief
Sakakibara et al. [112]	CW Laser, 960x960 pix <sup>2</sup> shadowgraphy	fluorescent particles 50 $\mu$ m	rectangular 150x150x270/500 mm <sup>3</sup>	~2.9 mm	-	cross correlation coefficient, signal-to-noise-ratio	- / method of multipass
Saito et al. [113]					surfactant concentration	rising path position, vorticity, bubble deformation	- / influence of surfactants on bubble and liquid motion
Sathe et al. [119]	Double pulsed Laser, DFM, 16Hz, 2048x2048 pix <sup>2</sup> , shadowgraphy	fluorescent particles 8 $\mu$ m	rectangular 200x15x500 mm <sup>3</sup>	0.3-15 mm	liquid velocity	bubble rise velocity, eddy energy	bubbly flow / comparison between single bubble behavior and bubble swarms
Sathe et al. [120]			+ cylindrical 150x650 mm <sup>2</sup>	-	geometry	velocity, eddy size, eddy energy	wavelet transformation and Eddy Isolation Method for flow interpretation / -
Meyer et al. [122]	Double pulsed Laser, DFM, 1376x1040 pix <sup>2</sup> , shadowgraphy	fluorescent particles 1.5 $\mu$ m	rectangular 2.04x2.04	~2.1 mm	-	velocity field surrounding the Taylor bubble	Taylor bubble / velocity field in the liquid film between bubble and wall

**Table 2.4: Recent publications dealing with experimental investigations of bubble swarms in bubble columns with rectangular cross section (based on [8])**

reference	setup geometry (height x width $d_w$ x depth $d_c$ ) [mm <sup>3</sup> ]	continuous phase	aerator type	gas flow rate $Q_g$ [m <sup>3</sup> /h]	superficial gas velocity $v_g$ [m/s]	specific aeration demand $SAD_m$ [m <sup>3</sup> /(hm <sup>2</sup> )]	varied parameters	bubble sizes $d_B$ , bubble velocities $w_B$ , gas hold-ups $\epsilon_g$
Böhm and Kraume [8]	1500 x 160 x 5-7	water / Xanthan solution / + different salts	pipe aerator (15 holes with $d=0.7$ or 1 mm)	$10^{-1}$ - $6 \cdot 10^{-1}$	$2.5 \cdot 10^{-2}$ - $2.1 \cdot 10^{-1}$	$3 \cdot 10^{-1}$ - 1.3	channel depth, gas flow rate, liquid flow rate, liquid viscosity	$\epsilon_g=3.4-58.2$ %
Gaucher et al. [47-51]	122 x 122 x 1-5	water / Xanthan solution / + different salts	pipe aerator (6 holes with $d=5$ or 6 mm) and slit	$1.8 \cdot 10^{-2}$ - $6.8 \cdot 10^{-1}$	$8.1 \cdot 10^{-3}$ - 1.56	$6 \cdot 10^{-1}$ - 23	gas flow rate + filtration	-
Ducom et al. [54]	147 x 70 x 5	water + different salts	pipe aerator (12 holes with $d=0.5$ mm)	$<5 \cdot 10^{-1}$	$<4 \cdot 10^{-1}$	$<24.9$	gas flow rate, liquid flow rate	-
Yamanoi and Kageyama [55]	600 x 211 x 5-10	water	nozzle ( $d=6$ mm) and glass ball filter	$7.2 \cdot 10^{-2}$ - $5.7 \cdot 10^{-1}$	$9.4 \cdot 10^{-3}$ - $1.5 \cdot 10^{-1}$	$2.8 \cdot 10^{-1}$ - 2.27	gas flow rate	$d_B=3.3-21$ mm $\epsilon_g=2-28$ %
Nagaoka et al. [75]	- x 400 x 32	water / + methyl cellulose	pipe aerator (63 holes with $d=0.8$ mm)	$4.1 \cdot 10^{-1}$ - 1.5	$9 \cdot 10^{-3}$ - $3.3 \cdot 10^{-2}$	-	gas flow rate, liquid viscosity	$d_B=3-40$ mm
Sathe et al. [119]	500 x 200 x 15	water	needle injector	$2.4 \cdot 10^{-1}$	$2.2 \cdot 10^{-2}$	1.2	-	$d_B=1-13$ mm $w_{B,rel}=30-70$ cm/s
Lundin and McCreedy [123]	- x 50 x 4	water / glycerol	fritted glass	$1.2 \cdot 10^{-2}$ - $6 \cdot 10^{-2}$	$1.6 \cdot 10^{-2}$ - $8.3 \cdot 10^{-2}$	-	gas flow rate, liquid flow rate, channel orientation, liquid phase	$w_{B,rel}=5-7$ cm/s
Acuna and Finch [124]	900 x 120 x 50	water, + polyglycol, + n-pentanol	slot sparger	-	-	-	gas flow rate	$d_B=0.5-4$ mm $w_B=19-31$ cm/s $\epsilon_g=6.1-15.2$ %
Hooshyar et al. [125]	1000 x 240 x 40	water	needle injector	$8.6 \cdot 10^{-1}$ - 3.4	$2.5 \cdot 10^{-2}$ - $10^{-1}$	1.8 - 7.2	gas flow rate	$d_B=1-8$ mm $w_B \leq 100$ cm/s $\epsilon_g=6-36$ %
Rabha und Buwa [126]	450 x 150 x 150	water	needle injector	-	-	-	bubble size	$d_B=1.5-4.75$ mm $w_B=12-42$ cm/s $\epsilon_g \leq 16$ %

**Table 2.4: Recent publications dealing with experimental investigations of bubble swarms in bubble columns with rectangular cross section (based on [8], continued)**

reference	setup geometry (height x width $d_w$ x depth $d_c$ ) [mm <sup>3</sup> ]	continuous phase	aerator type	gas flow rate $Q_g$ [m <sup>3</sup> /h]	superficial gas velocity $v_g$ [m/s]	specific aeration demand $SAD_m$ [m <sup>3</sup> /(hm <sup>2</sup> )]	varied parameters	bubble sizes $d_B$ , bubble velocities $w_B$ , gas hold-ups $\epsilon_g$
Li et al. [127]	1000 x 100 x 100	water / glycerol / + carboxymethyl cellulose / + polyacrylamide	single hole ( $d=2\text{mm}$ )	$1.4 \cdot 10^{-2}$ - $7.2 \cdot 10^{-2}$	$4 \cdot 10^{-4}$ - $2 \cdot 10^{-3}$	$7.0 \cdot 10^{-2}$ - $3.6 \cdot 10^{-1}$	gas flow rate, liquid viscosity	$\epsilon_g=5\text{-}17\%$
Bouche et al. [128, 129]	800 x 400 x 1	water + magnesium sulphate	capillary tubes	-	-	-	gas flow rate	$d_B=3.5\text{-}6.5\text{ mm}$ $\epsilon_g=1.4\text{-}13.6\%$

### 3 Scope and outline of this thesis

As mentioned before, most investigations in the field of fluid dynamic fouling mitigation have certain deficits. This thesis is the first work in this field to combine fundamental investigations of single bubbles (SB, **Figure 1.2c**) with the bubble swarm behavior (BS, **Figure 1.2d**) under the same conditions with a systematic, broad variation of parameters influencing the fluid dynamics of flat sheet MBRs.

The varied parameters were (see **Table 3.1** for an overview):

- channel depth  $d_c$  (= membrane spacing)

Small channel depths are beneficial for the packing density but in most cases such channels tend to block (as a development of a deposition layer cannot be avoided completely). In commercial products, a range of  $6 \text{ mm} < d_c < 11 \text{ mm}$  can be found. CFD simulations of single bubbles rising in channels with rectangular cross section showed high shear stress values for the 5 mm channel [17]. Therefore, in this thesis, channel depths of 3 mm, 5 mm and 7 mm were tested. The 3 mm channel is rather of academic interest due to the reasons mentioned before.

- in case of the single bubble experiments (SB): bubble size  $d_B$

The bubble size was varied in a range that was assumed for fine bubble aeration ( $3 \text{ mm} < d_B < 9 \text{ mm}$ ) as recommended by certain suppliers of flat sheet membrane modules. The bubble size used in this thesis is the diameter of a spherical bubble with a volume equal to the injected gas volume. For many parameter combinations, the generation of larger stable single bubbles was not possible as the entrance into the confining flow channel and/or flow conditions led to a breakage of the large bubble into smaller daughter bubbles. The bubble swarm experiments revealed that larger bubbles, evolving due to coalescence in the channel, can be stable.

- in case of bubble swarm experiments (BS): volumetric gas flow rate  $Q_g$

Several different values are used in membrane applications to express gas flow. The superficial gas velocity  $v_g$  (in m/s) and the gas flow rate  $Q_g$  (in m<sup>3</sup>/h) are common quantities for such experiments independent of the research field. Additionally, gas flows can be given as gas flow rate per membrane area  $SAD_m$  (specific aeration demand, in m<sup>3</sup>/(m<sup>2</sup>h)) or gas flow rate per membrane area and permeate flow  $SAD_p$  (in m<sup>3</sup>/m<sup>3</sup>) [1]. Based on the  $SAD_m$  recommended for commercial products by their suppliers ( $0.3 \text{ m}^3/(\text{m}^2\text{h}) < SAD_m < 1.28 \text{ m}^3/(\text{m}^2\text{h})$ ) [17], a gas flow rate range of  $0.1 \text{ m}^3/\text{h} < Q_g < 0.6 \text{ m}^3/\text{h}$  was chosen for this work. The  $SAD_m$  was chosen as basic value as it is independent of the channel depth and in contrast to, e.g., the superficial gas velocity also given by Prieske et al. [17], it can be specifically calculated for the investigated system. In case of the superficial gas velocity, it is not clear if it is the gas flow rate related to the free area between the membranes or, e.g., the free area above the aerator and below the actual membrane module (riser section).

- superficial co-current liquid velocity  $v_L$

Some groups took the co-current liquid velocity (also called superimposed liquid velocity) into account but did not vary it or did not control it. Prieske et al. [17] discussed influencing factors on the co-current liquid velocity in flat sheet membrane air lift loop reactors. As the self-establishing co-current liquid velocity is a function of various influencing factors such as, e.g., the tank and module geometry, it is

reasonable to rather control the liquid velocity in a range of interest ( $0 \text{ m/s} < v_L < 0.2 \text{ m/s}$ ) than let the liquid velocity be self-established in an experimental facility that has no overall relation to a real system.

- physical properties of the continuous phase

By using different continuous phases with Newtonian and non-Newtonian rheology and adding surfactants with other things being equal, the influence of the different characteristics can be quantified and Ozaki and Yamamoto's statement of the transferability of results found in water to real systems can be tested [46]. In contrast to the real activated sludge found in membrane bioreactors, here, model solutions were used which was a necessity for the applied measurement techniques. This led to the application of four different types of continuous phases (water [4, 6, 8], water with ions [2, 3, 5, 8], shear-thinning non-Newtonian Xanthan solution [6-8], shear-thinning non-Newtonian Xanthan solution with ions [8]). In contrast to the real three-phase system, in most cases no solid particles were added to the liquid, making it a two-phase system with liquid as the continuous phase (see respective grey boxes in **Figure 1.1**). Only the PIV measurements were done in a three-phase system, as particles are necessary for the measurement technique. Therefore, the two continuous phases, water with particles [2, 7] and Xanthan solution with particles [7], were only used for the PIV measurements. As the particles did not have an effect on the system (discussed in **Section 4.2**), these cases can be regarded as similar to the experiments without particles.

**Table 3.1: Overview of the different varied parameters for the investigations (SB: single bubble tests; BS: bubble swarm tests)**

measurement technique	channel depth $d_c$ [mm]	SB: bubble size $d_B$ [mm]	BS: gas volume flow rate $Q_g$ [L/h]	superimposed liquid velocity $v_L$ [m/s]	continuous phase
PIV	5, 7	3, 5, 7, 9	100, 200, 300, 400, 500, 600	SB: 0, 0.1, 0.2	SB: water (only in $d_c=7$ mm) Xanthan solution
HSC				SB: 0, 0.1, 0.2 in Xanthan solution also 0.125 and 0.235 BS: 0, 0.1, 0.2	SB: water Xanthan solution BS: water water + Na <sub>2</sub> SO <sub>4</sub> Xanthan solution Xanthan solution + Na <sub>2</sub> SO <sub>4</sub>
EDM	SB: 3, 5, 7 BS: 5, 7			SB: 0, 0.2 BS: 0, 0.1, 0.2	SB: water + EDM salts BS: water + EDM salts Xanthan solution + EDM salts

The applied measurement techniques were:

- high speed camera imaging (HSC, sometimes also called direct observation DO) [4, 6, 8] for the determination of the bubble rising behavior including rise velocity, rising path, bubble shape, etc.
- particle image velocimetry (PIV) [2, 7] analyzing the influence of the bubble on the surrounding liquid
- electrodiffusion method (EDM) [2, 3, 5, 8] providing the bubble induced wall shear stress

The results were in parts used to validate CFD simulations [17]. **Table 3.2** illustrates that, actually, CFD simulations would be the most powerful tool to do a comprehensive investigation of the system of interest. Potentially, every desired quantity could be studied in detail, locally and time resolved. On the downside, CFD simulations are no analytical solutions of the physical process. The mathematical problem has to be treated numerically with a solver for partial differential equation systems (which itself already leads to an error) and many complex physical processes have to be described by - more or less - simplifying models. Examples for models necessary in this investigation would be a multiphase model, a rheological model describing the non-Newtonian behavior, a turbulence model and, in case of the bubble swarm, a coalescence and breakage model. Böhm et al. [1] discussed CFD approaches from several working groups motivated by MBR systems. In most cases, a Newtonian continuous phase was chosen and, especially in case of bubble swarm simulations, usually multiphase models were chosen which do not resolve the two phases locally. Although only shortly discussed here, this already corroborates that such complex system simulations always have to be validated by experimental work. Still, as **Table 3.2** indicates, none of the measurement technique used here can cover all quantities of interest. The mentioned study by Prieske et al. [17] covered the CFD simulation of the single

**Table 3.2: Capabilities of CFD simulations in comparison to the applied measurement techniques in this work (CFD results in parts presented in [17])**

quantities of interest in this study		CFD	HSC	PIV at 14.2 Hz	EDM
qualitative	flow field	+		+	
	rising paths	+	+		
quantitative	absolute/relative rise velocity	+	+	(+)	(+)
	bubble shape quantities	+	+		
	amplitude of the bubble oscillation	+	+		
	frequency of the bubble oscillation	+	+		
	gas hold-up	(+)	+		
	surrounding liquid velocity	+		+	
	surrounding liquid vorticity	+		+	
	surrounding liquid shear stress	+		+	(+)
	wall shear stress	+		(+)	+

bubble ascent in a confining geometry. Here, it was still possible with a reasonable computational effort to gain a sufficient spatial and temporal resolution of this process. Therefore, these results can be used for comparison with the experimental single bubble results in this thesis. For the experimental bubble swarm results presented here, no comparable CFD study is at hand.

The determined quantities in this study were (SB: single bubble tests; BS: bubble swarm tests):

- absolute/relative terminal bubble rise velocity  $w_{B,abs}$ ,  $w_{B,rel}$  (SB) [4, 6]
- horizontal and vertical dimensions of the deformed bubble  $d_{B,h}$ ,  $d_{B,v}$  (SB) [6]
- amplitude of the bubble rising path oscillation  $\hat{x}$  (SB) [4, 6]
- frequency of the bubble rising path oscillation  $f_B$  (SB) [4, 6]
- gas hold-up  $\varepsilon_g$  (BS) [8]
- surrounding liquid velocity  $w_{abs}$  (SB) [7]
- surrounding liquid vorticity  $\vec{\omega}$  (SB) [7]
- surrounding liquid shear stress  $\tau_{liq}$  (sometimes also referred to as strain, shear, shear rate  $\gamma_{liq}$  (= velocity gradient), shear force, all with comparable definitions or related by simple calculations, SB) [7]
- wall shear rate  $\gamma_{glob}$ ,  $\gamma_{max}$ ,  $\gamma_{median}$ ,  $\gamma_{std}$  / wall shear stress  $\tau_{glob}$ ,  $\tau_{max}$ ,  $\tau_{median}$ ,  $\tau_{std}$  (SB/BS) [2, 3, 8]

Figure 3.1 shows the basic structure of the thesis. Based on a broad literature review on fluid dynamics in MBR

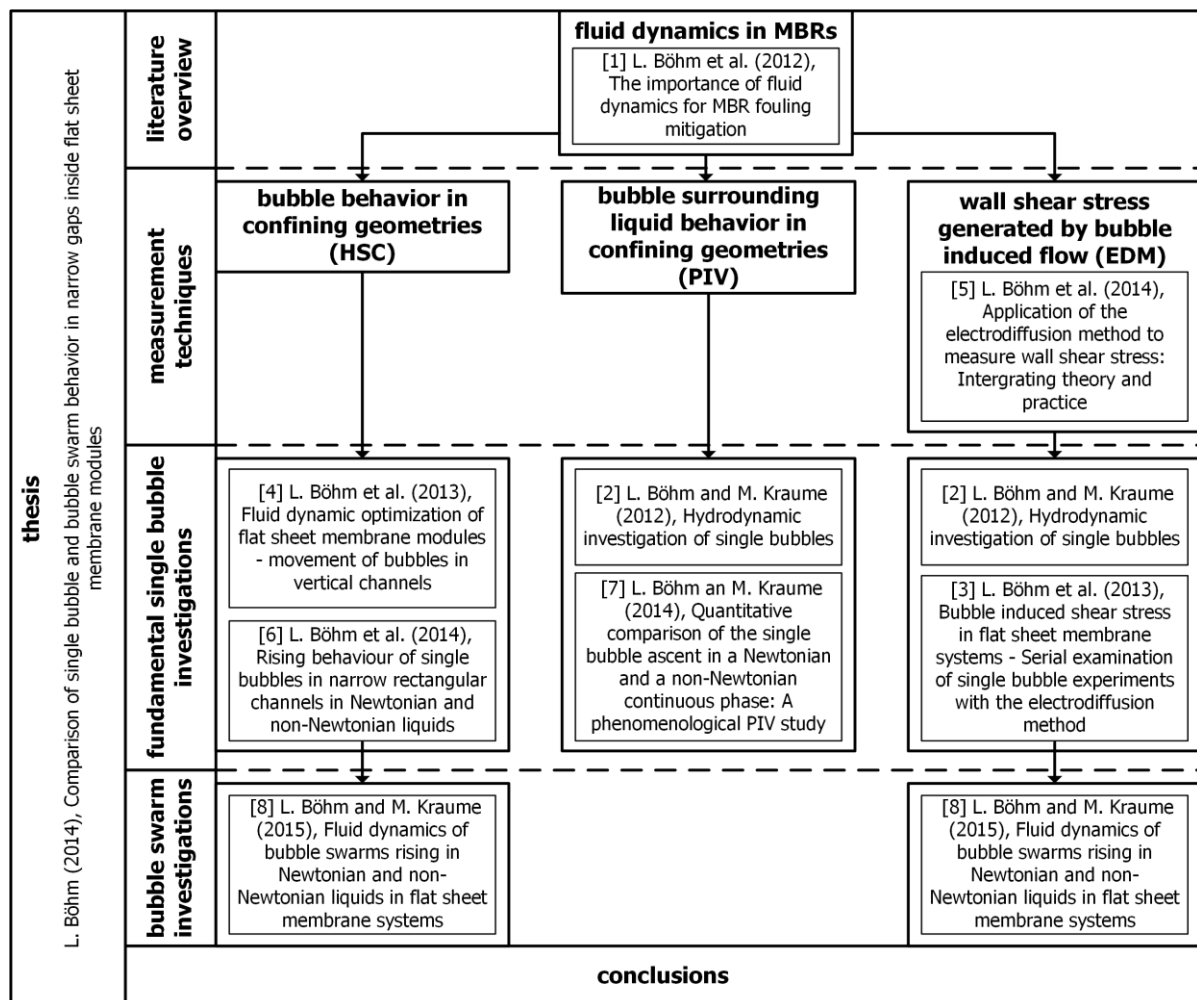


Figure 3.1: Structure of the thesis



systems [1] (in extracts in **Section 2**), a fundamental investigation of this multi-phase system is made. In the following, the material and methods are discussed. These include the experimental set-ups (**Section 4.1**) and the material properties of the used continuous phases (**Section 4.2**). The three different measurement techniques are explained as well (**Sections 4.3 to 4.5**), especially with respect to the way the respective data is analyzed. Going into more detail, for the electrodiffusion method, a fundamental literature review [5] was co-authored by the author of this thesis. It discusses 50 years of theory and application of the technique and recent developments. The results and discussion part is divided into the single bubble (**Section 5.1**) and bubble swarm experiments (**Section 5.2**). It starts with the analysis of the single bubble behavior, then is moving to its interaction with the surrounding liquid and finally is discussing the wall shear stress generated by the bubble induced liquid flow. Where applicable, the results are compared to literature and if possible cross-links are drawn for the results gained in this thesis. After a conclusion of the single bubble results, the bubble swarm results are presented. The general flow behavior, including the gas hold-ups, and the wall shear stress generated by the bubble swarm induced liquid flow are considered. Both quantities are again related to literature and correlations are given, describing the respective quantity in dependence of all varied parameters. Based on all the assembled information, engineering recommendations (**Section 5.3**) are given for flat sheet membrane modules. Finally, the work is concluded and an outlook is given (**Section 6**).

Here and in the following text, boxed paragraphs show intermediate conclusions:

Concluding the motivation of this work up to here, as indicated in **Section 1**, the common challenges in this field of research are complex (flow) systems, poor accessibility and the hard-to-determine quantity of interest. With the approach chosen here, a deeper understanding of the real systems is the aim. The rather academic approach of investigating the single bubble ascent before looking at the complex multiple bubble system is not supposed to be of sole fundamental interest without relation to the actual application. By comparing results of these cases, conclusions can be drawn for future investigations if results from one type of test can be transferred to the other one.

Besides the determination of the influence of each individual parameter, it is of great interest for the motivational system if, e.g., different liquid viscosities lead to differing recommendations for the operation and construction of flat sheet membrane modules.

## 4 Materials and methods

### 4.1 The experimental set-up

Several features were demanded of the ideal experimental set-up:

- as many as possible geometrical and operational parameter variations should be performed in one set-up
- usability for single bubble and bubble swarm experiments
- fully automated operation for serial examinations
- visual accessibility from all sides of the flow channel for the HSC and PIV investigations
- (removable) EDM sensor installation flush with the wall
- no metal parts in contact with the continuous phase (necessity for the EDM measurements)
- low overall liquid hold-up (as the EDM solution had to be separately disposed)

Not all requirements could be achieved (e.g., a variable channel depth and optical accessibility in the same flow channel). Therefore, a modular construction was chosen fulfilling most of the requirements. For the different measurements, individual, respective parts of it were varied. The basic components were the flow channel, a bubble injector system, a gas/liquid separator, a receiving tank for the continuous phase and a liquid pump for the generation of the co-current liquid flow (specific descriptions in the respective articles [2-8], see **Figure 3.1**). For the single bubble EDM measurements [2, 3], one flow channel was used for which the channel depths could be adjusted by inserting polyvinyl chloride (PVC) plates (**Figure 4.1a**). The number of inserted PVC plates, each with a thickness of 1 mm, defined the free spacing for the bubble ascent. Additionally, an acrylic glass plate had to be inserted in which the EDM sensors were installed. These tests were the only ones where a channel depth of 3 mm was tested. For all other experiments, two channels were used, each with a fixed, defined channel depth of 5 and 7 mm, respectively (**Figure 4.1b**). In all cases, the channel width  $d_w$  (= x-direction) was  $d_w = 0.16$  m which is more than a magnitude larger than the largest tested bubble size making an influence of the side walls on the bubble ascent negligible.

For the single bubble measurements, a 50 mL Hamilton GasTight syringe was used to generate bubbles of defined volumes corresponding to defined bubble diameters. The syringe was fixed on a Harvard Apparatus 11 Elite syringe pump. The gas was led through a polytetrafluoroethylene (PTFE) tube and a two-way-valve through a custom-built polyether ether ketone (PEEK) needle, inserted through a septum, into the flow channel. In the flow channel itself, the gas was collected in a bubble cup. Once the inserted gas coalesced to one bubble of the desired size, the bubble was released by turning the bubble cup with the help of a servomotor located outside of the channel and connected to the cup with a rotatable rod. Due to the deformation of the bubble, a control of the single bubble size based on recorded images was not possible. A repeatedly performed test was done where a defined number of bubbles ( $\sim 50$ ) with a defined size was collected at the outlet of the flow channel and the total gas volume was compared to the expected total volume of the respective number of single bubbles. This test only gave information about the average single bubble size of the collected bubbles but the differences between the collected and expected gas volumes were minimal (in the single-digit percentage range). This actual minimal difference could also be explained with the expansion of the bubble during its ascent. Assuming the ideal gas law is valid:

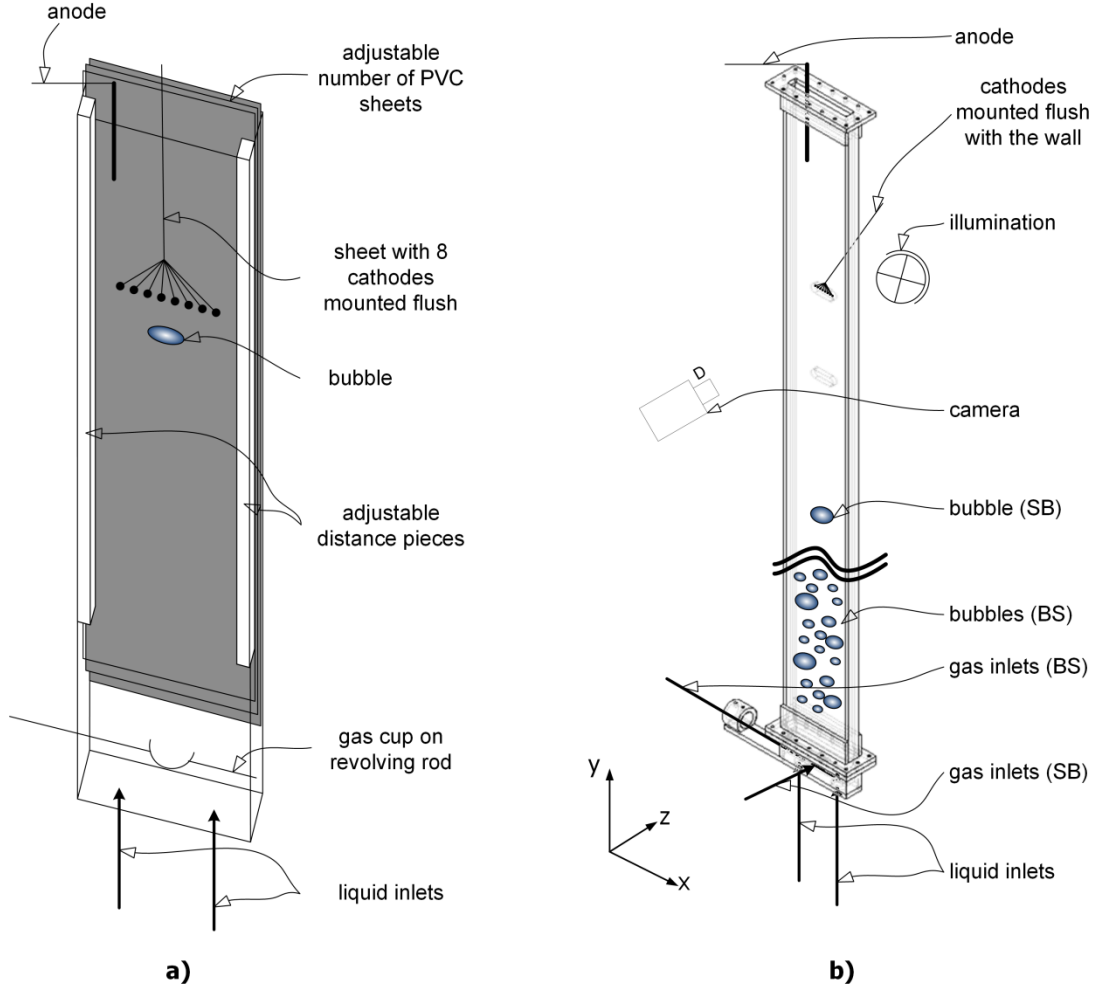


**Figure 4.1: (a) Scheme of the flow channel used in the single bubble EDM measurements (b) and of the flow channel used in the single bubble (SB) HSC/PIV and bubble swarm (BS) HSC/EDM measurements (in parts from [3, 6])**

$$V_B = \frac{MRT}{p} \quad (4.1)$$

(with  $V_B$  as the bubble volume in  $\text{m}^3$ ,  $M$  as the mass in kg,  $R$  as the specific gas constant in  $\text{J}/(\text{kgK})$ ,  $T$  as the temperature in K and  $p$  as the pressure in Pa). The pressure difference  $\Delta p$  between bubble cup and gas separator is a function of the hydrostatic head (assuming the pressure loss caused by the liquid flow is negligible) as described by

$$\Delta p = \rho_f g \Delta H \quad (4.2)$$

(with  $\rho_f$  as the liquid density in  $\text{kg}/\text{m}^3$ ,  $g$  as the gravitational constant in  $\text{m}/\text{s}^2$  and  $\Delta H$  as the liquid height in m). With a liquid height of 1.5 m, the bubble volume would increase by a factor of approx. 1.15. The diameter of the respective spherical bubble

$$d_B = \sqrt[3]{\frac{6 MRT}{\pi p}} \quad (4.3)$$

would change by a factor of  $1.15^{1/3} = 1.05$ . This increase in the bubble diameter during its ascent of 5 % is neglected in the following discussion, especially as the point for all measurement techniques was roughly half way between the inlet and the outlet reducing the error to 2.4 %.

For the bubble swarm experiments, the flange with the servomotor, bubble cup on the rotatable rod and the septum was replaced by a flange which contained the aerator. For this, a PVC pipe with 15 holes ranging over the whole width of the channel was used. In case of the gas hold-up measurements, the holes had a diameter of 1 mm and in case of the EDM measurements, the diameter was decreased to 0.7 mm. This was due to the fact that for some low gas flow rates in the non-Newtonian viscosity systems, the aeration was not uniformly distributed over the length of the aerator in case of the larger sparging holes. This was the case although the criteria for uniform aeration introduced by Mersmann [130] depending on a hole Weber number was fulfilled but this relationship was found for the aeration in Newtonian liquids and might not be applicable here. The aerator was fed by the pressurized air supplied by the in-house compressor. It was led through an air filter, a manometer, a Krohne DK46-800 flow meter and another manometer. The manometers were necessary to calculate the actual net volume gas flow from the scale of the flow meter with the help of the Krohne KROVASYS 4 software. Due to fluctuations mainly caused by fluctuating pressures in the aerated flow channel (as the hydrostatic head of the two-phase mixture in the channel is subject of fluctuations), the gas flow rate was set with an accuracy of approximately  $\pm 10$  %.

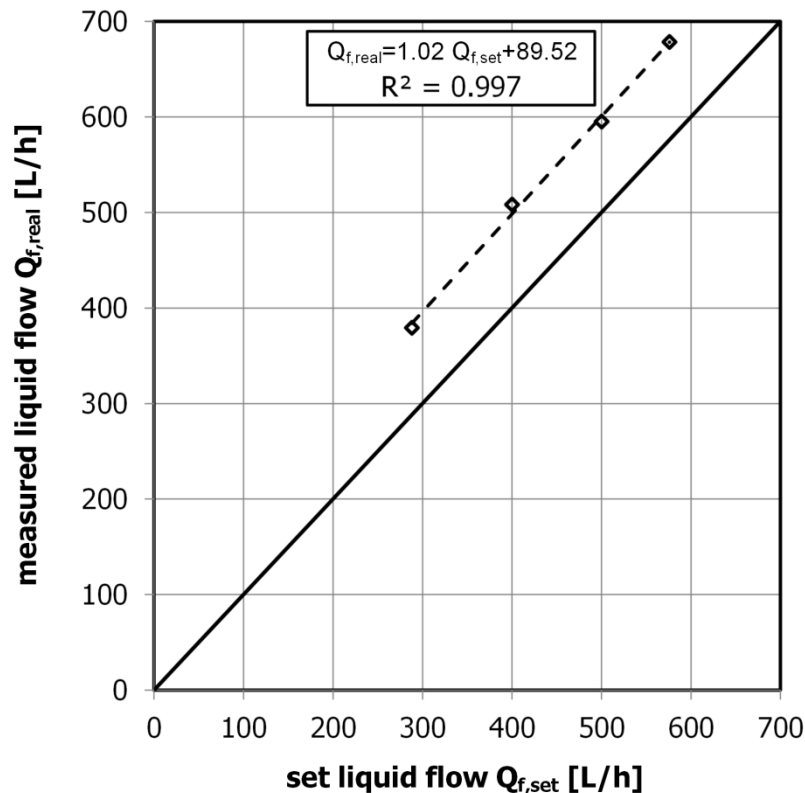
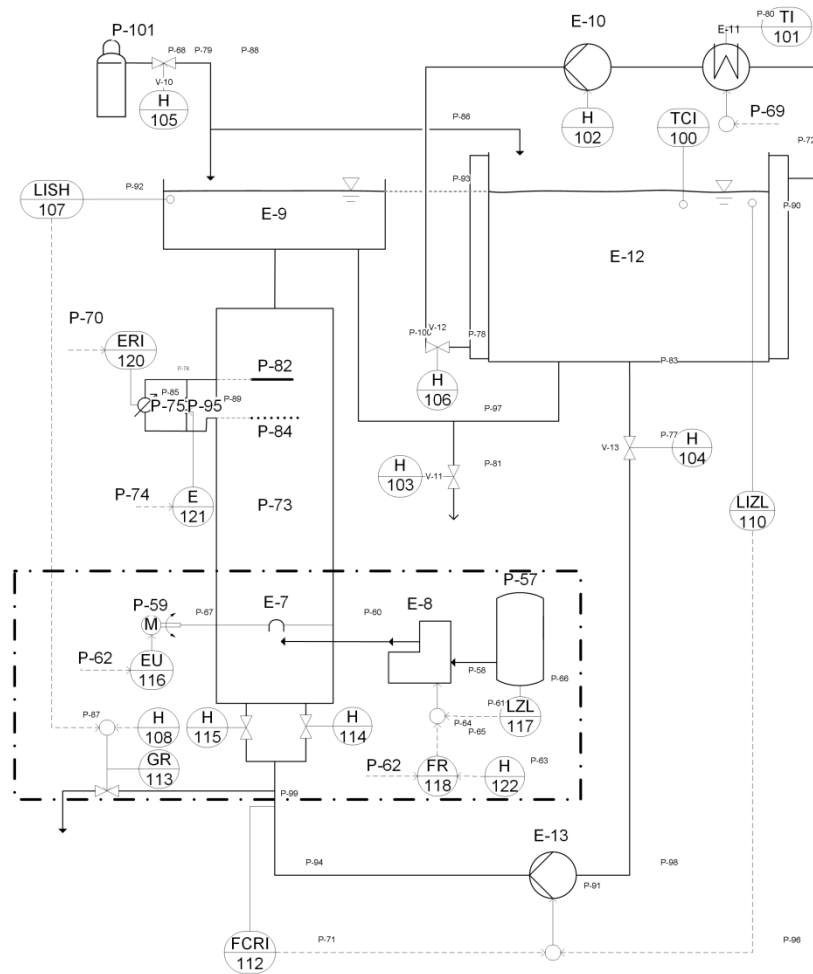


**Figure 4.2: Results of the calibration test of the propeller flow meter used with Xanthan solution**

**a)**

### single bubble (SB) configuration



**b)**

### **bubble swarm (BS) configuration**

All parts are equal to the SB configuration, only the lower part of the flow channel is changed (marked by the dashed/dotted line in both flow sheets).

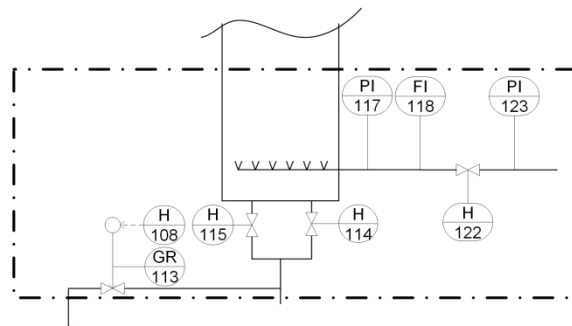


**Figure 4.3: (a) Flow sheet for the single bubble (SB) HSC/PIV/EDM and (b) the changed part for the bubble swarm (BS) HSC/EDM investigation (in parts from [3, 6])**

The liquid flow, generated by a Stübbe SMB50 centrifugal pump, was measured with a Honsberg flow transmitter Rototron RRO-025 rotor flow meter calibrated for water in a range between 0 and 1000 L/h. For the Xanthan solution, due to the differing rheological characteristic in comparison to water, a separate calibration was done for the flow meter. The results of the test are shown in **Figure 4.2**. Based on these results, the volumetric flow rate of the Xanthan solution had to be set respective to

$$Q_{f,set} = \frac{Q_{f,real} - 89,5 \frac{L}{h}}{1.02} \quad (4.4)$$

(with  $Q_{f,set}$  as the set and indicated and  $Q_{f,real}$  as the actual, real volumetric liquid flow rate in L/h).

The whole system was controlled with National Instruments LabVIEW (several versions starting from 2010, in the following only called LabVIEW). The process and instrumentation flow sheets for the single bubble and bubble swarm experiments are shown in **Figure 4.3a** and **Figure 4.3b**, respectively.

For the single bubble experiments, the whole process of

- injecting a defined gas volume,
- turning the bubble cup to release the bubble,
- returning the bubble cup to its initial position,
- all with a defined co-current liquid flow,

was controlled with LabVIEW. For the EDM (for which the flow sheet is shown in **Figure 4.3a**) and PIV measurements, the recording of the experimental data was included in the LabVIEW control either by directly recording the data (EDM) or sending out trigger signals to an external computer (PIV). The HSC data recording was started by hand. In bubble swarm experiments, the gas flow rate was set by hand and all data recordings (HSC/EDM) were started manually.

## 4.2 The continuous phases

As mentioned in **Section 2**, most fluid dynamic investigations in MBRs were carried out in water. In parts, this was done based on Ozaki and Yamamoto's conclusion that findings from fluid dynamic investigations made with water as the continuous phase can be transferred to real activated sludge systems [46]. This statement was based on a difference of the viscosity of 10 % between water and activated sludge ignoring the rheological characteristic of the sludge. Among other things, based on this statement, the continuous phases (without solids as apparent in waste water sludge) were chosen for this investigation with

- water as the reference system (here: deionized water),
- a non-Newtonian model solution, with rheological flow behavior representative for an 'average' MBR sludge and
- water and a non-Newtonian model solution each containing ions, as an approach to the complex composition of the mixed liquor in real MBRs.

Ratkovich et al. [45] and Rosenberger et al. [131] discussed the rheological behavior of activated sludge. Besides a different rheological behavior, higher values of the viscosity were found by Rosenberger et al. than mentioned by Ozaki and Yamamoto. Based on the Ostwald-de-Waele approach

$$\mu = K\dot{\gamma}^{n-1} \quad (4.5)$$

(with the flow consistency index  $K$  in  $\text{Pa s}^n$ , the shear rate  $\gamma$  in  $\text{s}^{-1}$  and the flow behavior index  $n$ ), Rosenberger et al. gave an equation which correlates the apparent viscosity  $\mu$  with the concentration of the mixed liquor suspended solids (MLSS) in the activated sludge described by:

$$\mu = \exp(1.9 \text{ MLSS}^{0.43}) \text{ mPas}^{-0.22 \text{ MLSS}^{0.37} - 1} \gamma^{-0.22 \text{ MLSS}^{0.37}} \quad (\mu \text{ in mPas, MLSS in g/L}) \quad (4.6)$$

With respect to the different systems investigated by Rosenberger et al. (municipal, various industrial waste waters, molasses), an MLSS concentration of 10 g/L is a typical value in the determined range of 2.7 g/L up to 55 g/L. Therefore, in this investigation, a rheology of an activated sludge with an MLSS concentration of 10 g/L was chosen as a typical mean value, i.e.:

$$\mu(c_{\text{MLSS}} = 10 \text{ g/L}) = 166 \text{ mPas}^{0.48} \gamma^{-0.52} \quad (4.7)$$

Higher MLSS concentrations lead to higher flow consistency indices lifting the general viscosity level but also enhance the reducing effect with increasing shear rate by lifting the flow behavior index. In **Figure 4.4**, the viscosity as calculated from eq. (4.7) is given as a function of the shear rate. For the whole plotted shear rate range which is realistic for an aerated system (as discussed, e.g., in [8]), the viscosity of the activated sludge is higher by a factor of at least 4, up to a factor of approximately 150 in comparison to the viscosity of water. Ozaki and Yamamoto investigated activated sludge with MLSS concentrations of 0.8 to 6 g/L. Although only valid above an MLSS concentration of 2.7 g/L, based on the correlation by Rosenberger et al., even for the lowest MLSS concentration of 0.8 g/L, this leads to a higher viscosity in comparison to water with a factor of 1.4 up to 5.6 (see **Figure 4.4**). Without even discussing fluid dynamic results up to this point, it can be stated that even for the MLSS concentration of 2 to 3 g/L which were the basis for Ozaki and Yamamoto's statement, the general validity of their assumption can be doubted.

As transparent solutions were necessary for most of the measurement techniques, activated sludge could not be used. Instead, a Xanthan gum solution (in the following called Xanthan solution) consisting of deionized water

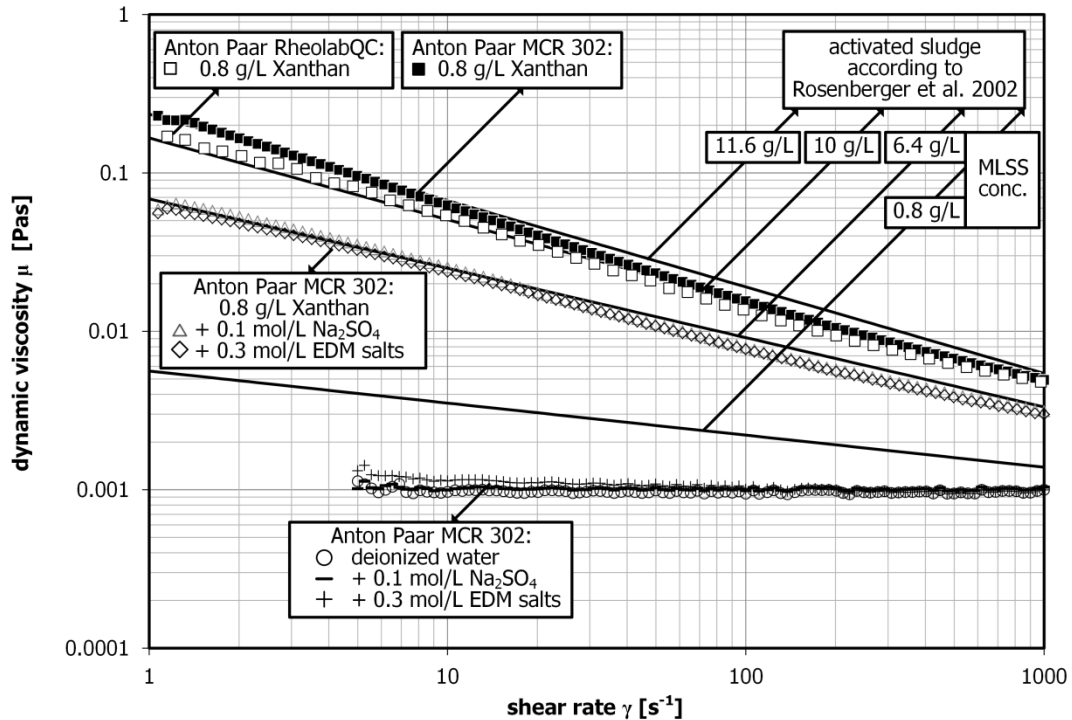


**Figure 4.4:** Apparent viscosity of the waters and different Xanthan solutions against the shear rate and of activated MBR sludge based on the correlation by Rosenberger et al. [131]

and 0.8 g/L Xanthan gum TER2000 (supplied by Colltec GmbH) was used. This kind of solution is transparent but shows a comparable rheological behavior to activated sludge. The rheology of the solution was measured in the laboratory with an Anton Paar RheolabQC rather in the beginning of the investigation (2011) and with an Anton Paar MCR302 at the end (2014). In the earlier tests, a solution of 0.8 g/L Xanthan gum in deionized water showed a very good fit to the respective activated sludge with 10 g/L MLSS (see **eq.(4.7)**) with a behavior described by:

$$\mu(c_{\text{Xanthan}} = 0.8 \text{ g/L}) = 173 \text{ mPas}^{0.47} \gamma^{-0.53} \quad (4.8)$$

The recent tests revealed changed  $K$  and  $n$  values respective to

$$\mu(c_{\text{Xanthan}} = 0.8 \text{ g/L}) = 238 \text{ mPas}^{0.42} \gamma^{-0.58}. \quad (4.9)$$

This is closer to an activated sludge with an MLSS concentration of 11.6 g/L with

$$\mu(c_{\text{MLSS}} = 11.6 \text{ g/L}) = 236 \text{ mPas}^{0.45} \gamma^{-0.55}. \quad (4.10)$$

Over the whole tested shear rate range, this makes an average difference of 20 % between the old and the new measurement. The change of the rheological behavior of the Xanthan solution can be designated to several reasons. The main reason is that the Xanthan gum itself is a biological product which can have minor differences from batch to batch. Additionally, the quality of the deionized water, the measurement system (measurement error in the range of 2 to 5 %) or the accuracy of the weighing of the Xanthan gum might be influencing factors. Activated sludge is a complex composition of several compounds. With liquors and ions in it, a coalescence hindrance system can be assumed for the bubble swarm. To simulate this coalescence hindrance, two surfactants were tested. For both, the surface-active agent sodium dodecyl sulphate (SDS) and the inorganic salt sodium sulphate  $\text{Na}_2\text{SO}_4$ , a decrease of the bubble sizes - the actual effect of the coalescence hindrance - were shown [132, 133]. In ionic systems, this effect is usually associated with the orientation of the ions on the surface of the, generally speaking, fluid particle with a repelling effect based on the charge. As the single bubble and bubble

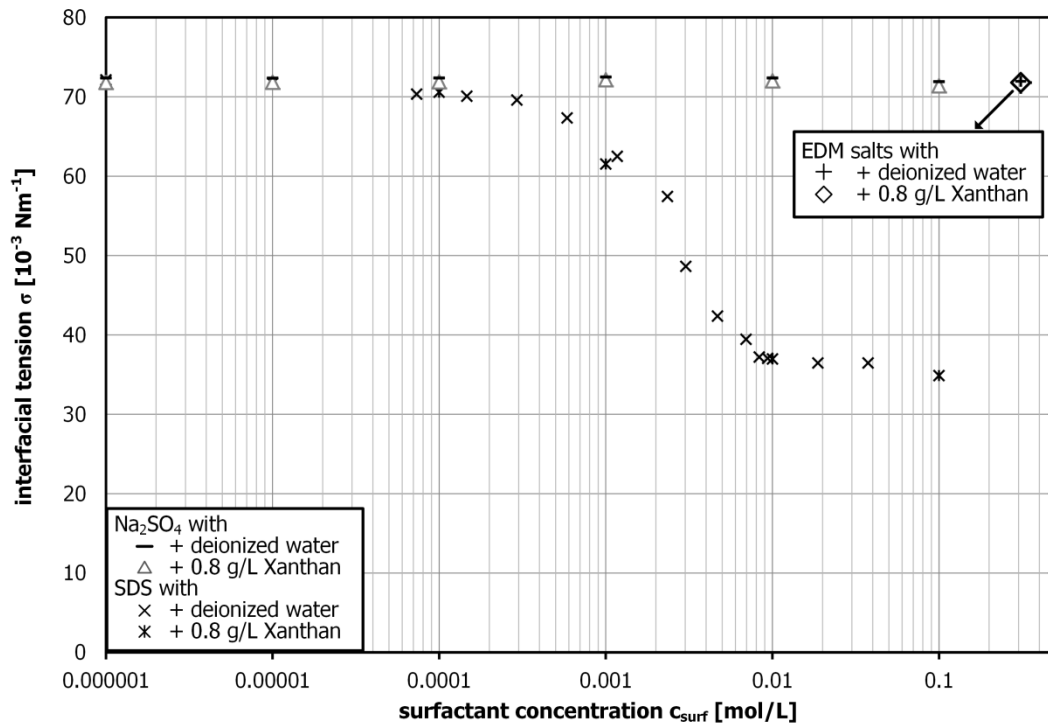


**Figure 4.5: Interfacial tension of water doped with sodium sulphate, SDS and the EDM salts**



swarm experiments in this investigation were supposed to be as similar as possible, a change of the interfacial tension should be as small as possible (a difference of the interfacial tension would lead, e.g., to a difference of the Eötvös number). In the following, the symbol  $\sigma$  will be used for the interfacial tension, common in German literature, in contrast to  $\gamma$ , common in international literature, to avoid confusions with the shear rate. **Figure 4.5** shows results of the interfacial tension measurements for different concentrations of SDS and sodium sulphate. For water and Xanthan solution, the interfacial tension is similar with  $\sigma_w = 72.05 \cdot 10^{-3}$  N/m for water and  $\sigma_x = 71.14 \cdot 10^{-3}$  N/m for Xanthan solution. Generally, the interfacial tension of water and Xanthan solution behaves similarly, even with surfactants. As expected, SDS was found to reduce the interfacial tension (by more than 50 %) while sodium sulphate did not affect the interfacial tension at all. Therefore, the bubble swarm experiments for the HSC measurements in the coalescence hindered system were performed with 0.1 mol/L sodium sulphate, ensuring a coalescence hindered system with comparable conditions to the experiments without ions (see **Table 4.1** for all interfacial tensions measured with a pendant drop system). While surface-active agents are known to influence the fluid dynamics of fluid particles by increasing the rigidity of the surface [107], the effect of the inorganic salt ions on the fluid dynamics of bubbles is not completely clear in literature. Maldonado et al. [134] showed an influence of the concentration of, i.a., sodium sulphate on the bubble shape and the resulting terminal rise velocity which, due to a lack of the influence on the interfacial tension, can only be a result of an effect on the internal circulation in the bubble.

For the EDM tests, a mixture of several salts, necessary for the measurement principle, were added to the deionized water or the Xanthan solution, respectively. For all tests, potassium hexacyanoferrate (III) with a concentration of 0.988 g/L, potassium hexacyanoferrate (II) with a concentration of 2.530 g/L and potassium chloride with a concentration of 22.368 g/L were added. Here, the interfacial tension is also similar to the case with water and sodium sulphate.

Zhong et al. [135] discussed the effect of ions on the rheological behavior of Xanthan solutions. The addition of ions can promote an ordered or a disordered state of the Xanthan molecule (below, or respectively above, a

**Table 4.1: Material properties of the different continuous phases (in parts based on [8])**

measurement technique	continuous phase	density $\rho$ [kg/m <sup>3</sup> ]	interfacial tension $\sigma$ [N/m]	flow consistency index $K$ [Pas <sup>n</sup> ]	flow behavior index $n$ [-]
HSC	water	998.2	$72.05 \cdot 10^{-3}$	$9.76 \cdot 10^{-4}$	1
	PIV Xanthan solution	used in [6]	$72.14 \cdot 10^{-3}$	0.173	0.47
		used in the thesis and [8]		0.238	0.42
	water + Na <sub>2</sub> SO <sub>4</sub>	1010.7	$71.90 \cdot 10^{-3}$	$1.01 \cdot 10^{-3}$	1
	Xanthan solution + Na <sub>2</sub> SO <sub>4</sub>	1011.3	$71.39 \cdot 10^{-3}$	0.066	0.54
EDM	water + EDM salts	1014.2	$71.96 \cdot 10^{-3}$	$1.04 \cdot 10^{-3}$	1
	Xanthan solution + EDM salts	1014.6	$71.80 \cdot 10^{-3}$	0.066	0.54

critical Xanthan concentration of 2 g/L) leading to a decrease, or respectively an increase, of the viscosity. Above a certain ionic strength (approx. 2 mmol/L), this effect is stable. **Figure 4.4** shows the rheological behavior of both Xanthan solutions with ions which are similar for both types of added ions (sodium sulphate and EDM salts) and described by

$$\mu(c_{Xanthan,w/ions} = 0.8 \text{ g/L}) = 65.8 \text{ mPas}^{0.54} \gamma^{-0.46}. \quad (4.11)$$

These types of Xanthan solutions with ions are comparable to activated sludge with an MLSS concentration of 6.4 g/L described by:

$$\mu(c_{MLSS} = 6.4 \text{ g/L}) = 68.6 \text{ mPas}^{0.56} \gamma^{-0.44}. \quad (4.12)$$

The effect of the ions on the viscosity of water is negligible (difference to deionized water around  $\pm 5\%$ ). **Table 4.1** shows all measured material properties for the different continuous phases.

For the PIV measurements (only performed for the single bubble rise), particles had to be added as this technique is based on the light scattering or fluorescence of particles (see **Section 4.4**). The used particles were made of poly methyl methacrylate (PMMA,  $\rho_p = 1190 \text{ kg/m}^3$ ) coated with Rhodamine B (supplied by microparticles GmbH). Although neutral buoyancy is favorable, a certain density difference in comparison to the used continuous phases was apparent (see **Table 4.1** for the densities of the continuous phases measured with an Anton Paar DSA 5000M). PIV tests were performed without any flow to see if a movement of the particles due to the gravitational force could be observed. With the used measurement settings, no such movement was found. The polydisperse particles were in a particle diameter range between 20 and 50  $\mu\text{m}$ . Although the particle concentration always had to be adjusted to the respective experiment, an average mass fraction of  $10^{-2} \text{ wt\%}$  can roughly be assumed for all experiments. For such low mass fractions, Hooshyar et al. [136] found no influence of solid particles on the bubble rise velocity. Additionally, Hooshyar et al. gave a critical Stokes number for Newtonian liquids

$$St = \frac{\tau_p}{\tau_b} = \frac{\frac{\rho_p d_p^2}{18\mu}}{\frac{d_b}{w_{B,rel}}} \quad (4.13)$$

of  $St_{crit} = 1$ , with no influence on the single bubble rise for  $St < 1$  (with  $\tau_p$  as the Stokes relaxation time of the particle,  $\tau_b$  as the characteristic time of the rising bubble,  $d_p$  as the particle diameter in m,  $\mu$  as the dynamic viscosity of the liquid in Pa s,  $d_b$  as the bubble diameter in m,  $w_{B,rel}$  as the relative terminal rise velocity of the bubble in m/s). Assuming the ‘worst’ case, for the largest solid particles and the smallest bubbles rising in water, a Stokes number of  $St = 10^{-2}$  was found. Therefore, the assumption of a negligible influence of the particles on the bubble ascent is valid.

In an attempt to do the same calculation for the non-Newtonian Xanthan solution, approximating the liquid viscosity  $\mu$  with

$$\mu = K \left( \frac{w_{B,rel}}{d_b} \right)^{n-1}, \quad (4.14)$$

a Stokes number would be calculated as:

$$St_{nN} = \frac{\frac{\rho_p d_p^2}{18}}{K \left( \frac{d_b}{w_{B,rel}} \right)^{n-2}} \quad (4.15)$$

With such a calculation, again in the worst case for the largest solid particles and the smallest bubbles, a Stokes number of  $St_{nN} = 3.6$  was found. Here, the Stokes number is above the critical value but still it is worth mentioning that Hooshyar et al. [136] did not test the influence of solid particles on bubbles rising in non-Newtonian continuous phases and even for such Stokes numbers, they did not find an influence on the bubble ascent due to the low mass fraction of the particles.

### 4.3 High Speed Camera Imaging (HSC)

For the high speed camera imaging of single bubbles [4, 6] and bubble swarms [8] the experimental setup consisted of:

- Photonfocus MV-D752-80-CL-8 CMOS progressive scan camera
  - 8-bit gray scale camera
  - maximum resolution of 752 px by 582 px (at 350 frames per second)
  - maximum frame rate of 63000 frames per second (at approx. 752 px by 1 px)
  - 10  $\mu$ s minimum time difference between the two images
  - maximum quantum efficiency at 570 nm wavelength of the light
  - lense: Nikon Nikkor AF 50 mm f/1.8D and Pentax 12 mm f/1.2
- illumination system
  - two tubular fluorescent lamps aligned vertically with the flow channel
  - power transformer for a change of the alternating current voltage from 50 Hz to 40 kHz to avoid different illumination intensities on the images recorded by the high speed camera due to overlaying frequencies of the illumination power supply and the recording instants of the camera
  - light diffusing paper to gain a uniform light intensity on the recorded image
- computer
  - setup software PFRemote 2.40
  - recording software Microdisplay 3
  - image analysis software National Instruments Vision Development Module in LabVIEW 2013 (and newer) and ImageJ (v.1.46 and newer)
  - data analysis software Microsoft Excel 2003 and 2010 and MathWorks MATLAB 2010 (and newer)

The image recording was performed at 100 frames per seconds with a resolution of 100 px by 582 px (SB, in the y-z-plane, see **Figure 4.6a**) or 200 frames per second at a resolution of 148 px by 582 px (SB and BS, in the x-y-plane). The automated image analysis performed with LabVIEW consisted of the following steps (further described in [137]):

- cutting of the images to the appropriate size
 

Due to practical reasons, the recorded images contained the side wall of the flow channel. The image that was used for the analysis was cut in a way that only inner flow-through-regions were part of the image.
- subtraction of the background image (without bubble/s) from the raw image (with bubble/s)

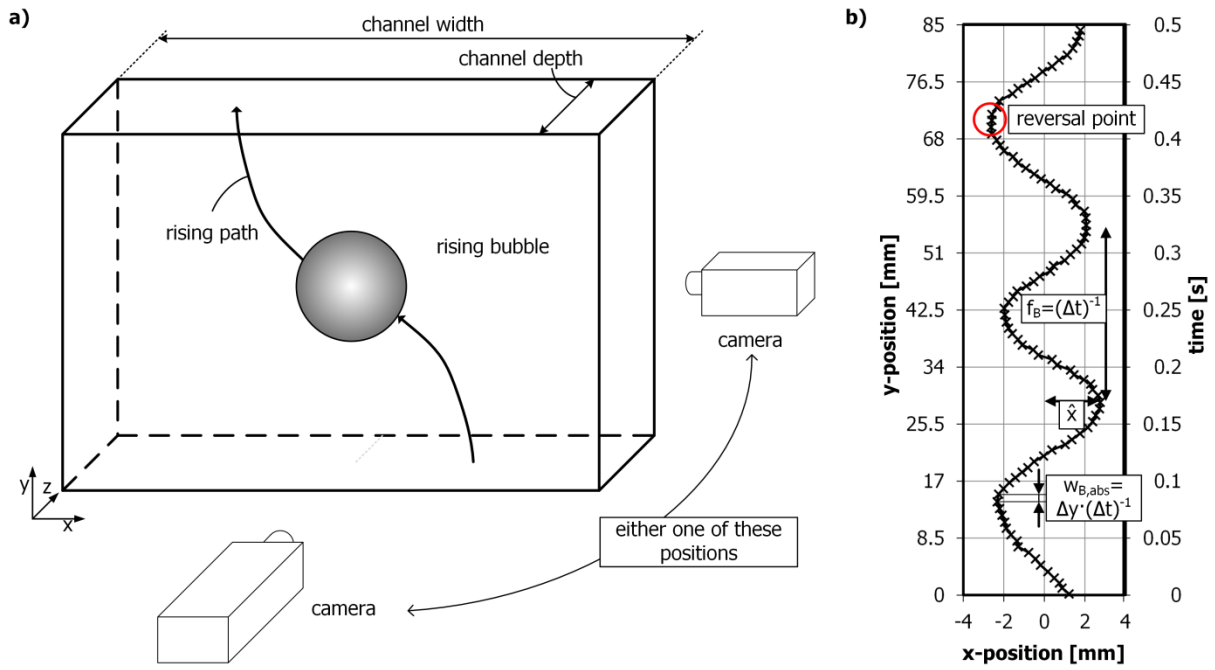


**Figure 4.6:** (a) Field of view in the HSC experiments, either for the movement parallel to the plates (x-y-plane) or between the plates (y-z-plane) and (b) example for a rising path of a single bubble ( $d_c = 5$  mm,  $d_B = 5$  mm,  $v_L = 0$  m/s) (based on [4])

To determine the bubble/s in the image, an image without bubble/s was subtracted so that ideally only pixels at positions where the edge of a bubble was located had gray scale values above zero.

- conversion of the 8-bit image into a binary image by setting a gray scale threshold

As in reality the background subtraction did not work perfectly (e.g., due to minor light fluctuations during the experiment), pixels had a gray scale value slightly above zero which were not related to a bubble edge. Therefore, a threshold gray scale value was chosen. If a pixel had a gray scale value below the threshold, its value was set to zero. Respectively, all pixels with gray scale values above the threshold got a value of one resulting in a binary image. As for the different experiments no objective way was found to set a threshold value, this was done by hand to ensure comparable conditions for all cases.

- edge detection and if necessary closing the edge/s

For further analysis, each individual bubble (in case of the bubble swarm) had to be defined which was done by finding closed edges. Each closed edge was one bubble. If edges were not completely closed (forming an open circular-like shape), these open edges were closed by a straight connection and all gray scale values of the pixels on this line were set to one.

- filling the area inside closed edges
- The gray scale values of all pixels inside a closed edge were set to one.
- export of the mass center/s of the bubble/s (SB, BS), vertical and horizontal dimensions of the bubble (SB) and area covered by the bubbles (BS) to Microsoft Excel

Of each individual detected bubble, the mass center and the dimensions in x-direction (horizontal) and in y-direction (vertical) was calculated. This data was exported to Microsoft Excel 2010 which was used to analyze the data.

In case of the single bubble, with the information about the mass center of the bubble (x- and y-coordinate) in consecutive images, the rising path can be assembled [4] and, with the knowledge about the interframe time, the absolute rise velocity and the amplitude and frequency of the oscillation can be determined [4, 6] (see **Figure 4.6b**). Additionally, the vertical (in y-direction) and horizontal dimensions (in x-direction) of the bubble are calculated. This information is used for further related calculations of, e.g., an adjusted friction factor [6]. Due to the oscillating movement of the bubble apparent in most cases, all quantities related to the bubble movement oscillated as well. Besides the natural oscillation of the determined quantities during one bubble ascent, a statistical fluctuation between the different measurements of one parameter combination was apparent as well. **Figure 4.7** shows - for an example parameter combination - the development of the mean value of the absolute terminal rise velocity of the bubble and its standard deviation (primary y-axis; the y-axis is scaled to the range between 17 and 19 cm/s to make the development observable). The secondary y-axis shows the development of the relative change of the mean and standard deviation. An amount of 40 measurements proved to be sufficient for relative changes below 1 %. In the actual experiments, at least 50 bubble ascents were recorded for each parameter combination to allow the deletion of potential outliers which were determined manually. For the bubble swarm experiments [8], the gas hold-up was quantified based on the area covered by the bubbles relative to the total area on the 2D images. Additionally, the overlaying of the determined mass centers of the bubbles of several consecutively recorded images allowed the qualitative illustration of bubble paths.

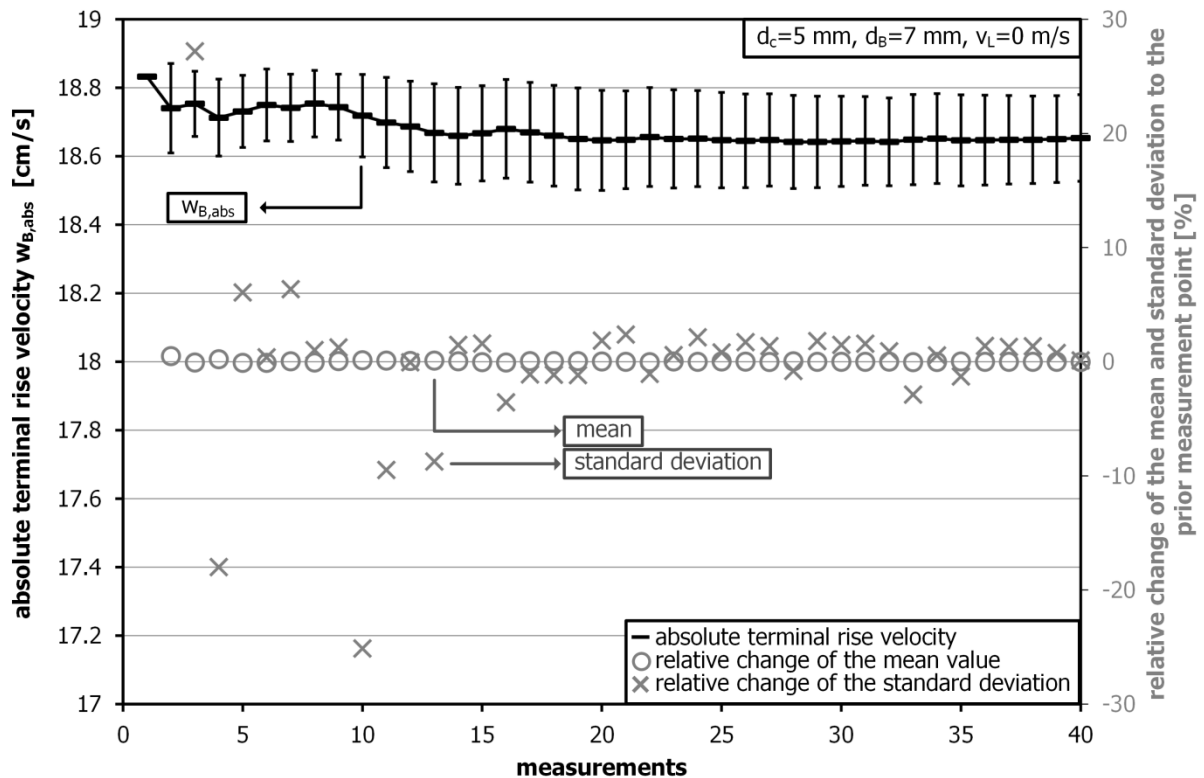


**Figure 4.7:** Development and the standard deviation of the mean absolute terminal rise velocity and the relative change of the mean and standard deviation in comparison to the prior measurement point against the number of measurements

## 4.4 Particle Image Velocimetry (PIV)

Particle image velocimetry is a measurement technique to determine fluid dynamic conditions based on the tracking of the movement of particle clusters within the fluid [138]. In this investigation, a LaVision Flowmaster 2D PIV system was used together with the DaVis 8 control and analysis software. The system consisted of:

- Imager Pro SX 5M CCD progressive scan camera
  - interline transfer CCD sensor for rapid charge transfer to the storage area
  - 12-bit gray scale camera
  - maximum resolution of 2456 px by 2058 px (at approx. 7 double frames per second)
  - maximum frame rate of 14.2 double frames per second (at approx. 2456 px by 800 px)
  - 600 ns minimum time difference between the two images of a double frame
  - maximum quantum efficiency at 532 nm wavelength of the light
  - lenses: Nikon Nikkor AF 50 mm f/1.8D and Navigon Zoom Lens (up to 28x magnification)
  - fluorescence edge filter cutting of light with a wavelength below 540 nm
  - the field of view size in this investigation was in all cases approximately 55 x 170 mm<sup>2</sup>
- Nitron NL 135-15 Nd:YAG PIV laser
  - dual laser head with a maximum repetition rate of 15 Hz each
  - light produced at 1064 nm, light emitted at 532 nm
  - 135 mJ maximum energy output
  - pulse width 5 ns
  - power supply unit with 650 W
  - attenuator for the control of the flash light energy of each laser head and general energy output
- laser guiding arm and several lenses for the positioning and spanning of the laser sheet used for the illumination
- computer
  - programmable timing unit PTU 9 for the reception of external trigger signals and trigger signal output for the camera and laser
  - software DaVis 8 controlling the PIV measurement and recording and analyzing the data
- PMMA particles coated with Rhodamine B since uncontrolled reflections of the laser light from the bubble surface have to be avoided for security reasons
  - density:  $\rho_P = 1190 \text{ kg/m}^3$
  - particle size range: 20 to 50  $\mu\text{m}$
  - Rhodamine B: 2-[6-(diethylamino)-3-(diethylimino)-3H-xanthen-yl] benzoic acid
  - for 532 nm light absorption, a maximum fluorescent light emission at 584 nm

In an ideal case, the particles move respective to their surrounding liquid (a discrepancy between the liquid and particle movement is mainly due to density differences between the liquid and the particle). The emitted light from the particles is recorded with the camera in a double frame mode with a defined time difference between the laser emissions of the two laser heads each illuminating one frame. The images are split up into interrogation windows of defined sizes each containing images of particle clusters. For each interrogation window, containing a defined number of pixels with respective gray scale values, a recalculation by fast Fourier transformation

(FFT) is done. Based on this calculation, the two images of the double frame can be compared with a cross correlation and, ideally, one intensity peak with a sufficient signal-to-noise ratio is found representing the most likely displacement of the particle cluster between the two images. The combination of the information about this displacement, equivalent to a certain distance, and the time difference between the two laser emissions give the representative velocity for this interrogation window. By doing this for all interrogation windows, a (2D) velocity vector field can be built up [139, 140]. Based on this knowledge, the experiment has to be designed respectively, i.e., with an appropriate particle size and concentration and a suitable time difference between the recordings of the double frame. Several analysis adjustments are discussed in literature for the improvement of the results, such as multi-pass analysis, grid refining schemes, image deformation schemes or multiple-grid analysis as well as post-processing procedures for the replacement of incorrect data [138].

In the PIV measurements performed for this study [2, 7], rather simple analysis types were used for the raw data. A multiple pass algorithm with two passes and a grid refinement were applied. This method of offsetting the interrogation window in the second pass in a way that the correlation peak shows only a minor pixel displacement, improves the signal-to-noise-ratio and reduces the resulting error [138]. Further post-processing was done based on a comparison procedure where every velocity vector is compared to its surrounding velocity vectors. The velocity vector is replaced if its direction and velocity magnitude is not within a certain limit of the average of the surrounding velocity vectors.

The challenge of the application of PIV in this thesis was less on the side of the actual PIV algorithm analysis but rather on the extraction of information from this data. The transient rising behavior of the bubble with an oscillating ascent through the field of view (**Figure 4.8**) basically only allowed an interpretation of instantaneous flow fields (**Figure 4.9a** in water). For steady state processes, an average flow field can be calculated from a certain number of double image recordings, compensating minor fluctuations of the system. As described in Böhm and Kraume [7], here, such an averaging is not possible. For transient periodic processes, e.g., the rotation of a propeller, the phase-locking procedure can be used for the generation of averaged flow fields by recording a certain number of double images at the same propeller angle during its rotation. As the bubble oscillation is a periodic process, the basic idea of this PIV operating type would be applicable here as well but it requires either

- an appropriate triggering (in case of the rotating propeller, e.g., a position detector on the shaft with a trigger signal output) or
- a sufficiently time-resolved recording that allows the extraction of flow fields related to fixed phases in the periodic movement.

Neither of these requirements could be fulfilled for this investigation:

- the triggering for a defined position of the bubble in its rising period is not possible. Theoretically - but not practically - this might be possible
  - with a simultaneous high speed imaging and a real-time analysis of the bubble movement or
  - if the rising paths of the bubbles were equal in all cases, then a trigger signal at the moment of the release of the bubble would be sufficient

- the maximum frame rate of the used PIV system of 14.2 Hz was too low to resolve the periodic movement of the bubble (the oscillation frequency was in a range of 5 to 10 Hz [6] requiring a frame rate of at least 100 to 200 Hz for a proper resolution of the movement)

Therefore, a modified quasi-phase-locked recording was introduced for this investigation [7]. Although the triggering of the PIV recording with the release of the bubble was not sufficient to record the bubble in the same phase of the rising period, this at least allowed recording images with the single bubbles roughly at the same position in the field of view (**Figure 4.9b**). As this still did not allow the calculation of averaged flow fields, the following procedure was introduced:

- For each individual bubble ascent the desired quantity was determined for each interrogation window within the recorded image.
- The values determined for each interrogation window for each separate bubble ascent were exported (without any information about the position of the respective interrogation window).
- This data was used for a statistical analysis showing the probability of the occurrence of the quantity in the flow field (as cumulative distribution functions (CDF), with an example shown in **Figure 4.9c** in a probability grid for the velocity magnitude  $w_{abs}$ ).
- Based on the idea of box-and-whisker plots, as commonly used in statistics, from the CDFs the 1st, 10th, 90th and 99th quantile (as indicated by the white, grey and black bar in **Figure 4.9c**) were extracted and used for the comparison.

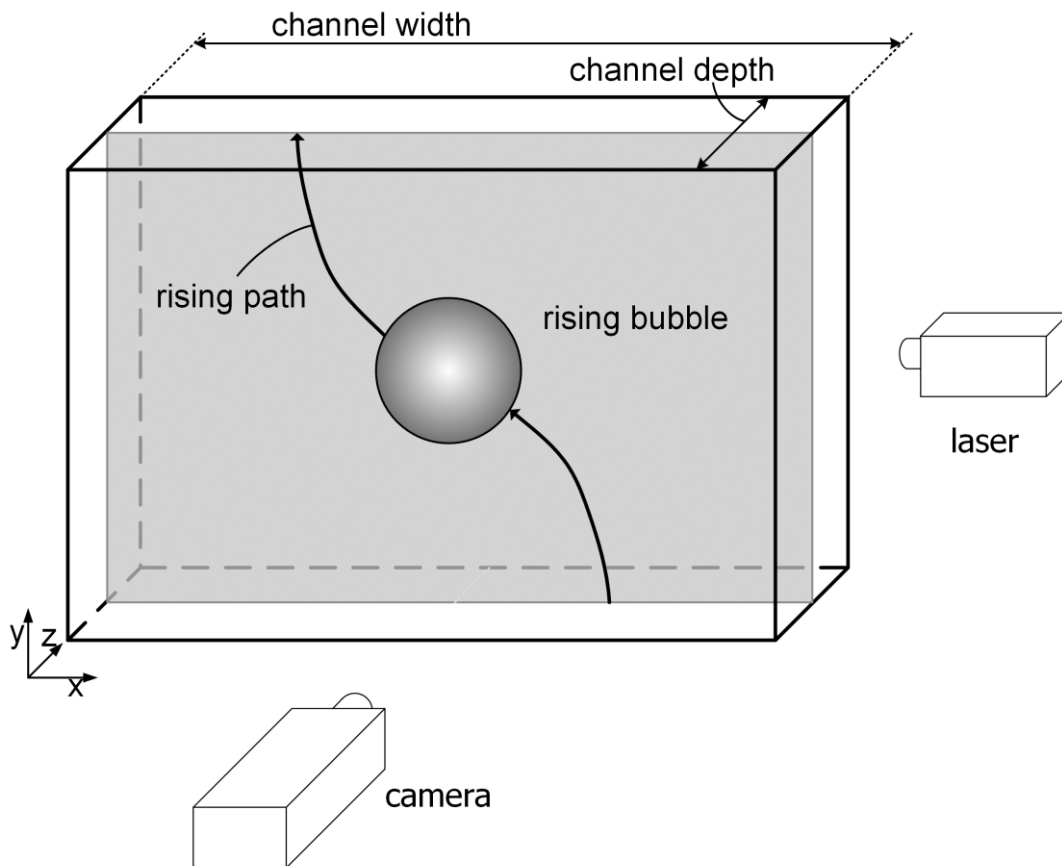


**Figure 4.8:** Field of view in the PIV measurements (retrieved from [7], based on [141])



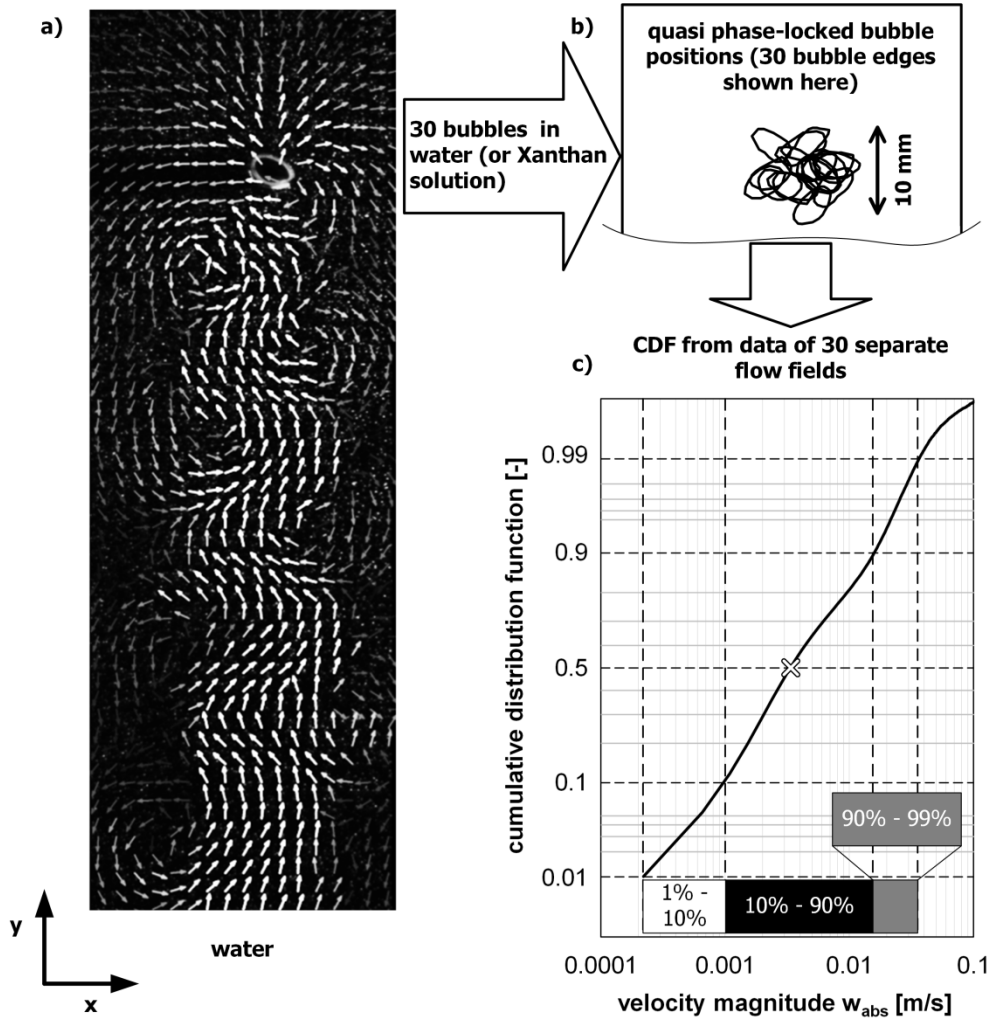


Figure 4.9: (a) Qualitative, instantaneous velocity fields (brighter color of the vectors indicating higher values of the velocity magnitude  $w_{abs}$ ) near the bubble in water, (b) position of the bubble for 30 bubble ascents with phase locked recording (here, e.g., in water) and (c) CDF of the velocity magnitude  $w_{abs}$  accumulated from 30 images plotted in a probability grid (based on [7])

An amount of approximately 30 measurements per parameter combination proved to be a sufficient data base for the CDFs. This type of analysis (here: done with MathWorks MATLAB) allows a quantitative comparison of the different parameter combinations in this study but also - potentially - allows the comparison with other systems.

The determined quantities were

- the velocity magnitude  $w_{abs}$ : absolute value of the velocity vector in x-y-direction  $|\overline{w_{xy}}|$ ,
- the vorticity  $\vec{\omega}$ : rotation of the velocity  $\overline{w_{xy}}$  around  $z$  calculated as  $\left(\frac{\partial w_y}{\partial x} - \frac{\partial w_x}{\partial y}\right) \vec{e}_z$  (not in this thesis; results shown in [7]),
- the shear rate  $\gamma_{liq}(yx)$ : calculated as  $\frac{\partial w_y}{\partial x}$ ,
- and the shear stress  $\tau_{liq}(yx)$ : calculated as  $K \left(\frac{\partial w_y}{\partial x}\right)^n$ .

All results are shown for the field of view in the x-y-plane in the symmetry plane between the walls. In a real flat sheet membrane system, this would be the symmetry plane between two membrane plates.

## 4.5 The electrodiffusion method (EDM)

The principle of the EDM was described in detail in Böhm et al. [5] and the articles discussing results gained by the EDM [2, 3, 8]. The basic components of this measurement technique are

- cathodes (here: 8 platinum wires with a diameter of 0.5 mm mounted flush with the flow channel wall with a distance of 5 mm between each other),
- an anode (here: platinum wire inserted into the flow channel) connected to a voltage source and
- an electrolyte solution (here: composed as described in **Section 4.2**) between the electrodes.

With the used electrolyte solution, a heterogeneous reaction ( $\text{Fe(CN)}_6^{-3} + \text{e}^- \rightarrow \text{Fe(CN)}_6^{-4}$ ) takes place at the electrodes measurable as a voltage drop (as this voltage drop is in the  $\mu\text{V}$  range, here a 1000 fold amplification was used). The voltage difference between the electrodes is set to a value (here: 500 mV) that guarantees a mass transfer limited system (limiting-current-condition). Therefore, the measured voltage drop only depends on the mass transfer which increases with higher convective mass transfer. Based on a mass balance, a relation for the current  $I$  (measured at 500 or 750 Hz;  $I$  is related to the voltage by Ohm's law; here, an Ohmic resistance with  $100.2 \Omega$  is used) and the wall shear rate  $\gamma_s$  (in  $\text{s}^{-1}$ ) can be found for the steady state

$$\gamma_s = k_{Lev}^{-3} I^3 \quad (4.16)$$

with  $k_{Lev}$  as the Leveque coefficient in  $\text{A/s}^{1/3}$  [142]. With all the assumptions made in the derivation and the setup used here, the wall shear rate is determined normal to the wall (z-direction) as

$$\gamma = \sqrt{\left(\frac{\partial w_y}{\partial x}\bigg|_{z=0}\right)^2 + \left(\frac{\partial w_x}{\partial y}\bigg|_{z=0}\right)^2} \quad (4.17)$$

The Leveque coefficient can be determined theoretically as a function of the electrode area, ion concentration and diffusion coefficient of the ions. In this study, the Leveque coefficient was determined by a calibration with defined shear rates to the electrodes. **Figure 4.10** illustrates the result of the calculation of the theoretical relative single-phase liquid velocity

$$\begin{aligned} \frac{w_y(x, z)}{v_L} &= \frac{3}{8} \left( \left[ 1 - \frac{6d_c}{d_w} \sum_{k=1}^{\infty} \frac{\tanh\left(\frac{\alpha_k d_w}{d_c}\right)}{\alpha_k^5} \right] \right)^{-1} \dots \\ &\dots \left[ 1 - \left(\frac{z}{d_c/2}\right)^2 + 4 \sum_{k=1}^{\infty} \frac{(-1)^k}{\alpha_k^3} \frac{\cosh\left(\frac{\alpha_k x}{d_c/2}\right)}{\cosh\left(\frac{\alpha_k d_w/2}{d_c/2}\right)} \cos\left(\frac{\alpha_k z}{d_c/2}\right) \right] \quad (4.18) \\ &\text{with } \alpha_k = (2k - 1) \frac{\pi}{2} \end{aligned}$$

based on Papanastasiou et al. [143] (Newtonian fluid in  $d_c = 7 \text{ mm}$ ,  $d_w = 0.16 \text{ m}$ ,  $v_L = 0.2 \text{ m/s}$ ). **Figure 4.10a** is a contour plot of the velocity distribution in the channel cross section, **Figure 4.10b** shows the velocity profile in the z-direction and **Figure 4.10c** shows the velocity profile in the x-direction, both at center position. Such theoretical calculations can be done for non-Newtonian liquids as well. For the simplified case of  $d_w \rightarrow \infty$ , based on the Navier-Stokes equation and the Ostwald-de Waele approach, a velocity profile of  $w_y$  as a function of  $z$  can be analytically calculated

$$\frac{w_y(z)}{v_L} = \frac{\left(1 - 2\frac{z}{d_c}\right)^{\frac{n+1}{n}} - 1}{\frac{n}{2n+1} - 1} \quad (4.19)$$

In **Figure 4.10b** and **c**, the velocity profiles of the single phase liquid flows of Xanthan solution with and without ions are included. For the cases with  $d_w \neq \infty$ , Muzychka and Edge [144] calculated theoretical shear rates which were used here to calibrate the system under the respective experimental conditions.

Most results in fluid dynamic research of MBR systems performed with the EDM were calculated using **equation (4.16)**. Actually most of these studies investigate transient systems. For those systems, several types of corrections can be found in literature for measured signals [5]. One equation taking the transient behavior into account is

$$\gamma_c = k_{Lev}^{-3} \left( I^3 + 2k_{Cot}^2 \frac{\partial I}{\partial t} \right) \quad (4.20)$$

with  $\gamma_c$  as the corrected shear rate in  $s^{-1}$ , the  $k_{Cot}$  as the Cottrell coefficient in  $As^{1/2}$  and  $t$  as the time in s. The Cottrell coefficient can be calculated theoretically as a function of the same quantities as the Leveque coefficient. Still, in this investigation the Cottrell coefficient was determined experimentally by voltage step experiments [145] (measured with a frequency of 4000 Hz). Where applicable in this investigation, results of both types of analyses are shown (in this thesis: SB: transient corrected, BS: steady analysis). Based on these shear rates, the respective shear stresses  $\tau$  (in Pa) are calculated using

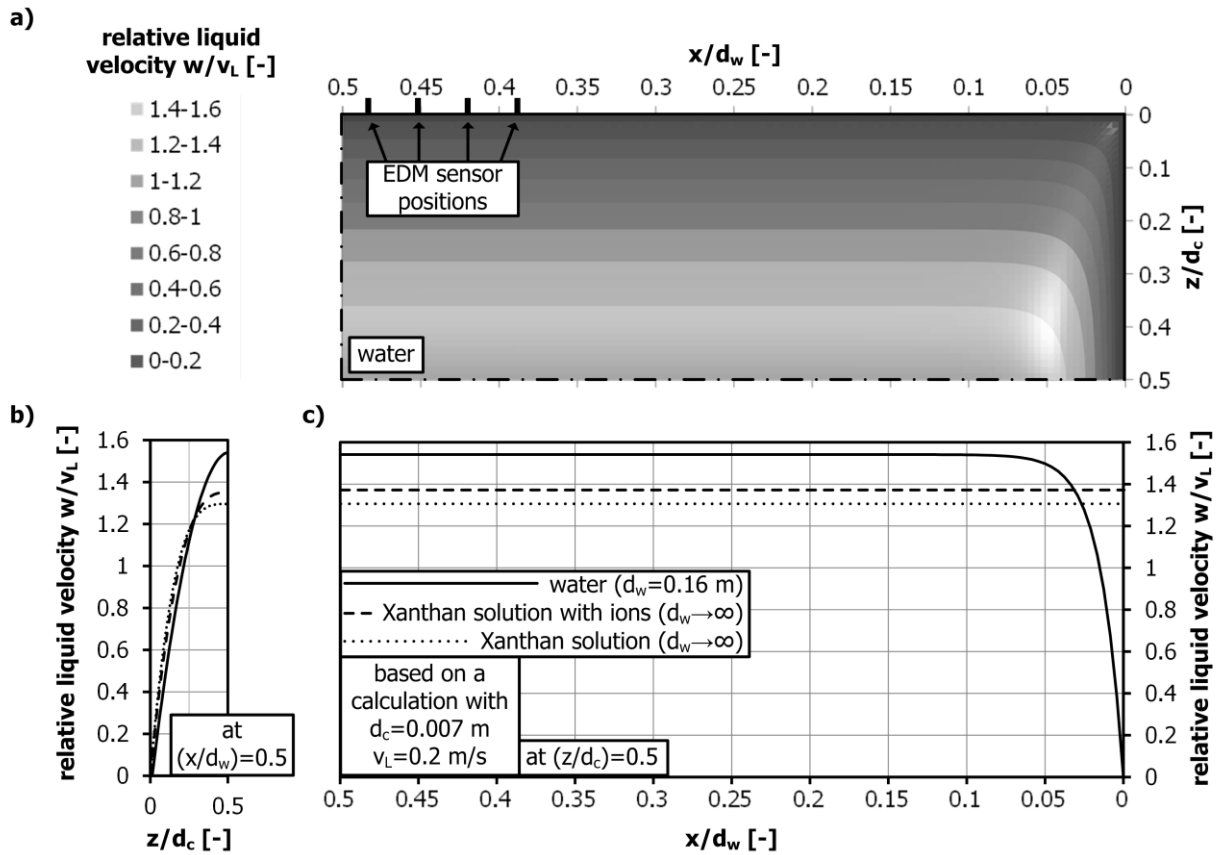


**Figure 4.10:** (a) Theoretical dimensionless liquid velocity profile in a rectangular cross section flow channel for water calculated based on Papanastasiou et al. [143] in the contour plot for one quarter of the cross section, (b) the velocity profile in  $z$ -direction at central  $x$ -position and (c) the velocity profile in  $x$ -direction at central  $z$ -position; (b) and (c) include velocity profiles for non-Newtonian liquids as well

$$\tau = K\dot{\gamma}^n \quad (4.21)$$

for both types of analyses (with  $n = 1$  and  $K = \mu$  for the Newtonian liquid).

The maximum wall shear stress and the global shear wall stress level were analyzed in case of the single bubble and the average shear stress and its fluctuations (represented by the standard deviation) in case of the bubble swarm.

**Figure 4.11a** shows the signal generated by one single bubble. For the analysis, from each of the single bubble rising events,

- the maximum wall shear stress value was determined and
- a global wall shear stress level was evaluated by analyzing all shear stress values in the time period found 0.5 s before and 1.5 s after the occurrence of the maximum shear stress value measured by the sensor which showed the maximum value and the two neighboring sensors.

From this data, CDFs were assembled showing the probability of the occurrence of certain maximum wall shear stress values  $\tau_{max}$  (**Figure 4.11b**) and global wall shear stress level values  $\tau_{glob}$  (**Figure 4.11c**), both plotted in a probability grid. Roughly 1500 single bubble rises were performed for each parameter combination. As discussed for the PIV experiments in **Section 4.4**, in the following the results are presented as a type of box-and-whisker plot, showing the 1st, 10th, 90th and 99th quantile from the CDFs (as indicated by the white, grey and black bar in **Figure 4.11b** and **c**).

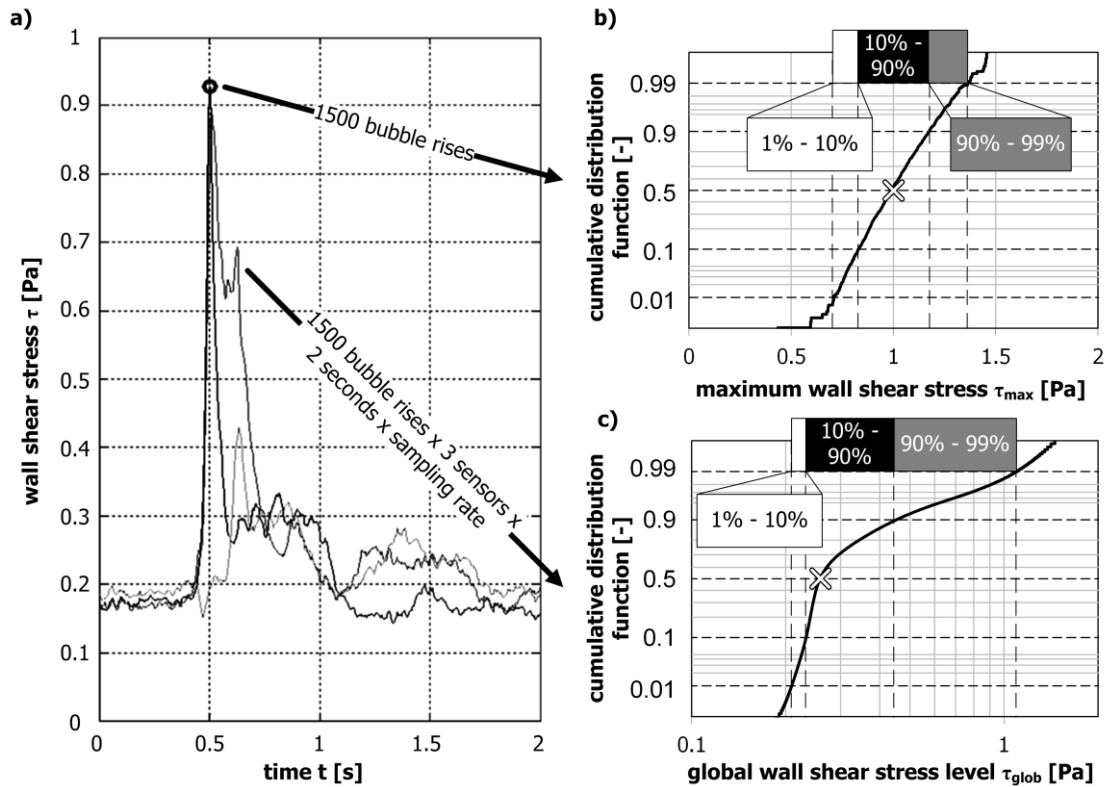


**Figure 4.11:** (a) Shear stress data over time of three sensors for one bubble ( $d_c = 7$  mm,  $d_B = 9$  mm,  $v_L = 0.2$  m/s) with the maximum shear stress marked with a black o, (b) the CDF plots based on 1500 bubble rises of the maximum shear stress, and (c) of the global shear stress level (median marked with a white x) (based on [3])

In case of the bubble swarm experiments, 5 measurements were carried out for every parameter combination, each for three seconds. The start of each measurement was not, as in the case of the single bubble experiments, associated to any particular event. The arithmetic mean and the standard deviation were determined based on the data of all sensors (example data shown in **Figure 4.12**).

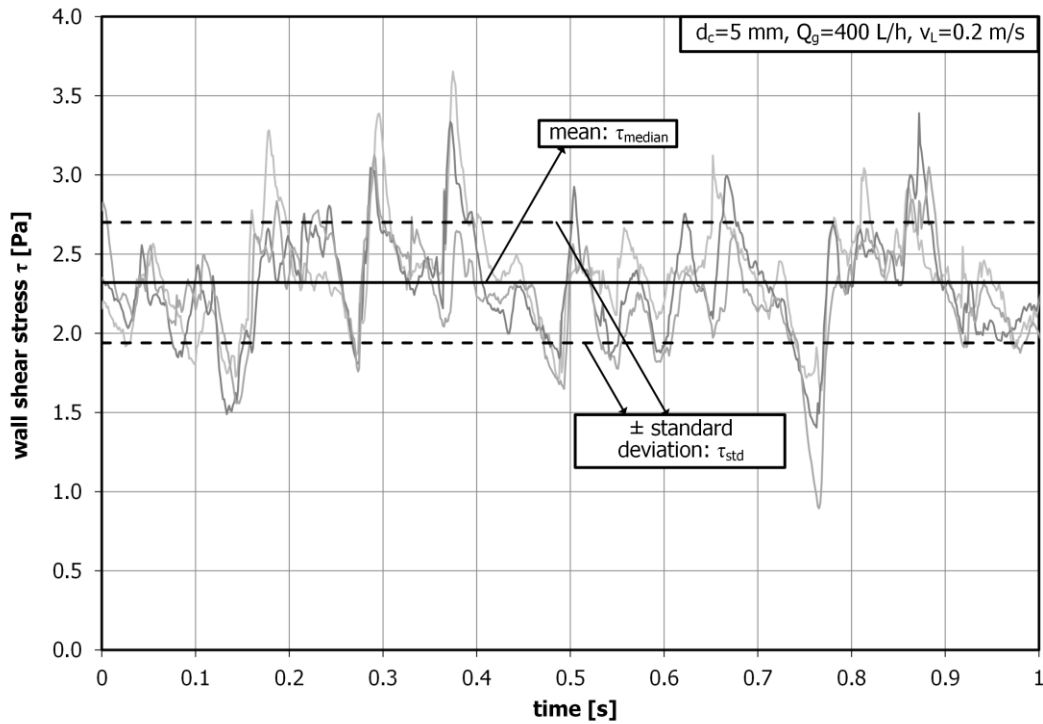


**Figure 4.12:** Shear stress data over time of three sensors for a bubble swarm ( $d_c = 5$  mm,  $Q_g = 400$  L/h,  $v_L = 0.2$  m/s) with the mean value and the standard deviation marked in the plot

## 5 Results and discussion

In this section, the fundamental behavior of single bubbles rising in confining geometries, their influence on the surrounding liquid and the generated wall shear stress are discussed first. This is followed by the discussion of bubble swarms in such systems. The bubble swarm behavior is also related to the previously discussed single bubble results. Boxed text parts contain intermediate conclusions at the appropriate points in the manuscript. Finally, a short cut method for the determination of bubble swarm generated wall shear stresses is presented and also compared to experimental values determined in the system. These results are used to extract engineering recommendations for flat sheet membrane systems.

### 5.1 Single bubbles rising in the flow channel

In this section, the single bubble ascent is the focus of the investigation. The influence of the varied parameters, inspired by the flat sheet membrane application, is discussed. The results are compared to results from literature, mostly found for freely rising bubbles in stagnant Newtonian liquids. The data is also compared to existing correlations and further new correlations are developed as well. All sections, for the bubble behavior, the liquid surrounding the bubble and the generated wall shear stress, include a selection of the results from the respective publication(s) and in **Section 5.1.4** tables are given, summarizing a qualitative overview of the effect of each varied parameter on the analyzed quantities.

#### 5.1.1 Rising behavior of a single bubble

This section covers the bubble dynamics (determined with HSC, based on [4, 6]). The terminal bubble rise velocity can be described by a momentum balance usually given by an equilibrium of the surface or resistance force and the difference between the gravitational and buoyancy force

$$d_B \pi \sigma = C_D \frac{\rho_f}{2} w_{B,rel}^2 \frac{\pi}{4} d_B^2 = \frac{\pi}{6} d_B^3 (\rho_f - \rho_g) g \quad (5.1)$$

(with  $C_D$  as the friction factor,  $w_{B,rel}$  as the relative rise velocity of the bubble in m/s and  $g$  as the gravitational constant in m/s<sup>2</sup>). This momentum balance is based on the two assumptions that the bubble has a spherical shape and that the bubble ascent is a steady state process (discrepancies, especially with regard to the spherical shape assumption, can be compensated by the friction factor). For a bubble rising in water in an unconfined environment, both assumptions are only valid up to a bubble diameter of approximately 1.3 mm (**Figure 5.1a**). The deformation with increasing bubble size is described in **Figure 5.1b** with the help of the Eötvös number

$$Eo = \frac{g(\rho_f - \rho_g)d_B^2}{\sigma} \quad (5.2)$$

(value ranges of the Eötvös number and the following dimensionless numbers are assembled in **Table 5.1**), the Morton number

$$Mo = \frac{g^{3n-2} K^4}{\rho_f^{2-n} \sigma^{n+2}} \quad (5.3)$$

and the Reynolds number

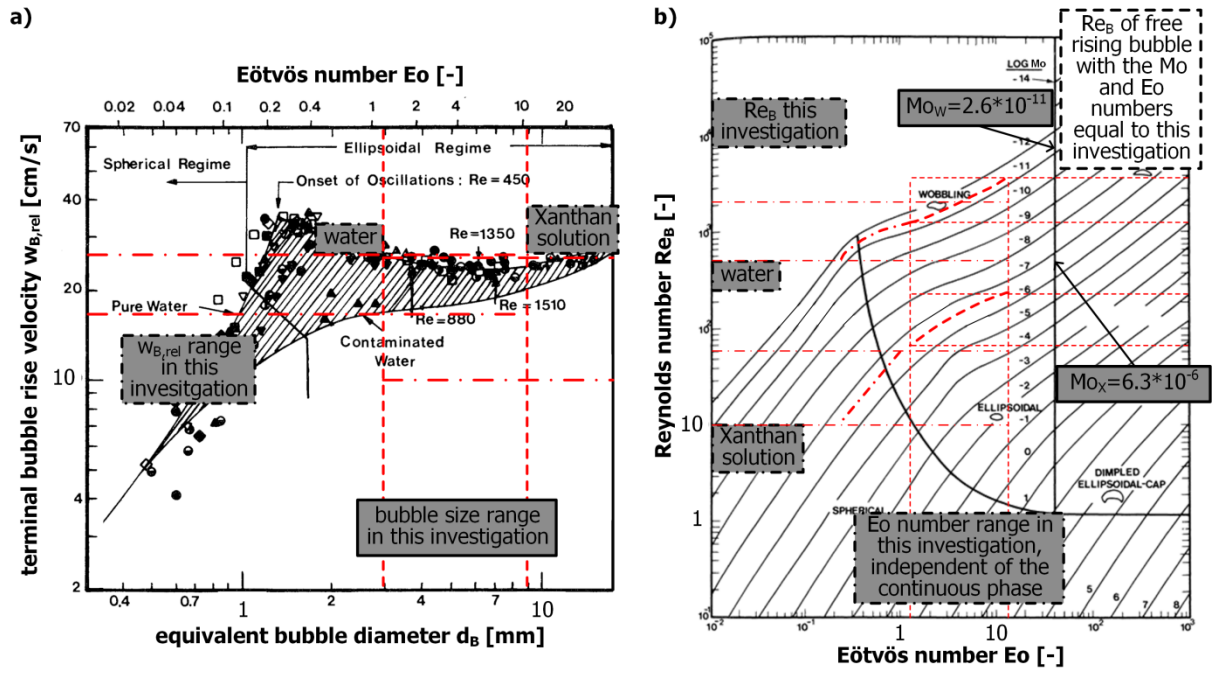


Figure 5.1: (a) Terminal bubble rise velocity in pure and contaminated water for freely rising bubbles and the respective value ranges of this investigation (illustrated as dash/dot-lines) and (b) the chart showing the shape regimes depending on the  $Re$ -,  $Eo$ - and  $Mo$ -number (dash/dot-lines for this investigation, dashed line for freely rising bubbles; based on [10])

$$Re_B = \frac{w_{B,rel}^{2-n} d_B^n \rho_f}{K} \quad (5.4)$$

The respective material properties were shown in **Table 4.1**. Although discussed in detail in the following, in **Figure 5.1a** the ranges of the relative terminal rise velocities of the bubbles rising in water and Xanthan solution found in this investigation are already included. It illustrates that the results found in water are in the same range as the data for freely rising bubbles in water. The results for the ascent in Xanthan solution overlap with the value range but the lowest value is significantly lower than for the freely rising bubble in water. This can also be found in the dimensionless diagram **Figure 5.1b**. For the ascent data from the confining geometry, it is not possible to include the data in the diagram and keep all three dimensionless numbers ( $Re_B$ ,  $Eo$ ,  $Mo$ ) at the values found in this work. E.g., if the respective  $Re_B$  and  $Eo$  value for one parameter combination were plotted in the diagram, this point would be on a wrong  $Mo$  number isoline.

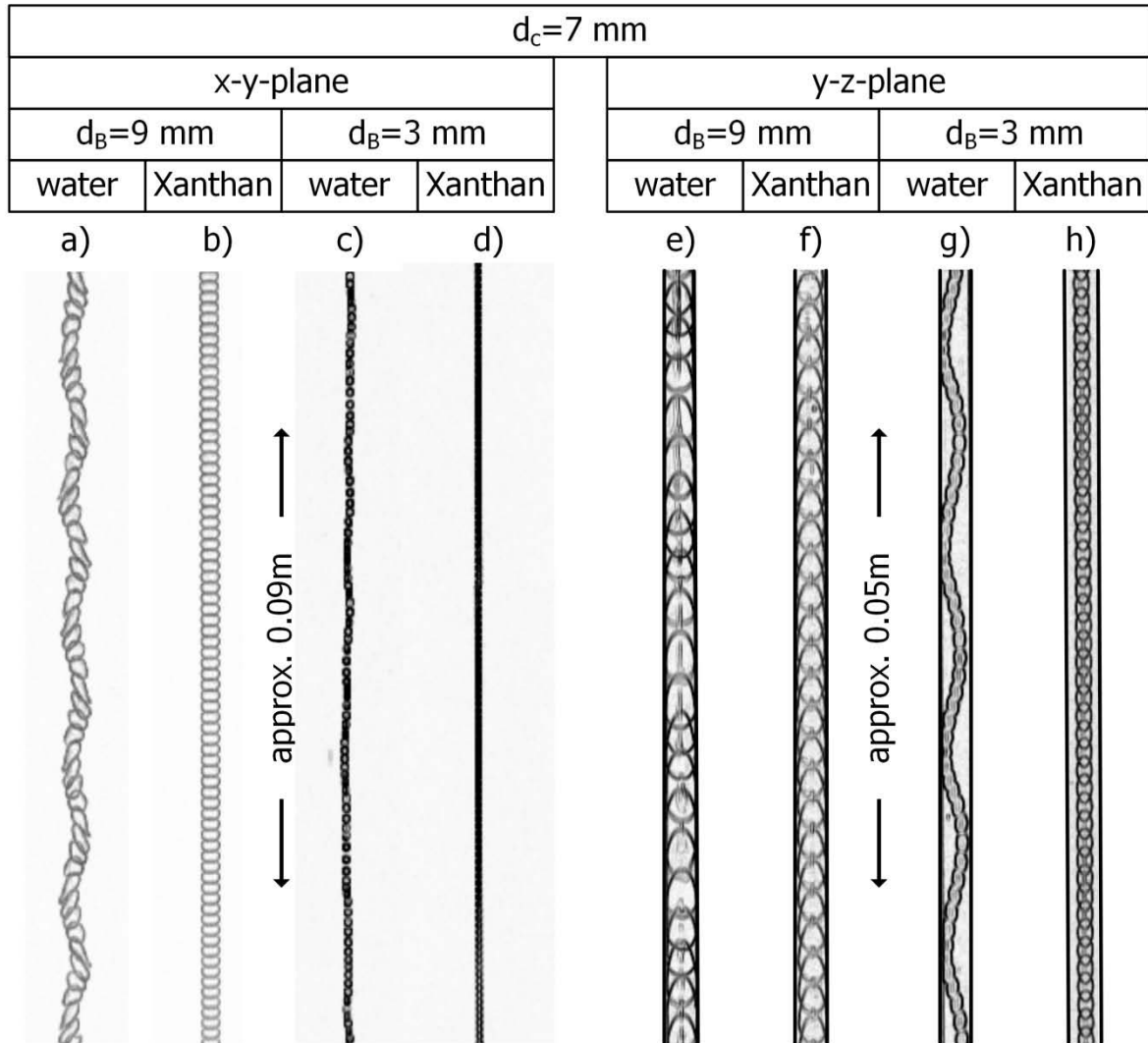
In water, a bubble shape between spherical and wobbling and in the Xanthan solution a bubble shape between spherical and ellipsoidal can be expected (this shape regime map in **Figure 5.1b** was developed for bubbles rising in Newtonian liquids). The deformation is accompanied by a change of the rising behavior in terms of a change in the rising paths [10] with

Table 5.1: Overview of dimensionless numbers determined in this work (based on [6])

continuous phase	$Mo$	$Eo$	$Re_B$	$We$	$Sr$
water	$2.6 \cdot 10^{-11}$	1.2 - 13	536 - 2175	1.3 - 7.2	0.095 - 0.25
Xanthan solution	$6.3 \cdot 10^{-6}$ (only for BS: with ions $2.65 \cdot 10^{-7}$ )		8.6 - 65		0.12 - 0.6

- a helical path (in water:  $1.3 \text{ mm} < d_B < 2.0 \text{ mm}$ ),
- a plane zig-zag turning into a helical path ( $2.0 \text{ mm} < d_B < 3.6 \text{ mm}$ ),
- a plane zig-zag path ( $3.6 \text{ mm} < d_B < 4.2 \text{ mm}$ ) and
- a straight path with rocking ( $4.2 \text{ mm} < d_B < 17.0 \text{ mm}$ ).

Therefore, in this investigation, at least in water, a transient motion of the bubble was expected [10]. **Figure 5.2** shows rising paths of bubbles in the x-y- (**Figure 5.2a to d**) and y-z-plane (**Figure 5.2e to h**) in water and Xanthan solution. **Figure 5.2a** and **e** show rising paths in water of a bubble with an equivalent bubble size larger than the channel depth. As described above, for this bubble size ( $d_B = 9 \text{ mm}$ ) a straight path with a rocking motion would be expected for the free bubble ascent. In contrast to this three-dimensional irregular motion, here the bubble is restricted to a two-dimensional movement due to the confining walls. Still, in the x-y-plane, a regular zig-zag-motion accompanied by a regular bubble deformation (which still might be called wobbling) was found. **Figure 5.2c** and **g** show rising paths in water of a bubble smaller than the channel depth. For this bubble size ( $d_B = 3 \text{ mm}$ ), the freely rising bubble moves in a plane zig-zag and then helical way. In the confining system, mostly the helical but also a two-dimensional zig-zag-movement (either in the x-y- or the y-z-plane) was



**Figure 5.2:** Rising paths in the front view of the channel (x-y-plane, a-d) and in the side view normal to the (y-z-plane, e-h) (based in parts on [6])



**Table 5.2: Investigated parameter combinations and respective symbols (S: CFD simulation in water, W: water, X: Xanthan solution, -: not tested) (based on [6])**

channel depth $d_c$ [mm]	5					7					
$v_L$ [m/s]	0	0.1	0.125	0.2	0.235	0	0.1	0.125	0.2	0.235	
continuous phase / simulation	W X S	W X	W X	W X S	W X	W X S	W X	W X	W X S	W X	
bubble size $d_B$ [mm]	3	○ ◇ ×	○ ◇	- ◇	● ◆ ×	- ◆	□ △ ×	□ △	- ▲	■ ▲ ×	- ▲
	5	○ ◇ ×	○ ◇	- ◇	● ◆ ×	- ◆	□ △ ×	□ △	- ▲	■ ▲ ×	- ▲
	7	○ ◇ ×	○ ◇	- ◇	● ◆ ×	- ◆	□ △ ×	□ △	- ▲	■ ▲ ×	- ▲
	9	○ ◇ -	- ◇	- ◇	- ◆ -	- ◆	□ △ -	□ △	- ▲	■ ▲ -	- ▲
	10	- - -	- -	- -	- - -	- -	- - ×	- -	- -	- - ×	- -

found. The bubble shape is between spherical and ellipsoidal. **Figure 5.2b** and **d**, and **f** and **h**, show rising paths under the same conditions as for water but in Xanthan solution. Basically, the bubble shape is mostly ellipsoidal and no oscillation can be seen in both cases. A steady, rectilinear motion is apparent in most cases. So from a qualitative point of view, as expected, a significant influence of the continuous phase on the bubble ascent is also expected quantitatively.

For the following part that shows all determined quantities, the used symbols are shown in **Table 5.2**. Due to the large amount of varied parameters, a straight-forward way of choosing the symbols in a way to understand the diagrams in detail without looking at the legend was not possible. It can generally be kept in mind that the darker the symbol is filled, the higher the superimposed liquid velocity was. Other than that, it was tried directly in the diagrams to distinguish between the water and Xanthan solution data by either showing separate diagrams for each liquid phase or by marking each related data specifically, where possible. Whenever trends are discussed in the text that are not directly observable in the respective diagram, this is specifically labeled in the appropriate place. Additionally, it can generally be stated that the literature correlations shown in the diagrams for comparison were determined for freely rising bubbles without superimposed liquid velocity.

**Figure 5.3** shows the relative terminal rise velocity of a bubble  $w_{B,rel}$  (in y-direction) calculated as

$$w_{B,rel} = w_{B,abs} - v_L \quad (5.5)$$

in comparison to the results for freely rising bubbles (for all cases, error bars are not included in the plots as the standard deviation was only marginal). In case of water as the continuous phase (**Figure 5.3a**), the results are compared to the data concluded by Clift et al. [10] as already shown in **Figure 5.1a**. The results lie between the data presented by Clift et al. for pure and contaminated water. Especially the results without superimposed liquid velocity are rather in the range of the results of freely rising bubbles in contaminated water. The contamination (e.g., with surfactants) mentioned by Clift et al. rigidifies the bubble surface by an adsorption of surfactant molecules on the bubble surface. Due to this, it behaves like a rigid particle without internal circulations in the fluid particle. Although no ultrapure water was used as continuous phase, the deionized water quality was high enough to ensure that such a state of contamination is not apparent in the system. Therefore, the reduced rising velocity in comparison to the freely rising bubble can be attributed to the wall effects in the confining system.

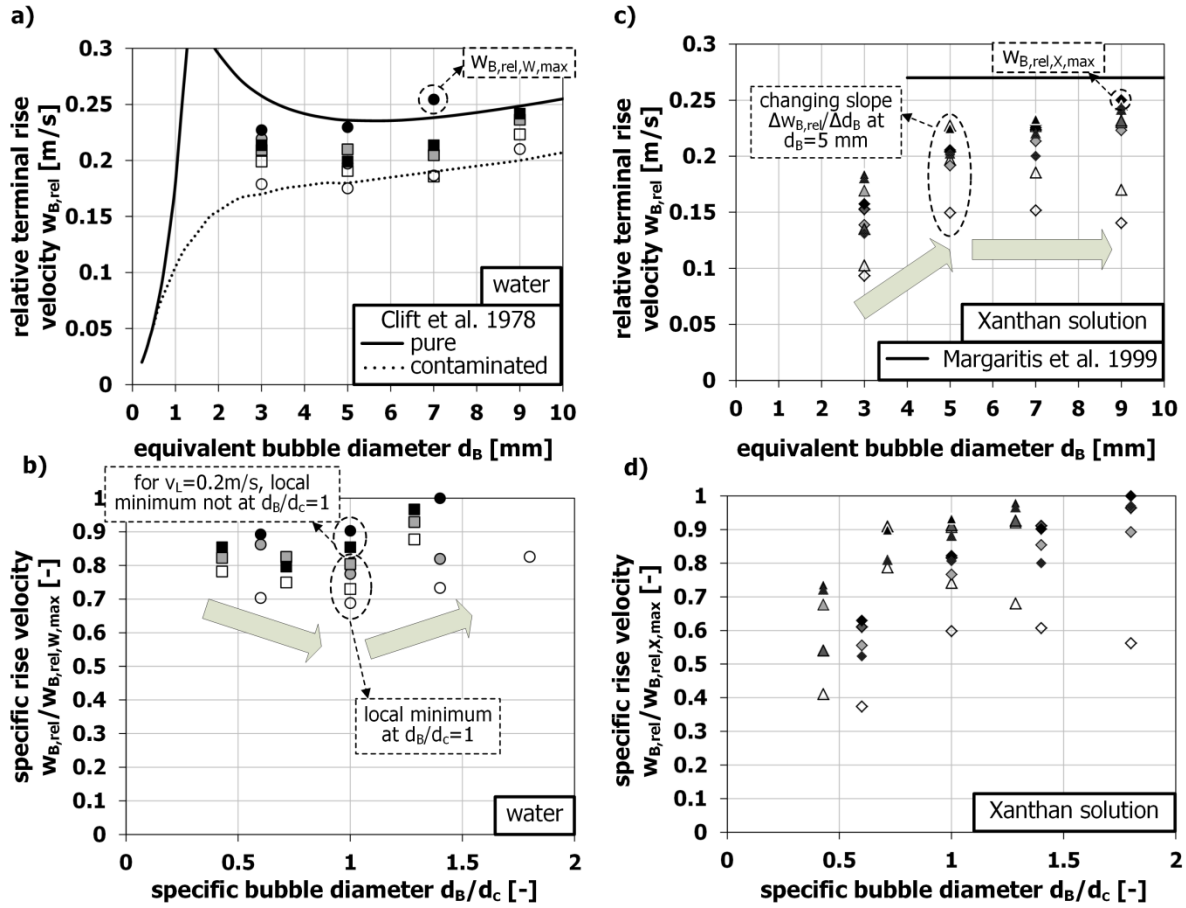


Figure 5.3: Relative terminal rise velocities of the single bubbles (a) in water and (c) in Xanthan solution (in comparison to Margaritis et al. [146]) and the specific rise velocities related to the respective maximum relative terminal rise velocity (b) in water and (d) Xanthan solution (symbols explained in Table 5.2; based on [6])

For parameter combinations with co-current liquid flow, especially in the case with confining walls, the subtraction of the superimposed liquid velocity might not really give comparable results for the relative rise velocity to the cases without co-current liquid velocity. The superimposed liquid velocity is the average velocity in the channel. As the bubble rises actually in a velocity profile with a zero velocity at the wall and a maximum velocity of approximately 1.5 times the average velocity in the center between the walls (see Figure 4.10b), the definition of the relative terminal rise velocity (eq.(5.5)) might actually not be applicable here.

The same data is shown as relative values  $w_{B,rel}/w_{B,rel,W,max}$  in Figure 5.3b, i.e., divided by the maximum value found in water in this investigation ( $d_c = 5$  mm,  $d_B = 7$  mm,  $v_L = 0.2$  m/s  $\Rightarrow w_{B,rel,W,max} = 0.25$  m/s). For all cases - except for the parameter combinations with a superimposed liquid velocity of 0.2 m/s - a (local) minimum was found for a relative bubble size  $d_B/d_c$  of 1. For freely rising bubbles in pure water, a local minimum also occurs around bubbles of 5 to 7 mm size which are the  $d_B/d_c$  values around 1. As this local minimum does not occur at  $d_B/d_c = 1$  for the cases with  $v_L = 0.2$  m/s, it can be concluded that the superimposed liquid velocity changes the rise behavior.

In case of Xanthan solution as the continuous phase (Figure 5.3c), the literature is not as clear on the bubble rise velocity. Chhabra [11] summarized several results of freely rising bubbles in non-Newtonian liquids but still no definite description and respective explanation was given. Basically two types of behaviors were found:

1. With increasing bubble size, an increase of the bubble rise velocity was found up to a certain bubble size where a jump of the rise velocity to a higher level is apparent. From there on, an increasing bubble size either leads to
  - a. a further increasing rise velocity or
  - b. it does not affect the rise velocity anymore.
2. In the other cases, the rise velocity increases with the bubble size and becomes constant once a certain bubble size is exceeded.

Margaritis et al. [146] discussed data for freely rising bubbles in Xanthan solutions and found a constant rising velocity of approximately 0.27 m/s for a bubble diameter larger than 4 mm, independent of the actual Xanthan concentration and, therefore, independent of the rheological properties of the continuous phase. In **Figure 5.3c**, all determined rise velocities are lower than the value found by Margaritis et al. [146]. Even without a superimposed liquid velocity, a significant increase (of 50 % for  $d_c = 5$  mm and 100 % for  $d_c = 7$  mm) of the rise velocity was found between the bubble sizes  $d_B = 3$  mm and  $d_B = 5$  mm, which is roughly in accordance with Margaritis et al. [146]. Exceeding bubble sizes of 5 mm, the rise velocity is approximately constant ( $d_c = 5$  mm) or even decreases ( $d_c = 7$  mm). In cases with superimposed liquid velocity, below a bubble size of 5 mm, the behavior is similar but for the larger bubbles still an increase of the rise velocity was found. As described for water, the bubbles rise here in a velocity profile as well (indicated in **Figure 4.10b**) which does not only lead to different velocities occurring on the bubble surface but also to a range of viscosities depending on the local velocity gradient (= shear rate) surrounding the bubble. **Figure 5.3d** shows the relative rise velocity  $w_{B,rel}/w_{B,rel,X,max}$  (related to the maximum value found in Xanthan solution in this investigation,  $d_c = 5$  mm,  $d_B = 9$  mm,  $v_L = 0.2$  m/s  $\Rightarrow w_{B,rel,X,max} = 0.25$  m/s). It illustrates that this complex combination of influencing parameters leads to a change of the rising behavior in comparison to water. In case of the non-Newtonian continuous phase, the viscosity reduces with increasing shear rate. It is a reasonable assumption that in the given confining geometry, in cases with superimposed liquid velocity, higher shear rates and therefore lower viscosities occur in the vicinity of the bubble (this will also be discussed in **Section 5.1.2**). This lowered viscosity is a potential explanation for the rise velocity increase. The specific bubble diameter does not seem to have a significant influence as the change of the velocity slope  $\Delta w_{B,rel}/\Delta d_B$  is generally lower for bubble diameters larger than 5 mm (see **Figure 5.3c**, based on the parameter combinations tested in this work).

As discussed, for the relative rise velocity mostly data for a Newtonian continuous phase can be found in the literature. The dimensionless friction factor  $C_D$  is a quantity for which Margartis et al. [146] found a correlation based on a broad range of bubble ascents in Newtonian liquid and different types of non-Newtonian polysaccharide solutions. In case of a Newtonian continuous phase, the friction factor is defined by

$$C_D = \frac{4}{3} \frac{|\rho_B - \rho_f|}{\rho_f} \frac{g d_B}{w_{B,rel}^2} \quad (5.6)$$

with correlations based on the Reynolds number  $Re_B$  [147, 148]. Very common is, e.g., the Hadamard-Rybszynski-equation for fluid particles in Newtonian liquids

$$C_{D,N} = \frac{24}{Re_B} Y \quad \text{with} \quad Y = \frac{\frac{2}{3} + \mu_B/\mu_L}{1 + \mu_B/\mu_L} = \frac{2}{3} \quad \text{for bubbles in Newtonian liquids} \quad (5.7)$$

A variation thereof is

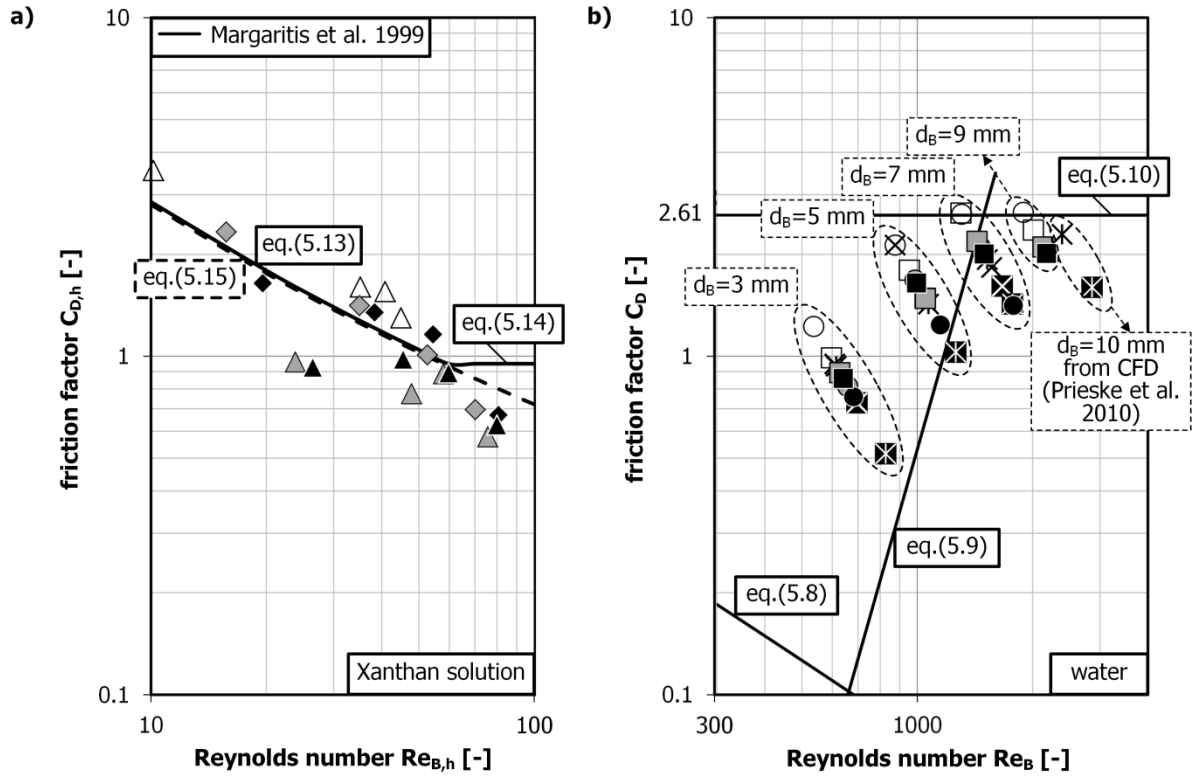


**Figure 5.4:** Friction factor against Reynolds number (a) calculated with the horizontal dimension of the bubble for Xanthan solution (in comparison to [146]) and (b) calculated with the equivalent bubble diameter for water (in parts retrieved from [6] with  $K = 0.238 \text{ Pas}^n$ ,  $n = 0.42$  for the Xanthan solution)

$$C_{D,N} = \frac{16}{Re_B} + \frac{14}{Re_B^{0.78}} \left( \frac{1}{1 + 10Re_B^{-0.6}} \right) \text{ for } Re_B < \left( \frac{768}{Mo} \right)^{\frac{1}{5}} \text{ (spherical bubbles)} \quad (5.8)$$

$$C_{D,N} = \frac{MoRe_B^4}{48} \text{ for } \left( \frac{768}{Mo} \right)^{\frac{1}{5}} < Re_B < \left( \frac{125.28}{Mo} \right)^{\frac{1}{4}} \quad (5.9)$$

$$C_{D,N} = 2.61 \text{ for } Re_B > \left( \frac{125.28}{Mo} \right)^{\frac{1}{4}}. \quad (5.10)$$

Margaritis et al. [146] calculated the friction factor  $C_{D,h}$  with the horizontal dimension of the bubble  $d_{B,h}$

$$C_{D,h} = \frac{4}{3} \frac{|\rho_B - \rho_f|}{\rho_f} \frac{gd_B^3}{w_{B,rel}^2 d_{B,h}^2} \quad (5.11)$$

taking the non-spherical shape of the bubble directly into account (but assuming a circular projection area of the bubble in the horizontal plane used in the calculation of the resistance force). The correlations they found are based on the Reynolds number  $Re_{B,h}$  (also applicable for non-Newtonian liquid phases)

$$Re_{B,h} = \frac{w_{B,rel}^{2-n} d_{B,h}^n \rho_f}{K} \quad (5.12)$$

calculated with the horizontal dimension. The correlations are

$$C_{D,nN} = \frac{16}{Re_{B,h}} (1 + 0.173Re_{B,h}^{0.657}) + \frac{0.413}{1 + 16300Re_{B,h}^{-1.09}} \text{ for } Re_{B,h} < 60 \quad (5.13)$$

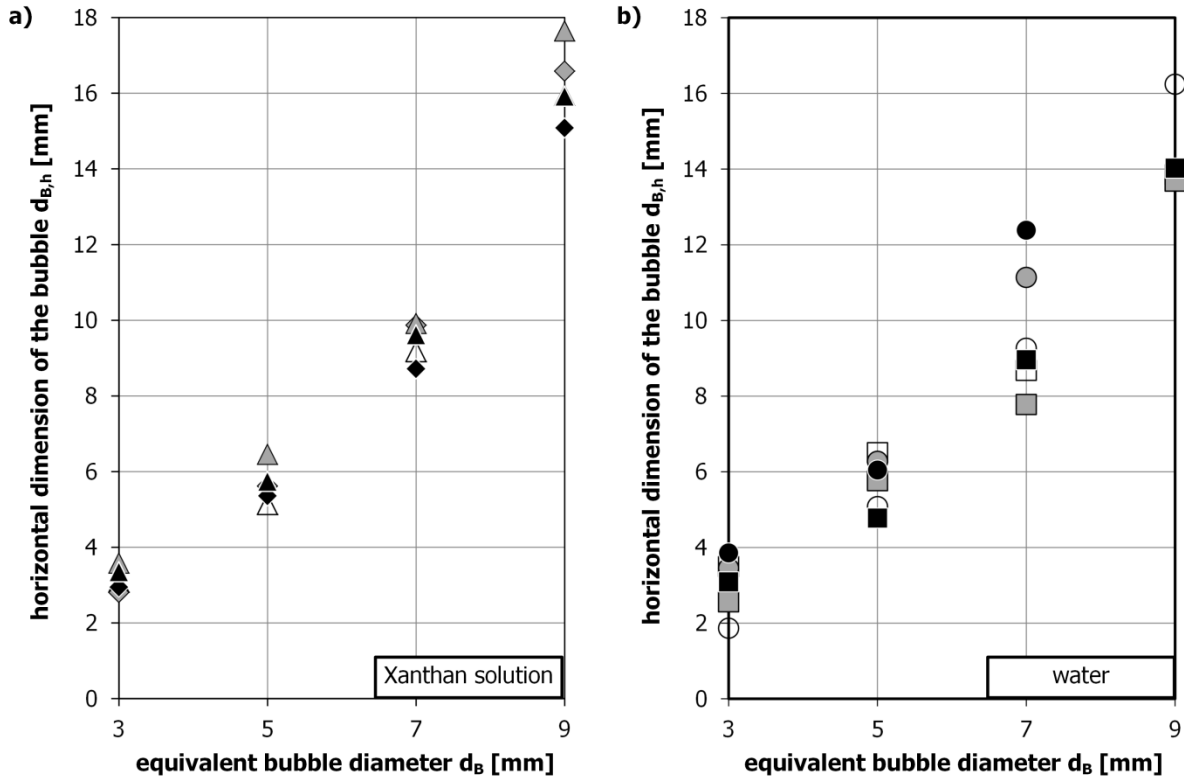


Figure 5.5: Horizontal dimension  $d_{B,h}$  of the bubble (a) in Xanthan solution and (b) in water (based on [6])

$$C_{D,nN} = 0.95 \text{ for } Re_{B,h} > 60 \quad (5.14)$$

but their experimental results scatter significantly around the correlations above  $Re_{B,h} > 20$ . These correlations and the experimental values found for the bubble ascent in Xanthan solutions are plotted in **Figure 5.4a**. See **Figure 5.5a**, for the horizontal dimension used in the calculation of the friction factor of the bubble rising in Xanthan solution. For completeness, **Figure 5.5b** shows the deformation results in water. The deformation results of both continuous phases are affected by the channel depth in comparison to freely rising bubbles (further discussed in [6]).

Although scattering around the friction factor correlations ( $R^2 = 0.81$ ), the experimental data still follows the same trend and an adjustment of Margaritis et.al.'s correlation with a prefactor

$$C_{D,nN,adj} = 0.98 \left( \frac{16}{Re_{B,h}} (1 + 0.173 Re_{B,h}^{0.657}) + \frac{0.413}{1 + 16300 Re_{B,h}^{-1.09}} \right) \text{ for } Re_{B,h} < 80 \quad (5.15)$$

reveals only a minor difference. Here and in the following, the coefficient of determination was calculated by comparing the measured value and the respective correlation value (according to a parity plot). This has to be mentioned here, as strictly speaking  $R^2$  can only be calculated for linear functions. The value of  $R^2$  found for eq.(5.15) is noteworthy as obviously the deformation and respective rise velocity behavior of the bubble in the confining geometry is comparable to that of freely rising bubbles.

The correlations eq.(5.8) to (5.10) and the bubble ascent data in water from this study can be found in **Figure 5.4b**. Here, first of all it is evident that the experimental data is in the same range as the data found for freely rising bubbles with increasing friction factors due to deformation. Furthermore, individual slopes are apparent for the values obtained for different bubble sizes. With increasing superimposed liquid velocity and increasing

channel depth, higher Reynolds numbers and respectively lower friction factors were found but the described effect of the channel depth decreases or is even reversed for increasing liquid velocities (due to the sheer amount of data points hardly visible in the plot).

Bringing the rise velocity and deformation parameters together in a dimensionless approach, Legendre et al. [149] derived a correlation for the Reynolds number as a function of the Weber number

$$We = \frac{\rho_f w_{B,rel}^2 d_B}{\sigma} \quad (5.16)$$

and the Morton number resulting in

$$Re_B = 2.05 We^{2/3} Mo^{-1/5} \quad (5.17)$$

for Newtonian liquids in a  $We^{2/3} Mo^{-1/5}$ -value range of  $5 \cdot 10^{-3}$  to  $4 \cdot 10^2$  (with the respective Reynolds number range  $10.2 \cdot 10^{-3}$  up to  $8.2 \cdot 10^3$ ). **Figure 5.6** shows the results of this investigation and, furthermore, the correlation by Legendre et al. From a qualitative point of view, the data follows the trend described by the **eq.(5.17)** although the validity for non-Newtonian liquids was not mentioned before. Additionally, approximately half of the values found in this investigation were above the validity limit of the correlation. From a quantitative point of view, the results found for the Xanthan solution are approx. 50 % below and the results in water approximately 50 % above the correlated values. With an adjustment of the prefactor and the exponent of the Weber number (the latter one only in case of results in water), the following correlations were found by regression for the bubble rising in water ( $R^2 = 0.97$ )

$$Re_{B,N,adj} = 3.29 We^{4/5} Mo^{-1/5} \quad (5.18)$$

and in Xanthan solution ( $R^2 = 0.98$ )

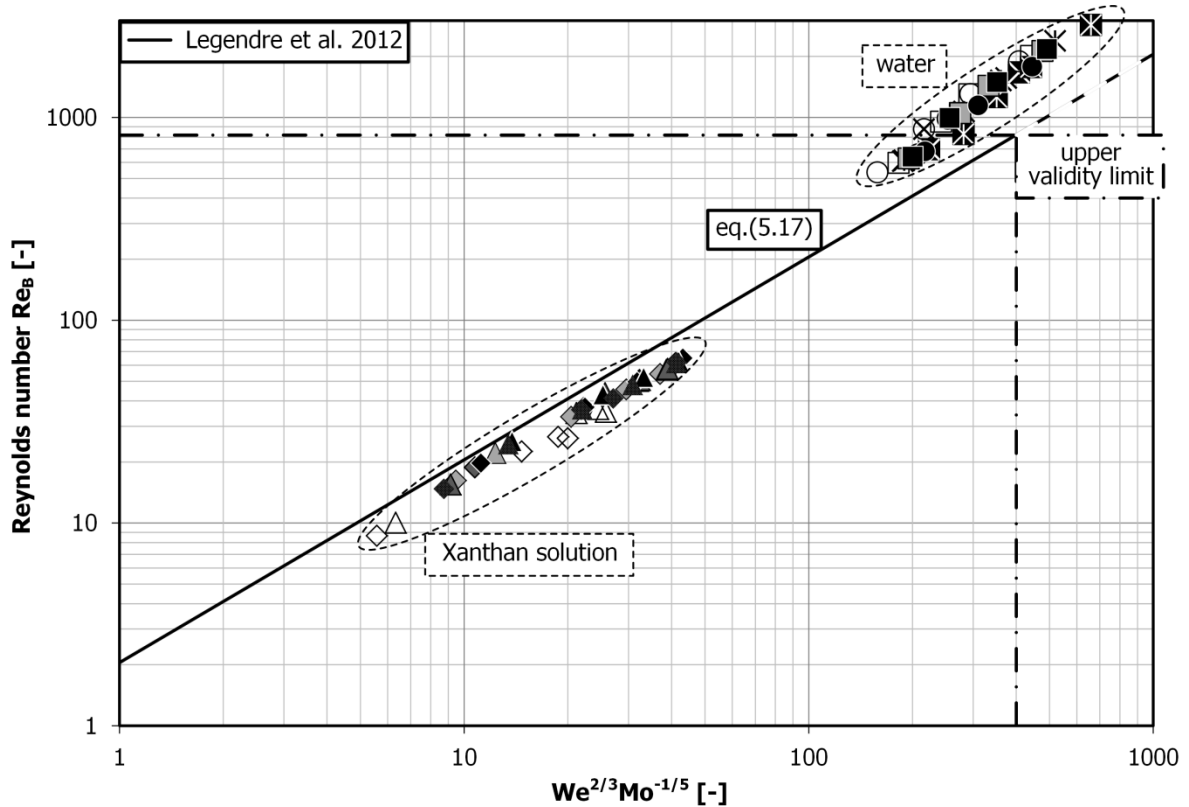


**Figure 5.6:** Relationship between the bubble Reynolds number and the Weber and Morton number (in parts retrieved from [6] with  $K = 0.238 \text{ Pas}^n$ ,  $n = 0.42$  for the Xanthan solution, in comparison to [149])

$$Re_{B,n,adj} = 1.54We^{2/3}Mo^{-1/5} \quad (5.19)$$

The similar behavior in case of Xanthan solution and corresponding differing behavior in water (regarding the exponents of  $We$  and  $Mo$ ) can be attributed to the fact that Legendre et al. investigated mainly systems without oscillations in the rising paths.

The oscillation of the bubble in water was already shown quantitatively in **Figure 4.6b** and qualitatively in **Figure 5.2**. The quantification of the frequency  $f_B$  (in Hz) and amplitude  $\hat{x}$  (displacement of the centroid in the x-direction in mm, **Figure 5.7a**) shows that besides the already mentioned deformation, a significant oscillation occurs as well. In water, for most parameter combinations, the frequency is in the range of 5 Hz (which is in accordance with literature, see, e.g., [93]) and the amplitude increases with the bubble diameter. An increase of the liquid velocity (or channel depth) leads to a lowered amplitude but it does not significantly affect the frequency. In Xanthan solution, only very low amplitudes often with very high frequencies were found (in **Figure 5.7a** only frequencies up to roughly 13 Hz are shown). The combination of low amplitudes with high frequencies makes the oscillation negligible in many cases in Xanthan solution. For these very low amplitudes, the high frequencies (above roughly 10 to 15 Hz) can also be data fragments of the automated data analysis. Therefore, this data is not shown here. Still, a close-up from the PIV measurements in **Figure 5.8**, further described in **Section 5.1.2**, actually visualizes these minor oscillations (as  $\Delta x_1 \neq \Delta x_2$ ). This figure shows a strongly deformed bubble. To emphasize the difference to a bubble rising in a Newtonian continuous phase again, **Figure 5.1a** and **b** can be used to find the approximate size of a bubble rising in water with the same Reynolds number (around  $Re_B = 50$ ). This bubble would be approx. 1 mm in size, spherical in shape and following a straight path during its ascent.

The general behavior, of an amplitude decrease with a frequency increase is illustrated in **Figure 5.7b** which

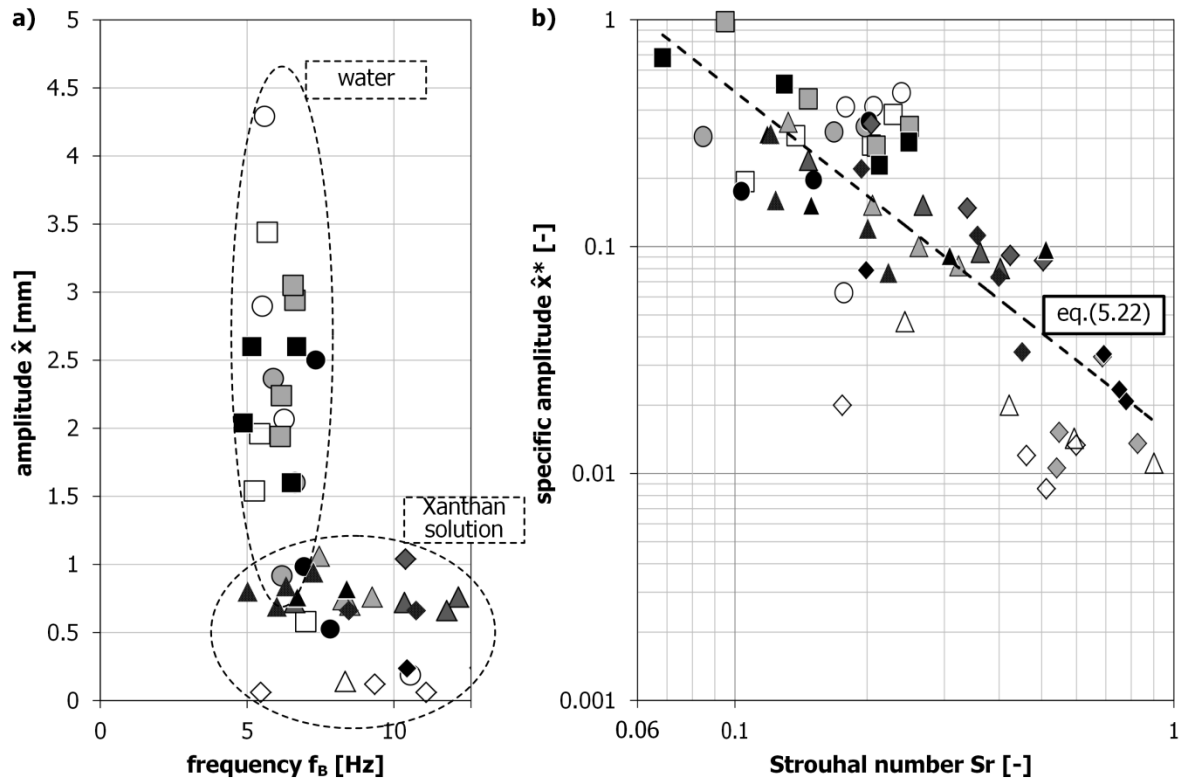


**Figure 5.7:** (a) Relationship between the amplitude and the frequency and (b) the specific amplitude and the Strouhal number (with  $K = 0.238 \text{ Pas}^n$ ,  $n = 0.42$  for the Xanthan solution; based on [6])

shows the specific amplitude

$$\hat{x}^* = \frac{\hat{x}}{d_B} \quad (5.20)$$

against the Strouhal number

$$Sr = \frac{f_B d_B}{w_{B,rel}} \quad (5.21)$$

Both are correlated by:

$$\hat{x}^* = 0.0145 Sr^{-1.52} \quad (5.22)$$

The low coefficient of determination ( $R^2 = 0.55$ ) indicates that more experiments should be done to prove the validity of the correlation but, generally, the correlation reflects the expected behavior of a lowered amplitude at higher frequencies.

In comparison to the behavior of freely rising bubbles often discussed in literature, the behavior here can still be calculated by similar correlations in spite of the 1. confining geometry, 2. a superimposed liquid velocity and 3. a non-Newtonian liquid phase. Especially in case of the dimensionless correlations, the complex interactions of the bubble deformation, the bubble oscillation and the respective rise velocity leads to comparable trends. The channel depth and superimposed liquid velocity show a complex interaction (e.g., in water at  $v_L = 0$  m/s:  $d_c \uparrow \Rightarrow w_{B,rel} \uparrow$ , at  $v_L = 0.2$  m/s:  $d_c \uparrow \Rightarrow w_{B,rel} \downarrow$ ). This cannot be explained yet to the full extent but the change of the oscillation parameters frequency and amplitude indicates a changed rising behavior (with  $v_L \uparrow$ ).

### 5.1.2 Flow field in the liquid surrounding single bubble

After the description of the bubble behavior itself, the liquid surrounding the single bubble is discussed in this section (determined with PIV, based on [2, 7]). Different oscillating behaviors during the rise were found for bubbles rising in water and Xanthan solution in the previous section. These different rising behaviors which are accompanied by different surrounding liquid behaviors are reflected in the respective Reynolds numbers as well. For bubbles in the size range investigated in this thesis, the free ascent in water was described by several authors. Of these, Brücker [93] gave one of the most comprehensive explanations of the oscillatory movement. The oscillatory movement is accompanied by a periodical vortex shedding, creating a Kármán vortex street in the wake of the bubble with counter-rotating vortices, both in the x-y- and x-z-plane (creating complex three-dimensional flow structures, **Figure 5.9**). Especially the vortices in the x-z-plane (horizontal plane ‘cutting’ through the wake of the bubble) can be used to explain the oscillatory movement. At the point where the movement in positive x-direction changes to a movement in negative x-direction or vice versa, the reversal point of the rising period (see, e.g., **Figure 4.6b**), two counter rotating vortices develop in the wake of the bubble in the x-z-plane in x-direction on the side indicated with ‘1’ in **Figure 5.9a**. The two counter rotating vortices in the x-z-plane are illustrated in the A-A-cut. This leads to a deflection of the main flow (which is in the y-direction) on this side of the bubble (side ‘1’), resulting in a slower flow in the y-direction. Therefore, due to the resulting lower pressure on the opposite side of the bubble (side ‘2’), this leads to a movement in that direction. This repeats periodically in a vice-versa way at both reversal points and, therefore, leads to the oscillatory movement. In **Figure 4.9a** and **Figure 5.9b** flow fields are shown for the oscillatory movement of different bubbles rising in water. This movement was also found in the simulations carried out by Prieske et al. [17] who did CFD simulations for similar parameter combinations (**Figure 5.9a**).



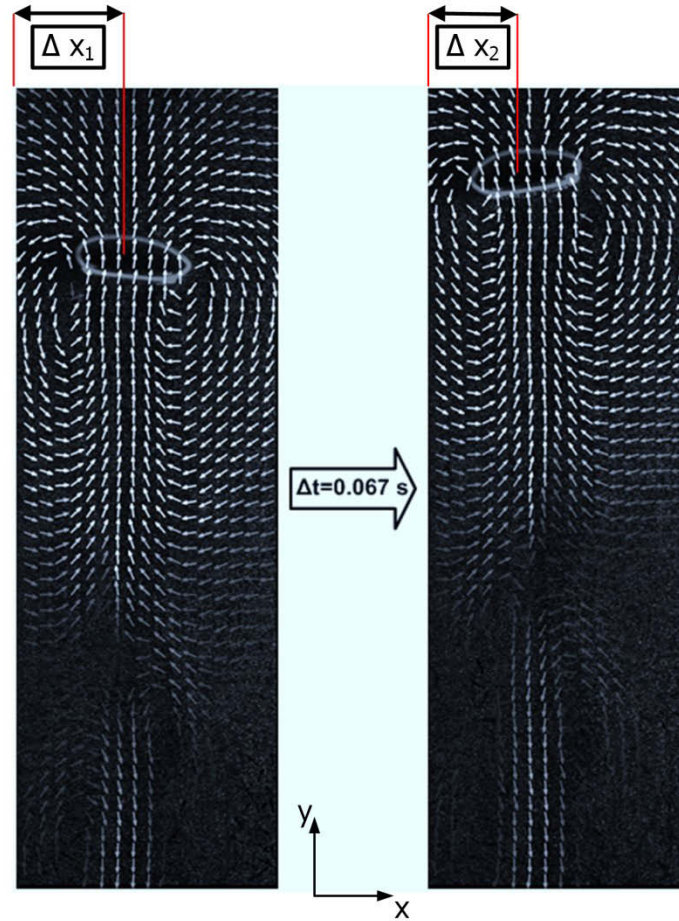


**Figure 5.8:** Two consecutively recorded flow fields determined with PIV for a large bubble ( $d_c = 7$  mm,  $d_B = 9$  mm,  $v_L = 0$  m/s) with a minor rising path oscillation (based on [7])

To be in the Reynolds number range as found with Xanthan solution as the continuous phase, a single bubble in water would be around 1 mm in size (based on **Figure 5.1a** and **b**). As discussed before, this bubble would have a spherical shape and would rise in a straight fashion. For such bubbles in Newtonian liquids, the surrounding liquid behavior is usually described by a zone above the bubble where the liquid is pushed upwards and a zone in the wake of the bubble where the liquid is dragged up [94, 101]. **Figure 5.10b** shows the flow field of a bubble rising in Xanthan solution as found in this investigation. As a logical consequence of the lack of oscillation found in **Section 5.1.1**, a symmetrical flow field was found near the bubble. Still, this flow field is different in comparison to the flow field expected in case of a Newtonian continuous phase. Funfschilling and Li [101] described the flow field around freely rising single bubbles in a shear-thinning, non-Newtonian continuous phase. In a system with viscosities approximately one order of magnitude higher in comparison to the Xanthan solution used here, they found a flow field qualitatively shown in **Figure 5.10a**, with three main flow zones. In zone I above the bubble, liquid is pushed upwards as it would be the case of a Newtonian continuous phase as well. The wake of the bubble on the other hand shows a different picture. Here, two zones can be found: in zone II, an upward flow occurs which lies like a conical coat around a central conical downward flow area (sometimes also referred to as ‘negative wake’, zone III). It was speculated that the central downward flow was due to the viscoelastic properties of the used continuous phase which lead to “central corridors of reduced viscosity” [103, 150, 151]. In this investigation with a generally lower viscosity level, negligible viscoelasticity and confining

geometry, a different flow field was found. Zone I, II and III as described above appeared here as well but zone I was a fully circulating flow around the bubble leading to an upward motion directly below the bubble (**Figure 5.10c**). Only at a certain distance from the bubble, in the wake, the flow is reversed (zone IV) and the downward flow develops as it was described above. As indicated already in **Section 5.1.1**, for the larger bubbles even an oscillation tendency was recognizable which established in an asymmetrical flow field. **Figure 5.8** shows two consecutively recorded images of a 9 mm bubble with the respective velocity vector field around it. While for the smaller bubbles a symmetrical flow reversal was found (zone V in **Figure 5.10c**) turning the flow from the central downward flow region (zone III) to the outer upward flow region (zone II), this flow reversal region is asymmetrical in case of the larger bubbles. It can be seen in **Figure 5.8**, that in the first recorded image at the far end of the bubble wake, a vortex on the right side is closer to the bubble than on the left side. In the second image, the wake is still asymmetrical. This oscillation is accompanied by a periodical deformation resulting in ratios of the vertical  $d_{B,v}$  and horizontal dimension  $d_{B,h}$  of the bubble as low as 0.38 (further discussed in [6]). As indicated in **Figure 5.10a**, this is actually also - in parts - in contrast to bubble shapes found by Funfschilling and Li [101] who introduced their qualitative flow field for a bubble with  $d_{B,v}/d_{B,h}$ -values above one. This qualitative discussion corroborates that the investigated non-Newtonian liquid is an intermediate case between the Newtonian liquid with a viscosity of water and the high viscosity level non-Newtonian liquid as investigated by Funfschilling and Li [101].

The newly developed way to analyze this highly transient process (as described in **Section 4.4**) allowed the comparison of quantitative data of all parameter combinations. Such a discussion can rarely be found in the articles dealing with investigations of the single bubble ascent with the help of PIV. Therefore, for the quantities

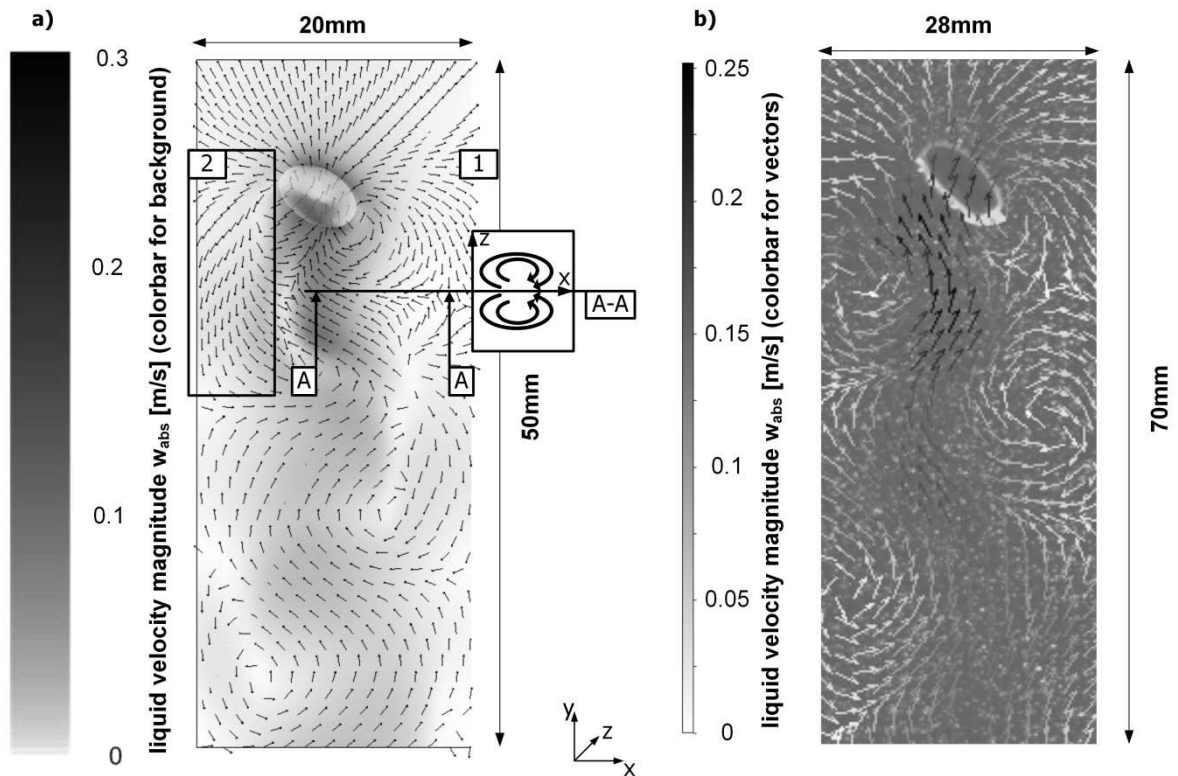


**Figure 5.9:** Flow pattern in the wake of a bubble rising in water (a) from CFD simulations ( $d_c = 5$  mm,  $d_B = 5$  mm, [17]) and (b) from PIV measurements ( $d_c = 5$  mm,  $d_B = 7$  mm) (based on [2])

presented here, no comparison to the literature of other working groups can be given. Where applicable, comparisons to own publications will be made.

**Figure 5.11** shows the velocity magnitude  $w_{abs}$  occurring in the liquid surrounding the bubble (as described in **Section 4.4**: the absolute value of the velocity vector in the x-y-direction  $|\vec{w}_{xy}|$ ) in water and Xanthan solution. The absolute terminal rise velocities of the respective single bubbles (as found in [6]) are incorporated in the plot. At first sight it is noticeable that - if applied - the superimposed liquid velocities dominate the velocity magnitude data as the median values are independent of the bubble size. This means that, if  $v_L > 0$ , the median values  $w_{abs,median}$  with or without additional bubble ascent are equal to the maximum velocity occurring in the velocity profile between the two walls ( $z = d_c/2$ ) as found for a single phase liquid flow (see also **Figure 4.10**). This is the case as the field of view was at the symmetry plane between the walls [7] (= x-y-plane at  $z = d_c/2$ ). Still, as the single liquid phase flow tests showed, the variation of velocities around the median value can be completely attributed to the influence of the bubble (for the single phase flow only the median value is shown as the fluctuation around it was negligible). For a constant bubble size, the liquid velocity magnitude intervals related to the probability ranges (1 to 99 %) are almost constant but shifted to a higher level by the superimposed liquid velocity. This shift is also found in the absolute terminal rise velocities of the single bubbles. Furthermore, it can be stated that the larger the bubble, the larger the liquid velocity interval and the more the interval overlaps with the absolute terminal rise velocity of the bubble. This can be attributed to a larger area in the recorded image that is affected by the bubble (also found by Jankhah and Bérubé [64] for larger bubbles). Therefore, the size of the recorded field of view has an influence on the presented velocity magnitude intervals. Here, in all cases the field of view was equally sized. Analysis tests were performed with adjusted fields of view sized relative to the tested bubble size, with five bubble diameters in width and ten bubble diameters in height

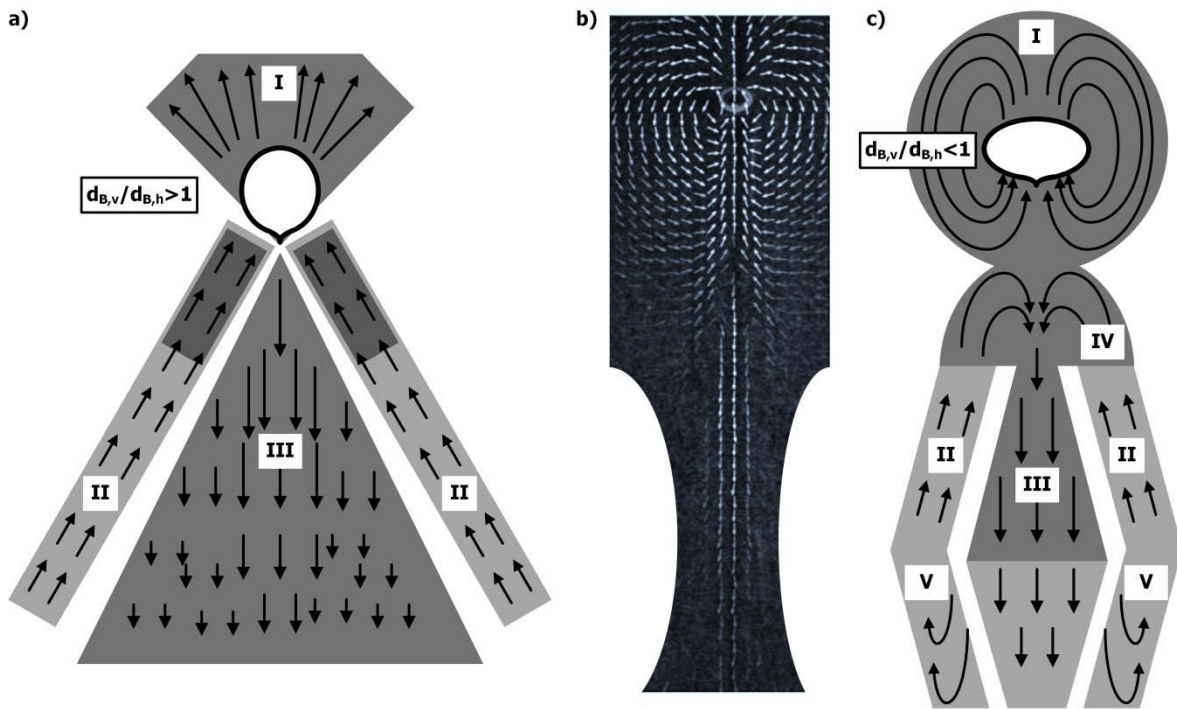


**Figure 5.10:** (a) Flow field around a freely rising bubble in a shear-thinning liquid as found by Funkschilling and Li [101], (b) flow field determined with PIV near a 5 mm bubble in the confining system ( $d_c = 5$  mm) and (c) qualitative flow field around the smaller bubbles as found in this investigation (based on [7])

(analogous to the previous CFD simulations [17]). This did not result in significant changes compared to the data presented here. Smaller relatively sized fields of view might have an effect but this was not further investigated here.

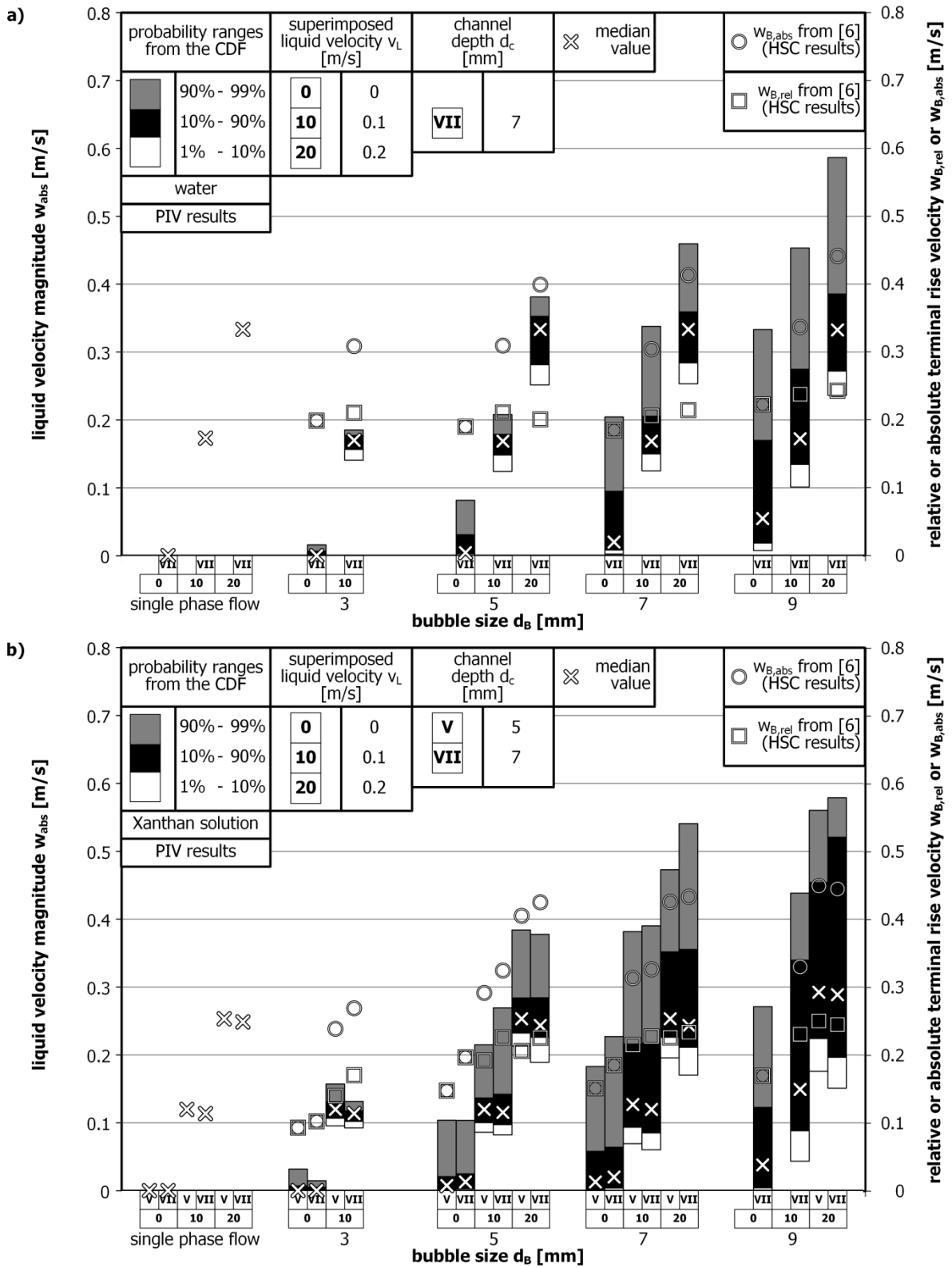


Figure 5.11: Velocity magnitude in the liquid surrounding the bubble (a) in water and (b) Xanthan solution together with the respective absolute and relative terminal rise velocities (based on data from [6, 7])

**Figure 5.12** shows the development of the 1 to 99 %-intervals of the velocity magnitude (related to the smallest 1 to 99 %-interval found for  $d_c = 5$  mm,  $d_B = 3$  mm) against the bubble size (related to smallest tested bubble size  $d_{B,min} = 3$  mm) for  $v_L = 0.1$  m/s. It illustrates that the velocity magnitude interval does not increase proportional to the bubble size but rather to the horizontal dimension of the bubble  $d_{B,h}$  (which is here also related to  $d_{B,min} = 3$  mm).

Only tested for Xanthan solution, the channel depth does not have a clear significant influence on the occurring liquid velocities (**Figure 5.11b**). Usually, the velocity magnitude intervals are larger in the 7 mm channel which can be attributed to the - in most cases - higher rise velocities of the bubble.

In **Section 5.1.1**, the oscillation behavior was discussed with larger amplitudes for larger bubbles (mainly found in water). In the PIV investigations, larger velocity magnitude intervals were found for larger bubbles. These findings combined substantiate that a much larger area is affected by larger bubbles in comparison to the area affected by smaller bubbles. This is not only due to the bubble size itself (covering already a larger area) but also to the rising and deformation behavior. Remembering the purpose of the bubble which is the cleaning of membranes covered with deposition layers, this simply means that larger bubbles have the potential to clean a larger membrane surface area.

With respect to the biological community in membrane bioreactors, the shear rates ( $\dot{\gamma}_{liq}(yx) = \frac{\partial w_y}{\partial x}$ ) as described in **Section 4.4**, for results see **Figure 5.13a**) and shear stresses (**Figure 5.13b**) in the liquid surrounding the bubble were analyzed. Microorganisms can be sensitive to the shear they are exposed to [152] which would be mainly the shear occurring in the bulk. Although they are not directly the shear rates/stresses at the wall and, thereby, responsible for the cleaning of the membranes, these values can still give an idea about the respective wall shear stress behavior. As the shear rates and the respective shear stresses were evenly distributed around a value of zero (as an example shown in **Figure 5.13a** for  $d_B = 3$  mm in water), only the probability ranges of 50 to 90 % and 90 to 99 % are shown in **Figure 5.13**. Therefore, the respective 1 and 10 % values are the values at 99 and 90 % multiplied by (-1). The shear rates which mainly appear in the wake of the bubble are, in case of water,

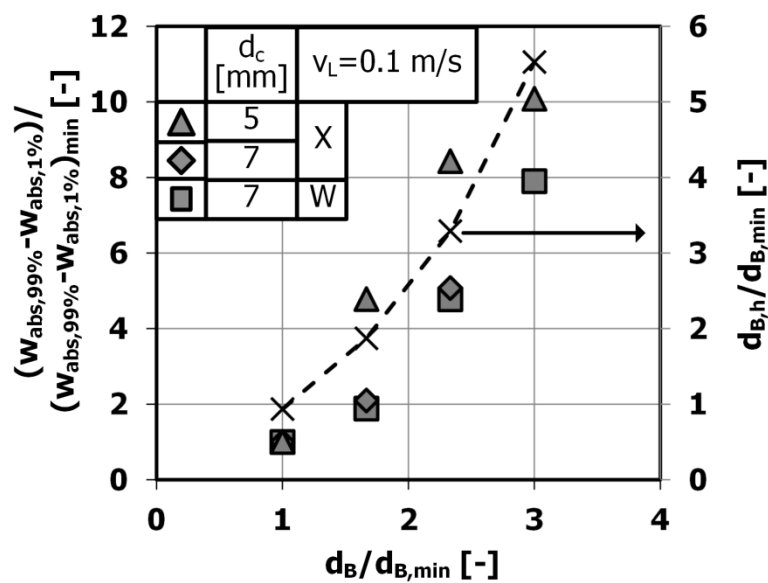
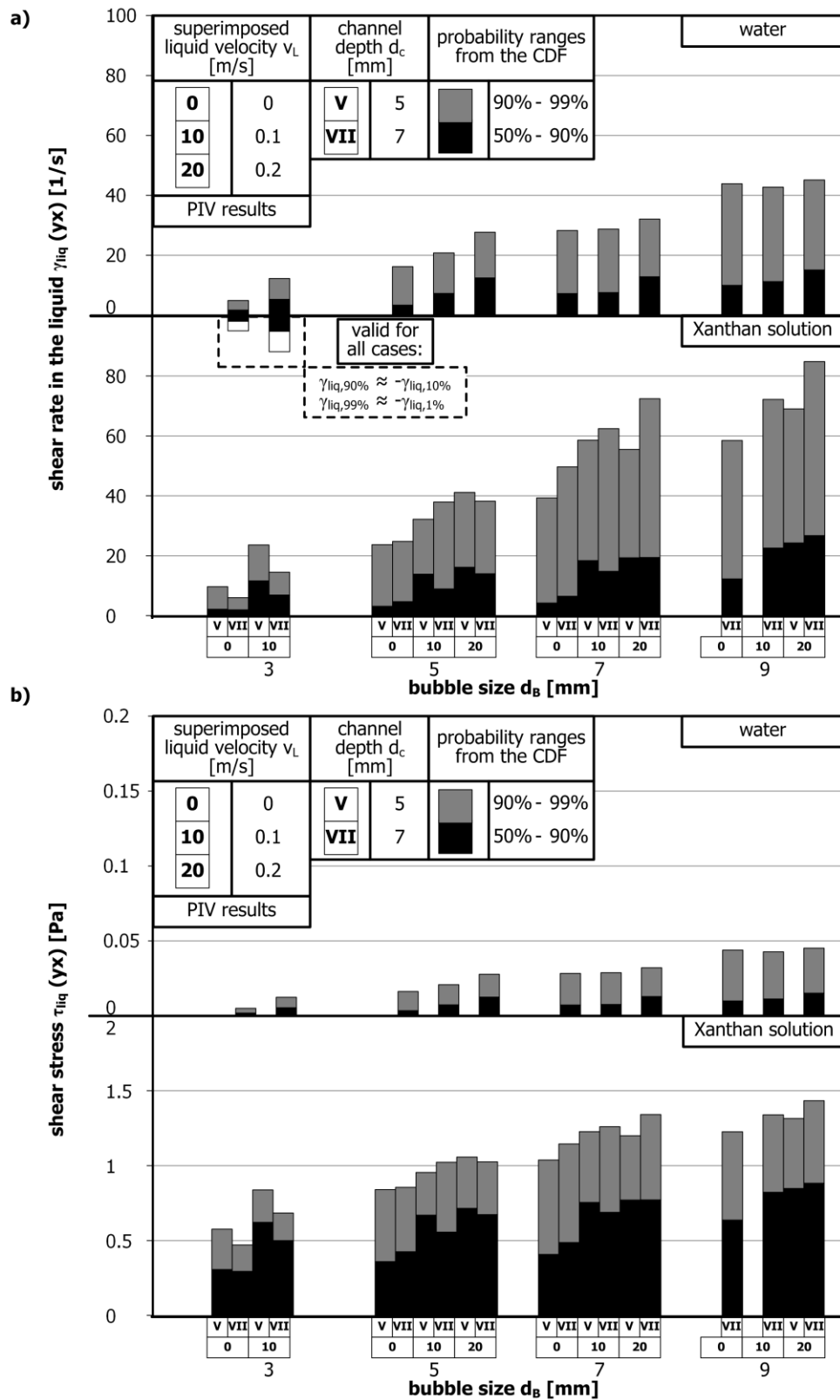


**Figure 5.12:** Relative velocity magnitude interval size in the liquid surrounding the bubble against the relative bubble size along with relative horizontal dimension of the bubble (based on data from [6, 7])

a result of the vortices and, in case of Xanthan solution, a result of the contrariwise flow regions with a sharp transition between each other. In case of water, the even distribution of the shear rate values around zero are a result of the periodic shedding of the counter-rotating vortices. In case of Xanthan solution, the symmetrical flow



field is the reason for the even distribution around zero. As found for the velocity magnitude, here the probability ranges tend to increase with increasing bubble size as well. For water, a change occurs with respect to the behavior with increasing superimposed liquid velocity. For 3 and 5 mm bubbles, the interval increases with superimposed liquid velocity, for 7 and 9 mm bubbles, the intervals are constant. This behavior change does not appear with Xanthan solution as the continuous phase. The respective relative bubble rise velocities are shown in **Figure 5.11**. For larger bubbles, the shear rates in Xanthan solution are much more sensitive to the superimposed liquid velocities than in water. Generally, the shear rate intervals in Xanthan solution are larger in comparison to water (by a factor of approximately 1.5 to 2) which can be attributed to the large areas of high shear rates in the flow reversal zones (zone IV and V and the region between zone II and III in **Figure 5.10c**). While the shear rates in water and Xanthan solution are still in the same order of magnitude, another picture is found for the shear stresses (**Figure 5.13b**). Due to the differing rheological characteristics of the two liquid phases, there is a difference of more than an order of magnitude between the shear stresses occurring in the Newtonian and non-Newtonian continuous phases. **Figure 5.14** illustrates this difference (shown for  $d_c = 7$  mm,  $v_L = 0.1$  m/s) by showing the factor between the 99 %-value of the shear rate and shear stress in Xanthan solution and water. Additionally, in case of Xanthan solution the calculation leads to a larger 50 to 90 % range of the occurring shear stress in the liquid surrounding the bubble in comparison to the shear rate ranges which is equivalent to a broader probability density distribution of the shear stress.

A fairly different liquid flow behavior was found for bubbles rising in water and Xanthan solution. Still, the occurring shear rates in the liquid surrounding the bubble are in the same order of magnitude (being higher for Xanthan solution, differing roughly by a factor of two). Due to the difference in the rheology, the occurring shear stresses, however, are off by an order of magnitude.

With the motivation of this project in mind, the shear stress occurring in the y-z-plane normal to the walls would be of even higher interest. Tests were also performed where the position of the camera and the laser were exchanged so that an image in the y-z-plane was recorded. This field of view would be equivalent to a plane normal to the membrane surfaces. Still, for several reasons these experiments were very challenging which is

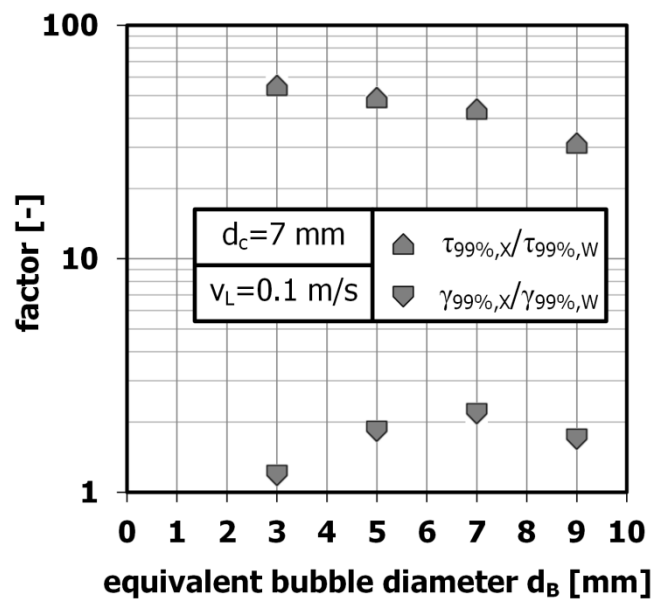


**Figure 5.14:** Factor between the 99 %-value of the shear rate and shear stress in water (W) and Xanthan solution (X) (based on data from [7])

why no statistically analyzed data is shown for this case. There were two main challenges related to this experiment:

- In order to obtain a detailed image, the field of view was much smaller in comparison to the previously described experiments. Roughly, the size was equal to one (= width of the image) by two channel depths (= height of the image) which means that, depending on the bubble size, large areas of the image were covered by the bubble itself (see **Figure 5.15a**). This also means that only in a very small time frame, the bubble is actually inside the field of view. As the camera had a maximum frame rate of 14.2 Hz, even in combination with the triggering used for the experiments described above, only rarely the bubbles were in the field of view or at a comparable position.
- Even if the bubble was at the right position in the image, especially in case of water (and larger bubbles in Xanthan solution) with strongly pronounced oscillations, the bubble was at different positions relative to the fixed laser sheet as indicated in **Figure 5.15b to d**. This means that of the rare recordings where the bubble was actually in the right position in the field of view, even less recordings show images where the laser sheet cuts through the center of the bubble.

Additionally, results of PIV measurements near a wall should generally be assessed very critically as, e.g., the particle concentration is usually not high enough for appropriately conducting the PIV algorithm (see, e.g., [153]). Therefore, only some qualitative results of experiments in water are discussed here. Besides **Figure 5.15a** which shows an almost symmetrical flow field around a 7 mm bubble in a 7 mm channel, **Figure 5.16** shows a compilation of some results which were determined for a 3 mm bubble rising in a 7 mm channel. **Figure 5.16a** shows the rising path of the bubble. Due to the lower frame rate in comparison to the HSC recordings (see, e.g.,

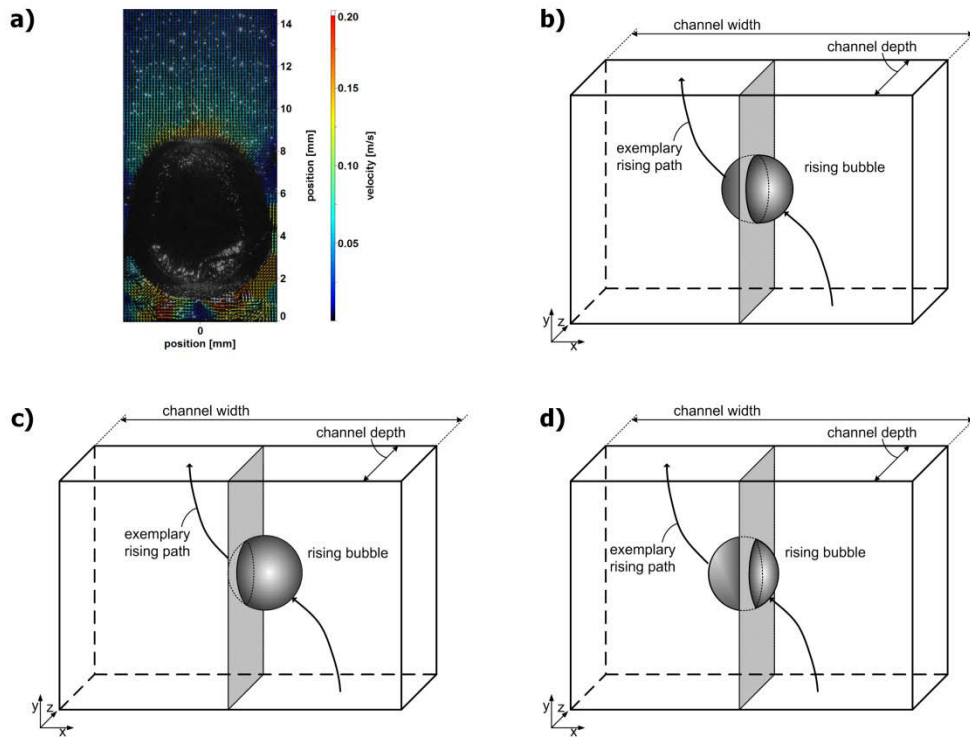


**Figure 5.15: (a) Flow field in the y-z-plane for  $d_c = 7$  mm and  $d_B = 7$  mm, (b) field of view for the test with exchanged camera and laser position to record the area between the walls in the y-z-plane, (c, d) potential out of plane positions of the bubble during the recording (based in parts on [141])**



**Figure 5.2)**, it is less precisely resolved. Besides the lower resolution of the rising path, at the y-positions 30 mm and 165 mm no bubble was found. Obviously, the laser sheet did not cut the bubble. For this case with a bubble oscillation in the y-z-plane, for the instant in time when the bubble was at the y-position 133 mm above the

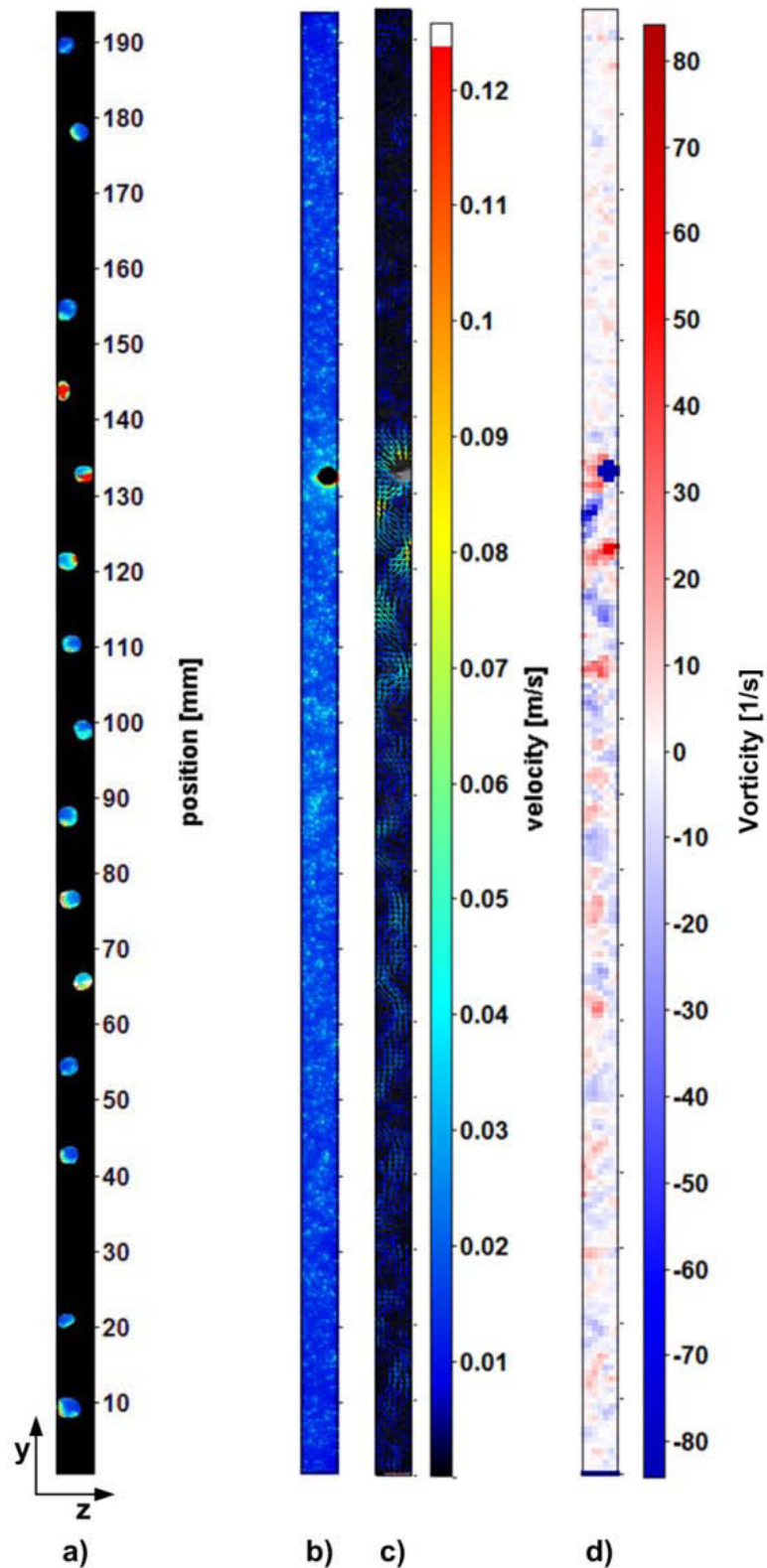


**Figure 5.16:** (a) Snapshots of one bubble oscillating between the walls in the y-z-plane, (b) raw PIV image of the bubble at a height of approx. 133 mm in the field of view, (c) according instantaneous flow field and (d) vorticity distribution for a 3 mm bubble in a 7 mm channel (retrieved from [154], based on [141])

lower end of the image (raw PIV image shown in **Figure 5.16b**), the velocity field was determined (**Figure 5.16c**; a precise resolution of the oscillation was shown in **Figure 5.2g**). Although the possibility to resolve the appearing vortices properly was limited for this image size, the meander like main flow structure is observable in the wake of the bubble and the determined vorticity field (**Figure 5.16d**, red and blue for the opposing algebraic signs of the vorticity) indicates the positions of the counter rotating vortices down to the lower end of the image. It took the bubble roughly 0.75 s from the entry into the field of view up to the shown position. In accordance with **Figure 4.11a**, this corroborates that, especially in case without superimposed liquid velocity, the liquid was affected by the bubble ascent for a certain time. From the author's experience with the PIV measurements where the fluorescent particles could be seen (as safety glasses cut out only the light wave length of the laser light), it could take up to 15 seconds, sometimes even more, for the liquid to be stagnant again. With superimposed liquid velocity, the duration of the bubble's influence on the flow field was rather in the range of 1 to 2 seconds.

Qualitatively, the flow fields in the y-z-plane normal to the walls can explain the bubble rising behavior. For  $d_B > d_c$ , a symmetrical flow field due to the confining walls is apparent and, for  $d_B < d_c$ , a flow field comparable to the ones found in the x-y-plane for the oscillating bubble was found.

### 5.1.3 Wall shear stress generated by a single bubble

In this section, the wall shear stress generated by single bubbles is discussed (determined with EDM, based on [2, 3]). These investigations were done with water doped with the EDM salts (potassium hexacyanoferrate (II) and (III) and potassium chloride). In this Newtonian system, the shear stress can be calculated by  $\tau = \mu \cdot \gamma$  with  $\mu = 1.04 \cdot 10^{-3}$  Pas (see also **Table 4.1**). Therefore, only the shear stress is discussed.

As described in **Section 4.5**, the global wall shear stress level  $\tau_{glob}$  and the maximum wall shear stress  $\tau_{max}$  were determined for the system. Without resolving it in detail, the global wall shear stress level gives a general idea about the occurring wall shear stress in the system. On the other hand, the maximum wall shear stress value describes a spatially and timely limited appearing value in case of the discrete event of the single bubble rise.

In **Section 5.1.2**, shear rate and shear stress results were shown as well. In contrast to here, the shear rate in the liquid, as gained with PIV, was determined in the symmetry plane between the walls ( $\gamma_{liq}(yx) = \frac{\partial w_y}{\partial x}$  at  $z = d_c/2$ ).

In this section, the wall shear rates are discussed which are the shear rates normal to the wall (y-z-plane at  $z = 0$ ). Hence, this is perpendicular to the plane investigated in the PIV experiments (see **eq.(4.17)**). The difference between the two planes was already illustrated in **Figure 4.10b** and **c**. Consequently, the shear rate (and shear stress) results from the PIV and the EDM investigations cannot be directly compared.

Before discussing results, influencing factors for the type of analysis performed here have to be mentioned. Especially for the comparison of different CDFs of the global wall shear stress level, as shown for one parameter combination in **Figure 4.11c**, the time period taken into account is an important parameter:

1. This duration for the analysis (0.5 s before the maximum value and 1.5 s after the peak), influences the  $\tau_{glob}$ -interval size. As discussed in **Section 5.1.2**, the time of influence of the bubble on the surrounding liquid is longer by an order of magnitude in the case without superimposed liquid velocity in comparison to the one with superimposed liquid velocity. This principle can be seen in **Figure 4.11a**. If, e.g., 0.25 s before and after the peak value would be the duration taken into account, it is plausible that the respective global wall shear stress level was higher in comparison to the result from the chosen

interval. The duration of two seconds was chosen as an intermediate duration for all experiments. For many parameter combinations this leads to a non-Gaussian distribution as shown in **Figure 4.11c**.

**Figure 5.17** shows CDFs of the maximum wall shear stress for the largest and the smallest tested bubble size in two different channel depths at the same superimposed liquid velocity. This example was selected here to illustrate that not in all cases a Gaussian distribution is apparent. For the bubbles with equivalent bubble diameters larger than the channel depth, a - in most parts - Gaussian distribution was found (proved by the straight line between 0.01 and 0.99 probability). For bubble sizes smaller than the channel depth, this is not the case. There are several reasons for this probability distribution behavior (the following points are valid for both maximum and global wall shear stress level):

2. To ensure that the signals of the separate sensors in the array do not electrically interact, they were installed with a distance of 5 mm between each other. This means that smaller bubbles could pass through space between two sensors. Therefore, potentially only the flow around the sides of the bubble and not necessarily the high shear stress zone in the liquid film between the bubble and the wall [3, 17] affected the result. Approx. 1500 single bubble ascents were taken into account for each parameter combination. This ensures that all potential passing ways between the extreme cases (centrally hitting one sensor or passing by exactly half way between two sensors) are sufficiently taken into account. Still, the result is affected by this situation in contrast to the results for larger bubbles. On the other hand, larger bubbles can be deformed strongly (see **Section 5.1.1**, **Figure 5.5**). Therefore, at least two if not all three sensors can potentially measure the signal of the high shear stress zone in the thin liquid

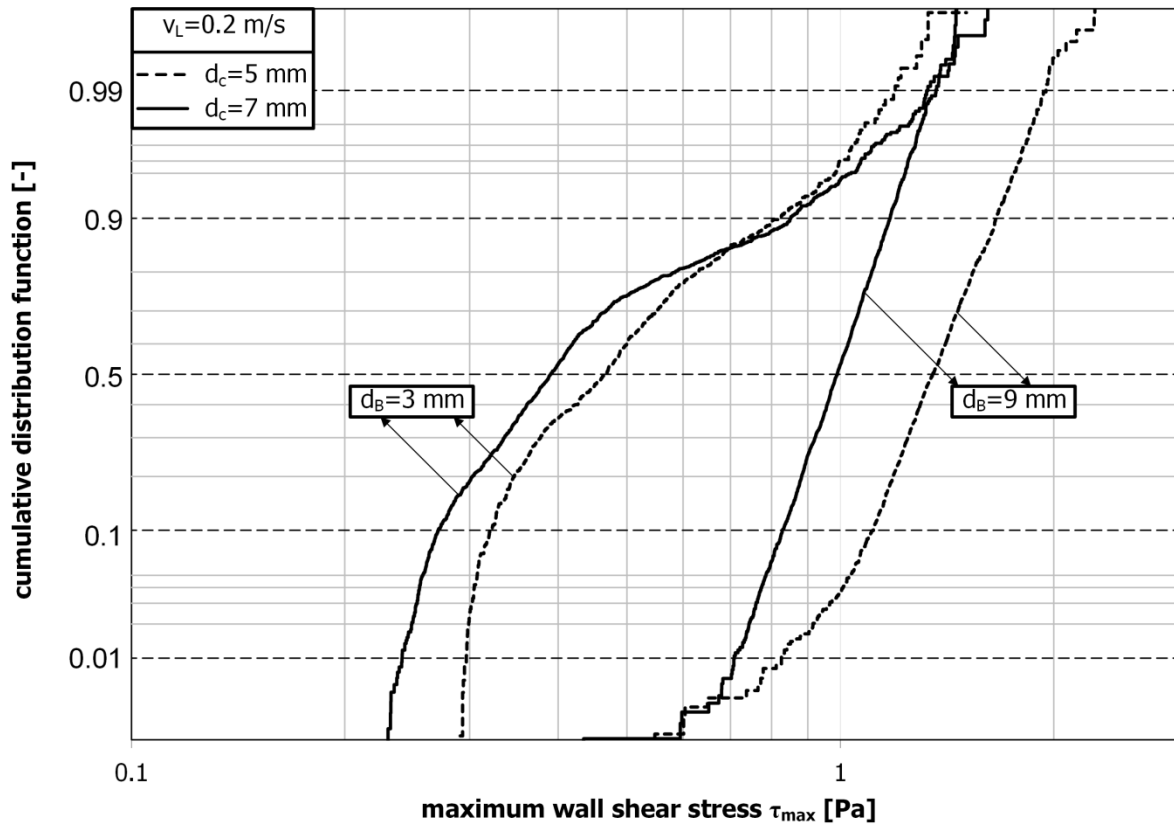


**Figure 5.17:** Cumulative distribution functions of the occurring maximum wall shear stress for different parameter combinations (steady state analysis)

film between the bubble and the wall. This can explain larger  $\tau_{glob}$ -interval sizes for cases where the bubble size is larger than the channel depth ( $d_B/d_c > 1$ ).

3. For the cases where the bubble size is smaller than the channel depth ( $d_B/d_c < 1$ ), the oscillation in the z-direction normal to the walls is also a potentially influencing factor as the sensor array is only located on one side of the wall (a rising path for such a case is shown in **Section 5.1.1, Figure 5.2g**). Assuming in this example that the sensor is installed on the right side of the channel, in the instant the bubble passes the sensor array, the bubble could be on the right side, the left side or somewhere in between in its oscillation period.

**Figure 5.18a** shows the probability ranges of the occurrence of the (magnitude of the) global wall shear stress level for the tested parameter combinations (assembled as described in **Figure 4.11b**). The size of the shear stress interval (1 to 99 %-value) gives an idea about the occurring fluctuations and the spatial distribution of the shear stress. With respect to the membrane application, the median value and the fluctuations are of particular interest. The median value is the occurring average value responsible for the detachment of deposition layers. Drews et al. [33] calculated critical particle diameters which are lifted from the membrane surface, depending on, i.a., the occurring wall shear stress. Especially with respect to membrane bioreactors, not only particulate deposition layers are of interest but also biofilms. As already mentioned in **Section 2**, several authors investigated the influence of shear stress on biofilms and found, e.g., an influence of the shear stress on the biofilm composition [36], on the release of fouling-promoting substances [19] and an influence of the shear stress fluctuations on the detachment of biofilms [35] with improved detachment at enhanced fluctuations.

Based on **Figure 5.18a**, the influence of the different parameters can be discussed. If a liquid velocity was superimposed, the occurring global wall shear stress level would be dominated by this flow as the median values were comparable in all of these cases. As previously mentioned, for some cases the duration taken into account for this determination can explain why the probability interval size decreases with increasing superimposed liquid velocity (at constant bubble size and channel depth). A comparable behavior was already mentioned previously for the occurring velocity magnitude investigated with PIV (**Figure 5.11**). On the other hand, here again, all fluctuations can be attributed to the flow generated by the bubble as the single phase flow showed negligible fluctuations. In most cases, an addition of a superimposed liquid velocity resulted in higher global wall shear stress levels; in all cases, at least when it comes to the (lowest =) 1 %-quantile. Mostly, it can be stated that an increasing bubble size and a decreasing channel depth lead to a higher global shear stress level. Regarding the channel depth, this is reasonable, as with a reduction of the channel depth, the confinement of the bubble is increased. As the same effect is valid for the flow around the bubble, higher velocity gradients at the wall (= wall shear rates) and therefore wall shear stresses appear.

It was mentioned previously that the shear stress results of the PIV experiments (described in **Section 5.1.2**) cannot be directly compared to the EDM results due to differing measurement planes. **Figure 5.13** shows the occurring shear stress in the liquid surrounding the bubble in the x-y-plane (at  $z = d_c/2$ ). As there were no walls in the field of view in the PIV measurements, the determined values are much lower in comparison to the wall shear stress measured with EDM (approximately by an order of magnitude). A multiplication of the 99 %- $\tau_{liq}$ -value (found with PIV; squares in **Figure 5.18a**) with a factor of 10 proves to be in fairly good agreement with the wall shear stresses from EDM. Most of these ( $10 \cdot \tau_{liq}$ )-values are between the 10 and 90 %-value limits of the global wall shear stress level for the respective parameter combination, thus giving a good estimate of  $\tau_{glob}$ .

In literature, no comparable investigation can be found that allow a direct comparison of these values. Ducom et al. [54] discussed the relative increase of the wall shear stress due to aeration (so a bubble swarm was used) in comparison to the single phase flow. They found factors between 1 and 4. This does not apply here when the

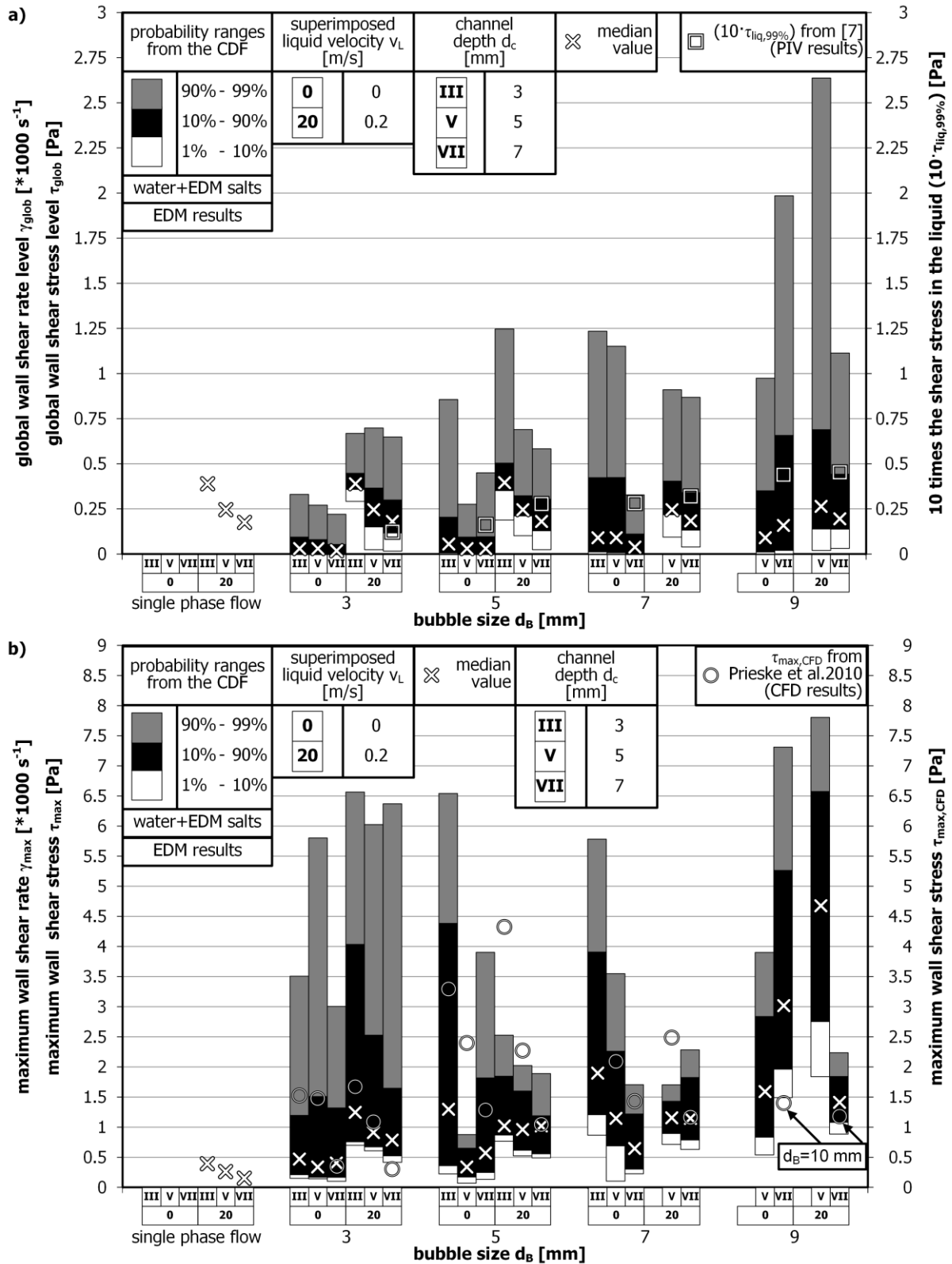


Figure 5.18: (a) Comparison of the probability ranges of the occurring global wall shear stress level to previously discussed PIV results [7] and (b) maximum wall shear stresses (transient corrected analysis) (based on [3]) compared to CFD [17]

medians of the global wall shear stress level (for the cases with  $v_L = 0.2$  m/s) are compared. For all of these cases, the respective median value for each channel depths was equal, with or without a bubble of any size (see **Figure 5.18a**). The second factor they introduced was comparing the interval size between the maximum and minimum wall shear stress value and the value generated by the single phase flow ( $(\tau_{max}-\tau_{min})/\tau_{single-phase}$ ) which is comparable to  $((\tau_{glob,99\%}-\tau_{glob,1\%})/\tau_{single-phase})$  in the given case. For this ratio, they found values of 5 to 45 at a channel depth of 5 mm. For the single bubble case here, ratios between 1 and 10 were found which is in good agreement with the results by Ducom et al. Especially, if it is taken into account that bubble sizes smaller than the channel depth were tested as well which was mostly not the case in their investigation. Ratkovich et al. [62] investigated the rise of Taylor bubbles in a tubular system with an inner diameter of 9.9 mm. They also evaluated the probability of the occurrence of the wall shear stress (including an algebraic sign as they evaluated the direction of the flow as well). The values they found were in a range of  $-2 \text{ Pa} < \tau < 1 \text{ Pa}$ . The respective absolute values are comparable to the values found in this investigation, especially for the cases with a bubble size larger than the channel depth where a thin liquid film appears as it is the case for the Taylor bubbles.

With increasing bubble size and decreasing channel depth, the global wall shear stress level increases and the fluctuations are promoted. The average wall shear stress is below 0.5 Pa but fluctuations can reach values over 2.5 Pa. Generally, the rising bubble induces fluctuations and it increases the occurring shear stress values significantly in comparison to the single-phase flow but the median value is not affected.

In **Figure 5.18b**, the maximum wall shear stress is plotted against the bubble size, channel depth and superimposed liquid velocity. So here, in contrast to the previously discussed global wall shear stress level, the maximum wall shear stress values which were the rarely occurring and locally limited were evaluated. In contrast to the global wall shear stress level, the results of the maximum wall shear stress were not dominated by the superimposed liquid velocity. As shown in **Figure 4.11a** where a superimposed liquid velocity of 0.2 m/s was applied, the maximum wall shear stress value is usually much higher in comparison to the value generated by the single phase liquid flow.

In most cases, the median values of the maximum wall shear stress increase with increasing bubble size, decreasing channel depth and increasing superimposed liquid velocity. These proportionalities are reasonable due to an enhanced confinement of the bubble (regarding  $d_B$  and  $d_c$ ) or, respectively, the lifting of the general wall shear stress level (regarding  $v_L$ ). With regard to the fluctuations, the interpretation is not as straight forward. The influencing factors ‘distance between the sensors’ and ‘bubble size to channel depth ratio’ do have an effect on the results as well:

- For  $d_B/d_c < 1$ , the fluctuations ( $= (\tau_{max,99\%}-\tau_{glob,1\%})$ ) are pronounced which might be attributed to the rising behavior of the bubble which oscillates between the walls. Therefore, it bounces against the wall periodically which might lead to thin liquid films between the bubble and the wall where high shear can occur. On the other hand, when the bubble bounces against the opposite wall when it passes by the sensor array, a much larger liquid film is apparent between the bubble and the wall leading to much lower values.
- For  $d_B/d_c > 1$ , the bubble is squeezed into the space between the walls and, therefore, the liquid films between the bubble and the wall are not undergoing such strong variation as in the case of  $d_B/d_c < 1$ . Still, the fluctuations ( $= (\tau_{max,99\%}-\tau_{glob,1\%})$ ) are also pronounced which might be attributed to the fact that the size of the area where the actual maximum shear stress occurs is fairly small (as found in the CFD

simulation done by Prieske et al. and in parts described in [17]). Consequently, the small sensors which have a certain distance between each other will not always be hit by this small peak area which leads to fluctuations in the results.

Therefore, due to these reasons, the results are not always easy to interpret. In comparison to the CFD values found by Prieske et al. [17] which were not affected by the practical limitations as described for the EDM (e.g., distance between the sensors), the median values found in the experiments were naturally lower in most cases. Even with the limitations of the EDM, most of the CFD results are at least in the 1 to 99 %-interval-range of the measured maximum wall shear stress results. In comparison to the previously discussed results by Ducom et al. [54] now  $((\tau_{max,99\%}-\tau_{glob,1\%})/\tau_{single-phase})$  can be calculated. This is actually closer to their  $((\tau_{max}-\tau_{min})/\tau_{single-phase})$ -ratio. Here, values for this ratio up to 30 were found which is even closer to the maximum ratio of 45 which was found in their investigation.

In comparison to the global wall shear stress level, the highest maximum wall shear stress values found in this investigation are in parts higher by an order of magnitude. Roughly, the two extreme cases of the smallest and the largest bubbles show high maximum wall shear stresses. The small bubble, experiencing an oscillation normal to the wall, gives this result most likely due to very thin liquid films occurring when the bubble bounces against the wall where the sensors are installed. The larger bubbles are squeezed into the confining channel and, therefore, a thin liquid film always occurs during the passage of the sensor array. The highest values of up to 7.75 Pa were found for a 9 mm bubble rising in a 5 mm channel with a superimposed liquid velocity of 0.2 m/s.

#### 5.1.4 Conclusions from the single bubble experiments

In this section about the single bubble ascent in a confining geometry, the bubble behavior itself, its interaction with the surrounding liquid and resulting wall shear stresses were discussed. The qualitative dependencies of all determined quantities and the varied parameters are collected in

- in **Table 5.3** (for the bubble behavior [4, 6]),
- in **Table 5.4** (for the bubble surrounding liquid including the vorticity which was not discussed in the frame of this thesis but in the respective publication [7] as the trends are similar to the ones discussed for the shear rate) and
- in **Table 5.5** (for the wall shear stress [2, 3]).

As single bubble ascents in unconfined geometries in stagnant Newtonian continuous liquid phases are a common topic in literature, the influence of the channel depth, superimposed liquid velocity and rheology were of particular interest here. In the investigated parameter ranges with a bubble size to channel depth ratio ( $d_B/d_C$ ) between 0.43 and 3, it depended on the quantity if the channel depth had a significant impact. Correlations found for freely rising bubbles worked (in parts) for this system as well.

One of the aims of this investigation was to check the statement by Ozaki and Yamamoto [46] that results from fluid dynamic investigations performed in water are transferrable to MBR systems which are operated with non-Newtonian activated sludge. Their statement was based on a 10 % higher viscosity of activated sludge in comparison to water. In this investigation, a model solution was used in the non-Newtonian fluid dynamic experiments with a rheology analogous to MBR sludge with an average MLSS concentration of 11.4 g/L. In the

**Table 5.3: Qualitative dependencies found in the single bubble behavior experiments (W: water; X: Xanthan solution, ↑: increasing value, ↓: decreasing value, const.: constant value/no clear trend)**

			absolute terminal rise velocity $w_{B,abs}$	relative terminal rise velocity $w_{B,rel}$	horizontal dimension of the bubble $d_{B,h}$	oscillation amplitude $\hat{x}$	oscillation frequency $f_B$
channel depth	↑	W	const.	↑ (with $v_L$ ↑: ↓)	const.	↑ (with $v_L$ ↑: ↓)	const.
		X	↑	↑	const.	↑	const.
bubble size	↑	W	const.	const.	↑	↑	const.
		X	1 <sup>st</sup> ↑ then const.	1 <sup>st</sup> ↑ then const. (with $v_L$ ↑: ↑)	↑	const.	const.
liquid velocity	↑	W	↑	↑	const.	↓	const.
		X	↑	↑	const.	const.	↓

**Table 5.4: Qualitative dependencies found in the single bubble surrounding liquid experiments (W: water; X: Xanthan solution, ↑: increasing value/range, ↓: decreasing value/range, const.: constant value/range; 1-99 %: probability range from the 1st to 99th percentile) (retrieved from [7], grey background is used for quantities not discussed in this thesis)**

			velocity magnitude $w_{abs}$		vorticity $\vec{\omega}$		shear rate $\gamma_{liq}$		shear stress $\tau_{liq}$	
			median	1-99 %	median	1-99 %	median	1-99 %	median	1-99 %
channel depth	↑	X	const.	const. or ↑	const.	const. or ↑	const.	const. or ↑	const.	const. or ↑
bubble size	↑	W	const.	↑	const.	↑	const.	↑	const.	↑
		X	const.	↑	const.	↑	const.	↑	const.	↑
liquid velocity	↑	W	↑	const.	const.	const. or ↑	const.	const. or ↑	const.	const. or ↑
		X	↑	const.	const.	↑	const.	↑	const.	↑

**Table 5.5: Qualitative dependencies found in the single bubble wall shear stress experiments (W: water+EDM salts, ↑: increasing value, ↓: decreasing value)**

			maximum wall shear stress $\tau_{max}$	global shear stress level $\tau_{glob}$
channel depth	↑	W	↓	↓
bubble size	↑	W	↑	↑
liquid velocity	↑	W	↑	↑

bubble surrounding liquid, shear rates in this Xanthan solution of up to  $80 \text{ s}^{-1}$  were found. Taking the highest wall shear rate generated by the single-phase flow into account ( $400 \text{ s}^{-1}$  for  $d_c = 3 \text{ mm}$  and  $v_L = 0.2 \text{ m/s}$ ) and assuming a factor of two between the shear rates in water and Xanthan solution (as discussed in the PIV investigations), a wall shear rate of  $2 \cdot 400 \text{ s}^{-1} = 800 \text{ s}^{-1}$  is found. These two cases ( $80 \text{ s}^{-1}$  and  $800 \text{ s}^{-1}$ ) lead to viscosities that are higher by a factor of at least  $\mu_{nN}/\mu_{water} = 20$  or 6 in comparison to water (see **Figure 4.4**). Even for the lowest MLSS concentration used by Ozaki and Yamamoto, the shear rate of  $800 \text{ s}^{-1}$  translates to a 40 % higher viscosity. Therefore, based on the actual measured shear rate data, already the statement about the viscosity relative to water cannot be confirmed. The factor between the viscosity levels of roughly an order of



magnitude between water and the non-Newtonian liquid phase did mostly not appear in the determined quantities. Although the rising behavior (oscillating in water in contrast to mostly non-oscillating in Xanthan solution) was different from a qualitative point of view, the relative terminal bubble rise velocities were mostly similar, especially in cases with superimposed liquid velocity. The interaction between a superimposed liquid velocity and the channel depth led to higher shear rates (in comparison to cases with  $v_L = 0$  m/s) especially normal to the confining walls. These higher shear rates led to a lowered viscosity in the vicinity of the bubble. Regarding the shear rates in the liquid surrounding the bubble, results in the Xanthan solution were roughly twice as high. Due to the different rheological behavior of the continuous phases, this results in significant differences regarding the occurring shear stresses close to the bubble. The wall shear stress measurements were only conducted for water (doped with ions) as the continuous phase. Interestingly, bubbles smaller than the channel depth showed high wall shear stress values due to the bouncing between the walls resulting from an oscillation normal to the wall. For bubbles larger than the channel depth, the high values were measured due to the larger area with a thin liquid film between the bubble and the wall.

From the varied parameters, the bubble size was found to have the strongest impact on the single bubble ascent. Most other parameters did not affect the measured quantities as much as it might have been expected, e.g., by the confining geometry. This applies as well for the viscosity which for the Xanthan solution is by an order of magnitude higher than that of water. This includes the shear rate results in the liquid surrounding the single bubble. The shear stress on the other hand is respectively significantly higher.

## 5.2 Bubble swarms rising in the flow channel

After the fundamental investigation of the single bubble ascent under completely defined conditions, in the following, the degree of complexity is increased. In a bubble swarm, due to, e.g., bubble interactions it is impossible to obtain a completely controlled system. The bubble swarm behavior will be qualitatively described with a special focus on the discussion of the influence of the continuous phases. In contrast to the single bubble experiments, this section does not only include the non-Newtonian characteristics but also the influence of ions. For the quantitative results, the influence of the varied parameters on the gas hold-up and the wall shear stress generated by the bubble swarm induced liquid flow is discussed. Additionally, the results are put into context with data from literature but a broad literature base is not at hand for the given geometry. Still, existing correlations are expanded or new correlations are developed to give mathematical equations describing the behavior.

### 5.2.1 Flow behavior of the bubble swarm

In this section, the general flow behavior and the resulting gas hold-up are discussed (determined with HSC, based on [8]). **Figure 5.19a to d** show images of the bubble patterns (in the x-y-plane) for the same parameter combination, just with differing continuous phases. Although in the previously described EDM measurements, ions were also used (in water), here, for the first time ions were added to the Xanthan solution. As described in **Section 4.2**, regarding the material properties, no difference was found between the addition of the EDM salts and sodium sulphate.

A significant effect of the type of continuous phase on the occurring bubble sizes was found. In contrast to water (**Figure 5.19a**) where intermediately sized bubbles occur, in Xanthan solution (**Figure 5.19c**) larger bubbles are apparent. This is in accordance with Wilkinson et al. [155] who reported that the bubble size is proportional to the viscosity of the liquid phase ( $d_B \sim \mu$ ). On the other hand, assuming a comparable initial bubble population in all cases above the aerator, this is in contradiction to Sanada et al. [156] and Chesters and Hofmann [157] who found a decreased coalescence tendency in high viscosity systems. These publications all discussed systems with (high viscosity) Newtonian continuous phases. Such publications are rarely found for non-Newtonian continuous phases and, if discussed, these investigations mainly deal with the coalescence of two bubbles and not the behavior of a complex, dynamic multiple bubble flow [11]. For Newtonian continuous phases (and water in particular), flow pattern maps can be found in literature showing the flow characteristics depending on the gas velocity. The given system can be seen as a bubble column (with stagnant water if  $v_L = 0$  m/s) or a pipe with a gas-liquid-two-phase flow (with co-current liquid velocity if  $v_L > 0$  m/s). In both cases, the behavior is often related to the diameter of the pipe (or column) or the cross section area. For comparison, the hydraulic diameter can be calculated for the non-circular cross section in this investigation. The hydraulic diameter  $d_h$  is calculated as

$$d_h = 4 \cdot \frac{\text{cross section area normal to main flow}}{\text{wetted circumference length}} = \frac{d_c d_w}{2d_c + 2d_w} \quad (5.23)$$

which leads to a hydraulic diameter of  $d_h = 9.7$  mm for the 5 mm channel and  $d_h = 13.4$  mm for the 7 mm channel (which is close to the hydraulic diameter for channels with an infinite width where the hydraulic diameter is two times the depth of channel).

Regarding the system as a (cylindrical) bubble column [158, 159], the flow should be homogeneous (at low gas velocity) and go through a transition state to the heterogeneous flow with a tendency to slug flows (for higher

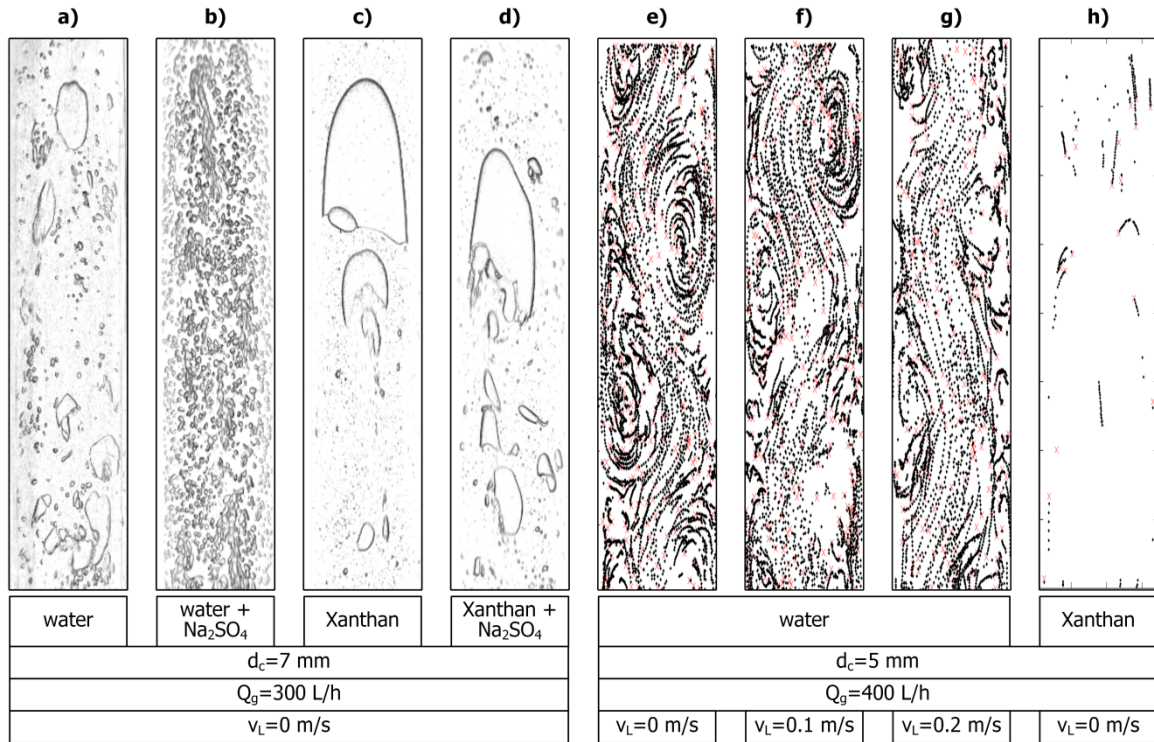


**Figure 5.19: Bubble patterns for the different continuous phases (a-d) and bubble paths for varied liquid velocities (e-h) recorded in the x-y-plane (based on [8])**

gas velocities). This is in accordance with the observations in the system, with an intermediate heterogeneous flow shown in **Figure 5.19a**. For the case with co-current liquid flow, with respect to the flow pattern map reported by Hewitt and Roberts [160], the flow pattern would be in the region between slug flow and bubbly flow. In the latter one the turbulence in the liquid flow leads to a break-up of the bubbles and, therefore, larger bubbles occur less frequently.

The addition of ions with the purpose to hinder coalescence leads to a homogeneous bubble flow pattern in case of water (**Figure 5.19b**). In case of the Xanthan solution, the addition of ions did not have this effect (**Figure 5.19d**) as frequently break-ups and coalescences of bubbles could be observed. Still, due to the viscosity lowering effect by the ions (resulting in an intermediate viscosity between that of water and Xanthan solution, as already explained in **Section 4.2**; see also **Table 4.1**), the system behaved noticeably more dynamic than in the Xanthan solution without ions.

Regarding the mean bubble diameter (= average diameter of a volume equivalent bubble), although not studied in all detail, a bubble size range between 5 and 30 mm was found with

- the largest bubbles in Xanthan solution,
- intermediately sized bubbles in water and Xanthan solution with ions and
- the smallest bubbles in water doped with ions.

Especially in case of the aqueous salt solutions, cross-links between the single bubble experiments and the bubble swarms can be drawn (which is done in the **Section 5.2.2**).

Besides the mentioned effect on the bubble pattern, e.g., the bubble paths are affected as well by the co-current liquid velocity. **Figure 5.19e** to **g** show bubble paths for the same parameter combination in water just with differing superimposed liquid velocities. Especially the case without superimposed liquid velocity (**Figure 5.19e**) shows the typical circulation cells where bubbles are dragged out of the main meander-like flow in the center of the reactor and pulled downwards at the outer region [161]. In cylindrical columns, the height of the circulation cells in which the bubbles rotate along with the liquid is usually in the range of the column diameter. From a qualitative point of view, this rule obviously does not apply for the rectangular cross section channel, as the height of the circulation cell is larger than the hydraulic diameter. Still, it can be stated that the circulation cells are rather in the size range of the width of the channel. With increasing superimposed liquid velocity (**Figure 5.19f** and **g**), due to the overlying liquid flow pushing the bubbles upwards, the circulation flow cells are less pronounced and the meander-like main flow structure is widened. For completeness, **Figure 5.19h** shows the same bubble path determination result for Xanthan solution as the continuous phase. As large bubbles dominate these flows (shown in **Figure 5.19c**), far less bubbles can be tracked and, therefore, the resulting images are less meaningful. For the given image, it can be stated that in the lower central position, a larger bubble rises upwards and in the upper region it pushes smaller bubbles to the side and downwards.

Qualitatively, the influence of the continuous phase is significant with larger bubbles occurring in the higher viscosity liquid and smaller bubbles occurring in the cases doped with ions. Qualitatively, it was shown that the bubble ascent in the bubble swarm is strongly affected by the superimposed liquid velocity reducing the tendency for circulation cells to occur.

A quantity, reflecting the qualitative phenomena described above, is the gas hold-up  $\varepsilon_g$ . The gas hold-up is a common topic in bubble swarm investigations in literature. Several correlations, mostly based on a physical background (e.g., the continuity equation or momentum balance), were suggested (usually based on tests in

cylindrical bubble columns, see, e.g., [162, 163]). Based on these correlations, none of which takes all influencing factors into account, several dependencies can be given for the gas hold-up (where the exponent  $m$  stands for different positive values):

- $\varepsilon_g \sim v_g^m$  ; a proportionality to the gas velocity is found, i.e., the more gas is introduced into the channel, the higher is the gas fraction
- $\varepsilon_g \sim w_{B,abs}^{-m}$  ; this inverse proportionality to the bubble rise velocity is due to the fact that the faster the bubbles rise, the faster they leave the column.

All the following proportionalities can also be explained by this statement:

- $\varepsilon_g \sim d_B^{-m}, v_L^{-m}, d_h^{\pm m}$  ; as shown in **Section 5.1.1** for the single bubble,  $w_{B,abs}$  increases with the bubble size and the superimposed liquid velocity. Although no significant difference between the two different channel depths was found here, in comparison to a freely rising bubble, the bubbles were decelerated by the confining geometry. So actually, a negative exponent  $m$  would be expected. In literature no clear statement was made regarding the influence of the bubble column diameter as its influence is usually neglected if it exceeds 0.15 m (which is not the case here).
- $\varepsilon_g \sim \sigma^{-m}, c_{surf}^m$  ; the interfacial tension is proportional to the bubble size ( $d_B \sim \sqrt{\sigma}$  and, therefore, bubble velocity). A low interfacial tension enhances the break-up of bubbles into smaller bubbles. As discussed in **Section 4.2**, surfactants can lead to a decrease of the interfacial tension. Therefore, regarding the influence of the surfactant concentration on the gas hold-up, the logic explained before works here as well. Even without an effect on the surface tension, the coalescence hindrance leads to smaller bubble sizes in the bubble swarm and, therefore, higher gas hold-ups.
- $\varepsilon_g \sim \mu^{-m}$  ; a higher viscosity of the continuous phase leads to lowered bubble rise velocities which actually would lead to a higher gas hold-up. It has to be kept in mind that the viscosity also has an effect on the bubble size with  $d_B \sim \mu$ . These two effects combined lead to an inverse proportionality of the gas hold-up and viscosity. The respective gas hold-up correlations taking the influence of the viscosity into account were derived for Newtonian liquids. As described in **Section 5.1.1**, in particular for the cases with superimposed liquid velocity, a significant deceleration of the bubble was not necessarily found in the non-Newtonian liquid phase in comparison to water. Still, Kawase and Moo-Young [164] found (although a weak but) basically the same proportionality for non-Newtonian continuous phases with  $\varepsilon_g \sim (K\gamma^n)^{-m}$ .

**Figure 5.20** shows the results of the gas hold-up for all tested parameter combinations. The results are plotted as a function of the gas flow rates which were equal for both channels but resulted in different superficial gas velocities (calculated as  $v_g = Q_g/(d_c \cdot d_w)$ ) when  $d_c$  was varied. As discussed above, the gas velocity is typically used to explain the gas hold-up behavior. For both channel depths, the respective superficial gas velocities are given at the bottom of the figure. Basically, most of the proportionalities discussed above can be found in the presented results as well, and the value range is respective to data from literature (e.g., in the already mentioned articles [162, 163]). The gas hold-ups found by Yamanoi and Kageyama [55], mentioned in **Section 2** as the most comparable system to the system investigated in this project, are also in the same range. Still, in contrast to this work, Yamanoi and Kageyama

- only investigated water as the continuous phase,

- did not set the co-current liquid velocity to defined values (resulting in self-established values in the range of  $0.15 \text{ m/s} < v_L < 0.72 \text{ m/s}$ ) and
- did not find an influence of the bubble size and the channel depth.

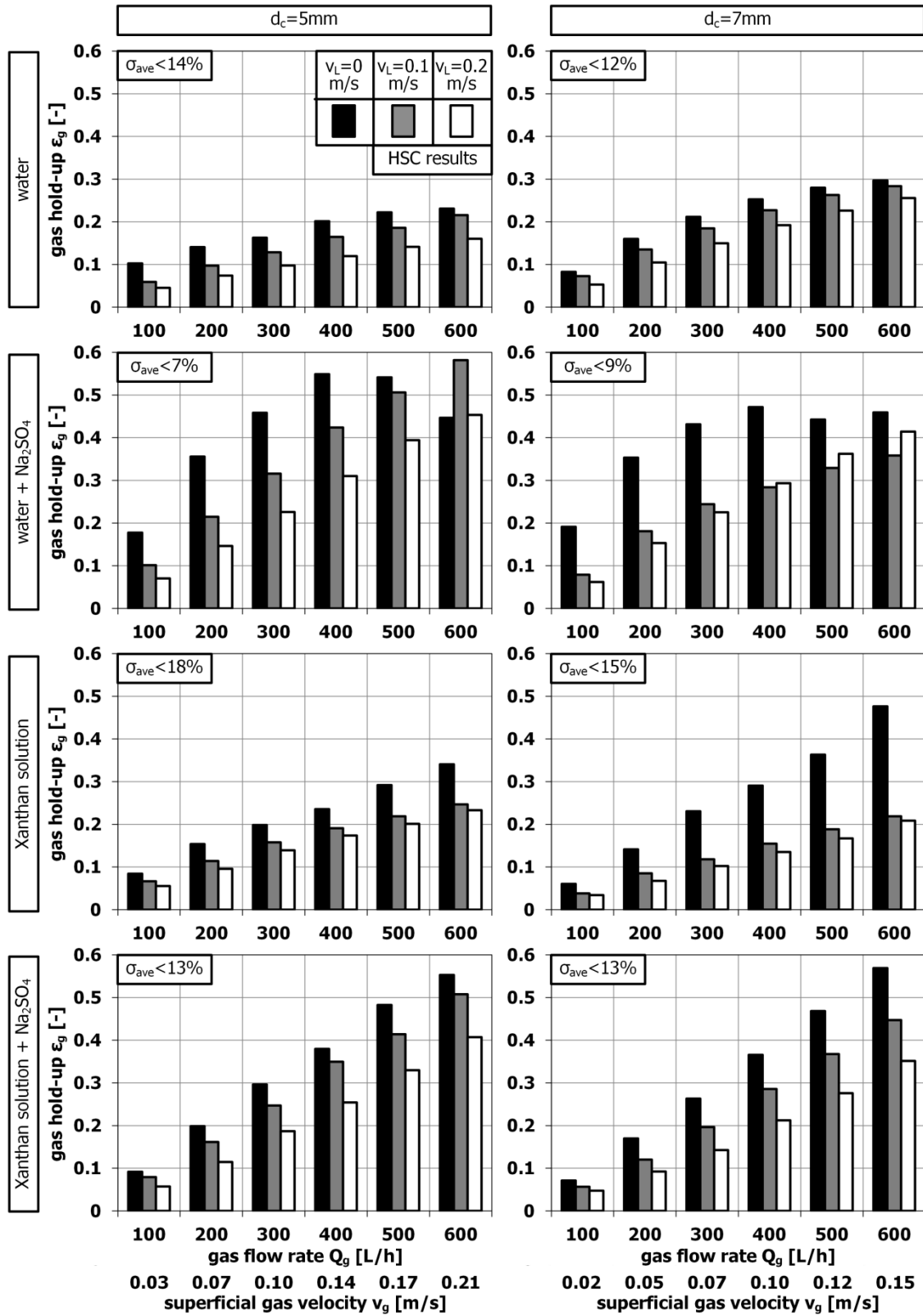


Figure 5.20: Gas hold-ups of the two different channel depths  $d_c$  and the four different continuous phases (based on [8])

The last point is rather surprising keeping the previously discussed proportionalities in mind.

For the results found here, three things are particularly worth discussing.

1. For water doped with ions, in cases without superimposed liquid velocity, a maximum gas hold-up is achieved at a gas flow rate around 400 L/h for both channels. This is the only case where this behavior was found. Ribeiro and Mewes [133] discussed such a behavior as well and found a maximum at a comparable superficial gas velocity. This overshooting can be explained with the transition region being, by nature, somewhere between homogeneous (narrow bubble size distribution) and heterogeneous flow (a rather bimodal bubble size distribution) and, therefore, cannot be described exactly.
2. Regarding the channel depths, for all continuous phases, if plotted against the superficial gas velocity, higher gas hold-ups were found for a larger channel depth. The published works are not clear about this. At least in case of Xanthan solution, this might be attributable to differing viscosity levels in the two different channels as discussed in **Section 5.1.4**. A smaller channel depth leads to higher shear rates (especially in the y-z-plane normal to the confining walls) leading to a lowered viscosity in the liquid, and in turn to higher bubble rise velocities and, therefore, a lowered gas hold-up ( $d_c \downarrow \Rightarrow \gamma \uparrow \Rightarrow \mu \downarrow \Rightarrow w_B \uparrow \Rightarrow \epsilon_g \downarrow$ ).
3. Regarding the viscosity, in comparison to water as continuous phase, in both higher viscosity systems, Xanthan solution with and without ions, higher gas hold-ups were found. Obviously, complex interactions between the conditions lead to this behavior. According to Wilkinson et al. [155], larger bubbles were found in the higher viscosity system. The increase in bubble size did not outbalance the decrease of the bubble rise velocity due to enhanced friction in the narrow channel. It has to be stated that this is an assumption as neither in the single bubble nor in the bubble swarm case, rise velocities of such large bubbles were investigated here. It is known for Taylor bubbles, from a certain size on, to have a constant rise velocity independent of the bubble size (see, e.g., [165]). In the intermediate viscosity liquid phase (Xanthan solution with ions), higher gas hold-ups were found in comparison to the values in Xanthan solution without ions which would be contradictory again to the prior statement. But here, as mentioned in the qualitative flow behavior discussion, smaller bubbles (with lower rise velocities) were apparent in comparison to the high viscosity system due to an enhanced dynamic flow behavior.

Of the gas hold-up correlations that can be found in literature, Akita and Yoshida's approach [163, 166]

$$\frac{\epsilon_g}{(1 - \epsilon_g)^4} = C_1 \left( \frac{g d_h^2 \rho_L}{\sigma} \right)^{C_2} \left( \frac{g d_h^3 \rho_L}{\mu_L^2} \right)^{C_3} \left( \frac{v_g}{\sqrt{g d_h}} \right) \quad (5.24)$$

takes most of the mentioned parameters into account. Still, it lacks the integration of the influence of

- the co-current liquid velocity,
- a coalescence hindrance surfactant and
- the effect of a non-Newtonian liquid.

To incorporate these parameters,

- a term including a ratio of the superficial gas velocity and the effective velocity  $v_g/(v_g + v_L)$ ,
- a term including a ratio of the hydraulic diameter and the bubble diameter  $d_h/d_B$  (i.a., depending on the addition of coalescence hindrance surfactants)

were additionally multiplied and

- the viscosity in the original equation was replaced by

$$\mu_L = K \left( \frac{v_g + v_L}{d_h} \right)^{n-1} \quad (5.25)$$

which assumes that in cases without co-current liquid flow, the occurring liquid velocities are in the same value range as the respective gas velocity.

With the additionally multiplied two terms and the replacement of the viscosity, a correlation (valid for  $v_g > 0$  m/s) was found

$$\frac{\varepsilon_g}{(1 - \varepsilon_g)^4} = 11.77 \left( \frac{g d_h^2 \rho_L}{\sigma} \right)^{0.49} \left( \frac{g d_h^{2n+1} \rho_L}{K^2 (v_g + v_L)^{2n-2}} \right)^{-0.14} \left( \frac{v_g}{\sqrt{g d_h}} \right)^{1.48} \left( \frac{v_g}{v_g + v_L} \right)^{0.71} \left( \frac{d_h}{d_B} \right)^{2.27} \quad (5.26)$$

A parity plot is shown in **Figure 5.21** ( $R^2 = 0.70$ ). For this correlation, bubble sizes were estimated for the different parameter combinations (an average bubble diameter of 10 mm in water with ions, 20 mm in pure water and Xanthan solution with ions and 30 mm in Xanthan solution was used). The estimation was based on a tentative determination of the bubble size. Accurate measurements of the respective bubble sizes might lead to an improved correlation with a higher coefficient of determination.

Where comparable, the gas hold-up behavior was in accordance with literature. Still, the influences of the viscosity and the channel depth show a behavior which cannot be explained to the full extent here. In both cases, an increase led to higher gas hold-up values. Obviously, complex interactions of these two parameters, with 1. the channel depth affecting the viscosity due to the occurring shear rates, and 2. both parameters combined affecting the bubble size and the bubble rise velocity, lead to this gas hold-up behavior. A correlation for the gas hold-up which is an extension of an existing model, was found that incorporates all varied parameters.

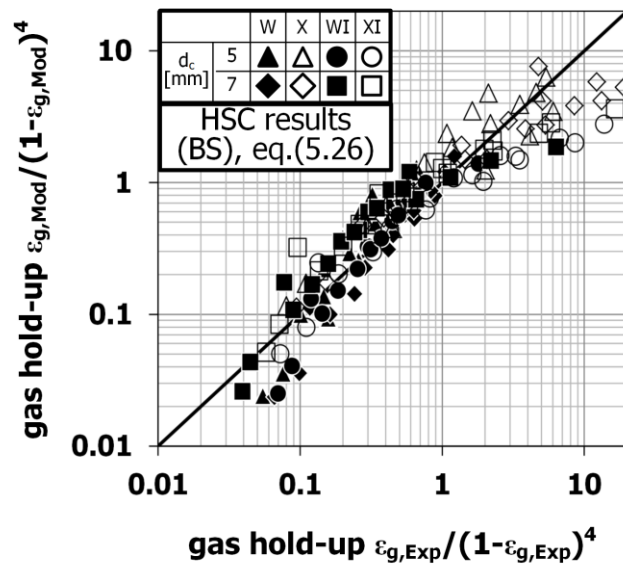


**Figure 5.21:** Parity plot for the gas hold-up with the modelled values based on eq.(5.26) against the experimental data (continuous phases W: water, WI: water+ions, X: Xanthan solution, XI: Xanthan solution with ions) (based on [8])

### 5.2.2 Wall shear stress generated by the bubble swarm

Finally, the wall shear stress generated by the two-phase flow is discussed (determined with EDM, based on [8]). Here, for the first time in this thesis, wall shear stress measurements were conducted in a gas-liquid-system with a non-Newtonian continuous liquid phase as well. In the single bubble experiments, the maximum occurring wall shear stress and the global wall shear stress level were determined. These wall shear stress measurements were performed for discrete bubble passages. Therefore, for each parameter combination, a specific maximum wall shear stress and a global wall shear stress level could be determined. This data was presented in box-and-whisker-plots, as not all of the values were normally distributed. In the bubble swarm experiments, as one can see in the bubble patterns in **Figure 5.19a to d**, a polydisperse bubble swarm and complex flow structures (**Figure 5.19e to g**) can be found in all cases. As described in **Section 4.5**, for every parameter combination, the wall shear stress was measured five times for one second. The combined data of all of these measurements for one parameter combination was normally distributed for all cases. Therefore, in contrast to the single bubble results, here the average wall shear stress (as the median) and the fluctuations (as the standard deviation) were determined. As mentioned in **Section 5.1.3**, the fluctuations are of special interest with respect to particulate deposition layers and biofilms.

In case of aqueous salt solutions, the wall shear stress can be calculated by the multiplication of the wall shear rate with the liquid viscosity ( $\mu_L = 1.04 \cdot 10^{-3}$  Pas, see also **Table 4.1**), which is why both quantities are plotted in the same diagram(s). **Figure 5.22** shows the results for the performed experiments, with one diagram for each channel depth (for clarity reasons, the median values are shown in a bar plot without the fluctuation included). Generally, it can be stated that qualitatively the average wall shear stress dependencies on the varied parameters were as expected. Increasing wall shear stress median values were found for

- a decreasing channel depth due to the enhanced confinement,
- an increasing gas flow rate (or superficial gas velocity) due to the pronounced complex flow structures generated by the gas in the system and
- an increasing co-current liquid velocity due to the generally higher liquid velocity level occurring in the bulk liquid and the thin liquid films between the bubbles and the wall.

In the 7 mm channel, median wall shear stress values up to 1.1 Pa and in the 5 mm channel values up to 3.4 Pa were found. The increase of the wall shear stress between the two channel depths by a factor of approximately 3 is rather high considering that the factor between the channel depths is only 1.4. Still, taking the single bubble results discussed in **Section 5.1.3** into account, such a pronounced difference was, in parts, found there as well (see **Figure 5.18b**,  $d_B = 9$  mm,  $v_L = 0.2$  m/s). In contrast to the single bubble results of the global wall shear stress level where the median (= 50 % value) was dominated by the superimposed liquid velocity, the median wall shear stress values of the bubble swarm were less dominated by the co-current liquid flow.

Taking the upper probability limit (= 99 %-quantile) of the global wall shear stress level, found for the single bubble, in **Figure 5.22** it can be seen that these results agree fairly well with the bubble swarm results. The global wall shear stress levels of the 9 mm bubble were chosen for the comparison here as this roughly fits the average bubble size found in the aqueous salt solution system as discussed in **Section 5.2.1**. In case of the 5 mm channel, the results of the single bubble for the case with and without superimposed liquid velocity basically frame the bubble swarm results. In the case of the 7 mm channel, the 99 % global wall shear stress level is



almost equal to the median wall shear stress at the highest gas flow rate and the same superimposed liquid velocity like in the single bubble experiment. In comparison to Ducom et al. [54] who found an increase of the average wall shear stress by the two-phase flow in comparison to the single phase flow by a factor of up to 4, here, factors of 7 to 26 in the 5 mm channel and 4 to 10 in the 7 mm channel were found. Therefore, Ducom et al.'s findings cannot be confirmed which might be attributed to a smaller parameter range as their experiments were rather focused on the spatial wall shear stress distribution over the wall. In a comparable gas velocity range, Yamanoi and Kageyama [55] found average wall shear stresses in a 5 mm channel with values up to 1.4 Pa and in a 7 mm channel up to 1.5 Pa. As in their experiments a self-establishing liquid velocity occurred, both results were found for a superimposed liquid velocity of approximately 0.5 m/s which is 2.5 times higher in comparison to the highest liquid velocity tested in this investigation. In spite of the higher superimposed liquid velocities, they did not find a significant enhancement of the wall shear stress. In their case, as it was already discussed for the gas hold-up in **Section 5.2.1**, again - rather surprisingly - no significant influence of the channel depth was found. Nagaoka et al. [75] also investigated an aerated rectangular cross section and found only average values of up to 0.3 Pa although their channel depth was 32 mm and, therefore, they investigated much lower superficial gas velocities.

Generally, the average wall shear stress generated by the bubble swarm in the aqueous salt solution as the continuous phase behaves as expected ( $d_c \downarrow, v_g \uparrow, v_L \uparrow \Rightarrow \tau_{median} \uparrow$ ) and the value range is in accordance with average wall shear stresses reported in literature (roughly  $0.5 \text{ Pa} < \tau_{median} < 3.4 \text{ Pa}$ ). The significant difference between the two tested channel depths is noteworthy, with average wall shear stress values in the narrower channel being three times higher.

**Figure 5.23** shows the wall shear rates and wall shear stresses found in the Xanthan solution with ions as the continuous phase. Here, the wall shear rates and wall shear stresses are plotted in separate diagrams, as the two quantities not only differ by a factor but the wall shear stress has to be calculated with the viscosity as described in **eq.(4.11)**. With some exceptions, the wall shear stress again behaves according to expectations regarding the varied parameters. Especially for the higher gas flow rates, the effect of the superimposed liquid velocity is not as significant as it was found for the Newtonian liquid phase. In contrast to the factor of three between the shear

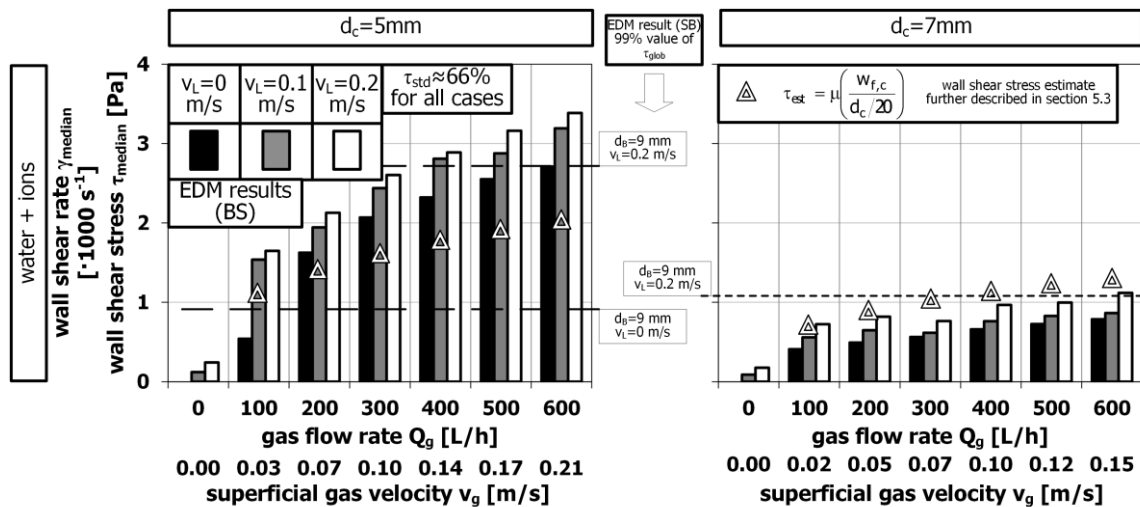


**Figure 5.22:** Median of the shear rates and shear stresses found in water+EDM salts for the two different channel depths  $d_c$  in comparison to global shear stress values  $\tau_{glob,99\%}$  found for single bubbles (dashed lines, data based on [3, 8]) and a wall shear stress estimate further described in Section 5.3 (triangles)

rates found in water for the two different channel depths, in the non-Newtonian liquid phase approximately a factor of 2 was found. Therefore, it can be stated that besides the gas flow rate, the channel depth has the most significant effect on the average wall shear rate for both continuous phases. Calculating the wall shear stress in the non-Newtonian liquid phase, with a factor of 1.5 between the respective values in the 5 and 7 mm channel the effect of the channel depth is reduced. In the 5 mm channel, the highest median wall shear stress values were comparable in the Newtonian ( $\approx 3.4$  Pa) and non-Newtonian ( $\approx 3.3$  Pa) liquid phase. In contrast to the behavior in water where a factor between the shear stress value at the highest and lowest gas flow rate was 5 fold, the relative difference in the Xanthan solution is less pronounced with a factor of up to 1.5. For these results, no cross-links to the previously discussed single bubble experiments can be drawn as the single bubble EDM measurement were only performed in aqueous salt solution and the single bubble PIV measurements were carried out in Xanthan solution without ions. Still, the result found in **Section 5.1.2**, i.e., that the shear stress occurring in water is twice that in Xanthan solution works here as well for the wall shear stress in the 7 mm channel.

In the literature, the only system that is roughly comparable to the one studied here was investigated by Nagaoka et al. [75]. They investigated Newtonian liquids with viscosities up to 15 times higher than that of water. In the shear rate range found in this investigation, the Xanthan solution with ions has viscosities 5 to 10 times higher in comparison to water. The highest average wall shear stress values Nagaoka et al. found were approximately 2 Pa in their 32 mm channel. The value, which was determined at a superficial gas velocity comparable to the lowest

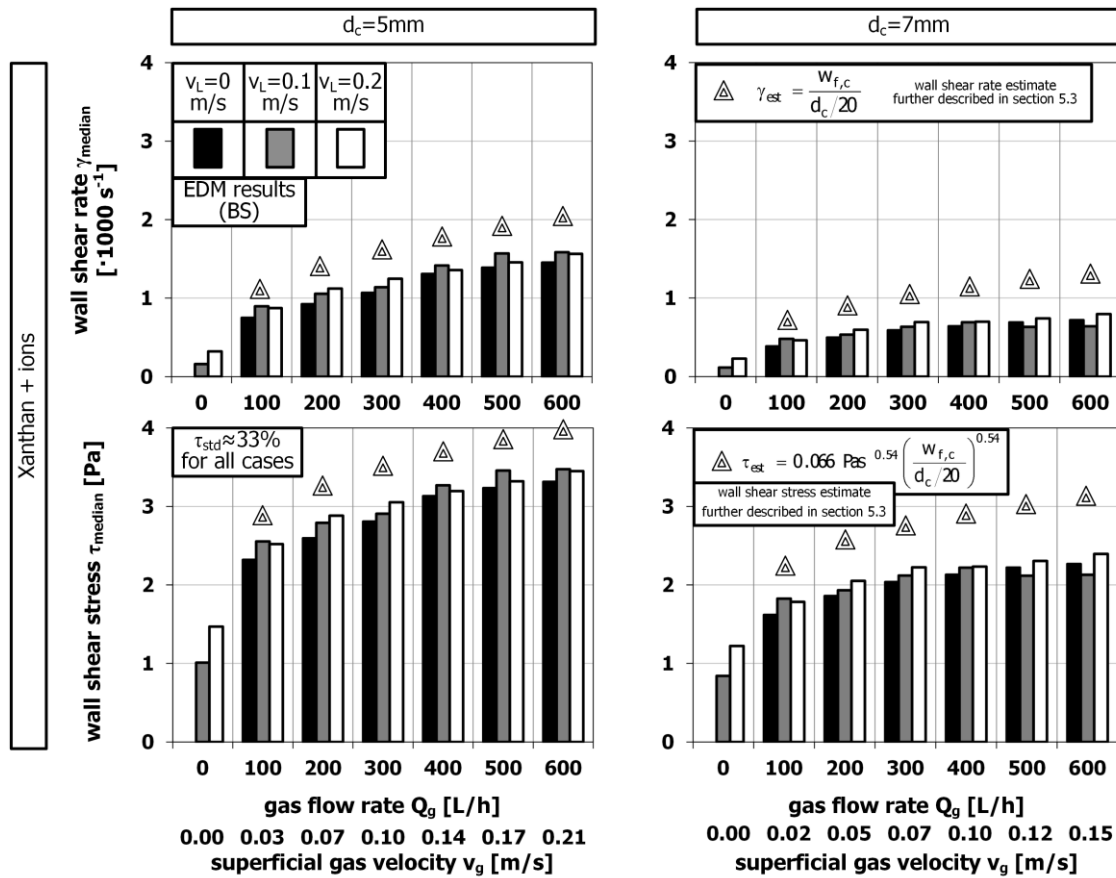


Figure 5.23: Median of the shear rates and shear stresses found in Xanthan solution+EDM salts for the two different channel depths  $d_c$  (based on [8]) and a wall shear rate and stress estimate further described in Section 5.3 (triangles)

investigated gas velocities in this investigation, is in the same range as the values found here for the narrower channels, with 2.5 Pa in the 5 mm channel and 1.8 Pa in the 7 mm channel.

Like found for the Newtonian continuous phase, in the non-Newtonian liquid the expected dependencies of the wall shear stress on the varied parameters were found as well ( $d_c \downarrow, v_g \uparrow, v_L \uparrow \Rightarrow \tau_{median} \uparrow$ ). In comparison to the tests in water, the wall shear rates  $\dot{\gamma}_{median}$  were lower (especially for the 5 mm channel). Still, due to the non-Newtonian rheological characteristics, the wall shear stresses  $\tau_{median}$  were mostly higher (especially for the 7 mm channel) with a value range of approx.  $1.0 \text{ Pa} < \tau_{median} < 3.4 \text{ Pa}$ . As already mentioned for the single bubble investigations, again, roughly a factor of two between the values determined in water and Xanthan solution (for the 7 mm channel) was found.

For the experimental results, a mathematical model was developed relating all varied parameters. The dimensionless average wall shear stress

$$\tau^* = \frac{\tau_{median}}{(\rho_L - \rho_B)gd_B} \quad (5.27)$$

which is related to the driving buoyancy force is described with help of the Reynolds number

$$Re_{nN} = \frac{(v_g + v_L)^{2-n} d_h^n \rho_L}{K} \quad (5.28)$$

developed for this application, and the confinement factor taking the bubble size into account as already used for the description of the gas hold-up in **Section 5.2.1**. Taking all results (except of the results in water in the 5 mm channel) into account (for  $v_g > 0 \text{ m/s}$ ), the correlation

$$\tau^* = 0.0037 Re_{nN}^{0.133} \left( \frac{d_B}{d_h} \right)^{1.1} \quad (5.29)$$

was found ( $R^2 = 0.90$ ). The regression was performed with the same estimated bubble sizes as used for the gas hold-up regression.

The fluctuations of the wall shear stress were determined as well. In their water based system, Yamanoi and Kageyama [55] found that the average wall shear stress values and the respective standard deviations were equal.

**Figure 5.24a** shows the standard deviation of the wall shear stress against the average value as found in this

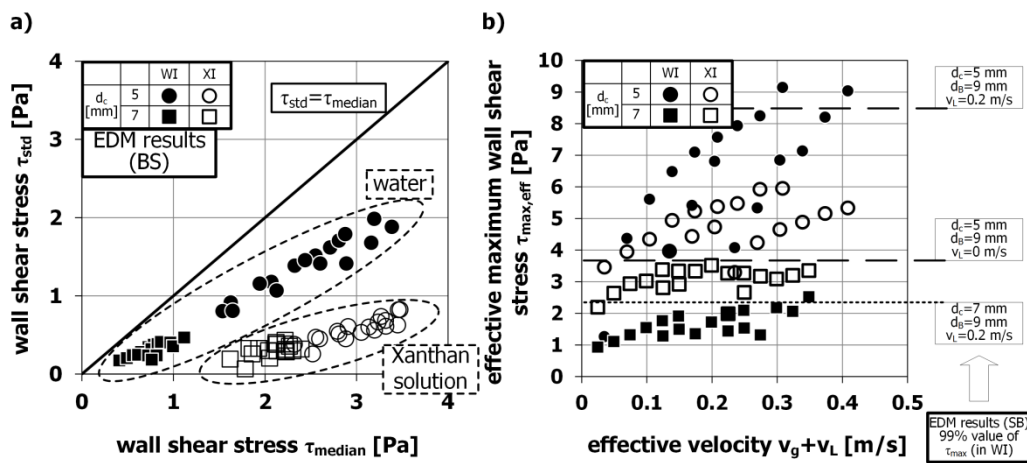


**Figure 5.24:** (a) Standard deviation (fluctuations) against the median of the wall shear stress and (b) effective maximum wall shear stress against effective velocity in comparison to maximum wall shear stress values found for single bubbles (WI: water+EDM salts, XI: Xanthan solution+EDM salts) (data based on [3, 8])

investigation for the Newtonian and non-Newtonian continuous liquid phase and with the bisecting line representing Yamanoi and Kageyama's result. It is obvious that for both cases the slope is lower in comparison to the mentioned case from literature with a slope of approximately 0.66 for aqueous salt solution and 0.33 for Xanthan solution with ions. The dampened fluctuations in water in comparison to Yamanoi and Kageyama might be attributed to the different measurement techniques. They used a shear stress scale which was able to determine the direction of the flow as well. Hence, they recorded positive and negative shear stress values. Here, only the magnitude of the shear stress could be determined which might have led to a lowered standard deviation value in comparison to their results. For the non-Newtonian liquid, the dampening effect was even enhanced which can be explained by the higher viscosity level. Still, Yamanoi and Kageyama's statement of increasing wall shear stress fluctuations with increasing average values applies here, too. Based on the average wall shear stress and the respective standard deviation, Nagaoka et al. [75] defined an effective maximum wall shear stress

$$\tau_{max,eff} = \tau_{median} + 3 \cdot \tau_{std} \quad (5.30)$$

which is equal to the probability of occurrence value of 99.7 % in the CDF. **Figure 5.24b** shows the effective maximum wall shear stress  $\tau_{max,eff}$  against the effective velocity ( $v_g + v_L$ ). For their highest superficial gas velocity (which was below the lowest gas velocity in this study), they found values for the effective maximum wall shear stress of up to 1.5 Pa in water and 8 Pa in the high viscosity Newtonian system. In this study, depending on the channel depth and liquid phase, different values were found. For the non-Newtonian liquid phase, in the 5 mm channel effective wall shear stress values up to 6.0 Pa and in the 7 mm channel up to 3.5 Pa were found. In the Newtonian liquid phase, in the 5 mm channel effective wall shear stress values up to 9.1 Pa and in the 7 mm channel up to 2.6 Pa were found. Like done for the average wall shear stress which was compared to the 99 % value of the global wall shear stress level determined for the single 9 mm bubble, here, the 99 % value of the maximum wall shear stress determined for the single 9 mm bubble is used for comparison with the results from the bubble swarm. Again, for both channel depths tested with the aqueous salt solution as the continuous phase, the results from the single bubble tests are in good agreement with the bubble swarm results.

Regarding the fluctuations of the wall shear stress, these increase with the average value. The increase is more enhanced in aqueous salt solution in comparison to Xanthan solution with ions due to the generally higher viscosity level of the non-Newtonian liquid. This is also due to differing flow behavior in the non-Newtonian system as described for the single bubble ascent. Consequently, the effective maximum wall shear stress ( $\tau_{median} + 3 \cdot \tau_{std}$ ) increased with the effective velocity ( $v_g + v_L$ ) as well, and the highest values were found in the 5 mm channel. The results are also comparable to global wall shear stress level values found in the single bubble experiments.

### 5.2.3 Conclusions from the bubble swarm experiments

In this section, the general flow behavior of a bubble swarm rising in a narrow rectangular channel was discussed including the gas hold-up and the wall shear stress generated by the liquid. In **Table 5.6**, the qualitative dependencies of the determined quantities on the varied parameters are collected.

As generally expected, a significant influence of the type of continuous phase was found on both quantities, the gas hold-up and the wall shear stress. This again underlines the contradiction to the statement by Ozaki and Yamamoto [46] that results found in water are transferable to real MBR systems. For both systems, besides the

**Table 5.6: Qualitative dependencies found in the bubble swarm behavior and wall shear stress experiments (W: water w/ and w/o EDM salts; X: Xanthan solution w/ and w/o EDM salts, ↑: increasing value, ↓: decreasing value, const.: constant value/no clear trend)**

			gas hold-up	wall shear stress
			$\varepsilon_g$	$\tau_{median/std}$
channel depth	↑	W	const.	↓
		X	const.	↓
superficial gas velocity	↑	W	↑	↑
		X	↑	↑
liquid velocity	↑	W	↓	↑
		X	↓	const.

continuous phase, the superficial gas velocity and the channel depth had the most significant influence.

In case of the gas hold-up experiments, the addition of ions with the purpose of a coalescence hindering led to an increase of the gas hold-up due to the reduction of the bubble size. In case of Xanthan solution, the observations (and the rheological measurements) indicate that this was less an effect of coalescence hindrance but rather of the enhanced dynamics. This more dynamic system was due to a viscosity lowering effect of the ions on the Xanthan solution as described in **Section 4.2**.

The wall shear stress results integrate fairly well into the context of the available literature regarding the average value, the standard deviation and the resulting effective maximum wall shear stress. Additionally, cross-links to the single bubble results could be drawn as well. The global wall shear stress level of the largest investigated single bubble was comparable to the average wall shear stress results found for the bubble swarm. The same is valid for the comparison of the maximum wall shear stress value of the single bubble and the effective maximum wall shear stress found for the bubble swarm.

For both properties, the gas hold-up and the wall shear stress, a significant influence of the channel depth, superficial gas velocity and the type of continuous phase was found. For the gas hold-ups, the highest value of 0.57 was found for an aqueous salt solution. In most other cases the values were between 0.2 and 0.4. The highest effective maximum wall shear stress was found for an aqueous salt solution with  $\tau_{median} + 3 \cdot \tau_{std} = 9.1$  Pa (due to an enhanced fluctuation in comparison to the results in Xanthan solution with ions) and for Xanthan solution with ions with  $\tau_{median} + 3 \cdot \tau_{std} = 6.0$  Pa, both in the 5 mm channel.

### 5.3 Engineering recommendations

In this section, the results found in this study are related to the application of interest, a flat sheet MBR operated as an air-lift loop reactor.

First of all, a short-cut method is suggested to calculate the average wall shear stress occurring in a flat sheet system. For bubble columns, Zehner [161] derived an equation for the liquid circulation velocity  $w_{f,c}$

$$w_{f,c} = \sqrt[3]{\frac{1}{2.5} \frac{\Delta \rho}{\rho_L} g D v_g} \quad (5.31)$$

which is the main flow velocity in a (cylindrical) bubble column with circulation cells. In **eq.(5.31)**,  $D$  is the column diameter following the idea that the height of the circulation cells is in the range of the column diameter. In case of the rectangular cross section column in this investigation, as discussed in **Section 5.2.1**, qualitative observations showed that the circulation cell height is in the range of the width of the channel (here  $d_w = 0.16$  m).

Therefore, in this case, the liquid circulation velocity is calculated with the width of the channel, i.e., the bubble column diameter  $D$  is replaced by  $d_w$  in **eq.(5.31)**. To calculate a representative shear rate for such a system, a characteristic length is needed as well. For this characteristic length, the film thickness between the bubbles and the wall is suggested here. For Taylor bubbles rising in a circular duct, Llewellyn et al. [167] found an equation for the film thickness  $\lambda$

$$\lambda = \frac{\sqrt{1+N}d_c-1}{N} \text{ with } N = \left( \frac{16}{9Fr_B} \frac{\rho_L^2 g}{\mu_L^2} \right)^{1/3} \text{ and } Fr_B = \frac{w_{B,rel}}{\sqrt{2gd_B}} \quad (5.32)$$

depending on several bubble and liquid properties. A film thickness roughly in the range of  $\lambda_{est} = d_c/20$  can be derived from this equation. Therefore, the estimated shear rate  $\gamma_{est}$  can be calculated by the following equation

$$\gamma_{est} = \frac{w_{f,c}}{\lambda_{est}} = \frac{\sqrt[3]{\frac{1}{2.5} \frac{\Delta \rho}{\rho_L} g d_w v_g}}{d_c/20} \quad (5.33)$$

which actually does not take a superimposed liquid velocity into account. Still, as this is only an estimate and as the differences between the results for different superimposed liquid velocities were not too strongly pronounced, this equation can still be used. The respective shear stress  $\tau_{est}$  is calculated as

$$\tau_{est} = K\gamma_{est}^n \quad (5.34)$$

**Figure 5.22** (for water with ions) and **Figure 5.23** (for Xanthan solution with ions) show the experimentally determined wall shear stresses (as already discussed in **Section 5.2.2**) together with estimated shear rates and shear stresses calculated from **eq.(5.33)** and **(5.34)**. In all cases, the estimations give a good idea about the occurring shear stresses, with an underestimation of the values for the 5 mm channel in water by a factor of 0.66 and an overestimation in all other cases (including the cases with Xanthan solution as the continuous phase) by a factor 1.3 to 1.5. In spite of the fact that the values do not perfectly fit the experimental data, this simple calculation can still be used to get an idea about the wall shear stress occurring in such aerated systems.

As the second deduction, especially with respect to the economical aspect of the aeration cost, **Figure 5.25**

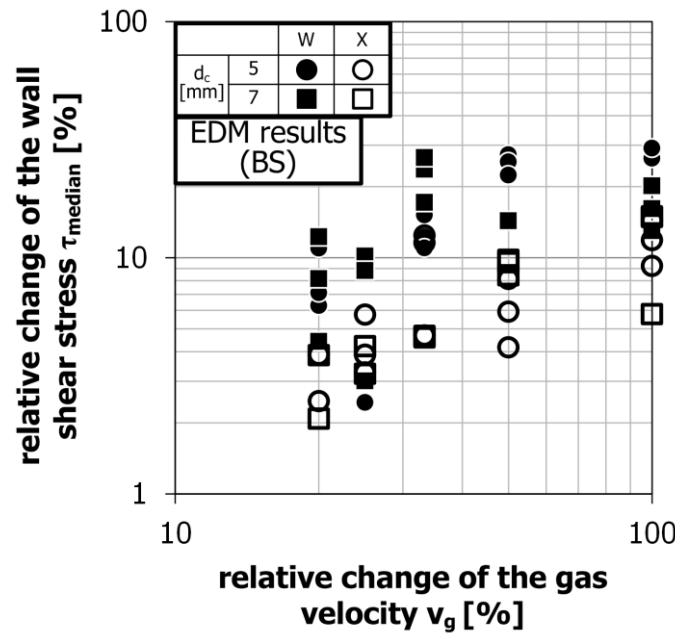


**Figure 5.25:** Relative change of the wall shear stress against the relative change of the gas velocity (data based on [8])

illustrates the relative change of the occurring average wall shear stress against the respective relative change of the gas velocity. To explain this plot, as an example, a calculation can be done: increasing the gas velocity in a 7 mm channel from  $v_g = 0.025$  m/s to  $v_g = 0.05$  m/s (relative change of 100 %) leads to a change of the median wall shear stress from  $\tau_{median} = 0.41$  Pa to  $\tau_{median} = 0.49$  Pa (relative change of 20 %). Roughly, it can be seen that a relative increase of the gas velocity leads to a lower relative increase of the average wall shear stress with a factor 0.3 for water and 0.15 for Xanthan solution. In numbers, this means, e.g., that a relative increase of the gas velocity by 100 % leads to an average wall shear stress increase of 30 % in water and 15 % in Xanthan solution. As the Xanthan solution behavior is closer to that of real activated sludge, this rather minor influence of a gas velocity change indicates that the construction aspect channel depth and the construction and operation aspect bubble size have a stronger influence on the cleaning potential of the system. This is an important information as the aeration costs are proportional to the compressor power input necessary for the aeration and, therefore, to the superficial gas velocity (operational cost  $\sim P = Q_g \Delta p = v_g A \Delta p \sim v_g$ ).

For the commercially available flat sheet membrane systems (data collected in Prieske et al. [17]), the respective average wall shear stress was calculated based on the developed wall shear stress correlation **eq.(5.29)**. **Figure 5.26** shows the shear stress results for the different systems (including the assumption of an intermediate superimposed liquid velocity of 0.1 m/s for all cases and a bubble size of 5 mm for the fine bubbling, 20 mm for the coarse bubbling and 10 mm where no information is given). The two systems with the highest shear stresses mainly show these results due to the coarse bubbling. This statement is underlined by **Figure 5.27** which shows the sensitivity of the average wall shear stress on the bubble size, the sum of the gas and liquid velocity, the flow consistency index and the hydraulic diameter (based on **eq.(5.27)** to **(5.29)**; calculated with  $n=0.54$ ). In the range of the varied parameters, the bubble size and the hydraulic diameter have the most significant influence.

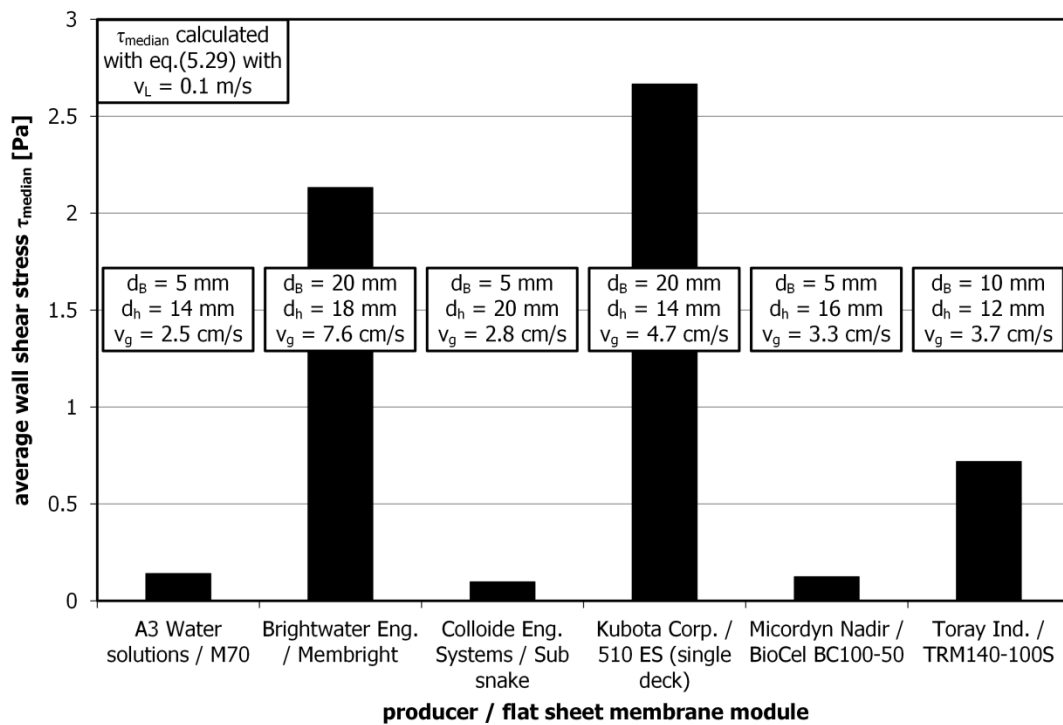


**Figure 5.26: Average wall shear stress (in an activated sludge with an MLSS concentration of 6.4 g/L equivalent to the system Xanthan solution+ions) for different commercially available flat sheet membrane modules calculated with the shear stress correlation found in this study (eq.(5.29))**

Although the gas velocity is the only property of the aforementioned ones that can be controlled during the operation of the flat sheet membrane module, this result rather suggests focusing beforehand on the constructional aspects. This includes not only the module itself but also the air sparger type as it, i.a., controls the appearing bubble sizes. Besides the resulting hypothesis that increasing gas flow rates (directly related to the operational cost) do not significantly affect the appearing shear stresses, the suggested larger bubble sizes potentially lead to lower operational cost as well. Larger bubbles lead overall to a lower surface area which is equivalent to lowered need of energy in comparison to the case with small bubbles and therefore a larger surface area.

Finally, following Drews et al.'s [33] approach of the calculation of a critical particle diameter (introduced in **Section 2**) above which the respective particles are detached from the membrane surface due to the occurring wall shear stress, **Figure 5.28** was assembled. Whenever the drag force  $F_{drag}$

$$F_{drag} = 3\pi\mu_L d_p J \quad (2.1)$$

which occurs due to a flux  $J$  normal to the membrane surface is lower than the lift force  $F_{lift}$

$$F_{lift} = 0.761 \frac{\tau^{1.5} d_p^3 \rho^{0.5}}{\mu} \quad (2.2)$$

the particle with the respective diameter will be drawn into the bulk flow away from the deposition layer on the membrane. Several assumptions had to be made to determine the critical particle diameters:

- a critical flux  $J_{crit}$  of 8 L/(m<sup>2</sup>h) which was mentioned in the tests reported by Drews et al. [33]
  - although not consistently determined in published work, the critical flux is generally regarded as the flux, from which on a further increase leads to an enhanced fouling tendency [19]
- a superficial liquid velocity of 0.2 m/s (which is equal to the highest velocity used in this study)
- in case of Xanthan solution, an intermediate viscosity at an respective intermediate shear rate of 1000 s<sup>-1</sup> calculated as  $\mu_{X,ave} = 0.065 \cdot (1000)^{-0.46}$  Pas = 0.0027 Pas
- an effective maximum wall shear stress value as determined in this study (see **Figure 5.24b**)

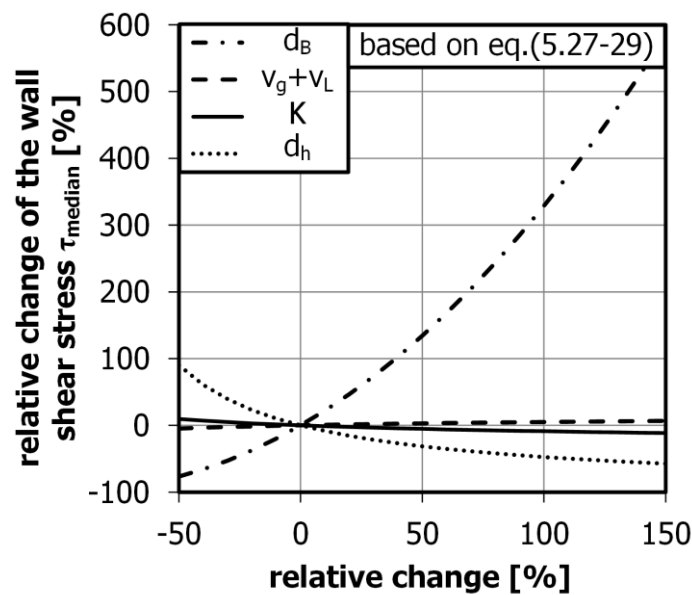


**Figure 5.27:** Sensitivity of the average shear stress on the bubble size, the sum of gas and liquid velocity, the flow consistency index and the hydraulic diameter (based of eq.(5.27) to (5.29))



The factor between the critical diameter found for water and Xanthan solution can be up to seven. In water, much smaller particles ( $d_p = 0.15 \mu\text{m}$  in the 5 mm channel,  $d_p = 0.45 \mu\text{m}$  in the 7 mm channel) can be detached in comparison to the higher viscosity non-Newtonian system ( $d_p = 0.65 \mu\text{m}$  in the 5 mm channel,  $d_p = 1.0 \mu\text{m}$  in the 7 mm channel). On the one hand side, in water a higher effective maximum wall shear stress was found, and on the other hand, in Xanthan solution the drag force is also higher in comparison to that in water due to the higher viscosity.

As described by Drews [19], a detachment of all particles above a fairly low particle diameter does not necessarily lead to a more economical performance in the long run. A deposition layer consisting of very small particles leads to a higher resistance in comparison to a deposition layer consisting of larger particles.

In this section, a short-cut method was suggested to calculate the average wall shear stress occurring in a narrow aerated system with a rectangular cross section. The comparison with the empirically determined wall shear stresses proved its applicability. Theoretically, a critical particle diameter that would be detached by the wall shear stress was evaluated. An estimation of the quality of commercial systems with respect to their cleaning potential was discussed as well. It was shown that especially in non-Newtonian systems, the effect of a stronger aeration does not reflect in same manner in the occurring wall shear stress. This leads to the suggestion to rather use a smaller channel depth or increase the occurring bubble size (at the same gas flow rate; construction aspects) than increase the gas flow which leads to high operation costs.

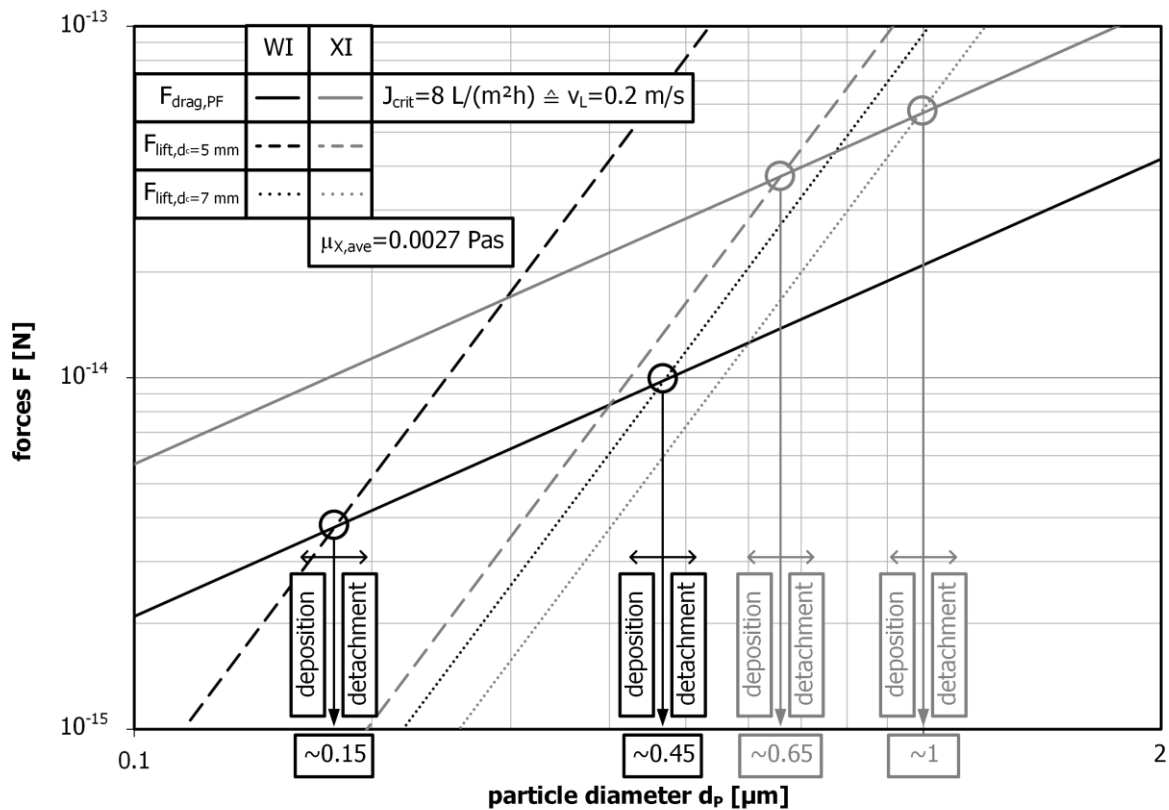


Figure 5.28: Forces acting on a particle (calculated with the effective maximum wall shear stress) against the particle diameter (data based on [8] and [33])

## 6 Summary

### 6.1 Conclusions

This study of the fluid dynamics in a gas-liquid-system inspired by a flat sheet membrane bioreactor was motivated by the fact that aeration is one of the main operation cost factors in such systems. This makes MBRs economically not competitive to conventional waste water treatment. One of the main purposes of the aeration is the cleaning of the membrane surfaces. The cleaning is due to the liquid flows generated by the bubble movement. These liquid flows between the membrane plates result in shear forces acting on the deposition layers, lifting particles back into the bulk flow and/or detaching biofilms from the membrane surface. Commercially available flat sheet membrane systems differ, i.e., in the spacing between the flat sheet membranes (in this study called channel depth), the recommended aeration intensity and the bubble size. This shows that - besides the commonly acknowledged positive effect of aeration on the operation of such systems - no commonly agreed understanding of the cleaning process is present in this field.

In this thesis, the chosen approach was to start with a fundamental investigation of a single bubble rising in a narrow channel with a rectangular cross section which represents the geometry between two flat sheet membrane plates in a flat sheet membrane module. This single bubble ascent in such a confining geometry, not yet sufficiently discussed in literature, was investigated for approximately 88 parameter combinations with varied channel depth, bubble size, superimposed liquid velocity and type of continuous phase with three different measurement techniques. In literature, channel depths in a range close to the bubble size and with co-current liquid velocities as influencing factors are rarely investigated. Regarding the continuous phase, a literature statement that results from fluid dynamic investigations performed in water are transferrable to real waste water systems was to be scrutinized. This added up to an experimental investigation of a total of approximately 45,000 single bubble ascents. Such a high number of runs was possible due to a fully automated experimental set-up allowing a sufficient statistical analysis of the data. The applied measurement techniques were high speed camera imaging (HSC) for the investigation of the bubble behavior, particle image velocimetry (PIV) for the investigation of the liquid flow surrounding the rising bubble and the electrodiffusion method (EDM) for the determination of the wall shear stress generated by the bubble induced liquid flows.

In comparison to the behavior of freely rising bubbles often discussed in literature, it was found that the behavior in the system investigated here can still be described by similar correlations. This was possible in spite of the confining geometry, superimposed liquid velocities and non-Newtonian liquid phases. Especially in case of the dimensionless correlations, the complex interaction between the bubble deformation, the bubble oscillation and the respective rise velocity leads to comparable trends. The channel depth and superimposed liquid velocity show a complex interaction (e.g., in water at  $v_L = 0$  m/s:  $d_c \uparrow \Rightarrow w_{B,rel} \uparrow$ , at  $v_L = 0.2$  m/s:  $d_c \uparrow \Rightarrow w_{B,rel} \downarrow$ ). This can potentially be attributed to a changed rising behavior as indicated by the determined oscillation parameters frequency and amplitude. The bubble-surrounding liquid velocities, determined in the PIV experiments, show that not only due to the bubble size itself but also due to their rising and deformation behavior, a much larger bubble-surrounding liquid volume is affected by larger bubbles in comparison to smaller bubbles.

Remembering the purpose of the bubble to clean membranes covered with deposition layers, this simply means that larger bubbles have the potential to clean a larger membrane surface area.

In spite of differing flow patterns around the bubble in water and Xanthan solution, the occurring shear rates in the liquid surrounding the bubble were still in the same value range. The shear rates in the Xanthan solution were about twice as high in comparison to values in water. Due to the difference of the rheology, the occurring shear stresses are off by an order of magnitude and more.

In the EDM experiments, it was found that with increasing bubble size and decreasing channel depth, the global wall shear stress level increases and the fluctuations are promoted. Generally, the rising bubble increases the shear stress values significantly in comparison to the single-phase flow but the median value is not affected. The highest maximum wall shear stress values found for the single bubbles are in parts higher by an order of magnitude in comparison to the global wall shear stress level.

Of all the varied parameters, the bubble size was found to have the strongest impact on the single bubble ascent. Most other parameters did not affect the quantities as much as expected, e.g., by the confining geometry and, especially, the rheology of the continuous phase. This includes the shear rate results in the liquid surrounding the single bubble. Still, the viscosity of the non-Newtonian liquid phase influenced the rising behavior from a qualitative point of view and led to shear stresses which were significantly higher in comparison to the ones found in water.

After the fundamental investigation of the single bubble ascent in the confining geometry, the bubble swarm behavior was investigated in the same geometry. Here again, high speed camera imaging (HSC) to investigate the bubble swarm behavior and the electrodiffusion method (EDM) to determine the wall shear stress generated by the bubble induced liquid flows were applied. Although bubble swarms are a common topic in engineering literature, this particular geometry is rather uncommon and respective correlations are rare. So the results found in this investigation are put into perspective of existing (cylindrical) bubble column literature and new correlations are given where applicable. Qualitatively, it was found that the influence of the continuous phase is strongly pronounced with larger bubbles occurring in the higher viscous liquid and smaller bubbles occurring in the cases doped with ions (for coalescence hindrance). Additionally, the bubble ascent in the bubble swarm is strongly affected by the superimposed liquid velocity reducing the tendency for circulation cells to occur.

Generally, the gas hold-up behavior was in accordance with bubble column literature. Still, viscosity and channel depth show a complex interaction on the gas hold-up behavior (an increase of either leads to higher gas hold-up values). In Xanthan solution, the channel depth affects the viscosity due to the occurring shear rates, and both parameters combined affect the bubble size and the bubble ascent. A correlation for the gas hold-up which is an extension of an existing model was derived that incorporates all varied parameters.

The dependencies of average wall shear stresses generated by the bubble swarm on the varied parameters were found as expected and the value range was in accordance with average wall shear stresses reported in literature. The significant difference between the two tested channel depths is noticeable, with average wall shear stress values in the narrower channel being higher three times (for aqueous salt solution). In comparison to the tests in water, in Xanthan solution with ions the wall shear rates were lower (especially for the 5 mm channel). On the other hand, the wall shear stresses were higher (especially for the 7 mm channel), again twice as high in Xanthan solution (for the 7 mm channel). The fluctuations of the wall shear stress increased along with the average value. This increase is more pronounced in the aqueous salt solution in comparison to Xanthan solution with ions. This

is due to the generally higher viscosity level. Consequently, the effective maximum wall shear stress increased with the effective velocity as well.

For both, the gas hold-up and the wall shear stress, a significant influence of the superficial gas velocity, the type of continuous phase and - in contrast to the single bubble experiments - also of the channel depth was found. The highest effective maximum wall shear stress was 9.1 Pa for aqueous salt solution (due to an enhanced fluctuation in comparison to the results in Xanthan solution with ions) and 6.0 Pa for Xanthan solution with ions, both in the 5 mm channel. These values can be fairly well related to the maximum wall shear stress results from the single bubble tests with comparable bubble sizes.

Based on the achieved knowledge, engineering recommendations were given regarding the cleaning potential. A short-cut method was suggested to calculate the average wall shear stress occurring in a narrow aerated system with a rectangular cross section. The comparison with the empirically determined wall shear stresses proved its applicability. An estimation of the quality of commercial systems with respect to their cleaning potential was done and it was shown that especially in non-Newtonian systems, the effect of a stronger aeration does not reflect in same manner in the occurring wall shear stress. This leads to the suggestion to rather use a smaller channel depth or increase the bubble size (construction aspects) than to increase the gas flow which leads to high operation costs.

## 6.2 Outlook

Regarding the single bubble experiments, it would be interesting to investigate the rise of a single bubble in a Newtonian liquid phase where the resulting bubble Reynolds number is in the same range as the bubble Reynolds number found for the ascent in the non-Newtonian liquid phase. Thus, it would be possible to determine specifically, on a quantitative base, the influence of the non-Newtonian characteristics in comparison to the Newtonian case at the same Reynolds number.

To get an even broader understanding of the respective influences, the experimental matrix of the varied parameters and their ranges could be expanded. This applies specifically for the bubble sizes where - with respect to the bubble swarm - larger bubble sizes could be investigated.

Regarding the measurement techniques, a parallel measurement with all three applied measurement techniques (like it was done, e.g., by Jankhah and Bérubé in a comparable system [64]) could give additional information about the bubble behavior. With such a setup, e.g., the maximum occurring shear stress value could be associated with the position of the bubble relative to the EDM sensor, the respective oscillation phase and the liquid flow generated at this exact moment. Regarding the HSC and PIV measurements, an investigation with multiple cameras would give an even more precise picture of the process of the bubble ascent, allowing a 3D-reconstruction of the bubble shape and a determination of the 3D-flow field around the bubble. For the PIV measurements in particular, a 3D-time-resolved measurement of the near wall flow field would be of interest as it could be used to quantify the wall shear rate that could be compared to the EDM results. Additionally, such an investigation could be used to determine the liquid film thickness between the bubble and the wall, to adjust the correlation presented in **Section 5.3** (for Taylor bubbles in circular ducts) to this case. Having mentioned all of this, the necessary measurement technique for such an investigation would be very expensive and regarding the quantitative result, the benefit would probably not be justified by the investment.

In case of the EDM measurements, besides the potential control measurement with PIV, a shear stress scale could be used like done by a few other groups in this field (e.g., [55, 75]). For a better understanding of the near wall flows, a three segmented EDM sensor could be used for the measurements (as suggested, e.g., by [168]) which allows the determination of the wall shear stress and the liquid flow direction at the same time. This could be used to determine flow reversals in the liquid film between the bubble and the wall or in the wake of the bubble due to the occurring vortices in the Kármán vortex street.

Regarding the bubble swarm, the influence of the channel width should be tested as in a real system this dimension is larger. The flow channel was mainly constructed to ensure a negligible effect of the side walls on the bubble ascent in the single bubble experiments and to make it comparable to tests in a pseudo-2D-model of a flat sheet membrane module existing in the laboratory (used, e.g., in [17]).

In the existing flow channel, first of all lower gas flow rates ( $< 100$  L/h) could be tested. The gas flow rates applied in this study were based on  $SAD_m$  values found for commercial products. Recalculated to the superficial gas velocity, this led to fairly high values in comparison to superficial gas velocities occurring in real systems (although it is not exactly known which cross section area the gas flow rate was related to in [17]).

Regarding recent developments in the field, the influence of differently designed spacers (as suggested, e.g., by [24]), intermittent and alternating aeration (as, e.g., done by Jankhah and Bérubé [64]) and the operation as a fluidized bed (see, e.g., [31]) could be evaluated.

Regarding the measurement techniques, first of all the gas hold-up measurements could be validated by parallel pressure difference measurements. As the bubble size was included in the correlations found for the bubble swarm quantities, either the measurements with the high speed camera should be more specifically designed for this purpose or another measurement technique should be applied (like, e.g., optical probes [169] although the strong deformation rather suggests adjusted imaging techniques [170]).

For the single bubble and bubble swarm experiments, a parallel filtration might be of interest as well since, e.g., Gaucher et al. [50] found higher shear stresses in case with filtration. In general, the addition of solid particles - either with the purpose of generating a fluidized bed as mentioned before or to have a suspension that could be filtered and, therefore, generate a deposition layer - can have an effect on the occurring bubbles as well, as described in **Section 4.2**, and therefore the general behavior of the system.

Finally, after the investigation of a single bubble in a single flow channel and a bubble swarm in the single flow channel, the EDM measurement technique could be applied in the pseudo-2D-model of a complete flat sheet membrane module mentioned above. This could be used to evaluate if in this system comparable shear stress values are found (which can be expected) and how the shear stress is distributed over the module taking a non-uniform aeration into account.

## 7 References

- [1] L. Böhm, A. Drews, H. Prieske, P. Bérubé and M. Kraume, The importance of fluid dynamics for MBR fouling mitigation, *Bioresour. Technol.* 122, 2012, 50-61. doi: 10.1016/j.biortech.2012.05.069.
- [2] L. Böhm and M. Kraume, Hydrodynamic investigation of single bubbles (presented at the 19th International Conference of Process Engineering and Chemical Plant Design, Krakow, Poland), *Czasopismo Techniczne Mechanika* 109, 5, 2012, 21-29.
- [3] L. Böhm, A. Drews and M. Kraume, Bubble induced shear stress in flat sheet membrane systems - Serial examination of single bubble experiments with the electrodiffusion method, *J. Membr. Sci.* 437, 2013, 131-140. doi: 10.1016/j.memsci.2013.02.036.
- [4] L. Böhm, H. Prieske and M. Kraume, Fluid dynamic optimization of flat sheet membrane modules - movement of bubbles in vertical channels (presented at the 11th International Conference on Chemical and Process Engineering, Milan, Italy), *Chem. Eng. Trans.* 32, 2013, 1501-1506. doi: 10.3303/CET1332251.
- [5] L. Böhm, S. Jankhah, J. Tihon, P. Bérubé and M. Kraume, Application of the electrodiffusion method to measure wall shear stress: Intergrating theory and practice, *Chem. Eng. Technol.* 37, 6, 2014, 938-950. doi: 10.1002/ceat.201400026.
- [6] L. Böhm, T. Kurita, K. Kimura and M. Kraume, Rising behaviour of single bubbles in narrow rectangular channels in Newtonian and non-Newtonian liquids, *Int. J. Multiphase Flow* 65, 2014, 11-23. doi: 10.1016/j.ijmultiphaseflow.2014.05.001.
- [7] L. Böhm and M. Kraume, Quantitative comparison of the single bubble ascent in a Newtonian and a non-Newtonian continuous phase: A phenomenological PIV study, *Exp. Fluids* submitted, 2014, .
- [8] L. Böhm and M. Kraume, Fluid dynamics of bubble swarms rising in Newtonian and non-Newtonian liquids in flat sheet membrane systems, *J. Membr. Sci.* 475, 2015, 533-544. doi: 10.1016/j.memsci.2014.11.003.
- [9] S. Cremante, *Leonardo da Vinci: The complete works*, David & Charles Limited, 2013.
- [10] R. Clift, J. Grace and M. Weber, *Bubbles, drops and particles*, Academic Press New York, 1978.
- [11] R. Chhabra, *Bubbles, drops, and particles in non-Newtonian fluids*, CRC Boca Raton, 2006.
- [12] S. G. Kandlikar, Controlling bubble motion over heated surface through evaporation momentum force to enhance pool boiling heat transfer, *Appl. Phys. Lett.* 102, 5, 2013, 051611. doi: <http://dx.doi.org/10.1063/1.4791682>.
- [13] S. S. Murshed, C. N. Castroke, M. Lourenço, M. Lopes and F. Santos, A review of boiling and convective heat transfer with nanofluids, *Renewable Sustainable Energy Rev.* 15, 5, 2011, 2342-2354. doi: <http://dx.doi.org/10.1016/j.rser.2011.02.016>.
- [14] J. Francois, N. Dietrich, P. Guiraud and A. Cockx, Direct measurement of mass transfer around a single bubble by micro-PLIFI, *Chem. Eng. Sci.* 66, 14, 2011, 3328-3338. doi: <http://dx.doi.org/10.1016/j.ces.2011.01.049>.
- [15] D. Colombet, D. Legendre, A. Cockx, P. Guiraud, F. Risso, C. Daniel and S. Galinat, Experimental study of mass transfer in a dense bubble swarm, *Chem. Eng. Sci.* 66, 14, 2011, 3432-3440. doi: <http://dx.doi.org/10.1016/j.ces.2011.01.020>.

- [16] S. Judd, *The MBR book: principles and applications of membrane bioreactors for water and wastewater treatment*, Butterworth-Heinemann, Oxford, 2010.
- [17] H. Prieske, L. Böhm, A. Drews and M. Kraume, Optimised hydrodynamics for membrane bioreactors with immersed flat sheet membrane modules (presented at the 5th IWA specialised membrane technology conference for water & wastewater treatment. Beijing, China), *Desalin. Water Treat.* 8, 1-3, 2010, 270-276. doi: 10.5004/dwt.2010.1784.
- [18] Z. Cui, S. Chang and A. Fane, The use of gas bubbling to enhance membrane processes, *J. Membr. Sci.* 221, 1-2, 2003, 1-35. doi: 10.1016/S0376-7388(03)00246-1.
- [19] A. Drews, Membrane fouling in membrane bioreactors—Characterisation, contradictions, cause and cures, *J. Membr. Sci.* 363, 1-2, 2010, 1 - 28. doi: DOI: 10.1016/j.memsci.2010.06.046.
- [20] P. Le-Clech, V. Chen and T. A. Fane, Fouling in membrane bioreactors used in wastewater treatment, *J. Membr. Sci.* 284, 1-2, 2006, 17 - 53. doi: 10.1016/j.memsci.2006.08.019.
- [21] Z. Wang, J. Ma, C. Y. Tang, K. Kimura, Q. Wang and X. Han, Membrane cleaning in membrane bioreactors: A review, *J. Membr. Sci.* 468, 2014, 276-307. doi: <http://dx.doi.org/10.1016/j.memsci.2014.05.060>.
- [22] Y. Wibisono, E. Cornelissen, A. Kemperman, W. Meervan der and K. Nijmeijer, Two-phase flow in membrane processes: A technology with a future, *J. Membr. Sci.* 453, 0, 2014, 566-602. doi: <http://dx.doi.org/10.1016/j.memsci.2013.10.072>.
- [23] M. Kraume and A. Drews, Membrane Bioreactors in Waste Water Treatment - Status and Trends, *Chem. Eng. Technol.* 33, 8, 2010, 1251-1259. doi: 10.1002/ceat.201000104.
- [24] N. V. Ndinisa, A. G. Fane and D. E. Wiley, Fouling Control in a Submerged Flat Sheet Membrane System: Part I - Bubbling and Hydrodynamic Effects, *Sep. Sci. Technol.* 41, 7, 2006, 1383-1409. doi: 10.1080/01496390600633873.
- [25] N. Ndinisa, A. Fane, D. Wiley and D. Fletcher, Fouling Control in a Submerged Flat Sheet Membrane System: Part II - Two Phase Flow Characterization and CFD Simulations, *Sep. Sci. Technol.* 41, 7, 2006, 1411-1445. doi: 10.1080/01496390600633915.
- [26] H.-Y. Yu, L.-Q. Liu, Z.-Q. Tang, M.-G. Yan, J.-S. Gu and X.-W. Wei, Mitigated membrane fouling in an SMBR by surface modification, *J. Membr. Sci.* 310, 1-2, 2008, 409-417. doi: <http://dx.doi.org/10.1016/j.memsci.2007.11.017>.
- [27] J. Wu, P. Le-Clech, R. M. Stuetz, A. G. Fane and V. Chen, Novel filtration mode for fouling limitation in membrane bioreactors, *Water Res.* 42, 14, 2008, 3677-3684. doi: <http://dx.doi.org/10.1016/j.watres.2008.06.004>.
- [28] I. Ivanovic and T. Leiknes, Impact of aeration rates on particle colloidal fraction in the biofilm membrane bioreactor (BF-MBR), *Desalination* 231, 1-3, 2008, 180-190. doi: <http://dx.doi.org/10.1016/j.desal.2007.11.046>.
- [29] J. Busch, A. Cruse and W. Marquardt, Modeling submerged hollow-fiber membrane filtration for wastewater treatment, *J. Membr. Sci.* 288, 1-2, 2007, 94 - 111. doi: DOI: 10.1016/j.memsci.2006.11.008.
- [30] V. Iversen, S. Hermann, A. Drews, J. Münz, G. G., E. Fatarella, B. Lesjean, L. Böhm and M. Kraume, Textiles for the filtration of activated sludge in membrane bioreactors MBRs (Presentation), *Proceedings of the Filtech 2009*, 2009.

- [31] H.-H. Ngo, W. Guo and W. Xing, Evaluation of a novel sponge-submerged membrane bioreactor (SSMBR) for sustainable water reclamation, *Bioresour. Technol.* 99, 7, 2008, 2429-2435. doi: <http://dx.doi.org/10.1016/j.biortech.2007.04.067>.
- [32] K.-M. Yeon, W.-S. Cheong, H.-S. Oh, W.-N. Lee, B.-K. Hwang, C.-H. Lee, H. Beyenal and Z. Lewandowski, Quorum Sensing: A New Biofouling Control Paradigm in a Membrane Bioreactor for Advanced Wastewater Treatment, *Environ. Sci. Technol.* 43, 2, 2009, 380-385. doi: 10.1021/es8019275.
- [33] A. Drews, H. Prieske, E.-L. Meyer, G. Senger and M. Kraume, Advantageous and detrimental effects of air sparging in membrane filtration: Bubble movement, exerted shear and particle classification, *Desalination* 250, 3, 2010, 1083 - 1086. doi: 10.1016/j.desal.2009.09.113.
- [34] G. Belfort, R. H. Davis and A. L. Zydney, The behavior of suspensions and macromolecular solutions in crossflow microfiltration, *J. Membr. Sci.* 96, 1-2, 1994, 1-58. doi: [http://dx.doi.org/10.1016/0376-7388\(94\)00119-7](http://dx.doi.org/10.1016/0376-7388(94)00119-7).
- [35] J.-C. Ochoa, C. Coufort, R. Escudié, A. Liné and E. Paul, Influence of non-uniform distribution of shear stress on aerobic biofilms, *Chem. Eng. Sci.* 62, 14, 2007, 3672 - 3684. doi: 10.1016/j.ces.2007.03.023.
- [36] A. Rochex, J.-J. Godon, N. Bernet and R. Escudié, Role of shear stress on composition, diversity and dynamics of biofilm bacterial communities, *Water Res.* 42, 20, 2008, 4915-4922. doi: <http://dx.doi.org/10.1016/j.watres.2008.09.015>.
- [37] E. Tardieu, A. Grasmick, V. Geaugey and J. Manem, Influence of hydrodynamics on fouling velocity in a recirculated MBR for wastewater treatment, *J. Membr. Sci.* 156, 1, 1999, 131-140. doi: [http://dx.doi.org/10.1016/S0376-7388\(98\)00343-3](http://dx.doi.org/10.1016/S0376-7388(98)00343-3).
- [38] B. Verrecht, S. Judd, G. Guglielmi, C. Brepols and J. Mulder, An aeration energy model for an immersed membrane bioreactor, *Water Res.* 42, 19, 2008, 4761 - 4770. doi: DOI: 10.1016/j.watres.2008.09.013.
- [39] C. Chan, P. Bérubé and E. Hall, Relationship between types of surface shear stress profiles and membrane fouling, *Water Res.* 45, 19, 2011, 6403 - 6416. doi: 10.1016/j.watres.2011.09.031.
- [40] H. E. Wray, R. C. Andrews and P. R. Bérubé, Surface shear stress and membrane fouling when considering natural water matrices, *Desalination* 330, 0, 2013, 22 - 27. doi: <http://dx.doi.org/10.1016/j.desal.2013.09.018>.
- [41] H. E. Wray, R. C. Andrews and P. R. Bérubé, Surface shear stress and retention of emerging contaminants during ultrafiltration for drinking water treatment, *Sep. Purif. Technol.* 122, 2014, 183 - 191. doi: <http://dx.doi.org/10.1016/j.seppur.2013.11.003>.
- [42] D. Ye, S. Saadat-Sanei and P. Bérubé, Pulse bubble sparging for the control of hydraulically reversible fouling in submerged hollow fiber membrane systems, *Sep. Purif. Technol.* 123, 0, 2014, 153 - 163. doi: <http://dx.doi.org/10.1016/j.seppur.2013.12.011>.
- [43] A. Bennett, Energy efficiency: Wastewater treatment and energy production, *Filtr. Sep.* 44, 10, 2007, 16-19. doi: [http://dx.doi.org/10.1016/S0015-1882\(07\)70319-1](http://dx.doi.org/10.1016/S0015-1882(07)70319-1).
- [44] J. Noble, GE ZeeWeed MBR technology for pharmaceutical wastewater treatment, *Membr. Technol.* 2006, 9, 2006, 7-9. doi: [http://dx.doi.org/10.1016/S0958-2118\(06\)70790-X](http://dx.doi.org/10.1016/S0958-2118(06)70790-X).
- [45] N. Ratkovich, W. Horn, F. Helmus, S. Rosenberger, W. Naessens, I. Nopens and T. Bentzen, Activated sludge rheology: A critical review on data collection and modelling, *Water Res.* 47, 2, 2012, 463-482. doi: 10.1016/j.watres.2012.11.021.



- [46] N. Ozaki and K. Yamamoto, Hydraulic effects on sludge accumulation on membrane surface in crossflow filtration, *Water Res.* 35, 13, 2001, 3137-3146. doi: 10.1016/S0043-1354(01)00046-X.
- [47] C. Gaucher, P. Jaouen, J. Comiti and P. Legentilhomme, Determination of cake thickness and porosity during cross-flow ultrafiltration on a plane ceramic membrane surface using an electrochemical method, *J. Membr. Sci.* 210, 2, 2002, 245 - 258. doi: 10.1016/S0376-7388(02)00355-1.
- [48] C. Gaucher, P. Legentilhomme, P. Jaouen, J. Comiti and J. Pruvost, Hydrodynamics study in a plane ultrafiltration module using an electrochemical method and particle image velocimetry visualization, *Exp. Fluids* 32, 2002, 283-293. doi: 10.1007/s003480100317.
- [49] C. Gaucher, P. Legentilhomme, P. Jaouen and J. Comiti, Influence of Fluid Distribution on the Wall Shear Stress in a Plane Ultrafiltration Module Using an Electrochemical Method, *Chem. Eng. Res. Des.* 80, 1, 2002, 111 - 120. doi: 10.1205/026387602753393286.
- [50] C. Gaucher, P. Jaouen, P. Legentilhomme and J. Comiti, Suction effect on the shear stress at a plane ultrafiltration ceramic membrane surface, *Sep. Sci. Technol.* 37, 10, 2002, 2251-2270. doi: 10.1081/SS-120003512.
- [51] C. Gaucher, P. Jaouen, P. Legentilhomme and J. Comiti, Influence of fluid distribution on the ultrafiltration performance of a ceramic flat sheet membrane, *Sep. Sci. Technol.* 38, 9, 2003, 1949-1962. doi: 10.1081/SS-120020128.
- [52] K. Essemiani, G. Ducom, C. Cabassud and A. Liné, Spherical cap bubbles in a flat sheet nanofiltration module: experiments and numerical simulation, *Chem. Eng. Sci.* 56, 21-22, 2001, 6321 - 6327. doi: DOI: 10.1016/S0009-2509(01)00282-2.
- [53] G. Ducom, F.-P. Puech and C. Cabassud, Air sparging with flat sheet nanofiltration: a link between wall shear stresses and flux enhancement, *Desalination* 145, 1-3, 2002, 97 - 102. doi: DOI: 10.1016/S0011-9164(02)00392-2.
- [54] G. Ducom, F.-P. Puech and C. Cabassud, Gas/Liquid Two-phase Flow in a Flat Sheet Filtration Module: Measurement of Local Wall Shear Stresses, *Can. J. Chem. Eng.* 81, 3-4, 2003, 771-775. doi: 10.1002/cjce.5450810358.
- [55] I. Yamanoi and K. Kageyama, Evaluation of bubble flow properties between flat sheet membranes in membrane bioreactor, *J. Membr. Sci.* 360, 1-2, 2010, 102-108. doi: 10.1016/j.memsci.2010.05.006.
- [56] P. Bérubé, G. Afonso, F. Taghipour and C. Chan, Quantifying the shear at the surface of submerged hollow fiber membranes, *J. Membr. Sci.* 279, 1-2, 2006, 495 - 505. doi: DOI: 10.1016/j.memsci.2005.12.043.
- [57] C. Chan, P. Bérubé and E. Hall, Shear profiles inside gas sparged submerged hollow fiber membrane modules, *J. Membr. Sci.* 297, 1-2, 2007, 104 - 120. doi: DOI: 10.1016/j.memsci.2007.03.032.
- [58] B. Fulton, J. Redwood, M. Tourais and P. Bérubé, Distribution of surface shear forces and bubble characteristics in full-scale gas sparged submerged hollow fiber membrane modules, *Desalination* 281, 2011, 128 - 141. doi: DOI: 10.1016/j.desal.2011.07.050.
- [59] B. Fulton and P. Bérubé, Optimizing the sparging condition and membrane module spacing for a ZW500 submerged hollow fiber membrane system, *Desalin. Water Treat.* 42, 1-3, 2012, 8-16. .
- [60] N. Ratkovich, C. C. V. Chan, P. R. Bérubé and I. Nopens, Analysis of shear stress and energy consumption in a tubular airlift membrane system, *Water Sci. Technol.* 64, 1, 2011, 189-198. doi: 10.2166/wst.2011.521.

- [61] N. Ratkovich, P. Bérubé and I. Nopens, Assessment of mass transfer coefficients in coalescing slug flow in vertical pipes and applications to tubular airlift membrane bioreactors, *Chem. Eng. Sci.* 66, 6, 2011, 1254-1268. doi: DOI: 10.1016/j.ces.2010.12.034.
- [62] N. Ratkovich, C. Chan, P. Bérubé and I. Nopens, Experimental study and CFD modelling of a two-phase slug flow for an airlift tubular membrane, *Chem. Eng. Sci.* 64, 16, 2009, 3576 - 3584. doi: DOI: 10.1016/j.ces.2009.04.048.
- [63] S. Jankhah and P. R. Bérubé, Pulse bubble sparging for fouling control, *Sep. Purif. Technol.* 134, 0, 2014, 58 - 65. doi: <http://dx.doi.org/10.1016/j.seppur.2014.07.023>.
- [64] S. Jankhah and P. R. Bérubé, Power induced by bubbles of different sizes and frequencies on to hollow fibers in submerged membrane systems, *Water Res.* 47, 17, 2013, 6516-6526. doi: <http://dx.doi.org/10.1016/j.watres.2013.08.020>.
- [65] K. Zhang, Z. Cui and R. Field, Effect of bubble size and frequency on mass transfer in flat sheet MBR, *J. Membr. Sci.* 332, 1-2, 2009, 30-37. doi: 10.1016/j.memsci.2009.01.033.
- [66] R. H. Davis and S. A. Birdsell, Hydrodynamic model and experiments for crossflow microfiltration, *Chem. Eng. Commun.* 49, 4-6, 1987, 217-234. doi: 10.1080/00986448708911804.
- [67] A. Khalili-Garakani, M. Mehrnia, N. Mostoufi and M. Sarrafzadeh, Flow Characteristics in an Airlift Membrane Bioreactor, *Proc. of Chemical Product and Process Modeling*, 2009.
- [68] A. Khalili-Garakani, M. R. Mehrnia, N. Mostoufi and M. H. Sarrafzadeh, Analyze and control fouling in an airlift membrane bioreactor: CFD simulation and experimental studies, *Process Biochem.* 46, 5, 2011, 1138-1145. doi: 10.1016/j.procbio.2011.01.036.
- [69] Q. Li, R. Ghosh, S. Bellara, Z. Cui and D. Pepper, Enhancement of ultrafiltration by gas sparging with flat sheet membrane modules, *Sep. Purif. Technol.* 14, 1-3, 1998, 79-83. doi: 10.1016/S1383-5866(98)00062-8.
- [70] J. Phattaranawik, A. G. Fane, A. C. S. Pasquier and W. Bing, Membrane bioreactor with bubble-size transformer: Design and fouling control, *AIChE J.* 53, 1, 2007, 243-248. doi: 10.1002/aic.11040.
- [71] H. Prieske, A. Drews and M. Kraume, Prediction of the circulation velocity in a membrane bioreactor, *Desalination* 231, 1-3, 2008, 219-226. doi: DOI: 10.1016/j.desal.2007.12.010.
- [72] N. Ratkovich, C. C. V. Chan, P. R. Bérubé and I. Nopens, Investigation of the effect of viscosity on slug flow in airlift tubular membranes in search of a sludge surrogate, *Water Sci. Technol.* 61, 7, 2010, 1801-1809. doi: 10.2166/wst.2010.118.
- [73] A. Drews, H. Prieske and M. Kraume, Optimierung der Blasen- und Zirkulationsströmung in Membranbelebungsreaktoren (in German), *Chem. Ing. Tech.* 80, 12, 2008, 1795–1801. doi: 10.1002/cite.200800149.
- [74] Y. Ye, V. Chen and P. Le-Clech, Evolution of fouling deposition and removal on hollow fibre membrane during filtration with periodical backwash, *Desalination* 283, 0, 2011, 198 - 205. doi: 10.1016/j.desal.2011.03.087.
- [75] H. Nagaoka, A. Tanaka and Y. Toriizuka, Measurement of effective shear stress working on flat-sheet membrane by air-scrabbling, *Water Sci. Technol. : Water Supply* 3, 5-6, 2003, 423-428. .
- [76] P. Le-Clech, Z. Cao, P. Wan, D. Wiley and A. Fane, The application of constant temperature anemometry to membrane processes, *J. Membr. Sci.* 284, 1-2, 2006, 416 - 423. doi: 10.1016/j.memsci.2006.08.015.

- [77] F. Wicaksana, A. G. Fane and A. W.-K. Law, The use of Constant Temperature Anemometry for permeate flow distribution measurement in a submerged hollow fibre system, *J. Membr. Sci.* 339, 1-2, 2009, 195 - 203. doi: DOI: 10.1016/j.memsci.2009.04.050.
- [78] L. Martinelli, C. Guigui and A. Line, Characterisation of hydrodynamics induced by air injection related to membrane fouling behaviour, *Desalination* 250, 2, 2010, 587-591. doi: 10.1016/j.desal.2009.09.029.
- [79] S. T. Wereley, A. Akonur and R. M. Lueptow, Particle-fluid velocities and fouling in rotating filtration of a suspension, *J. Membr. Sci.* 209, 2, 2002, 469-484. doi: 10.1016/S0376-7388(02)00365-4.
- [80] K. Y. Chung, W. A. Edelstein and G. Belfort, Dean vortices with wall flux in a curved channel membrane system.: 6. Two dimensional magnetic resonance imaging of the velocity field in a curved impermeable slit, *J. Membr. Sci.* 81, 1-2, 1993, 151 - 162. doi: 10.1016/0376-7388(93)85039-Y.
- [81] C. A. Heath, G. Belfort, B. E. Hammer, S. D. Mirer and J. M. Pimbley, Magnetic resonance imaging and modeling of flow in hollow-fiber bioreactors, *AIChE J.* 36, 4, 1990, 547-558. doi: 10.1002/aic.690360406.
- [82] B. J. Pangrle, E. G. Walsh, S. Moore and D. DiBiasio, Investigation of fluid flow patterns in a hollow fiber module using magnetic resonance velocity imaging, *Biotechnol. Tech.* 3, 1989, 67-72. .
- [83] B. Pangrle, E. Walsh, S. Moore and D. DiBiasio, Magnetic resonance imaging of laminar flow in porous tube and shell systems, *Chem. Eng. Sci.* 47, 3, 1992, 517-526. doi: 10.1016/0009-2509(92)80001-S.
- [84] C. K. Poh, P. A. Hardy, Z. Liao, Z. Huang, W. R. Clark and D. Gao, Effect of Flow Baffles on the Dialysate Flow Distribution of Hollow-Fiber Hemodialyzers: A Nonintrusive Experimental Study Using MRI, *J. Biomech. Eng.* 125, 4, 2003, 481-489. doi: 10.1115/1.1590355.
- [85] L. Nguyen, M. Schwarze, A. Drews, M. Kraume, R. Schomäcker and L. Böhm, Influence of Non-ionic Surfactants on Reverse Micellar-enhanced Ultrafiltration (presented at the Euromembrane 2012, London, Great Britain), *Procedia Eng.* 44, 0, 2012, 1692 - 1694. doi: <http://dx.doi.org/10.1016/j.proeng.2012.08.911>.
- [86] A. Sofia, W. J. Ng and S. L. Ong, Engineering design approaches for minimum fouling in submerged MBR, *Desalination* 160, 1, 2004, 67-74. doi: DOI: 10.1016/S0011-9164(04)90018-5.
- [87] D. Tacke, J. Pinnekamp, H. Prieske and M. Kraume, Membrane bioreactor aeration: investigation of the velocity flow pattern, *Water Sci. Technol.* 57, 4, 2008, 559-565. doi: 10.2166/wst.2008.123.
- [88] A. Acharya, R. Mashelkar and J. Ulbrecht, Mechanics of bubble motion and deformation in non-newtonian media, *Chem. Eng. Sci.* 32, 8, 1977, 863 - 872. doi: 10.1016/0009-2509(77)80072-9.
- [89] C. Clanet, P. Héraud and G. Searby, On the motion of bubbles in vertical tubes of arbitrary cross-sections: some complements to the Dumitrescu-Taylor problem, *J. Fluid Mech.* 519, 2004, 359-376. doi: 10.1017/S0022112004001296.
- [90] D. Dekée, P. Carreau and J. Mordarski, Bubble velocity and coalescence in viscoelastic liquids, *Chem. Eng. Sci.* 41, 9, 1986, 2273 - 2283. doi: 10.1016/0009-2509(86)85078-3.
- [91] K. Ellingsen and F. Risso, On the rise of an ellipsoidal bubble in water: oscillatory paths and liquid-induced velocity, *J. Fluid Mech.* 440, 2001, 235-268. doi: 10.1017/S0022112001004761.
- [92] B. Figueroa-Espinoza, R. Zenit and D. Legendre, The effect of confinement on the motion of a single clean bubble, *J. Fluid Mech.* 616, 2008, 419-443. doi: 10.1017/S0022112008004072.
- [93] C. Brücker, Structure and dynamics of the wake of bubbles and its relevance for bubble interaction, *Phys. Fluids* 11, 7, 1999, 1781-1796. doi: 10.1063/1.870043.

- [94] Z. Liu, Y. Zheng, L. Jia and Q. Zhang, Study of bubble induced flow structure using PIV, *Chem. Eng. Sci.* 60, 13, 2005, 3537-3552. doi: 10.1016/j.ces.2004.03.049.
- [95] C. Maneri and N. Zuber, An experimental study of plane bubbles rising at inclination, *Int. J. Multiphase Flow* 1, 5, 1974, 623 - 645. doi: 10.1016/0301-9322(74)90022-6.
- [96] T. Miyahara and S. Yamanaka, Mechanics of Motion and Deformation of a Single Bubble Rising through Quiescent Highly Viscous Newtonian and Non-Newtonian Media, *J. Chem. Eng. Jpn.* 26, 3, 1993, 297-302. doi: 10.1252/jcej.26.29.
- [97] A. Tokuhiro, M. Maekawa, K. Iizuka, K. Hishida and M. Maeda, Turbulent flow past a bubble and an ellipsoid using shadow-image and PIV techniques, *Int. J. Multiphase Flow* 24, 8, 1998, 1383-1406. doi: 10.1016/S0301-9322(98)00024-X.
- [98] A. Fujiwara, A. Tokuhiro and K. Hishida, Application of PIV/LIF and Shadow-Image to a Bubble Rising in a Linear Shear Flow Field, 10th Int Symp on Applications of Laser Techniques to Fluid Mechanics, 2000.
- [99] A. Fujiwara, Y. Danmoto and K. Hishida, Bubble Deformation and Surrounding Flow Structure Measured by PIV/LIF and Shadow Image Technique, *ASME Conference Proceedings*, 2003.
- [100] A. Fujiwara, Y. Danmoto, K. Hishida and M. Maeda, Bubble deformation and flow structure measured by double shadow images and PIV/LIF, *Exp. Fluids* 36, 1, 2004, 157-165. doi: 10.1007/s00348-003-0691-0.
- [101] D. Funfschilling and H. Li, Flow of non-Newtonian fluids around bubbles: PIV measurements and birefringence visualisation, *Chem. Eng. Sci.* 56, 3, 2001, 1137-1141. doi: 10.1016/S0009-2509(00)00332-8.
- [102] X. Frank, H. Z. Li, D. Funfschilling, F. Burdin and Y. Ma, Bubble Motion in Non-Newtonian Fluids and Suspensions, *Can. J. Chem. Eng.* 81, 3-4, 2003, 483-490. doi: 10.1002/cjce.5450810321.
- [103] D. Funfschilling and H. Li, Effects of the Injection Period on the Rise Velocity and Shape of a Bubble in a Non-Newtonian Fluid, *Chem. Eng. Res. Des.* 84, 10, 2006, 875-883. doi: 10.1205/cherd.01229.
- [104] H. Z. Li, X. Frank, D. Funfschilling and P. Diard, Bubbles' rising dynamics in polymeric solutions, *Phys. Lett. A* 325, 1, 2004, 43 - 50. doi: 10.1016/j.physleta.2004.03.023.
- [105] M. Roudet, V. Roig, A.-M. Billet and F. Risso, Paths and shapes of two-dimensional rising bubbles at high-Reynolds number, *Proceedings of the ICMF 2007, 6th International Conference on Multiphase Flow*, 2007.
- [106] T. Sanada, M. Shirota and M. Watanabe, Bubble wake visualization by using photochromic dye, *Chem. Eng. Sci.* 62, 24, 2007, 7264 - 7273. doi: 10.1016/j.ces.2007.08.037.
- [107] S. Takagi and Y. Matsumoto, Surfactant Effects on Bubble Motion and Bubbly Flows, *Annu. Rev. Fluid Mech.* 43, 1, 2011, 615-636. doi: 10.1146/annurev-fluid-122109-160756.
- [108] Y.-A. Hassan, J. Ortiz-Villafuerte and W.-D. Schmidl, Three-dimensional measurements of single bubble dynamics in a small diameter pipe using stereoscopic Particle Image Velocimetry, *Int. J. Multiphase Flow* 27, 5, 2001, 817-842. doi: 10.1016/S0301-9322(00)00054-9.
- [109] J. Ortiz-Villafuerte, W. D. Schmidl and Y. A. Hassan, Three-dimensional PTV study of the surrounding flow and wake of a bubble rising in a stagnant liquid, *Exp. Fluids* 29, 1, 2000, 202-210. doi: 10.1007/s003480070022.
- [110] K. Dewsbury, D. Karamanev and A. Margaritis, Hydrodynamic characteristics of free rise of light solid particles and gas bubbles in non-Newtonian liquids, *Chem. Eng. Sci.* 54, 21, 1999, 4825 - 4830. doi: 10.1016/S0009-2509(99)00200-6.

- [111] N. M. S. Hassan, M. M. K. Khan, M. G. Rasul and D. W. Rackemann, An Experimental Investigation of Bubble Rise Characteristics in a Crystal Suspended Non-Newtonian Fluid, AIP Conference Proceedings 1027, 1, 2008, 743-745. doi: 10.1063/1.2964831.
- [112] K. Sakakibara, M. Yamada, Y. Miyamoto and T. Saito, Measurement of the surrounding liquid motion of a single rising bubble using a Dual-Camera PIV system, Flow Meas. Instrum. 18, 5-6, 2007, 211 - 215. doi: 10.1016/j.flowmeasinst.2007.07.003.
- [113] T. Saito, K. Sakakibara, Y. Miyamoto and M. Yamada, A study of surfactant effects on the liquid-phase motion around a zigzagging-ascent bubble using a recursive cross-correlation PIV, Chem. Eng. J. 158, 1, 2010, 39-50. doi: 10.1016/j.cej.2008.07.021.
- [114] K. Yoshimoto and T. Saito, 3-dimensional liquid motion around a zigzagging ascent bubble measured using tomographic Stereo PIV, Proceedings of the 15th International Symposium on Applications of laser techniques to Fluid mechanics, 2010.
- [115] A. W. G. Vriesde, A. Biesheuvel and L. Wijngaarden van, Notes on the path and wake of a gas bubble rising in pure water, Int. J. Multiphase Flow 28, 11, 2002, 1823-1835. doi: 10.1016/S0301-9322(02)00036-8.
- [116] B. G. M. Wachem van and J. C. Schouten, Experimental validation of 3-D lagrangian VOF model: Bubble shape and rise velocity, AIChE J. 48, 12, 2002, 2744-2753. doi: 10.1002/aic.690481205.
- [117] A. Zaruba, D. Lucas, H.-M. Prasser and T. Höhne, Bubble-wall interactions in a vertical gas-liquid flow: Bouncing, sliding and bubble deformations, Chem. Eng. Sci. 62, 6, 2007, 1591 - 1605. doi: 10.1016/j.ces.2006.11.044.
- [118] L. Zhang, C. Yang and Z.-S. Mao, Unsteady motion of a single bubble in highly viscous liquid and empirical correlation of drag coefficient, Chem. Eng. Sci. 63, 8, 2008, 2099 - 2106. doi: 10.1016/j.ces.2008.01.010.
- [119] M. J. Sathe, I. H. Thaker, T. E. Strand and J. B. Joshi, Advanced PIV/LIF and shadowgraphy system to visualize flow structure in two-phase bubbly flows, Chem. Eng. Sci. 65, 8, 2010, 2431-2442. doi: 10.1016/j.ces.2009.11.014.
- [120] M. J. Sathe, C. S. Mathpati, S. S. Deshpande, Z. Khan, K. Ekambara and J. B. Joshi, Investigation of flow structures and transport phenomena in bubble columns using Particle Image Velocimetry and miniature pressure sensors, Chem. Eng. Sci. 66, 14, 2011, 3087-3107. doi: 10.1016/j.ces.2011.04.002.
- [121] M. J. Sathe, J. B. Joshi and G. Evans, Characterization of Turbulence in Rectangular Bubble Column, Chem. Eng. Sci. 100, 2013, 52-68. doi: 10.1016/j.ces.2013.01.004.
- [122] C. Meyer, M. Hoffmann and M. Schlüter, Micro-PIV analysis of gas-liquid Taylor flow in a vertical oriented square shaped fluidic channel, Int. J. Multiphase Flow 67, 0, 2014, 140 - 148. doi: <http://dx.doi.org/10.1016/j.ijmultiphaseflow.2014.07.004>.
- [123] M. D. Lundin and M. J. McCready, Modeling of bubble coalescence in bubbly co-current flows restricted by confined geometry, Chem. Eng. Sci. 64, 18, 2009, 4060 - 4067. doi: <http://dx.doi.org/10.1016/j.ces.2009.06.020>.
- [124] C. Acuna and J. Finch, Tracking velocity of multiple bubbles in a swarm, Int. J. Miner. Process. 94, 3-4, 2010, 147 - 158. doi: 10.1016/j.minpro.2010.02.001.

- [125] N. Hooshyar, P. J. Hamersma, R. F. Mudde and J. R. Ommenvan, Gas Fraction and Bubble Dynamics in Structured Slurry Bubble Columns, *Ind. Eng. Chem. Res.* 49, 21, 2010, 10689-10697. doi: 10.1021/ie100528c.
- [126] S. S. Rabha and V. V. Buwa, Experimental Investigations of Rise Behavior of Monodispersed/Polydispersed Bubbly Flows in Quiescent Liquids, *Ind. Eng. Chem. Res.* 49, 21, 2010, 10615-10626. doi: 10.1021/ie1006454.
- [127] S. Li, C. Zhu, T. Fu and Y. Ma, Study on the mass transfer of bubble swarms in three different rheological fluids, *Int. J. Heat Mass Transfer* 55, 21-22, 2012, 6010 - 6016. doi: <http://dx.doi.org/10.1016/j.ijheatmasstransfer.2012.06.011>.
- [128] E. Bouche, V. Roig, F. Risso and A. Billet, Homogeneous swarm of high-Reynolds-number bubbles rising within a thin gap. Part 1. Bubble dynamics, *J. Fluid Mech.* 704, 2012, 211-231. doi: 10.1017/jfm.2012.233.
- [129] E. Bouche, S. Cazin, V. Roig and F. Risso, Mixing in a swarm of bubbles rising in a confined cell measured by mean of PLIF with two different dyes, *Exp. Fluids* 54, 6, 2013, 1-9. doi: 10.1007/s00348-013-1552-0.
- [130] A. Mersmann, Auslegung und Maßstabsvergrößerung von Blasen- und Tropfensäulen, *Chem. Ing. Tech.* 49, 9, 1977, 679-691. doi: 10.1002/cite.330490902.
- [131] S. Rosenberger, K. Kubin and M. Kraume, Rheology of Activated Sludge in Membrane Bioreactors, *Eng. Life Sci.* 2, 9, 2002, 269-275. doi: 10.1002/1618-2863(20020910)2:9<269::AID-ELSC269>3.0.CO;2-V.
- [132] G. Keitel and U. Onken, Inhibition of bubble coalescence by solutes in air/water dispersions, *Chem. Eng. Sci.* 37, 11, 1982, 1635 - 1638. doi: 10.1016/0009-2509(82)80033-X.
- [133] C. J. Ribeiro and D. Mewes, The influence of electrolytes on gas hold-up and regime transition in bubble columns, *Chem. Eng. Sci.* 62, 17, 2007, 4501-4509. doi: 10.1016/j.ces.2007.05.032.
- [134] M. Maldonado, J. Quinn, C. Gomez and J. Finch, An experimental study examining the relationship between bubble shape and rise velocity, *Chem. Eng. Sci.* 98, 2013, 7 - 11. doi: 10.1016/j.ces.2013.04.050.
- [135] L. Zhong, M. Oostrom, M. Truex, V. Vermeul and J. Szecsody, Rheological behavior of xanthan gum solution related to shear thinning fluid delivery for subsurface remediation, *J. Hazard. Mater.* 244-245, 2013, 160 - 170. doi: 10.1016/j.jhazmat.2012.11.028.
- [136] N. Hooshyar, J. R. Ommenvan, P. J. Hamersma, S. Sundaresan and R. F. Mudde, Dynamics of Single Rising Bubbles in Neutrally Buoyant Liquid-Solid Suspensions, *Phys. Rev. Lett.* 110, 2013, 244501. doi: 10.1103/PhysRevLett.110.244501.
- [137] S. Pietsch, Untersuchung von Blasenschwärmen in einem rechtwinkligen Kanal mit Hilfe von Hochgeschwindigkeitskameraaufnahmen, Bachelor thesis, Technische Universität Berlin, (2014).
- [138] M. Raffel, C. Willert and J. Kompenhans, *Particle Image Velocimetry: a practical guide*, Springer Berlin, 2007.
- [139] C. Willert and M. Gharib, Digital particle image velocimetry, *Exp. Fluids* 10, 4, 1991, 181-193. doi: 10.1007/BF00190388.
- [140] J. Westerweel, Fundamentals of digital particle image velocimetry, *Meas. Sci. Technol.* 8, 12, 1997, 1379. doi: 10.1088/0957-0233/8/12/002.

- [141] E. Lenhart, Visualisierung der Strömungsverhältnisse beim Aufstieg von Einzelblasen in engen Kanälen mit Hilfe von Particle Image Velocimetry, Diploma thesis, Technische Universität Berlin, (2012).
- [142] L. Reiss and T. Hanratty, Measurement of instantaneous rates of mass transfer to a small sink on a wall, *AIChE J.* 8, 2, 1962, 245-247. doi: 10.1002/aic.690080223.
- [143] T. Papanastasiou, G. Georgiou and A. Alexandrou, *Viscous fluid flow*, CRC Boca Raton, 2000.
- [144] Y. Muzychka and J. Edge, Laminar Non-Newtonian Fluid Flow in Noncircular Ducts and Microchannels, *J. Fluids Eng.* 130, 11, 2008, 111201. doi: 10.1115/1.2979005.
- [145] V. Sobolik, J. Tihon, O. Wein and K. Wichterle, Calibration of electrodiffusion friction probes using a voltage-step transient, *J. Appl. Electrochem.* 28, 1998, 329-335. doi: 10.1023/A:1003224018571.
- [146] A. Margaritis, D. W. Bokkelt and D. G. Karamanev, Bubble rise velocities and drag coefficients in non-Newtonian polysaccharide solutions, *Biotechnol. Bioeng.* 64, 3, 1999, 257-266. doi: 10.1002/(SICI)1097-0290(19990805)64:3<257::AID-BIT1>3.0.CO;2-F.
- [147] H. Brauer, Particle-fluid transport process, in: *Fortschritte der Verfahrenstechnik* 17, VDI Verlag, 1979, pp. 61-99.
- [148] J. Harper, The motion of bubbles and drops through liquids, *Adv. Appl. Mech.* 12, 59, 1972, 129. .
- [149] D. Legendre, R. Zenit and J. Velez-Cordero, On the deformation of gas bubbles in liquids, *Phys. Fluids* 24, 4, 2012, 043303. doi: 10.1063/1.4705527.
- [150] V. Ambeskar and R. Mashelkar, On the role of stress-induced migration on time-dependent terminal velocities of falling spheres, *Rheol. Acta* 29, 3, 1990, 182-191. doi: 10.1007/BF01331354.
- [151] D. Joseph, Y. Liu, M. Poletto and J. Feng, Aggregation and dispersion of spheres falling in viscoelastic liquids, *J. Non-Newtonian Fluid Mech.* 54, 1994, 45-86. doi: [http://dx.doi.org/10.1016/0377-0257\(94\)80015-4](http://dx.doi.org/10.1016/0377-0257(94)80015-4).
- [152] P. Jonczyk, M. Takenberg, S. Hartwig, S. Beutel, R. G. Berger and T. Scheper, Cultivation of shear stress sensitive microorganisms in disposable bag reactor systems, *J. Biotechnol.* 167, 4, 2013, 370-376. doi: <http://dx.doi.org/10.1016/j.jbiotec.2013.07.018>.
- [153] C. Kähler, U. Scholz and J. Ortmanns, Wall-shear-stress and near-wall turbulence measurements up to single pixel resolution by means of long-distance micro-PIV, *Exp. Fluids* 41, 2006, 327-341. .
- [154] L. Böhm and M. Kraume, Investigation of single bubbles rising in narrow rectangular channels with Particle Image Velocimetry, *Proceedings of the 16th International Symposium on Applications of Laser Techniques to Fluid Mechanics*, Lisbon, Portugal, 2012.
- [155] P. M. Wilkinson, H. Haringa and L. L. V. Dierendonck, Mass transfer and bubble size in a bubble column under pressure, *Chem. Eng. Sci.* 49, 9, 1994, 1417-1427. doi: 10.1016/0009-2509(93)E0022-5.
- [156] T. Sanada, M. Watanabe and T. Fukano, Effects of viscosity on coalescence of a bubble upon impact with a free surface, *Chem. Eng. Sci.* 60, 19, 2005, 5372-5384. doi: 10.1016/j.ces.2005.04.077.
- [157] A. Chesters and G. Hofman, Bubble coalescence in pure liquids, *Appl. Sci. Res.* 38, 1, 1982, 353-361. doi: 10.1007/BF00385965.
- [158] Y. T. Shah, B. G. Kelkar, S. P. Godbole and W.-D. Deckwer, Design parameters estimations for bubble column reactors, *AIChE J.* 28, 3, 1982, 353-379. doi: 10.1002/aic.690280302.
- [159] N. Deen, R. Mudde, J. Kuipers, P. Zehner and M. Kraume, *Bubble Columns*, Ullmann's encyclopedia of industrial chemistry, Wiley-VCH Verlag GmbH & Co. KGaA, 2012, pp. 359-379.

- [160] G. Hewitt and D. Roberts, Studies of two-phase flow patterns by simultaneous X-ray and flash photography, AERE-M-2159, Atomic Energy Research Establishment, Harwell England, 1969.
- [161] P. Zehner and M. Kraume, Bubble Columns, Ullmann's encyclopedia of industrial chemistry, Wiley-VCH Verlag GmbH & Co. KGaA, 2005, pp. 1-34.
- [162] J. Hills, The operation of a bubble column at high throughputs: I. Gas holdup measurements, Chem. Eng. J. 12, 2, 1976, 89-99. doi: 10.1016/0300-9467(76)87002-5.
- [163] K. Akita and F. Yoshida, Bubble size, interfacial area, and liquid-phase mass transfer coefficient in bubble columns, Ind. Eng. Chem. Process Des. Dev. 13, 1, 1974, 84-91. doi: 10.1021/i260049a016.
- [164] Y. Kawase and M. Moo-Young, Theoretical prediction of gas hold-up in bubble columns with Newtonian and non-Newtonian fluids, Ind. Eng. Chem. Res. 26, 5, 1987, 933-937. doi: 10.1021/ie00065a014.
- [165] F. Viana, R. Pardo, R. Yanez, J. L. Trallero and D. D. Joseph, Universal correlation for the rise velocity of long gas bubbles in round pipes, J. Fluid Mech. 494, 2003, 379-398. doi: 10.1017/S0022112003006165.
- [166] K. Akita and F. Yoshida, Gas holdup and volumetric mass transfer coefficient in bubble columns. Effects of liquid properties, Ind. Eng. Chem. Process Des. Dev. 12, 1, 1973, 76-80. doi: 10.1021/i260045a015.
- [167] E. W. Llewellyn, E. Del Bello, J. Taddeucci, P. Scarlato and S. J. Lane, The thickness of the falling film of liquid around a Taylor bubble, Proc. R. Soc. London, Ser. A 2011, doi: 10.1098/rspa.2011.0476.
- [168] V. Sobolik, J. Tihon, J. Pauli and U. Onken, Sensitivity of three-segment electrodiffusion probes to eddy shedding, Exp. Fluids 16, 1994, 368-374. .
- [169] Y. Mizushima and T. Saito, Improving Practical Performance of Single-tip-optical-fibre Probing for Measurement of Bubble-Swarm Motion and Properties in a Large Diameter Bubble Column, Chem. Eng Trans. 32, 2013, 1513-1518. doi: DOI:10.3303/CET1332253.
- [170] R. Panckow, S. Maaß, J. Emmerich and M. Kraume, Automated quantification of bubble size distributions in an agitated air/water system, Chem. Ing. Tech. 85, 7, 2013, 1036-1045. doi: 10.1002/cite.201200228.



## 8 Appendix

### 8.1 Own publications and presentations

#### 8.1.1 Articles in Journals

Prieske, H., Böhm, L. Drews, A., Kraume, M., Optimised hydrodynamics for membrane bioreactors with immersed flat sheet membrane modules, *Desal. Water Treat.* 18, (2010) 270-276.

Böhm, L., Drews, A., Prieske, H., Bérubé, P. R. and Kraume, M., The importance of fluid dynamics for MBR fouling mitigation, *Bioresour. Technol.* 122, (2012) 50-61.

Böhm, L. and Kraume, M., Hydrodynamic investigation of single bubbles, *Czasopismo Techniczne Mechanika*, 190, 5, (2012) 21-29.

Böhm, L., Drews, A. and Kraume, M., Bubble induced shear stress in flat sheet membrane systems - Serial examination of single bubble experiments with the electrodiffusion method, *J. Membr. Sci.* 437, (2013) 131-140.

Böhm, L., Prieske, H. and Kraume, M., Fluid Dynamic Optimization of Flat Sheet Membrane Modules – Movement of Bubbles in Vertical Channels, *Chem. Eng. Trans.* 32, (2013) 1501-506.

Böhm, L., Jankhah, S., Tihon, J., Bérubé, P. and Kraume, M., Application of the electrodiffusion method to measure wall shear stress: Intergrating theory and practice, *Chem. Eng. Technol.* 37, 6, (2014) 938-950.

Böhm, L., Kurita, T., Kimura, K. and Kraume, M., Comparison of the rising behaviour of single bubbles in narrow rectangular channels in Newtonian and non-Newtonian liquids by serial examinations with a high speed camera, *Int. J. Multiphase Flow* 65, (2014) 11-23.

Böhm, L., and Kraume, M., Quantitative comparison of the single bubble ascent in a Newtonian and a non-Newtonian continuous phase: A phenomenological PIV study, *Exp. Fluids*, (2014) submitted.

L. Böhm and M. Kraume, Fluid dynamics of bubble swarms rising in Newtonian and non-Newtonian liquids in flat sheet membrane systems, *J. Membr. Sci.* 475, (2015) 533-544.

### 8.1.2 Presentations and Posters with publication in Proceedings

(\*presenting author)

Prieske, H., Böhm, L., \*Drews, A. and Kraume, M., Optimised hydrodynamics for membrane bioreactors with immersed flat sheet membrane modules. 5th IWA specialised membrane technology conference for water & wastewater treatment. Beijing, China, (2009) 1: 514-515. (Presentation)

Iversen, V., Hermann, S., Drews, A., Münz, J., Götz, G., Fatarella, E., Lesjean, B., \*Böhm, L. and Kraume, M., Textiles for the filtration of activated sludge in membrane bioreactors (MBRs), Filtech 2009. Wiesbaden, Germany. (2009) II: II-694 - II-701. (Presentation)

Prieske, H., \*Böhm, L., Drews, A. and Kraume, M., Improved deposition control for membrane bioreactors with immersed flat sheet membrane modules, Filtech 2009. Wiesbaden, Germany. (2009) II: II-615 - II-622. (Presentation)

\*Prieske, H., Böhm, L., Drews, A. and Kraume, M., Fluidodynamische Auslegung von Membranbioreaktoren unter dem Aspekt der effektiven Deckschichtkontrolle, 8. Aachener Tagung Wasser und Membranen. Aachen, Germany, R. A. Aachener Verfahrenstechnik, 52056 Aachen. Aachen, Die deutsche Bibliothek - CIP Einheitsaufnahme, (2009) 1: A16-1 - A16-10 (Presentation)

Böhm, L., Bérubé, P. and Kraume, M., Messung von Schubspannungen beim Aufstieg von Einzelblasen, ProcessNet-Jahrestagung 2010, Aachen, Germany, Chem. Ing. Tech. 82, (2010) 1397 - 1397. (Poster)

Böhm, L., Prieske, H., Bérubé, P. and Kraume, M., Investigation of single bubbles rising between parallel plates, Aachener Membran Kolloquium 2010, Aachen, Germany, Deutsche Nationalbibliothek: (2010) 791. (Poster)

\*Al-Shamary, L., Böhm, L., Kraume, M., Optimized hydrodynamics for membrane bioreactor with immersed flat sheet membrane modules, Filtech 2011, Wiesbaden, Germany, (2012).

\*Böhm, L. and Kraume, M., Investigation of single bubbles rising in narrow rectangular channels with Particle Image Velocimetry, 16th Int Symp on Applications of Laser Techniques to Fluid Mechanics, Lisbon, Portugal, (2012). (Presentation)

Böhm, L. and \*Kraume, M. (2012) Hydrodynamic investigation of single bubbles. 19th International Conference of Process Engineering and Chemical Plant Design 2012, Krakau, Poland. (Presentation)

\*Böhm, L., Prieske, H. and Kraume, M., Optimierung der Reinigung von Plattenmembranmodulen mittels Untersuchung der Schubspannung, DECHEMA Jahrestagung 2012, Karlsruhe, Germany, Chem. Ing. Tech., 84, 6, (2012) 1366. (Presentation)

Nguyen, L.A.T., Schwarze, M., Drews, A., Kraume, M., Schomäcker, R. and \*Böhm, L., Influence of Non-ionic Surfactants on Reverse Micellar-enhanced Ultrafiltration, Euromembrane 2012, London, Great Britain, Procedia Eng., 44, (2012) 1692-1694. (Poster)

Al-Shamary, L., Prieske, H., Kraume, M. and \*Böhm, L., Optimized Hydrodynamics for Membrane Bioreactors with Newtonian and non-Newtonian Fluids, Euromembrane 2012, London, Great Britain, Procedia Eng., 44, (2012) 723–724. (Poster)

Böhm, L. Prieske, H. and Kraume, M., Experimental and Numerical Investigation of Air Scouring Inside Flat Sheet Membrane Modules, Euromembrane 2012, London, Great Britain, Procedia Eng., 44, (2012) 535-536. (Presentation)

\*Böhm, L. and Kraume, M., Untersuchung des Aufstiegs von Einzelblasen in Newtonschen und nicht-Newtonschen Fluiden mittels PIV, 21st Fachtagung Lasermethoden in der Strömungsmesstechnik. München, Germany, (2013) 66-1 - 66-6. (Presentation)

Böhm, L., Prieske, H. and \*Kraume, M., Fluid Dynamic Optimization of Flat Sheet Membrane Modules – Movement of Bubbles in Vertical Channels, 11th International Conference on Chemical and Process Engineering, Milan, Italy, (2013). (Presentation)

\*Böhm, L. and Kraume, M., Von der Einzelblase zum Blasenschwarm – Eine Grundlagenuntersuchung im rechtwinkligen Kanal. ProcessNet Jahrestagung der Fachgemeinschaft Fluidodynamik und Trenntechnik, Würzburg, Germany. Chem. Ing. Tech. 85, (2013) 1423-1424 (Poster)

\*Böhm, L. and Kraume, M., Is it reasonable to use air-water model systems in fluid dynamic investigations of MBRs? 2nd International Workshop MBR for the next generation, Berlin, Germany, (2013). (Presentation)

Böhm, L. and \*Kraume, M., Einfluss der Flüssigkeitsrheologie auf das Blasenschwarmverhalten in Flachmembranmodulen, ProcessNet-Jahrestagung und 31. DECHEMA-Jahrestagung der Biotechnologen, Aachen, Germany. Chem. Ing. Tech. (2014). (Presentation)

### 8.1.3 Presentations and Posters without publication

(\*presenting author)

Böhm, L., Prieske, H. and Kraume, M., Numerische Simulation der Blasenbewegung zwischen ebenen Platten, Jahrestreffen der ProcessNet-Fachausschüsse Computational Fluid Dynamics, Mischvorgänge und Extraktion. Fulda, Germany, (2009). (Poster)

\*Böhm, L., Prieske, H., Drews, A. and Kraume, M., Optimization of bubble movement on flat sheet membrane modules, 3rd workshop on CFD modelling in MBR applications, Toulouse, France, (2009). (Presentation)

\*Böhm, L., Prieske, H., Bérubé, P.R. and Kraume, M., Optimierung eines Plattenmembranmoduls mittels Untersuchung des Aufstiegs von Einzelblasen zwischen Platten, ProcessNet Jahrestreffen der Fachausschüsse Lebensmittelverfahrenstechnik und Mehrphasenströmungen, Frankfurt, Germany, (2010). (Presentation)

Böhm, L., Prieske, H., Bérubé, P. and Kraume, M., Numerische und experimentelle Untersuchung des Aufstiegs von Einzelblasen zwischen senkrechten Platten, ProcessNet Jahrestreffen der Fachausschüsse Computational Fluid Dynamics und Wärme- und Stoffübertragung. Hamburg, Germany, (2010). (Poster)

Böhm, L., Prieske, H., Al-Shamary, L., Bérubé, P. and \*Kraume, M., Optimizing the cleaning of flat sheet membrane modules by numerical and experimental investigation of bubble movement between plates. AMS6/IMSTEC10. Sydney, Australia, (2010). (Presentation)

Prieske, H., Al-Shamary, L., Böhm, L. and \*Kraume, M., Optimised MBR design and aeration for enhanced deposition control, 3rd Oxford water and membrane research event, Oxford, Great Britain, (2010). (Presentation)

\*Böhm, L. and Kraume, M., Numerical and experimental investigation of the rise of bubbles in a rectangular channel with regard to membrane module optimization, Colloquium at the ASCR ICPF, Prague, Czech Republic, (2010). (Presentation)

\*Böhm, L. and Kraume, M., Improved deposition control for membrane bioreactors with immersed flat sheet membrane modules, Colloquium at the UBC Department of Civil Engineering, Vancouver, Canada, (2010). (Presentation)

\*Böhm, L., Prieske, H., Al-Shamary, L., Drews, A., Kraume, M., Investigation of bubble movement on flat sheet membrane modules, 4th workshop on CFD modelling in MBR applications, Aachen, Germany, (2011). (Presentation)

Bentzen, T.R., Ratkovich, N., \*Böhm, L., Rasmussen, M.R., Numerical modelling of two types of MBR, 4th workshop on CFD modelling in MBR applications, Aachen, Germany, (2011). (Presentation)

\*Böhm, L., Jankhah, S., Bérubé, P. R., and Kraume, M., Optimization of the fouling mitigation in membrane systems – A collaborative approach for flat sheets and hollow fibres, 6th IWA Specialist Conference on Membrane Technology for Water & Wastewater Treatment, Aachen, Germany, (2011). (Presentation)

Böhm, L., Prieske, H., and \*Kraume, M., Determination of shear stress around single bubbles between flat sheet membranes, 1st international symposium on Multiscale Multiphase Process Engineering (MMPE) Kanazawa, Japan, (2011). (Poster)

Böhm, L. and \*Kraume, M., Bestimmung der durch Einzelblasen erzeugten Scherraten in rechtwinkligen Kanälen, ProcessNet Jahrestreffen der Fachgruppen Mischvorgänge und Mehrphasenströmungen, Weimar, Germany, (2012). (Poster)

\*Böhm, L. and Kraume, M., Untersuchung des Aufstiegs von Einzelblasen in rechtwinkligen Kanälen mittels Hochgeschwindigkeitskamera, ProcessNet Jahrestreffen der Fachgruppen Extraktion und Mehrphasenströmungen, Baden-Baden, Germany, (2013). (Poster)

\*Böhm, L. and Kraume, M., A fundamental investigation of single bubble and bubble swarm behavior with respect to fouling prevention in membrane systems, AIChE Annual Meeting 2013, San Francisco, USA, (2013). (Presentation)

Prieske, H., Böhm, L. \*Drews, A. and Kraume, M., Hydrodynamics of non-Newtonian fluids in MBR with flat sheet modules, 10. Aachener Tagung Wasser und Membranen, Aachen, Germany, (2013). (Presentation)

\*Böhm, L. and Kraume, M., Bubble induced flow in flat sheet membrane systems - Serial examination of single bubble experiments, Torino Membrane Symposium - Membranes for liquid separation and water treatment: Environmental applications and future perspectives, Torino, Italy, (2013). (Presentation)

\*Böhm, L. and Kraume, M., Untersuchung des Blasenschwarmverhaltens in Newtonschen und nicht-Newtonschen Fluiden, ProcessNet Jahrestreffen der Fachgruppen Mehrphasenströmungen und Wärme- und Stoffübertragung, Fulda, Germany, (2014). (Presentation)

\*Böhm, L. and Kraume, M., Influence of the liquid rheology on the behavior of bubble swarms in flat sheet membrane modules, DECHEMA Infotag Membrantechnik „Neuentwicklungen Cross Flow Filtration - Membranen, Module und Prozesse“, Frankfurt a.M., Germany, (2014). (Poster)

\*Böhm, L. and Kraume, M., Mass transfer from bubbles to reactive liquid phases, 2nd International Symposium on Multiscale Multiphase Process Engineering (MMPE), Hamburg, Germany, (2014). (Poster)

\*Böhm, L. and Kraume, M., Bubble swarms rising in Newtonian and non-Newtonian liquids, 2nd International Symposium on Multiscale Multiphase Process Engineering (MMPE), Hamburg, Germany, (2014). (Poster)

Böhm, L. and \*Kraume, M., Wall shear stress generated by bubble swarms in Newtonian and non-Newtonian liquids, AIChE Annual Meeting 2014, Atlanta, USA, (2014). (Presentation)

### 8.1.4 Supervised student projects

Fleck, A., Bestimmung der Scherspannung beim Aufstieg von Einzelblasen in engen Kanälen mit Hilfe der Elektrodiffrusionsmethode. Bachelor thesis, (2010).

Karsten, T., Automatisierung der Messung von Scherspannungen beim Aufstieg von Einzelblasen in engen Kanälen. Bachelor thesis, (2011).

Kolev, N., Messung der Scherraten beim Aufstieg von Einzelblasen. Intership, (2011).

Lenhart, E., Visualisierung der Strömungsverhältnisse beim Aufstieg von Einzelblasen in engen Kanälen mit Hilfe von Particle Image Velocimetry. Diploma thesis, (2012).

Ruiken, J.P., Messung und Auswertung von Scherspannungen beim Aufstieg von Einzelblasen in engen Kanälen. Bachelor thesis, (2012).

Kolev, N., Auswertung der Strömungsverhältnisse beim Aufstieg von Einzelblasen in engen Kanälen mit Hilfe von Particle Image Velocimetry. Bachelor thesis, (2012).

Sowerwine, K., Investigation of the rise of single bubbles with a high speed camera. Internship, (2012).

Schallau, P., Untersuchung des Aufstiegs von Einzelblasen in einem rechtwinkligen Kanal mit Hilfe von Hochgeschwindigkeitskameraaufnahmen. Bachelor thesis, (2013).

Kurita, T., High speed camera investigation of the rise of single bubbles in non-Newtonian liquids. Intership, (2013).

Kohtz, S., Untersuchung des Einflusses von Wänden und der Rheologie auf den Aufstieg von Einzelblasen mit Hilfe der Particle Image Velocimetry. Diploma thesis, (2014).

Pietsch, S., Untersuchung von Blasenschwärmen in einem rechtwinkligen Kanal mit Hilfe von Hochgeschwindigkeitskameraaufnahmen. Bachelor thesis, (2014).

Wörtzel, J., Messung von Scherspannungen beim Aufstieg von Einzelblasen in nicht-Newtonschen Medien. Internship, (2014).

Sobocinski, P., Untersuchung von Blasenschwärmen in einem rechtwinkligen Kanal mit Hilfe der Elektrodiffrusionsmethode. Bachelor thesis, under review (2014).

## 8.2 Own publications used for the cumulative thesis (full text)

This thesis is based on the following publications which are ordered chronologically.

- [1] L. Böhm, A. Drews, H. Prieske, P. Bérubé and M. Kraume, The importance of fluid dynamics for MBR fouling mitigation, *Bioresour. Technol.* 122, (2012) 50 - 61
- [2] L. Böhm and M. Kraume, Hydrodynamic investigation of single bubbles (presented at the 19th International Conference of Process Engineering and Chemical Plant Design, Krakow, Poland), *Czasopismo Techniczne Mechanika* 109, 5 (2012) 21-29
- [3] L. Böhm, A. Drews and M. Kraume, Bubble induced shear stress in flat sheet membrane systems - Serial examination of single bubble experiments with the electrodiffusion method, *J. Membr. Sci.* 437, (2013) 131-140
- [4] L. Böhm, H. Prieske and M. Kraume, Fluid dynamic optimization of flat sheet membrane modules - movement of bubbles in vertical channels (presented at the 11th International Conference on Chemical and Process Engineering, Milan, Italy), *Chem. Eng. Trans.* 32, (2013) 1501-1506
- [5] L. Böhm, S. Jankhah, J. Tihon, P. Bérubé and M. Kraume, Application of the electrodiffusion method to measure wall shear stress: Intergrating theory and practice, *Chem. Eng. Technol.* 37, 6 (2014) 938-950
- [6] L. Böhm, T. Kurita, K. Kimura and M. Kraume, Rising behaviour of single bubbles in narrow rectangular channels in Newtonian and non-Newtonian liquids, *Int. J. Multiphase Flow* 65, (2014) 11-23
- [7] L. Böhm and M. Kraume, Quantitative comparison of the single bubble ascent in a Newtonian and a non-Newtonian continuous phase: A phenomenological PIV study, *Exp. Fluids* submitted, (2014)
- [8] L. Böhm and M. Kraume, Fluid dynamics of bubble swarms rising in Newtonian and non-Newtonian liquids in flat sheet membrane systems, *J. Membr. Sci.* 475, (2015) 533-544